Electron Microscopy of Nanostructures in Cells

Køble, Carsten

Publication date:
2014

Document Version
Publisher's PDF, also known as Version of record

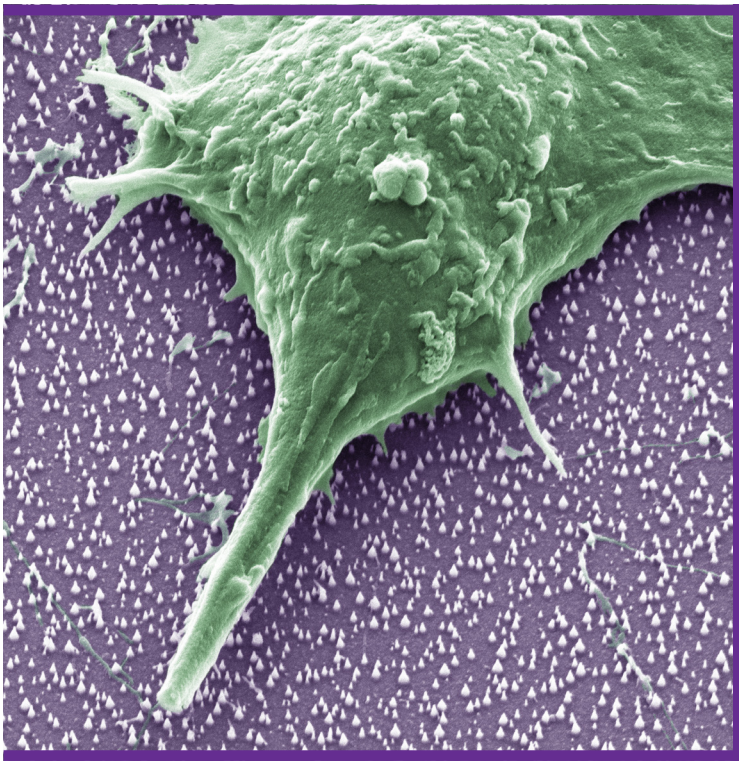

Electron Microscopy of Nanostructures in Cells

Carsten Køhler
PhD Thesis August 2014

DTU Nanotech
Department of Micro- and Nanotechnology

Electron Microscopy of Nanostructures in Cells

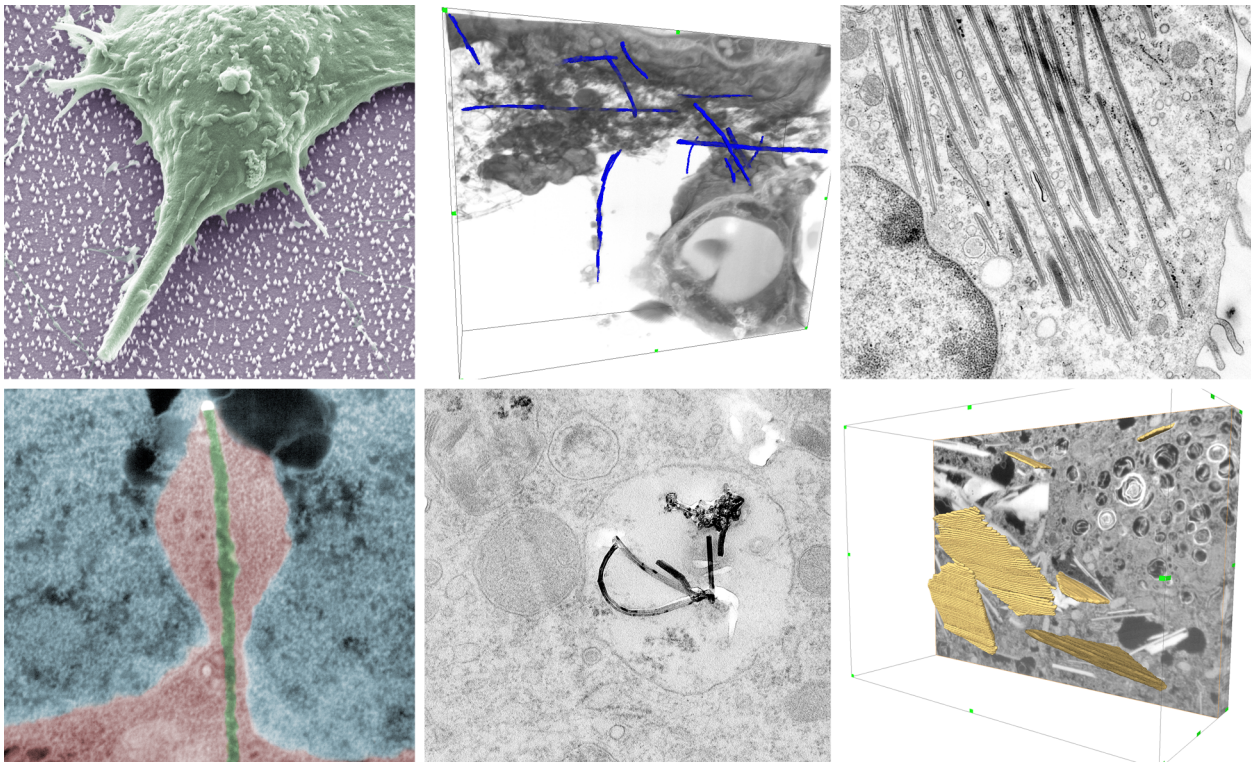

Ph.D. Thesis by Carsten Køhler

August 2014

Department of Micro- and Nanotechnology

Technical University of Denmark

Front page picture from the top left: Dried cell on nanostructures. CNT traced (blue) in lung tissue. ECP crystals in alveolar macrophage. Green nanowire in a fibroblast. CNTs in vesicles. 3D FIB-SEM image of ECP crystals in an alveolar macrophage.

Preface

In this thesis the main results obtained during my Ph.D. project are described. Work was mainly carried out at the Department of Micro- and Nanotechnology, Technical University of Denmark (DTU Nanotech). Electron microscopy was carried out at Center for Electron Nanoscopy (DTU CEN) and at the Core Facility for Integrated Microscopy at Copenhagen University. Additionally, The Food & Environment Research Agency (York, UK) was visited and minor experiments carried out at Lund University (Lund, Sweden).

I have been supervised by Associate professor Kristian Mølhave from DTU Nanotech, Professor Klaus Qvortrup from University of Copenhagen, and Professor Ulla Vogel from the National Research Centre for the Working Environment (NRCWE). My primary work has been funded by DTU Nanotech, DTU CEN, and NRCWE while some travel expenses have been covered by the Otto Mønsted foundation.

First and foremost I would like to thank my three supervisors: Kristian for always being positive and having a thousand ideas to share and for being attentive of the person behind the Ph.D. student; Klaus for his helpfulness and readiness to share his knowledge, and of course also for not getting too upset when we ruined his brand new 30,000 DKK diamond knife; and Ulla for her toxicological expertise and for providing interesting samples capable of destroying expensive diamond knives.

I would also like to thank all the people that have helped with practical support and fruitful discussions during the past three years. In particular, senior researcher Anne Saber and Ph.D. student Sarah Søs Poulsen from NRWCE, Adam Fuller and Louise Jensen from DTU CEN together with Ramon Liebrechts, Zhila Nikrozi and the rest of the staff at the Core Facility for Integrated Microscopy (CFIM) at the University of Copenhagen.

For the past three years, my project has been enriched by collaborations. To name a few: Ph.D. student Henrik Persson, Associate professor Christelle Prinz both from Lund University, together with people from the FP7-Nanolyse project, NRCWE and DTU Environment.

Thanks to the Molecular Windows group, which I have now had the pleasure of being part of for more than 4 years during my master and Ph.D. project. Finally, I would like to thank my family and friends for their support and my girlfriend for her understanding and affection.

Table of Contents

Preface ..... **iii**
Abstract ..... **v**
Resumé (dansk) ..... **vi**
List of publications ..... **vii**
1 Introduction **9**
1.1 Nanostructures 10
1.2 Toxicity of nanostructures 14
1.3 Project goals and thesis outline 18
2 Nanostructure visualisation methods in soft matter **19**
2.1 Light microscopy 19
2.2 Electron microscopy 22
2.3 Sample preparation for Biological electron microscopy 27
2.4 Electron microscopes used in this thesis 32
3 Cellular interactions with nanostructured substrates **37**
3.1 State-of-art 37
3.2 Paper I 41
3.3 Paper VI summary 58
3.4 Summary 60
4 Electron microscopy of CNTs in lung tissue **61**
4.1 Tissue fixation 61
4.2 Paper II 62
4.3 CNT contrast 76
4.4 Summary 76
5 CNT distribution and interaction with exposed mouse lung **77**
5.1 Cells of the respiratory system 77
5.2 Paper III 79
5.3 Additional notes on ECP crystals and Chi3L3 94
5.4 Summary 95
6 Conclusion & outlook **97**
6.1 Outlook 98
7 Appendices **101**
Dissemination activities 101
List of publications 103
Selected supplementary information for Paper I 105
Carbon nanotube characteristics 110
Additional structures and cells found in lung tissue 111
Selected supplementary information for Paper III 112
Other projects 115
Bibliography **119**

Abstract

Nanostructures are small objects with a huge potential. They can be engineered in an endless number of different shapes and sizes and have almost as many future uses. Nanostructures have recently garnered an increasing interest from the life-sciences as nanostructures have the potential to be used in brain-machine interfaces, for drug delivery and for interfacing with cells. The potential health risks associated with nanostructures are also becoming a more pressing issue with the increased production and use of nanostructures. Developing and testing tools for visualising nanostructures interacting with cells is therefore increasingly more relevant from both an engineering and a toxicological viewpoint.

My work involves developing and exploring electron microscopy (EM) for imaging nanostructures in cells, for the purpose of understanding nanostructure-cell interactions in terms of their possibilities in science and concerns in toxicology.

In the present work, EM methods for imaging nanostructure-cell interactions have been explored, and the complex interactions documented and ordered. In particular the usability of the focused ion beam scanning electron microscope (FIB-SEM) was explored. Using EM techniques, unique images aiding in the interpretation of nanostructure's influence on cells have been provided. For instance, FIB-SEM showcased how nanowires perturbed the nuclear envelope, and helped establish that nanowires can be enveloped by a thin outer membrane deep within the cell.

With respect to the concern of nanostructure toxicology, we have focused on investigating the time effects and visualising the interaction of carbon nanotubes (CNTs) with lung tissue. A basic CNT distribution development model was developed, and the investigations helped verify observations made using single cells in literature. Furthermore, EM proved valuable as it revealed an unnoticed CNT effect. FIB-SEM helped establish that the effect was linked to eosionophilic crystalline pneumonia (ECP).

Resumé (dansk)

Nanostrukturer er små objekter med et stort potentiale. Især indenfor bioteknologien har vi i de seneste år set en øget interesse for nanostrukturer, da de har potentiale for at kunne bruges til at undersøge cellers fundamentale virkemåde, ved at skabe elektroder der kan måle og påvirke individuelle celler. Der er dog også mulige helbreds risici forbundet med nanostrukturer, da en øget produktion og udbredelse af nanostrukturer gør, at vi mennesker har større risiko for at blive eksponeret. Vigtigheden af at udvikle metoder til at visualisere nanostrukturer i biologiske prøver er derfor voksende, da disse skal bruges til at udvikle nanostrukturelle apparater og undersøge deres toksiske effekter.

Mit projekt omhandler netop udviklingen og undersøgelsen af elektron mikroskopiske (EM) metoder for at visualisere nanostrukturer i celler, både i forbindelse med nanostrukturers muligheder og deres potentielle negative effekter. Ved at bruge FIB-SEM, en EM teknik som gør brug af både elektroner og ioner, er der især blevet fokuseret på at skaffe unikke billeder af cellers interaktion med nanostrukturer. De cellulære interaktioner som vi har observeret, er blevet dokumenteret og organiseret, og skal bruges til at øge vores forståelse af interaktionerne.

Visualiseringen af mulige toksiske effekter er foretaget i lunger, som er eksponeret med kulstof nanorør (CNTs). Her undersøgte vi effekten af CNTs på tre forskellige tidspunkter, og udarbejdede en model, for hvorledes CNT distributionen ændrede sig over tid. EM afslørede en hidtil ukendt effekt af CNT eksponeringen i form af krystallinske strukturer i makrofager. Genekspression, transmissions-EM og FIB-SEM hjalp med at afgøre, at de krystallinske strukturer var forbundet med eosinofilt krystallinsk lungebetændelse (ECP).

List of publications

Key papers

The thesis is based on the following key papers:

I Wierzbicki R[§], Købler C[§], Jensen MRB, Łopacińska J, Schmidt MS, et al. (**2013**). *Mapping the Complex Morphology of Cell Interactions with Nanowire Substrates Using FIB-SEM*. PLoS ONE.

II Købler C, Saber AT, Jacobsen NR, Wallin H, Vogel U, et al. (**2014**). *FIB-SEM imaging of carbon nanotubes in mouse lung tissue*. Analytical and Bioanalytical Chemistry.

III Købler C, Poulsen SS, Saber AT, Jacobsen NR, Wallin H, et al. (**Ready for submission**). *Subcellular distribution and effects of carbon nanotubes in mouse lung over time*.

Additional papers

Additionally, I have contributed to the following peer-reviewed papers:

IV Łopacińska JM, Grădinaru C, Wierzbicki R, Købler C, Schmidt MS, et al. (**2012**). *Cell motility, morphology, viability and proliferation in response to nanotopography on silicon black*. Nanoscale.

V Jensen E, Købler C, Jensen PS, Mølhave K (**2013**). *In-situ SEM microchip setup for electrochemical experiments with water based solutions*. Ultramicroscopy.

VI Persson H, Købler C, Mølhave K, Samuelson L, Tegenfeldt JO, et al. (**2013**). *Fibroblasts Cultured on Nanowires Exhibit Low Motility, Impaired Cell Division, and DNA Damage*. Small.

VII Loeschner K, Navratilova J, Købler C, Mølhave K, Wagner S, et al. (**2013**). *Detection and characterization of silver nanoparticles in chicken meat by asymmetric flow field flow fractionation with detection by conventional or single particle ICP-MS*. Analytical and Bioanalytical Chemistry.

VIII Poulsen SS, Jacobsen NR, Labib S, Wu D, Købler C, et al. (**2013**). *Transcriptomic Analysis Reveals Novel Mechanistic Insight into Murine Biological Responses to Multi-Walled Carbon Nanotubes in Lungs and Cultured Lung Epithelial Cells*. PLoS ONE.

IX Poulsen SS, Saber AT, Williams A, Andersen O, Købler C, et al. (**Submitted to ACS Nano**). *Different lengths of multi-walled carbon nanotubes cause similar effects in inflammatory response pathways, but differences in the expression of genes involved in fibrosis in mouse lung*.

X Loeschner K, Navratilova J, Grombe R, Linsinger TPJ, Købler C, et al. (**Submitted to Food Chemistry**). *In-house validation of a method for determination of silver nanoparticles in chicken meat based on asymmetric flow-field flow fractionation and ICP-MS detection*.

§ Co-first author

Chapter 1

Introduction

Since Richard Feynman's now famous speech about the potential of nanotechnology in 1959, researchers around the world have been involved in transforming the concept of nanotechnology into a science and an industry.

Nanotechnology has now progressed so much that engineered nanostructures are believed to be able to play an integral part in biotechnology and medicine. For instance, nanostructues have the potential to improve brain-machine interfaces, thereby allowing finer manipulation of prosthetic limbs and aide in treating neurological disorders. However, to design nanostructures for interfacing with biological cells or tissue, we need to understand how they interact on the nanoscale. In addition, as the capability of producing nanostructures has developed, nanostructure availability and usage is increasing in both industrial production and in consumer products. This results in an increased human exposure to engineered nanostructures, and may cause toxicity if the body is not able to clear or degrade the nanostructures effectively. To comprehend the possible dangers and to investigate what happens in the body when exposed to nanostructures, we need to uncover the nanoscale interactions between cells and nanostructures.

One way of elucidating the nanoscale interactions is to image those using microscopes, which is the main focus of this thesis. Conventional light microscopes are limited by the wavelength of visible light in accordance to the diffraction limit, which is a fundamental factor influencing the obtainable resolution of microscopes as stated by Ernst Abbe in 1873. This means that the resolution of conventional light microscopes is limited to about 200-300 nm, and since nanostructures are typically below 100 nm, hence imaging of nanostructures using conventional techniques is not feasible. Instead, microscopy of nanosized objects was made possible with the invention of the electron microscope by Max Knoll and Ernst Ruska in 1931. Electron microscopes use electrons instead of photons for producing images. Since electrons can have wavelengths in the sub-picometre range compared to the hundreds of nanometres for visible light, the diffraction limit is drastically lowered, and this allows for sub-nanometre resolution in state-of-art electron microscopes.

My Ph.D. project revolves around imaging the interaction between nanostructures and cells, and exploring electron microscopy techniques. Therefore, I will give a short introduction to the investigated nanostructures and describe why we would want to deliberately expose cells to nanostructures (Section 1.1). Some of the concerns regarding nanoparticle toxicity will also be discussed (Section 1.2). Finally, this chapter will describe my project goals and an outline of the thesis.

1.1 Nanostructures

Nanostructures come in many shapes and sizes, and are basically any structures having one or more dimensions in the nanoscale (typically 1-100 nm). Nanostructures can be comprised of metals, organic, and non-organic components. Today, there are a variety of methods for manufacturing nanostructures. It can be as simple as mixing a few chemicals or as complex as requiring expensive equipment. Nanostructures can also be found in nature, for instance DNA and proteins in cells are in the nanoscale and so are some of the structures on the scales of certain butterflies. Natural nanostructures have been studied and imaged for many years and although we do not fully understand how all cells, genes or proteins function, many of the nanoscopic structures have been uncovered and methods for further study have been developed. Therefore, for studying nanostructures inside cells, the scope of this thesis has been limited to considering man-made nanostructures, as these have potential in developing revolutionary devices and serve as a new potential health hazard.

The focus of this Ph.D. project has been placed on two different kinds of nanostructures, namely: nanowire substrates and free carbon nanotubes. In the following, the reason for choosing these nanostructures, together with their possible applications and how they can be fabricated will be described.

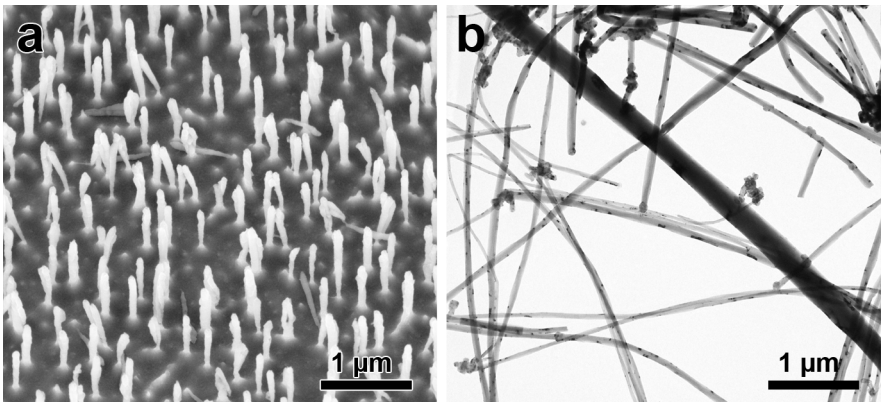

Illustration 1.1: Electron microscopy images of nanostructures. A) Scanning electron microscopy (SEM) of silicon nanostructures on a substrate. C) Transmission electron microscopy (TEM) of carbon nanotubes on a thin film.

1.1.1 Nanowire substrates

Nanowires are nano-sized structures with a large height to width aspect ratio. They are typically made from semiconductor materials (silicon, gallium phosphide, etc.), but can also contain metals and are manufactured using a wide range of micro- and nanofabrication methods [1]. Nanowires have the potential to be used for high performance solar cells [2], energy storage [3] and sensors [4].

Nanowire substrates were chosen due to the increasing amount of interest they are gaining in cell biology. Nanowires can for instance be used in bioelectronic interfaces, where the high sensitivity of the nanowire sensors and their nanometre scale can be used to investigate the propagation of nerve signals. Current bioelectronic interfaces rely on micrometre to milimetre large electrodes to manipulate prosthetic limbs and treat neurological disorders (e.g. Parkinson's disease, OCD and depression). Since one square milimetre of brain tissue contains about 1 million neurons [5], the current technology is

limited to coarse large-scale investigations. Nanowires are per definition very thin, and they can therefore be placed in dense arrays making it possible to follow neuronal signals at high spatial resolution in the future [6]. In addition, the size of the nanowires means that they can be less intrusive and can be incorporated intracellularly thereby increasing the signal-to-noise ratio of the bioelectronic interface [5]. In fact, Suyatin et al., experimented with using a nanowire based electrode for neural recordings in an anaesthetised rat (Illustration 1.2 a). Although they did not have read-out from individual nanowires they managed to obtain repeated neuronal readings as a proof of concept [7].

Nanowire substrates can also be used in the development of biomolecular delivery methods [8]–[10]. Biomolecular delivery is used to study cellular functions by introducing molecules such as DNA and proteins and observing how the cell responds (Illustration 1.2 b). Nanotechnology can be used to produce small unobtrusive structures that can penetrate cultured cells and introduce biomolecules to cells at a higher efficiency and with minimal physical damage. Furthermore, nanostructured substrates also have potential for controlling cell differentiation, movement and growth [11]–[15].

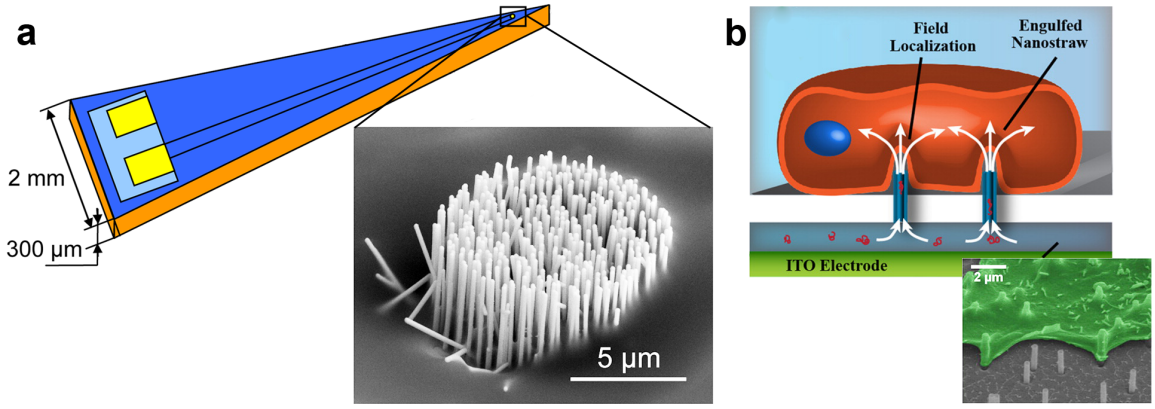

Illustration 1.2: A) Sketch of device used for neurological recordings in a rat brain. The insert, shows a SEM image of the nanowire electrode. Adapted from Suyatin et al., 2013. B) A principle sketch of biomolecular delivery into a cell using an underlying channel, and a SEM image showing a cellular membrane (green) interfacing with nanowire substrate. Adapted from Xie et al., 2013.

To engineer nanostructured devices that can be used for biological applications, we need to start mapping and characterising the nanowire-cell interactions by electron microscopy. However, one of the challenges in imaging cells interfacing with nanostructured substrates is that the substrates themselves often provide certain obstacles when processing for electron microscopy. Therefore part of this thesis is focused on developing and testing electron microscopy methods for imaging cells cultured on nanowire substrates (Chapter 3).

The substrates chosen in this work were manufactured using two different methods, involving either VLS-growth (Paper VI) or RIE etching (Paper I and IV). Vapour-liquid solid (VLS) growth is obtained using catalytic particles, which in our case were deposited randomly on the substrate. The nanowire sizes are determined by the size of the catalytic particle used for growth. The catalytic particle is melted at elevated temperatures and saturated with precursor gases whose components precipitate in the liquid-solid phase resulting in the growth of nanostructures [14], [16] (Illustration 1.3). VLS growth can produce tall and very high aspect ratio nanowires, and can also be used to produce nanowires in periodic arrays by the controlled placement of catalytic particles.

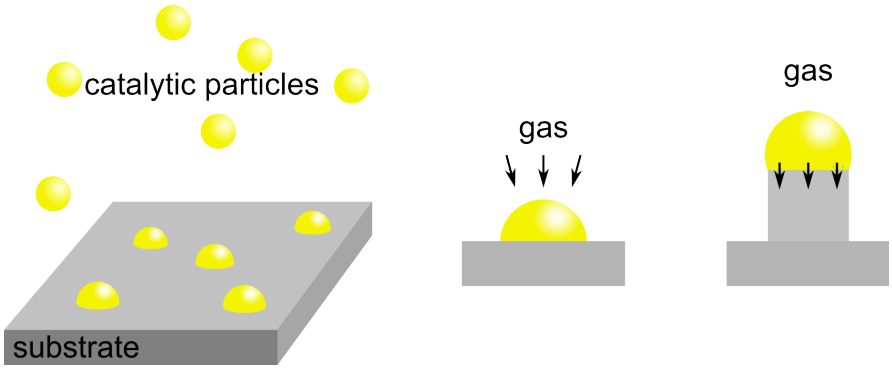

Illustration 1.3: Sketch of how the VLS process can be used to make nanostructures. Particles are deposited on the substrate, the precursor gases introduced which precipitates via the catalysts and forms the nanostructures.

In the unmasked reactive-ion etching process (RIE), there is no use of catalytic particles; rather the structures are formed by the removal of material not protected by micromasks during plasma etching. Micromasks are for example dirt and native oxide on the substrate, but are also created in the process when ions occasionally sputter and ion oxidise material from the surface which redeposit on the substrate [17], [18]. In a process where the substrate is etched and passivated (protected), material is preferably removed directionally (anisotropically), forming nanostructures under the right conditions called silicon black or nanograss [17], [19], also see Illustration 1.1 a. By tweaking the growth conditions, the size, density and shape of the nanostructures can be altered, but it is inherently a random process.

1.1.2 Carbon nanotubes

Carbon nanotubes (CNTs) are high aspect ratio nanostructures, which consist of cylindrically ordered graphene layers (Illustration 1.4 a), and were first discovered about 50 years ago [20]. CNTs have single- or multiple rolled up sheets of graphene and are appropriately named single walled CNTs (SWCNT) or multi-walled CNTs (MWCNT).

Diameters typically range from 0.8-2 nm and 5-100 nm for SWCNT and MWCNTs respectively, while they can be less than 100 nm long and up to several centimetres long [21]. CNTs can have a wide variety of physical and chemical characteristics, but are generally known for their excellent mechanical and electrical properties. Individual CNTs have been reported as reaching tensile strengths up to 20 times larger than steel, while others are more thermally conductive than diamond [21]. Single or ordered CNTs can be used in transistors, biosensors or actuators [21]–[23].

In biology, CNTs are also considered as intracellular electrodes, and for biomolecular delivery [24]. However, since ordering and making uniform CNTs is challenging, the bulk of the current production focuses on implementing disordered CNTs in composite materials.

CNTs can be added to composite materials to increase the electrical conductance or strength of the material. Even adding small amounts of CNTs to epoxy resin can increase the fracture toughness significantly [25], this can for instance be used to produce stronger and lighter wind turbine blades. Outside of composite materials, disordered CNTs have the potential for decreasing the catalyst usage in fuel cells, and for purifying contaminated water [21].

The increased use of CNTs in products is giving rise to increasing concerns about unintentional and harmful human exposure. Therefore, to compliment the investigations of nanowire interactions with cells, I also focus on imaging unintentional biological exposure to nanostructures. CNTs in this thesis are therefore mainly studied in relation to their potential toxicity and interaction with the immune system (Section 1.2) – this is achieved by studying the CNT deposition in mice lungs. For imaging CNTs in lungs, the composition of the CNTs and their mechanical strength give rise to some additional challenges which will be discussed in Chapter 4.

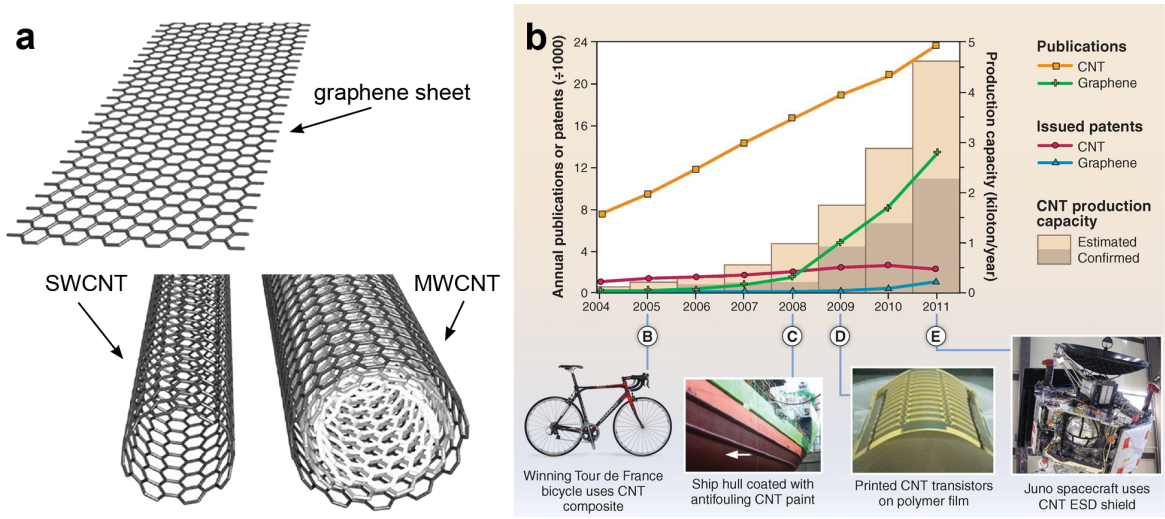

Illustration 1.4: A) Sketch of graphene, SWCNT and MWCNT. Graphene is a single atomic layer of carbon atoms placed in a hexagonal pattern. SWCNT and MWCNTs are respectively a single or multiple graphene sheets rolled into a tube. Adapted from Graham et al., 2005. B) Graph showing the increased number of publications and the production capacity until 2011, along with images of CNT uses. Image from De Volder et al., 2013.

In principle fabrication of carbon nanotubes is quite simple, and only requires energy, available carbon molecules and a place for them to form which preferably acts as a catalyst. For example 20-60 nm diameter wide carbon nanotubes (along with other carbon structures) can be formed on a nichrome[1] wire placed in a methane flame for about 15 minutes (Yuan et al., 2001). Simply making CNTs is therefore fairly easy; the complicated part is being able to control CNT synthesis for uniformity and placement and at low costs. For this, the chemical vapour deposition (CVD) method has become the dominant CNT production method [21].

CVD growth of CNTs involves catalytic particles such as nickel, cobalt or iron which are deposited on the substrate, the size of which influences the diameter of the CNTs. In much the same manner as VLS growth described previously, the sample is heated and gasses containing carbon are led into the chamber which breaks apart at the catalyst interface and forms CNTs. By tweaking the catalyst material and the growth conditions the number of imperfections, impurities, CNT lengths, and the number of walls can be controlled to a certain degree [26]. In addition, instead of obtaining randomly oriented CNTs it is possible to let them grow vertically by applying a strong electric field.

1 Non-magnetic alloy composed of nickel, chromium, and iron.

1.2 Toxicity of nanostructures

Particle toxicology started out in the early 20th century by investigating the effects of particle exposure when mining quartz, coal and asbestos. In the 1980s and 1990s focus was directed towards the toxicity of glass fibres and environmental particles. Today, the commercialisation of nanostructures has meant that 'nanotoxicology' dominates the field of toxicology [27].

Some of the first evidence of size dependent toxicity was found in the 1990s by Oberdörster and Ferin. Compared to 250-500 nm sized particles, larger pulmonary inflammation and particle translocation[2] were observed in rats exposed to 20 nm particles [28], [29]. Several examples of particle size dependent toxicity then followed for materials such as PTFE, polystyrene and TiO_2 particles [30]–[32]. The reason for this increased effect in toxicity appear to be related to the larger specific surface area (surface area per mass) for smaller particles. Therefore, it was suggested that toxicity should be related to the total surface area of the exposure rather than the mass [30], [32].

Besides their potential larger reactivity, smaller particles stay airborne for longer and can potentially be inhaled deeper into the lung. Depending on particle size and shape, deposition in the lungs is dominated by impaction, sedimentation, or diffusion [33]. Larger particles are deposited in the upper airways due to impaction or sedimentation, whereas smaller particles can reach the lower airway passages and deposit via Brownian diffusion, thereby overwhelming the immune system (Illustration 1.5). This is naturally very concerning as pulmonary exposure is considered to be one of the most important pathways into the body for unintentional exposures – which is why CNT interaction with lungs is studied in this work.

So size does matter, which explains the increasing interest in 'nanotoxicology'. However, it is also important to note that so far there has not been observed any drastic toxicity increase simply due to the particles being smaller than a certain size. Instead, the toxic pathways are similar to larger particles and the observed effects are a gradual magnification of intrinsic toxicity related to the material [34]. Nanoparticles are therefore not inherently toxic due to their size, but their toxicity is dependent on shape, chemistry, surface properties, persistence, etc.

2 A transfer of nanoparticles from one system to another, e.g. from the pulmonary to the circulatory or lymphatic system.

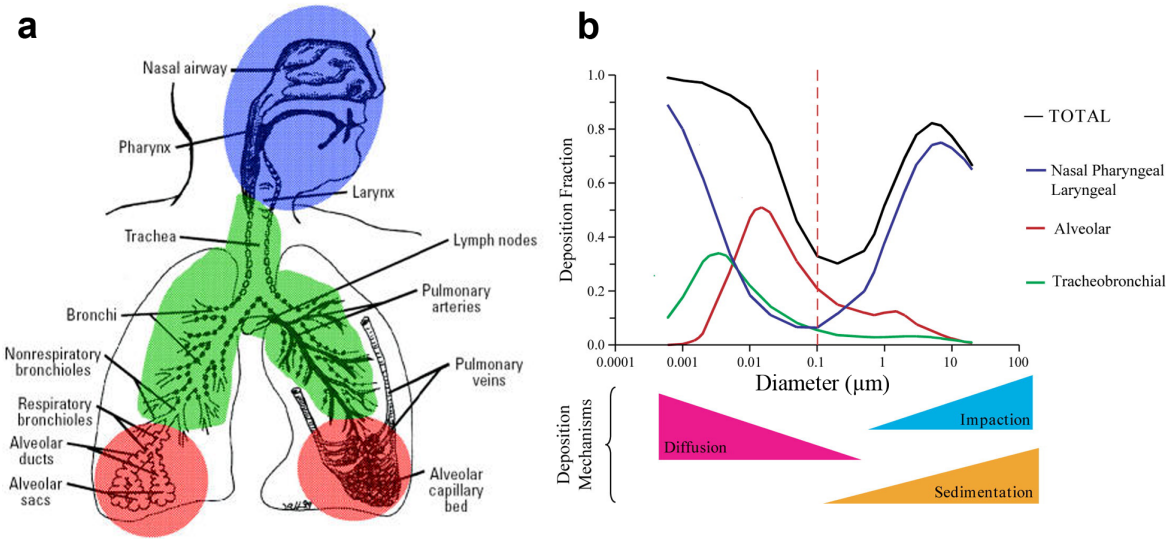

Illustration 1.5: Pulmonary exposure model showing where particles are deposited. A) Schematic view of the lung and airways. B) Graph showing the fraction of particles deposited and where they are deposited (blue, red or green areas depicted on the lung sketch. The fraction of particles reaching and depositing deep in the lung (red) increases below 100 nm and peaks at about 10-20 nm. Images are from Oberdörster et al., 2005 and 2007.

1.2.1 Carbon nanotube toxicity

The toxicity of carbon nanotubes (CNTs) is of particular concern, due to them being produced in large quantities, their chemical stability, and their similarity to asbestos fibres. Additionally, even long CNTs can have comparable small aerodynamical diameters[3] [34] making them able to deposit in the lower airways.

The concerns have been strengthened as pulmonary exposure to CNTs in a number of animal studies have shown an asbestos-like toxicological response characterised by inflammation, granulomas, and fibrosis with low no-effect levels [35]–[37]. In particular very long CNTs (>10 µm) with a high length-to-width ratio appears to cause asbestos-like toxic effect when inhaled [38], [39], whereas smaller CNTs does not, albeit small CNTs also results in toxic effects. Alveolar macrophages, typically responsible for clearing particles, can internalise up to about 10 µm long CNTs. However, the CNTs are very structurally stable, and as such the macrophages cannot degrade them. Hence CNTs persist in the macrophages and if they are not cleared via the mucociliary escalator (Cf. Section 1.2.3) they can remain in the lung for much of an individual's life or clear via other pathways [40]. A recent study has documented that a single inhalation of CNTs can accumulate in the liver and spleen one year after exposure, albeit it only reached less than 1% of the original dose [41].

1.2.2 *In vivo* and *in vitro*

In experimental life sciences and within this thesis, the term *in vitro* ('in glass') refers to experiments performed in artificial environments such as petri-dishes, test tubes etc., whereas *in vivo* ('within the living') refers to experiments performed in whole living organisms such as animals or humans.

For investigating nanostructure interactions with cells, *in vitro* experiments are typically

3 For irregular particles the aerodynamical diameter describes the settling velocity in relation to a model spherical particle.

used when attempting to design nanostructured devices, while *in vivo* experiments are performed for investigating the toxicological effects of nanostructures. However, in some cases nanostructured devices have reached a point where *in vivo* experiments are performed (e.g. for neural recordings in rats Illustration 1.2 a).

The primary reason for performing animal experiments is to put the investigations into a more physiologically relevant model. *In vitro* experiments are typically performed with a single cell type, whereas the human immune system consists of many different cell types, a wide variety of proteins and complex signalling pathways and tissue responses [42]. Additionally, many cell lines used *in vitro* are of cancer origin which undergo rapid cell division and mutations, and as such do not resemble normal tissue found in the organism.

Despite the obvious drawbacks of *in vitro* experiments, the need for testing more and more engineered nanoproducts, together with the goal of limiting animal experimentation, has meant that *in vitro* experiments are increasingly being incorporated into toxicological assessments [43]. The main reasons for looking into *in vitro* experiments for toxicology is that it is: cheaper, avoids animal exposure, and experiments can be repeated and statistically verified (*in vivo* experiments are generally not repeated due to animal experimentation legislature).

The present thesis does not aim at investigating the biological difference between *in vivo* and *in vitro* reactions to nanostructures, as this would be too extensive. However, this was part of the aim of Paper VIII, which uncovered that cultured cells and lung tissue response responded similarly to CNT exposure, but that the underlying mechanisms where different. The focus of this work is to study the nanoscale interactions both *in vitro* and *in vivo*. Hopefully the mixture of *in vitro* and *in vivo* samples in electron microscopy testing and development will result in the development of methods which can be applied to other use-cases than those directly discussed in this thesis.

1.2.3 A brief overview of the respiratory system

The lung was chosen as the *in vivo* test system used to study CNT toxicity, due to it being the primary route of toxicological concern and relevance when dealing with CNT exposure [44].

Air is drawn into the lungs when they are expanded by the diaphragm. Air then travels through the mouth or nose, and then through the trachea (windpipe) before reaching the lungs (Illustration 1.6). In the lungs the air is branched into bronchi and bronchioles which are smaller and smaller air tubes until the alveoli are reached. The main gas exchange occurs in the alveoli, where blood in thin capillaries is oxygenated and returns to the heart to be pumped around by the circulatory system. Due to the lungs function of oxygenating blood, the tissue is spongy and porous (Illustration 1.6 b-c). Compared to electron microscopy of cells cultured on nanostructured substrates: Lung tissue is mostly devoid of cells and the placement of the nanostructures are not well defined. Part of the challenge is therefore to be able to find the proverbial needle in a hay-stack that interacts with tissue (Cf. Chapter 4).

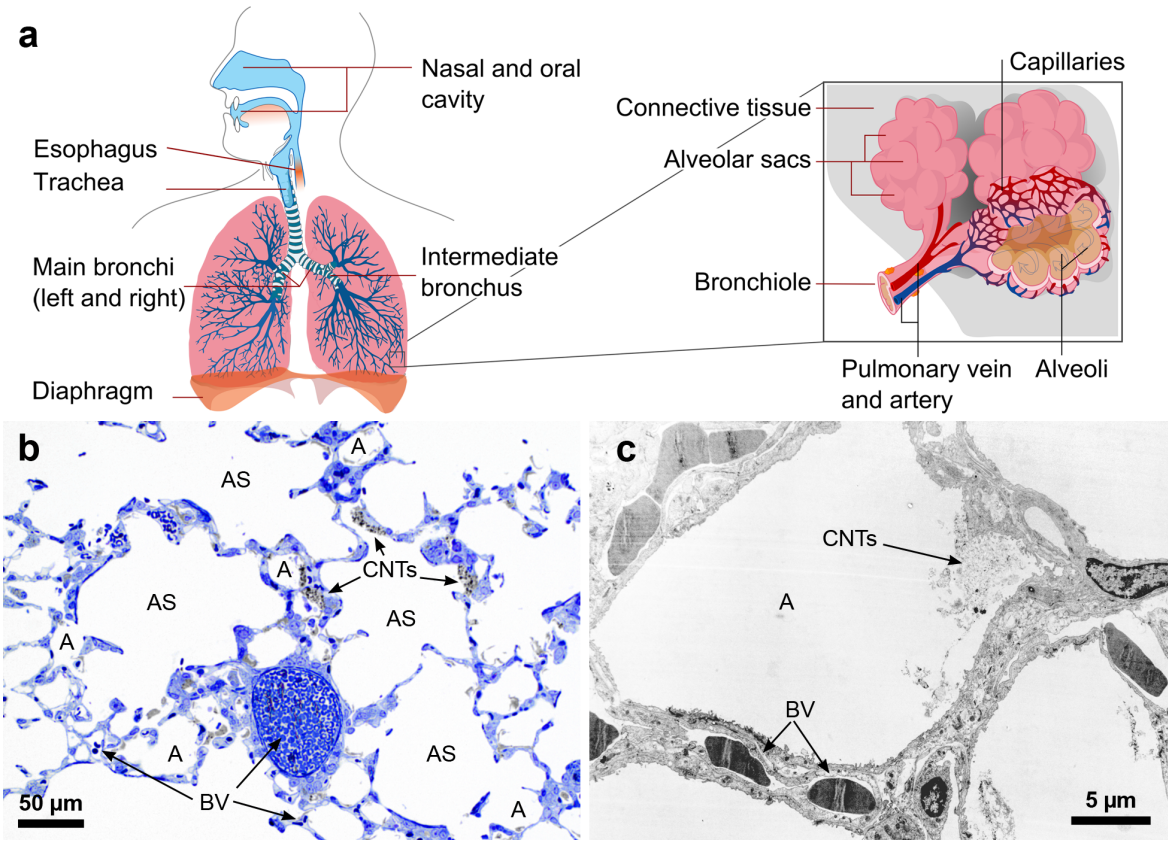

Illustration 1.6: A) Overview of the respiratory system, illustrating how the air ducts branches out. The air ducts ends in the alveoli where blood is oxygenated. Figure adapted from "Respiratory system complete" by LadyofHats, Wikimedia Commons. B) Light micrograph of lung tissue showing the alveolar sacs and alveoli. C) TEM image of an alveolar sac showing their close relation to blood capillaries. Alveoli (A), Alveolar sac (AS), blood vessel (BV), and CNTs have been marked on the micrographs.

To avoid particle deposition and accumulation in the lungs, the trachea and bronchioles are lined with ciliated and mucous excreting cells forming the mucociliary escalator. Particles are 'captured' by the sticky mucous lining the airways, and ciliated cells pushes the mucous layer up to the pharynx where it can be swallowed. The mucociliary escalator is responsible for transporting large amounts of inhaled particles to the stomach where they are excreted or decomposed by gastric acid. Furthermore, white blood cells patrol the lungs, where in particular macrophages are responsible for clearing particles. Alveolar macrophages phagocytose (engulf) the particles and if possible degrade them, otherwise particle containing macrophages travel to the stomach via the mucociliary escalator thereby clearing the particles in about 24 hours depending on the exposure [45]. However, difficult to clear particles and/or high particle concentrations may overwhelm and impair clearing mechanisms [46]. This may cause particles to translocate to other systems and macrophages may use alternative and slower (> 1 month) clearing pathways or remain in the lung for years [47].

The effects of particle exposures are linked to how they are handled by the respiratory system, and hence particle uptake and interactions with cells should be studied for several time points. Therefore, we study CNT-cell interaction and distribution *in vivo* at 3 post-exposure times (Chapter 5).

1.3 Project goals and thesis outline

In order to be able to design nanostructure devices for investigating biological cells and to understand CNT toxicity, our goal is to increase our knowledge of how cells interact with nanostructures by using electron microscopy. The main goals of this project are therefore to:

- Develop and explore electron microscopic techniques for imaging hard-to-microtome samples, and for imaging 3D structures in tissue.
- Map and document cellular interactions with nanostructures grown on a substrate and CNTs in an inhalation exposure scenario.
- Investigate the time dependent distribution of CNTs *in vivo.*

My work attempting to reach these goals is described in this thesis and has been ordered into six chapters which cover:

Chapter 1	Introduces the motivation, general concepts in the thesis and the project goals.
Chapter 2	Describes and introduces light- and electron microscopic imaging techniques, together with relevant sample preparation methods for biological electron microscopy.
Chapter 3	Maps the observed *in vitro* cellular interactions with nanostructured substrates. It includes an introduction to what is currently known about cell-nanostructure interactions and FIB-SEM method development.
Chapter 4	Describes how FIB-SEM imaging of CNTs in lung tissue can be performed and compares with standard TEM imaging.
Chapter 5	Here the ultrastructural time dependent CNT distribution in lung tissue 1, 3, and 28 days after exposure is documented, together with CNT-cell interactions *in vivo*. Additionally, the findings are related to toxicological data such as gene expression and cell counts.
Chapter 6	Concludes and gives an outlook on the work performed.

Chapter 2

Nanostructure visualisation methods in soft matter

This chapter will briefly describe a selection of the methods used for imaging nanostructures in cells, as an understanding of this is indispensable for the work carried out in this thesis.

High resolution light microscopy (LM) will be introduced in section 2.1, while the basic principles of electron microscopy (EM) and the main methods will be covered in section 2.2. Furthermore, the different sample preparation strategies for biological samples will be highlighted (Section 2.3), together with the particular electron microscopes used in this thesis (Section 2.4).

Before introducing the different methods, it is important to note that there is no one superior method and every method has its own strengths and weaknesses. One should therefore choose carefully and preferably apply more than one method. This also includes the usage of quantitative characterisations methods such as mass spectroscopy, dynamic light scattering and surface area measurements, together with the usage of biological tests and assays which is outside the scope of this chapter.

2.1 Light microscopy

Since the invention of light microscopy (LM) it has been the golden standard for understanding the microscopic world. LM has developed from simple microscopy setups to complex and expensive high resolution microscopes. Although conventional wide-field transmission, reflective and fluorescent light microscopy has its place in investigating the effects of nanostructures, they do not have the resolution needed to resolve nanostructures. Therefore, this section will focus on high resolution techniques more often used to investigate nanostructure interaction with biological samples, together with a few methods which might prove valuable in the future.

2.1.1 High resolution light microscopy

One of the earliest methods for increasing the practical resolution of light microscopy was to deconvolute image stacks. This method is based on a computational reconstruction of the imaged object, where the knowledge of the optical distortions present in the system is used to improve image contrast and resolution. However this technique relies on mathematics and qualified guess work [48], and does not introduce new imaging techniques.

In contrast, confocal laser scanning microscopy (CLSM) relies on a radically different optical path compared to standard wide-field microscopy (Illustration 2.1). Instead of illuminating the whole observable sample (wide-field), CLSM uses a point laser source which is scanned across the sample. Most commonly the sample is stained with fluorescent markers which are excited by the laser, thereby emitting light which is directed to a detector. CLSM is built with several pinholes to limit out of focus light by constricting the excitation source and the detected light (Illustration 2.1). The laser is scanned in the XY-plane, and the pinholes make it possibly to scan individual Z-planes, thereby allowing for 3D imaging of the sample. The CLSM only provides a limited improvement in XY resolution compared to the wide-field microscope, and it requires very small pinholes excluding much of the illumination giving poor signal-to-noise ratio [48]. The main advantage of CLSM over wide-field is the increased Z-resolution, but this is still limited to about 500 nm.

In relation to imaging nanostructures in cells using CLSM, one of the main obstacles is that most nanostructures are not fluorescent, although it is possible to fabricate fluorescent nanostructures [49]. Alternatively, Berthing et al., utilised a specific membrane stain, making it possible to image the effects of the nanostructures, despite not being able to resolve them [50], also see Illustration 2.2 A.

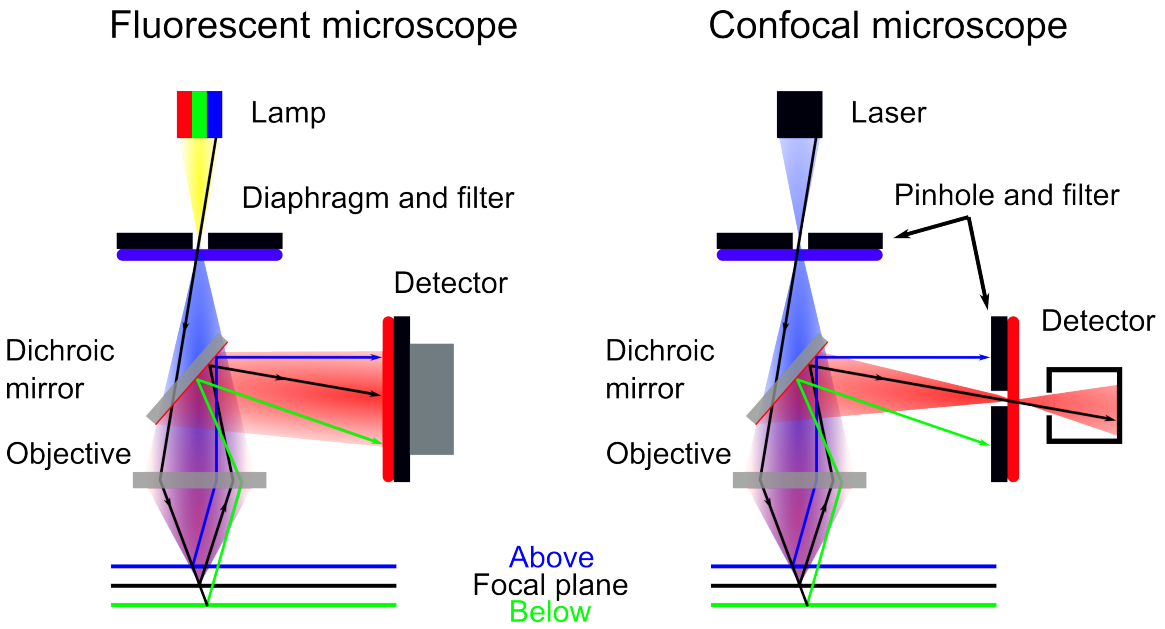

Illustration 2.1 Principle sketches of a wide-field fluorescent and a confocal microscope. Fluorescent microscope: White light is generated by a lamp and passed through a 'blue pass' filter and illuminates the sample. The blue light excites the sample which emits red light which is directed towards the detector via the dichroic mirror that reflects certain wavelengths. Out of focus light stemming from above (blue line) and below (green line) the focal plane is also detected. Confocal microscope: Laser light of a certain wavelength (blue) is used and directed onto the sample. The out of focus light emitted from the sample is excluded using a small pinhole before the detector.

CLSM is an excellent and versatile tool, but it is not a true high resolution technique capable of 'breaking' Abbe's classical resolution limit. One way of obtaining a higher spatial resolution (20-120 nm) is to use evanescent waves (e.g. Near-field scanning optical microscopy, SNOM), but this involves placement of the detector less than a wavelength away from the sample, making it less relevant for imaging nanostructures in cells. Instead, structured illumination microscopy (SIM) can improve the resolution to 50-130 nm,

depending on the particular technique [48]. SIM works by imaging the sample with a non-uniform illumination, which results in a diffracted Moiré pattern containing otherwise non-visible information in the frequency space [51]. By shifting the non-uniform illumination several times and applying a computational reconstruction it is possible to extract spatial information from the frequency space. Likewise, techniques exist which deplete the fluorophores around a certain spot (e.g. stimulated emission depletion, STED), effectively minimising the excitable spot, resulting in 20-50 nm resolution (Illustration 2.2 B). High resolution techniques coupled with fluorescent labelling of nanostructures or organelles, may give valuable information in the future, especially in terms of investigating the dynamics as imaging can be performed on living cells.

Currently, what these techniques have in common is that they require specialised equipment and can be challenging to apply satisfactorily on samples investigated in this thesis, as they all impose certain restraints on the samples. Some require transparent samples, some are more suitable on certain types of samples such as filaments or particles (pointilism), while others only image a very limited thickness of the sample (SNOM) or require very stable samples (STED). Additionally, some methods require special fluorescent dyes, and as with the CLSM one should also worry about having to be able to stain the nanostructures. More information about super-resolution fluorescence techniques can be found in the review [48].

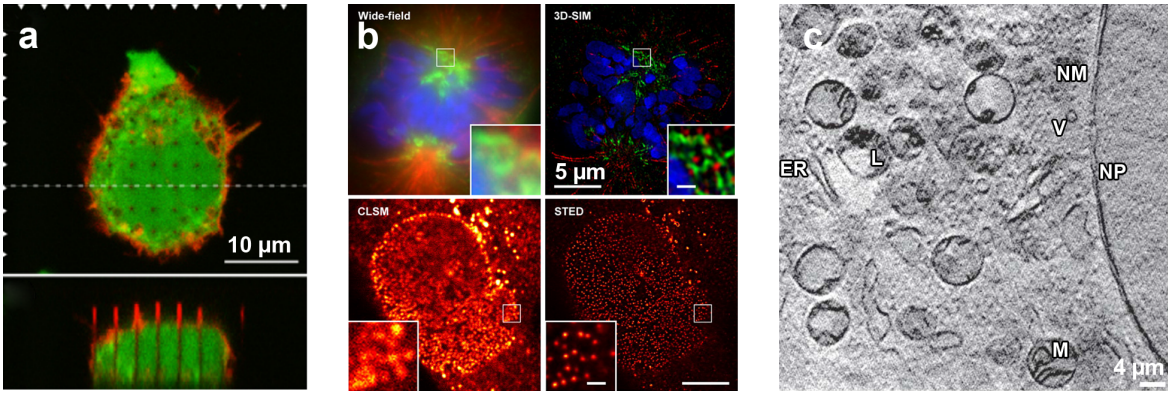

Illustration 2.2: A) CLSM image of nanowires which appear to be piercing the cell, but is in fact covered by a thin plasma membrane (red coloured), from Berthing et al., 2012. B) Example images showing how wide-field flourescence microscopy compares to SIM (top), and how CLSM compares to STED (bottom). Scale bar in the insert are 0.5 µm. Images from Schermelleh et al., 2010. C) X-ray image of cellular organelles such as the nuclear membrane (NM), nuclear pores (NP), lysosomes (L), endoplasmic reticulum (ER), mitochondria (M) and vesicles (V), from Schneider et al., 2010.

2.1.2 X-ray microscopy

Abbe's diffraction based resolution limit can be lowered by using X-rays having much smaller wavelengths (0.01-10 nm) than visible light. X-ray microscopy currently provides imaging resolutions between visible light- and electron microscopy, and imaging is possible on unstained wet samples. In the simplest terms, X-ray microscopes works by passing X-rays through the sample and onto a detector. Contrast is formed by absorption of X-rays, and requires a bright and collimated[4] source. A resolution of 70 nm in unstained frozen samples has been obtained on cells, revealing plasma membranes and details in the mitochondria (Illustration 2.2 C), and allowing for 3D reconstruction and segmentation of cell organelles [52]. Currently, in order to get sub-100 nm resolution, access to an

4 A perfectly collimated light source is composed of parallel light rays which do not spread during propagation.

expensive synchrotron source is needed, but developments in X-ray optics and X-ray sources may lead to resolutions better than 10 nm [52]. X-ray microscopy would then be a very powerful method. For a review of X-ray microscopic studies on bio- and nanomaterials refer to [53].

2.2 Electron microscopy

The main reason for using electron microscopy (EM) instead of light microscopy (LM) is the increased resolution obtainable with EM due to the lowering of the diffraction limit. This section will describe the basic electron-sample interaction, together with the two main types of electron microscopes (SEM and TEM), and some typical variations applicable to biological samples.

2.2.1 Electron scattering

When high energy electrons are directed onto a sample, they scatters as they move through the material, without scattering the sample would not affect the electron beam and would be invisible. Depending on the electron scattering mechanisms in play and the electron microscope, a wide variety of signals can be detected and used for imaging or sample characterisation (Illustration 2.3). Hence, understanding the concept of electron scattering (electron-sample interaction) mechanisms, generally divided into elastic and inelastic, is important in understanding how EM works.

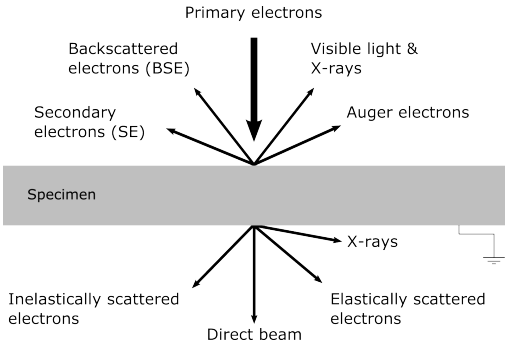

Illustration 2.3: The primary electrons are generated by the electron microscope and directed onto the sample. The primary electrons scatter and interact with the sample giving rise to many types of signals.

The interaction cross section (σ_{atom}) is used to describe the possibility of an electron scattering event on an atom in the sample. σ_{atom} varies with electron energy, such that increasing acceleration voltage (E_0) will decrease the cross section and thus the possibility of a scattering event. The mean free path before a scattering event (λ), can be used to describe the scattering probability (p) in a sample with a certain thickness (t) as a function of the cross section in the simplified equations below:

$$\lambda = \frac{1}{\sigma_{total}} = \frac{A}{N_0 \sigma_{atom} \rho} \quad (1)$$

$$p = \frac{t}{\lambda} = \frac{N_0 \sigma_{atom} \rho t}{A} \quad (2)$$

N_0 is Avogadro's number in units of atoms · mol^{-1}, and A is the atomic weight of the atoms involved in the scattering event (kg · mol^{-1}). These formulas describing the probability of scattering indicate how electrons interact with the sample and thereby how contrast is formed. The larger the cross section of a particular atom (σ_{atom}), sample thickness (t), or

density (ρ) the larger the scattering probability. For a more detailed description refer to [54].

Elastic scattering occurs when electrons are electrostatically deflected by either the positive nucleus of an atom or its negatively charged electron cloud without losing any energy. Elastically (forward) scattered electrons are used in transmission electron microscopy (TEM) where the direct beam is used for imaging, contrast is either obtained via mass-thickness, diffraction or phase contrast. Elastically (backscattered) electrons are rarely used for TEM imaging, due to the limited samples thickness and high acceleration voltage. Instead, backscattered electrons are widely used in SEM imaging for obtaining contrast dependent on atomic number (Z-contrast).

The atomic number dependent contrast (mass-thickness contrast) which is most commonly used for biological samples relies on incoherent[5] elastic scattering (Rutherford scattering). A simplified equation, ignoring relativistic effects, for the Rutherford cross section (σ_R) shows that the cross section is strongly dependent on the atomic number (Z) and the acceleration voltage of the electrons (E_0).

$$\sigma_R(\theta) \propto \frac{e^4 Z^2}{(\pi \varepsilon_0 E_0)^2} \tag{3}$$

The higher the atomic number, the more of the primary electrons are scattered, leaving them out of the direct beam imaged causing darker areas in TEM. Diffraction and phase contrast both rely on the coherent[4] electron scattering, and is rarely used in biological samples [54].

Inelastic scattering occurs when the impinging electron collides with electrons bound to the atoms in the sample. This gives rise to various kinds of secondary signals, some of which contain material composition information, e.g. and Auger electrons X-rays. Auger electrons and X-rays are emitted from the sample during the atomic relaxation after an electron has knocked out an inner core electron. The X-rays and Auger electrons thereby carry information about the inner structures of the atoms in the sample, making it possible to distinguish between materials. In terms of imaging, one of the main uses of inelastic scattered electrons is secondary electron (SE) imaging in SEM. SE are generated by inelastic scattering event with electrons loosely bound the outer layers of the atom, the primary electron usually maintains most of the energy and penetrate deeper into the sample, thereby generating a cascade of SE. Secondary electrons typically have energies up to 50 eV, which means that they easily scatter, possibly making new SE and only escape to the detector if they are generated near the surface. This makes SE-SEM imaging very surface sensitive.

Inelastic scattering give rise to a great variety of signals, but it is unfortunately also responsible for damaging the sample. Inelastic scattering can break chemical bonds by altering the electron configuration in the sample. Furthermore, inelastic scattering also occurs if electrons hits an atom in the sample. Depending on the binding energy of the atom, the energetic electron can displace atoms, in some cases ejecting them from the surface, or loose energy to the sample causing sample heating. Although beam damage can be limited via cooling, coatings, etc., it is unavoidable and the effects on the sample

5 Coherency describes the phase and wavelength relation between electrons. Coherent electrons have the same wavelength and phase, whereas incoherent electrons are out of phase and have varying wavelengths.

should be considered.

2.2.2 Transmission electron microscopy

TEM function in much the same way as light microscopes, where an electron source is used instead of a bulb. This could typically be a thermionic emission, field emission electron source or a mixture of the two. Using high voltage electric fields, electrons are accelerated down towards the sample, and along the way the beam passes a variety of electromagnetic lenses and apertures which focuses the beam. This occurs under ultra-high vacuum to avoid unwanted electron scattering *en route* to the sample. The electron beam is transmitted through the thin sample and an image formed from transmitted electrons on a sensor below the sample (cf. Illustration 2.4).

Typically high acceleration voltages of around 80 kV to 300 kV are used in TEM. The purpose of these high acceleration voltages is to ensure electrons are transmitted through the sample (lower scattering probability at high energies, Equation 3).

In TEM the sample thickness is a very limiting factor for the samples to be investigated. Biological samples should preferably be less than 100 nm thick, whereas material scientists in some cases go below 50 nm to achieve ultra-high resolution imaging [54]. This limitation often makes sample preparation for TEM challenging. The obtainable resolution with TEM is in the sub-nanometre (<1 nm) scale [54], but for biological samples this is usually limited to around 2 nm [55].

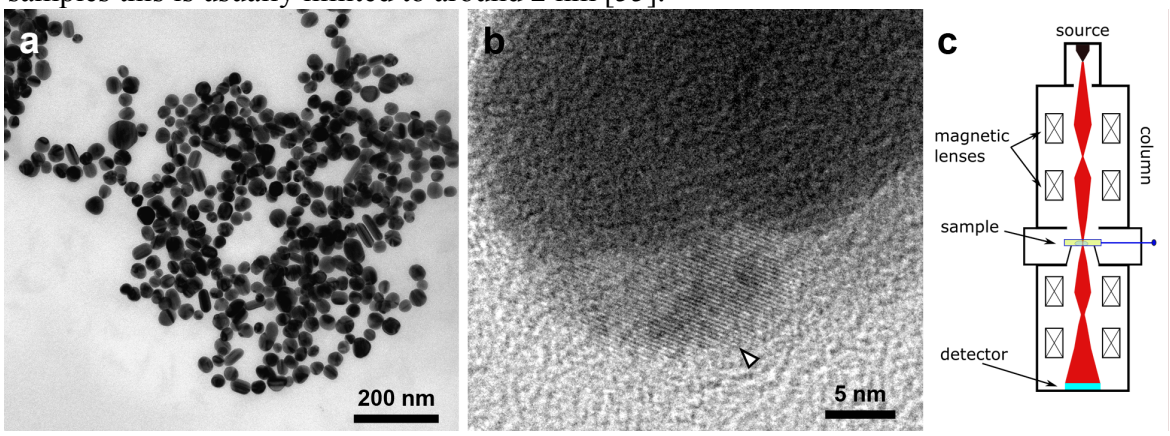

Illustration 2.4: A) Overview TEM micrograph of silver nanoparticles on a support film (Paper VII). B) Silver nanoparticle showing lattice fringes (arrowhead). C) Schematic representation of TEM, where electrons are directed from the electron source down onto the sample via magnetic lenses and onto a detector in the bottom.

HAADF-STEM

To increase the mass-thickness contrast in TEM samples, high-angle angular dark field scanning-TEM imaging can be used (HAADF-STEM). STEM imaging is performed by scanning a finely focused electron beam across the sample, and detecting the transmitted electrons. It is useful on low-contrast samples, but suffers slightly in terms of resolution. In HAADF mode, STEM is an especially useful technique for low contrast polymer and biological samples relying on Z-contrast. As described, the mass-thickness contrast relies on Rutherford scattering, but at low angles (< 5 deg) it competes with Bragg-diffraction caused contrast. By limiting imaging to high annular angles (+5 deg), one excludes the direct beam from the image (dark field) and Bragg scattering is usually negligible. Imaging contrast will therefore mainly be due to Rutherford scattering and thus be highly dependent on the atomic number and density (Z-contrast) [54]. An analysis on stained

cells revealed a 5-fold contrast increase using HAADF-STEM over BF-TEM [56], while it also has been useful for imaging crystalline carbon nanoparticles in non-stained samples [57].

EF-TEM

Energy filtered TEM, as the name implies, creates images from electrons in a selected energy-loss range. By using an energy filter, electrons with a certain energy loss can be used for imaging. Since the energy loss is related to the material and its electronic configuration, one can gain an insight into the composition of the samples, but it can also be used to control contrast even in non-stained samples [57]. Additionally, zero-loss EF-TEM can be used to improve the contrast in thicker samples, by avoiding the inelastically scattered electrons in the sample that blurs the image due to chromatic aberrations in the lens.

2.2.3 Scanning electron microscopy

SEM use an electron source similar to TEM, but instead of illuminating the whole sample at once, the electron beam is focused into a probe and scanned over the surface. The primary electron beam impinging on the sample causes the generation of secondary electrons (SE) and backscattered electrons (BSE). Usually the low energetic SE escaping the surface of the sample is attracted and detected by an Everhart-Thornley detector (ETD), while higher energy backscattered electrons are detected by a solid state detector mounted on the exit point of the primary beam (pole piece). The SE are used to form images representing the surface topography of the sample, whereas BSE gives better Z-contrast as previously discussed (Section 2.2.1).

Compared to TEM, SEM is operated at low electron voltages, where typically between 1 kV and 30 kV are used. This is because images are formed from electrons escaping the surface, and if higher energy electrons were used, the signal would not escape but would rather be stopped deep in the sample, which causes increased beam damage and charge build up. To limit charge build-up in the sample in poorly conducting samples, the sample can be coated with a conductive layer and connected to ground (stage). Also, to limit charging of biological/wet samples, environmental SEM can be used which allows for SEM imaging of wet samples by use of an intricate pumping system [58].

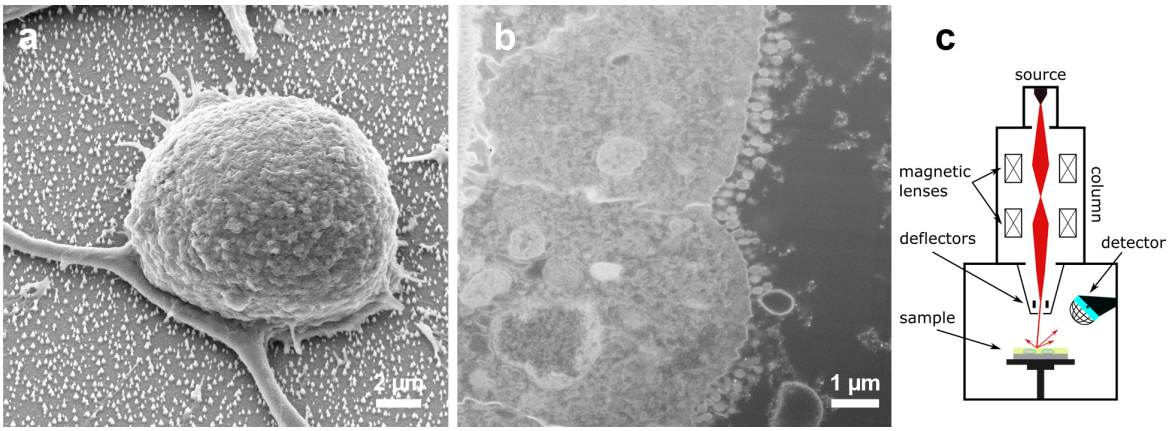

Illustration 2.5: A) SE-SEM image showing the topography of a dried cell on silicon nanowires (Paper IV). B) BSE-SEM image of the gut of an epoxy embedded daphnia (Appendix F). C) Sketch of SEM principle, where the electron beam is focused into a spot and scanned across the surface.

FIB-SEM

A focused ion beam (FIB) can be used for deposition of metals, for milling material, or as a very surface sensitive imaging technique. The most common FIB source, used in combination with a SEM (FIB-SEM), is based on gallium ions obtained from a liquid-metal ion source. Solid gallium is heated, and flows down to the tip of a tungsten needle, where a large electric field is used to cause ionisation and emission of gallium ions (Ga+). In much the same manner as the electron beam, the ion beam is focused using electromagnetic lenses and directed onto the sample. Due to the size of ions the FIB is much more damaging to the surface than SEM and consequently FIB can be used to sputter atoms from the surface (milling). This has been used for micro-machining devices [59]. The FIB-SEM has also found use in biology as a 3D imaging tool [60]–[63], here the FIB-SEM cycles between removing part of the sample with the ion beam and imaging it with the SEM (slice-and view) (Illustration 2.6). In addition, the FIB can be used as a deposition tool. Using a gaseous injection system (GIS), precursor gasses (typically platinum based) are injected close to the surface. The ion beam reacts and degrades the gas, leaving the intended deposited material on the sample.

FIB-SEM on biological samples usually requires resin embedding to form a vacuum stable cured block (Section 2.3.2). Prior to FIB-SEM, the block should be securely attached to an aluminium stub (Illustration 2.6 a), and a thin conductive layer (e.g. gold, platinum or carbon) should be deposited to help dissipate charge build-up. Prior to actual FIB-SEM imaging, the block should be prepared using the FIB source, often this includes: milling of a U-shaped trench around the area of interest to avoid redeposition of material during FIB-SEM slice and view, and FIB assisted deposition of platinum to protect and stabilise the area of interest (Illustration 2.6 c). It can easily take 1 hour to form the U-shaped trench and deposit platinum, it is therefore important to find a suitable area of interest using SEM prior to FIB preparation of the block. We localised areas of interest by: high energy SEM imaging (Paper I), by correlating SEM images with light microscopy images (Paper VI), and by localising areas where protruding nanostructures interact with tissue (Paper II).

Over the years several milling geometries have been used, the current standard method (tilted-milling) involves a 52 degree tilt of the sample such that the ion beam is perpendicular to the surface (Illustration 2.6 c). Using this method one can make the necessary trenches [61], [64] or alternatively trim the block with an ultramicrotome such that the region of interest is directly accessible [60], [65]. However, the 52 degree tilt means that the SEM image is formed on a slanted angle, which makes them susceptible to shadowing effects if imaging in a deep hole, and it effectively diminishes the resolution as the SEM image is a projection of a slanted surface. To limit this issue, and allow for milling of large (un-tiltable) samples, non-tilted milling can be performed [63], [66]. This in return means that non-standard image reconstruction is needed, and we risk introducing artefacts when imaging nanostructured substrates as we have documented and described (Paper I). Additionally, we have developed and demonstrated the double-non-tilted method for obtaining FIB-SEM images from samples with a rough surface (Paper II).

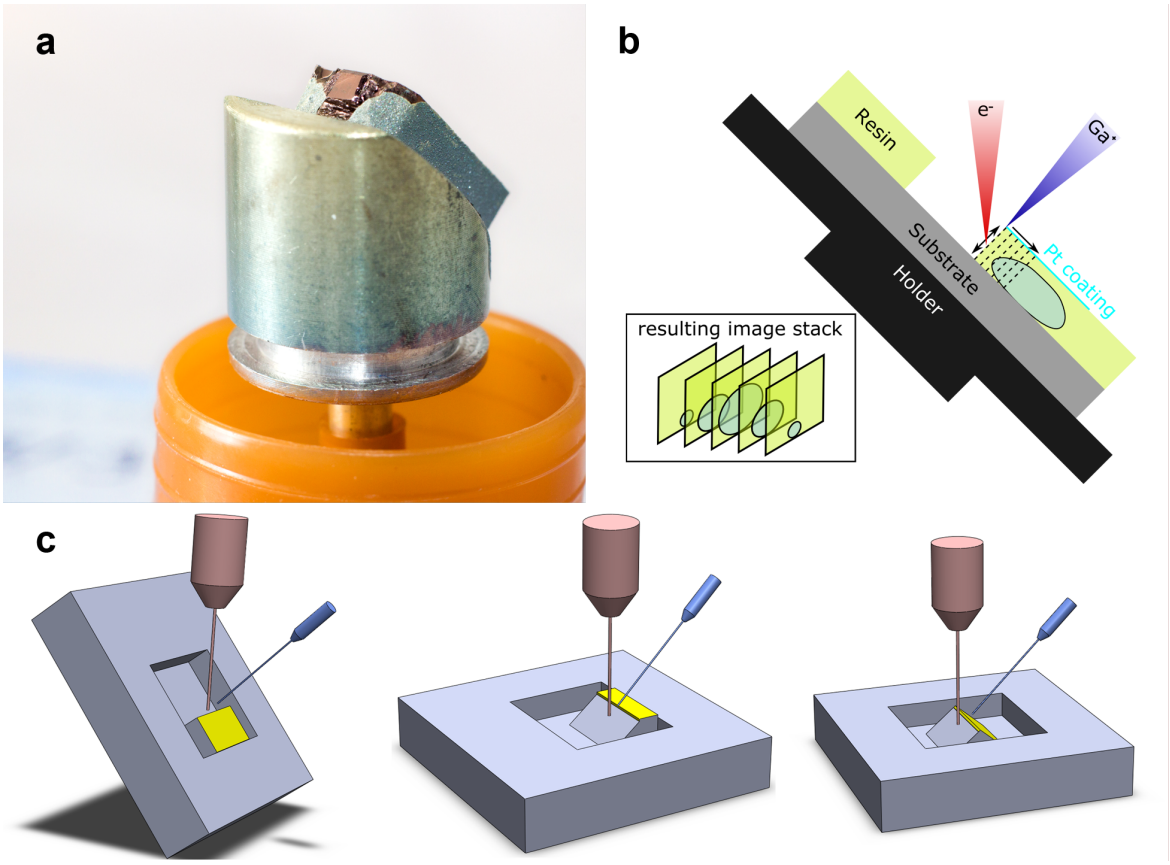

Illustration 2.6 Overview of our sample preparation for FIB-SEM slice-and-view. A) Tissue samples were trimmed using an ultramicrotome, mounted on a aluminium stub, secured using a conductive paste and coated with gold. Samples with cells on nanostructures were polished using rotating abrasive discs instead of microtomy (not shown). B) Schematic of the FIB-SEM slice-and-view principle. The ion beam is at a 38 degree angle to the electron beam. C) 3D representation of the milling geometries used: Tilted, non-tilted milling and double-non-tilted milling. The sketches illustrate the electron beam (red), ion beam (blue), the trench and the platinum coating (yellow).

2.3 Sample preparation for Biological electron microscopy

Biological samples are unfortunately not well suited for electron microscopy: they are not conductive, they are wet and will evaporate in the vacuum chamber, and they offer limited contrast. Biological samples such as cells, bacteria and tissues therefore often need to go through extensive processing before being imaged. Generally, the process requires some form of sample fixation (stopping biological function), dehydration (removal of water) and staining (to increase contrast). The three mostly used methods of obtaining this includes: drying, embedding, and freezing.

2.3.1 Drying

One way of eliminating water from a biological sample is quite simply to dry it. This results in perfectly vacuum compatible samples which can be imaged in TEM if they are thin enough and SEM if they are coated with a thin conductive layer. However, simply drying wet biological samples will result in massive artefacts due to surface tension

induced forces when the liquid evaporates causing cells and tissue to collapse.

Critical point drying

In order to limit drying artefacts, the samples can be chemically fixed (Section 2.3.2) to ensure structural stability, additionally the sample can be dried 'gently' via critical point drying (CPD), a technique commonly used for SEM sample preparation of cells cultured on nanostructures.

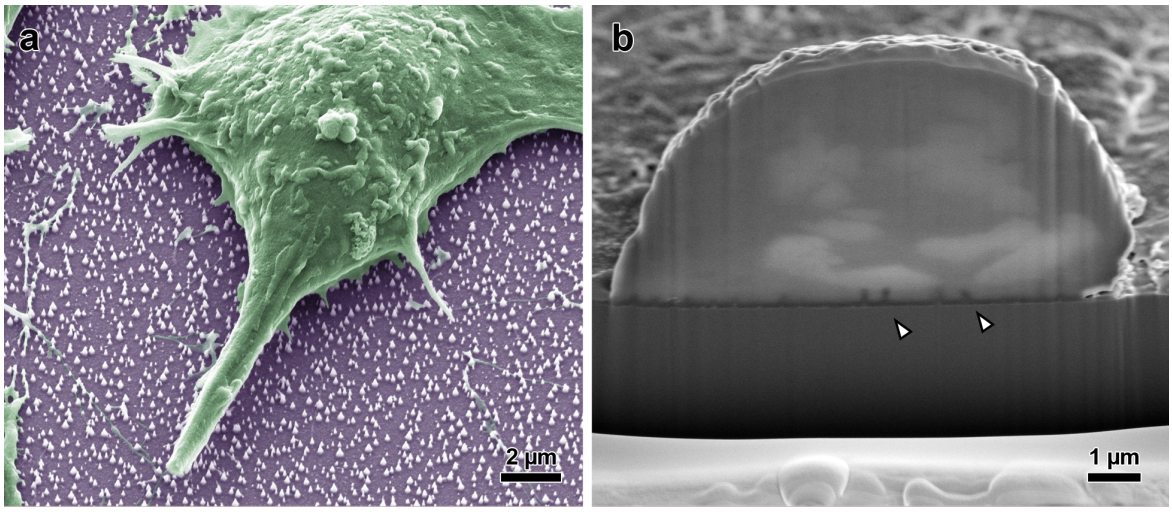

Illustration 2.7: Dried cell on nanostructures. A) False colour SEM image of a chemically fixed and dehydrated cell on nanostructured substrate. B) SEM image of the insides of a dehydrated cell as revealed by FIB milling. The nanostructures (arrowheads) can be discerned, but there is almost no intracellular contrast present, although the sample was heavy metal stained with osmium tetroxide.

During critical point drying the forces acting on the samples is limited by avoiding the water-gas phase. The sample is dehydrated via the supercritical region where there is no distinction between the gas and liquid phases. To reach the supercritical region the liquid is heated and pressurised. The supercritical region for water is reached by heating in excess of 300 ˚C while being pressurised to more than 200 bar which would cause heat damage to the biological sample. Instead liquid CO_2 is typically used as it reaches the supercritical point at about 31 ˚C at 34 bar for CO_2. However, CO_2 is not miscible with water so acetone is often used as an intermediate fluid to remove water. The acetone is then washed away with liquid CO_2 and the sample heated and pressurised until the supercritical point, after which the pressure can be lowered allowing the CO_2 to evaporate having avoided the liquid-gas phase.

Drying makes it possible to obtain excellent SEM images showing cells interacting with nanostructured substrates [50], [67] or even for visualising tissue [68], [69], although with limited intracellular detail [70], [71] – which is also shown in Illustration 2.7 b.

Negative stain

Another way of preserving the structure of organisms during drying is to use a negative stain. This is a simple and fast method to study cell components, proteins, viruses and other similarly small objects typically using TEM, but it is not well suited for studying larger samples such as entire cells or tissue. The stain should not chemically interact with the sample, although this is often not completely avoidable. Negative staining is performed by mixing the wet specimen with the negative stain of high atomic number and a small droplet pipetted onto a TEM grid with a support film. Most of the mixture is removed by blotting and the remaining left to dry. The negative stain dries faster and

enters hydrophilic regions in the sample leaving the electron dense material to envelope the sample during drying. The negative stain thereby encapsulates the sample, preserves its structure, provides Z-contrast in the TEM and minimises irradiation damage. The pH of the negative stain can be tuned to limit chemical interaction, such that it is repelled from the mostly negatively charged proteins. Uranyl acetate is an example of a negative stain, which also can work as a positive stain as described later (Section 2.3.2).

2.3.2 Embedding

Instead of drying the samples, which distorts the finer intracellular structures, an often used technique is to embed the samples in a vacuum compatible epoxy resin. In order to preserve the ultrastructure of the sample, the embedding process requires several steps before obtaining a sample suitable for EM, such as: chemical fixation, staining, dehydration and embedding. This method is the preferred technique in this thesis as it is well suited for both studying cells grown on nanostructures and tissue samples. It is a well-documented technique which has been used for many years as it preserves the ultrastructure nicely and results in stable samples which are easy to handle and store. The following sections will describe the processes usually applied in more detail.

Chemical fixation

First off, the biological processes of the sample need to be stopped, and the structures stabilised and preserved as close to their native state as possible. Non-coagulative fixatives, such as the commonly used glutaraldehyde, formaldehyde, and osmium tetroxide, stabilise proteins such that they cannot agglomerate later due to coagulating fixatives (e.g. ethanol). Coagulating fixatives causes rearrangement and agglomeration of cellular proteins and distorts the finer cell structures during the dehydration process if it had not been for the primary fixative [72].

The fixatives discussed in this section (additive fixatives) mainly do two things to stabilise the molecular structure. They become part of the proteins and create crosslinks which hold them together and fixates the structure. Secondly, they denature proteins[6] making them less soluble in water, thereby protecting them from being extracted from the cell during processing.

Formaldehyde is widely used for embedding in paraffin blocks destined for light microscopical investigations. It is a small molecule which penetrates tissue rapidly. However, fixation in formaldehyde is not very stable, as some of the chemical processes fixing the proteins are reversible during electron microscopy processing. Instead glutaraldehyde is often used in electron microscopy. Glutaraldehyde is a much larger molecule so it penetrates the tissue slower, but in return it fixes faster and forms bonds which are irreversible [73]. In some instances formaldehyde and glutaraldehyde is mixed to ensure fast penetration and irreversible protein crosslinking.

Before the introduction of glutaraldehyde, osmium tetroxide was used to fixate biological samples for EM. Osmium tetroxide in particular fixes lipids, e.g. cell membranes, and it is extremely toxic and penetrates tissue very slowly. Hence osmium tetroxide is not optimal for handling during fixation of larger tissues in larger animal experiments. In addition, osmium tetroxide does not fix the majority of proteins and carbohydrates, and it is therefore currently mostly used as a postfixative as it fixes lipids, but also introduces

6 Denaturation of proteins changes their physical configuration and alters their properties. Boiling an egg to make the egg whites solid is an example of denaturation process.

contrast to the sample due to the heavy metal compounds.

To be able to preserve the ultrastructure of the sample it is important that the fixation process is fast and uniform in the entire sample to limit post-mortem morphology changes. In particular for fixing tissue, one should therefore consider the limitations of the selected fixative in terms of penetration depth and speed of fixation. To ensure uniform and fast fixation, tissue blocks for fixing should be no more than 0.5 mm^3 for osmium fixed samples, whereas larger samples (1-2 mm^3 depending on the tissue) can be used when fixing with glutaraldehyde [72]. This is naturally an issue when considering fixing entire organs of lab animals. The preferred method is to inject fixative into the circulatory system associated with the targeted organ (vascular perfusion), which ensures that fixative is distributed evenly in the organ before further handling. If this is not an option, one can rely on simply extraction and subsequent immersing of the tissue in fixative well knowingly that quality of fixation will decrease deeper in the organ. The animal studies performed in this work, relied on the latter approach (Chapter 5).

Besides the choice of fixative, the buffers used to ensure a proper osmolarity and pH is equally important. If these are not chosen wisely one risks influencing the ultrastructure greatly. The osmotic pressure as exerted by two liquids on either side of a membrane, e.g. cellular membrane, is described by its osmolarity. If either liquid contains more or less solutes which cannot cross the membrane, water crosses to even out the osmotic pressure causing either swelling or shrinking of the cell. Likewise, the pH changes the way the fixative interacts with the proteins, where lower pH is more suited for preserving nuclear constituents and higher pH enhances protein crosslinking [72].

Contrasting

Biological samples are often stained with heavy metals such as osmium tetroxide to induce better Z-contrast. Samples can be stained prior to embedding (*en bloc)* or embedded TEM sections can be stained (poststain). For a comparison of different preparation methods for FIB-SEM investigation of biological samples refer to [74]. The contrasting agents used in this work will be described very briefly and includes: osmium tetroxide, potassium ferricyanide, tannic acid, uranyl acetate, and lead citrate, together with an additional paragraph on ruthenium red.

Osmium tetroxide has already been mentioned in its fixative capacity, and as noted it has a high atomic number (76) and can thereby induce contrast in particularly lipid rich structures e.g. cellular membrane, ribosomes and golgi. Osmium tetroxide further permeabilises cellular structures making it insensitive to osmotic pressure differences.

Potassium ferricyanide is often used in mixture with osmium tetroxide as intermediate compounds are formed in the mixture which enhances the osmium contrast. Especially, membrane and glycogen contrast is increased compared to pure osmium tetroxide, while ribosome and nuclear chromatin contrast is decreased.

Tannic acid is a naturally occurring substance and only consist of low molecular weight carbon, hydrogen, and oxygen making it a poor contrasting material in itself. Instead, it can be used as a supplementary fixative thereby making glutaraldehyde cells less susceptible to towards drying artefacts as it aids in protecting from protein extraction during the dehydration process. In addition, it works as a mordant, reacting with membrane bound osmium and improves binding of other stains such as uranyl acetate or lead citrate [72].

Uranyl acetate contains uranium having an atomic number of 92 which means that it can effectively introduce Z-contrast in the samples. It is a general stain which can be used as a negative and positive stain. Uranyl acetate binds to both positive and negative protein side groups and in particular with phosphate and amino groups, thereby staining phospholipids in membranes and nucleic acids (including DNA) [75]. Uranyl acetate can both be used *en bloc* and to penetrate and stain entire ultra-sections. Uranyl acetate should be handled with care, it is sensitive to light, the solution deteriorates over time, and there is a risk of uranyl acetate precipitation due to poor filtration or prolonged staining [75].

Lead citrate is, like uranyl acetate, useful for both *en bloc* and ultra-section staining, but in this work only used as a poststain of TEM sections. Lead citrate stains membranes, proteins, nucleic acids and glycogen, and is enhanced by previous osmium tetroxide staining. Lead citrate is also known to easily precipitate, and when this occurs the mixture should be discarded.

Ruthenium red is not a standard stain as it has a large molecular size which means that it does not easily cross plasma membranes, and is consequently known for producing irregular staining due to this. It has however been shown to effectively stain and preserve the lung lining, which might be useful in terms of studying CNT penetration of lungs.

Embedding and sectioning

After staining, samples are embedded to preserve their structure, make them vacuum compatible and to allow for sectioning. Some embedding media are water-miscible, but most are water-immiscible (Epon, araldite, spurrs) and require dehydration in solvents prior to infiltration. Epon is the embedding material used in this work, and it is an epoxy resin, which hardens during thermal curing. It is miscible with ethanol, but even more so with propylene oxide which is then typically used in the final dehydration step before infiltration. Both the dehydration and infiltration should be done gradually to avoid extraction of cellular constituents and to ensure proper infiltration. It is beneficial to avoid high relative air humidity (+60%) to prevent holes in the specimen during dehydration and infiltration [72]. After embedding, samples can be thin sectioned for TEM using an ultramicrotome or imaged with FIB-SEM (Paper II).

2.3.3 Cryo-fixation

Cryo-fixation can in certain cases get closer to preserving biological structures in a more natural state than drying and chemical fixation, as it can occur very rapidly and preserves the water in the sample, e.g. [76], [77]. However, ice crystals are formed during normal freezing of samples containing water, and as ice crystals forms only water is incorporated in them which mean that as they grow larger they push aside cellular components and distorts the ultrastructure. To avoid ice crystal formation and obtain amorphous ice, or to at least limit ice crystal size, rapid freezing (in excess of 10,000 K/s) or freezing at high pressures can be used.

Rapid freezing can be obtained via plunge- or impact freezing. In plunge freezing the sample is quickly dropped in cryogenic gasses such as nitrogen or ethane. Impact freezing is essentially performed by cooling down metal and rapidly placing it in contact with the sample. Due to the poor heat conductivity of water, good freezing without visible crystal formation can only be obtained to a depth of about 10 μm with these methods [75]. For freezing larger samples, high pressure freezing can be used. High pressures, usually around 2050 bar, reduce the rate of ice crystal nucleation, and slow their growth hence

lowering the necessary cooling rate for vitrification to about 100 k/s. This means that samples 0.5 mm thick can adequately be frozen.

After cryo-preservation samples should be kept cold and can be imaged in the SEM or TEM (depending on the method used).

In SEM the sample would in many cases be covered with ice, to expose the underlying sample cryo FIB-SEM or freeze fracture can be performed [78]. For TEM, a very thin sample is needed either obtained via cryo-ultramicrotomy, by plunge freezing of a TEM grid with a very fine liquid layer or by cryo-FIB [79], [80]. Freeze-substitution can be used to induce contrast and embed the samples into resin, somewhat similar to the embedding process described, albeit at lower temperatures. Freeze-substitution allows for correlated imaging with immunostains, and limits loss of lipids and proteins during dehydration [75].

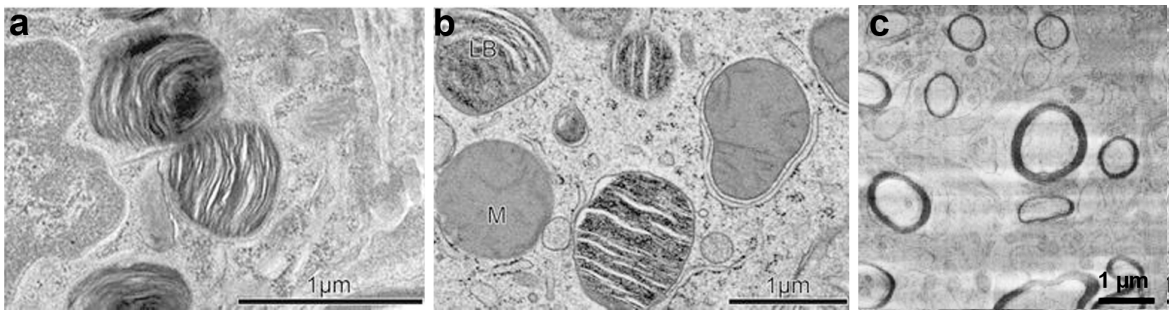

Illustration 2.8: A) TEM of chemically fixed and embedded lamella bodies. B) TEM of high-pressure frozen sample showing a different morphology of the lamella bodies (LB). From Vanhecke et al., 2010. C) Cryo-FIB-SEM of mouse optic nerve. From Schertel et al., 2013.

Cryo-fixation is an excellent technique for preserving the ultrastructure of cells and microorganisms, but is mainly reserved for studies requiring very high resolution, as it is complicated and expensive to perform – especially on tissue and cells on nanostructured substrates.

2.4 Electron microscopes used in this thesis

I was fortunate enough to be associated with both the Center for Electron Nanoscopy at the Technical University of Denmark (DTU CEN), and the Core Facility for Integrated Microscopy at Copenhagen University (CFIM), giving me ample opportunity in selecting and experimenting with finding the right microscopes for my purpose. Generally, throughout my project, the choice was between high resolution microscopes at DTU CEN and slightly worse resolution but better contrast on biological samples at CFIM. For future reference, this section will briefly describe the used microscopes and in which particular situation these were chosen.

2.4.1 FEI Quanta 200 FEG

The QuantaFEG is a medium-range SEM located at DTU CEN, with additional STEM, environmental SEM and cryogenic capabilities. Due to its lower cost and simplicity (not dual-beam or immersion) it was preferred for obtaining SE images of dried cells on nanostructures (Paper IV), and for imaging protruding CNTs (Paper II) – the low-vacuum capabilities were also useful for charging samples. The STEM capability gave fair resolution and contrast and had the possibility of containing 6 grids so repeated venting and pumping could be avoided. Unless there was a need for imaging both transmitted and secondary electrons (Illustration 2.9 a-b), or using the microscopes other modalities, a designated TEM was preferred over the STEM due to the improve resolution (Illustration 2.9 b-c).

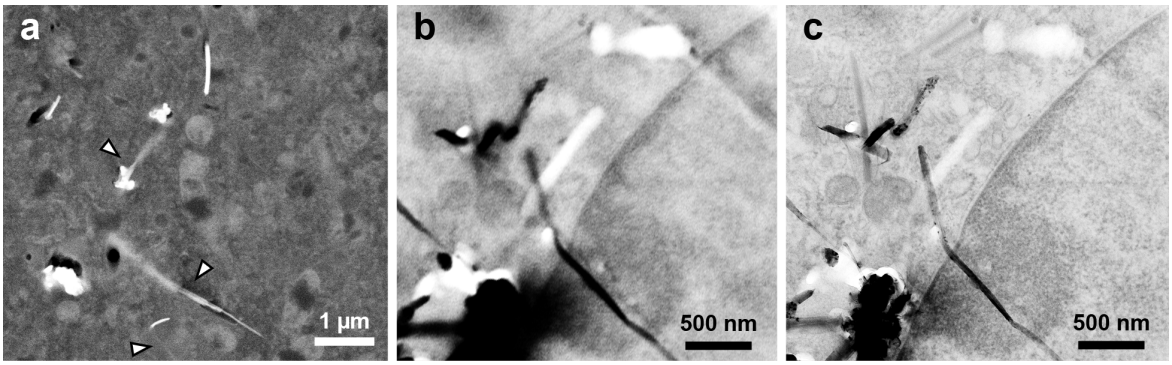

Illustration 2.9: Comparison of TEM and SEM-STEM of lung tissue. A) SE-SEM image showing how CNTs protrude from the thin section are brighter and more sharply defined, than the part of the CNTs that is situated in the thin section (arrowheads). B) QuantaFEG SEM-STEM image of CNTs in a cell. C) CM 100 TEM micrograph of the same sample area showing improved resolution.

2.4.2 FEI Quanta 3D FEG

The FIB-SEM located at CFIM has a coincident point[7] at 10 mm allowing for investigation of relatively large and uneven samples. However, for FIB-SEM imaging of biological samples typically the high contrast vCD detector is inserted under the pole piece, limiting the freedom of movement for larger samples.

The high contrast vCD detector meant that this microscope was preferred for 3D FIB-SEM of lung tissue. Additionally, the FIB provided smoother milling of the CNTs, possibly due to higher chamber pressure allowing for easier milling of CNTs than in the Helios (Paper II).

7 The distance to the sample where both the ion- and electron beam are in focus at the same place.

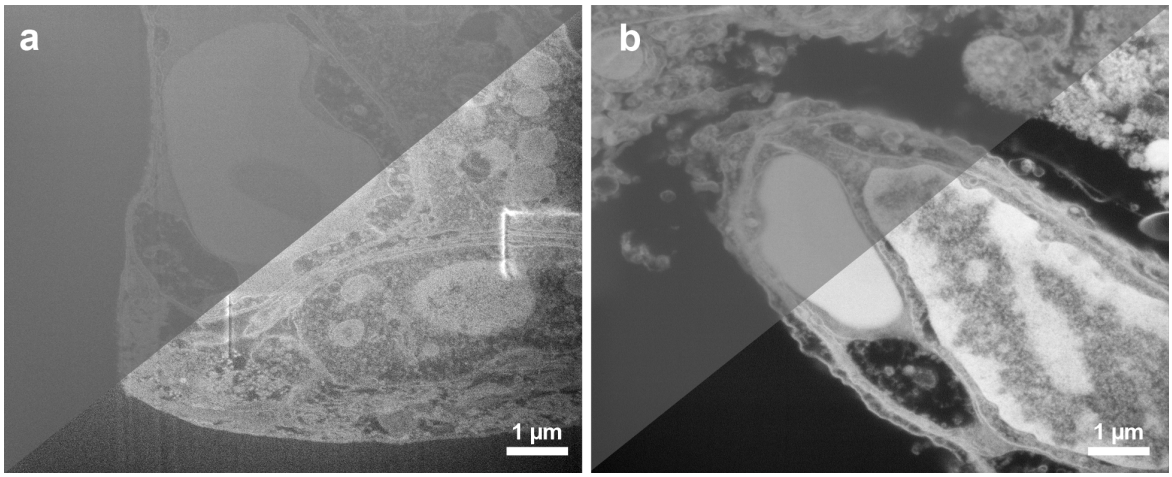

Illustration 2.10: FIB-SEM images of lung tissue illustrating the difference a designated high contrast backscatter detector makes. A) SE image obtained with the Helios in-lens system, the processed image show significant noise in the dark regions. B) Obtained with the Quanta FEG 3D vCD detector, having low noise when image adjusted. Images were obtained with similar imaging conditions, including the same pixel-size and pixel dwell time, and presented in both an unprocessed and a manual contrast/brightness adjusted version.

2.4.3 FEI Helios Nanolab 600

High-end FIB-SEM located at DTU CEN, with in-column detector and EDS. Compared to the Quanta FEG, the Helios has better resolution which in particular was due to the immersion mode, but even though the in-column detector could be setup to preferentially detect backscattered electrons, the contrast was not as good as a designated backscatter detector. However, in the ending phase of my project an angular backscatter detector (ABS) was installed, providing excellent high resolution images with good contrast.

The microscope was primarily used when high resolution FIB-SEM images were required (e.g. Paper VI), but the newly installed ABS detector makes the microscope very promising for future use. Albeit care must be taken as the detector is inserted by the pole piece and when the coincident point of the FIB-SEM is at about 4 mm this does not leave much room for tilting the sample and hence the sample should be mounted on a pre-tilted sample holder. When using only the in-lens detector large samples can easily be tilted. The Helios is more cumbersome to operate, with slower pump down time and it can be a hassle to turn immersion mode on and off during imaging and milling.

2.4.4 Philips CM 100 BioTWIN

Located at the CFIM, the CM 100 is a basic TEM meant for biological applications with a minimum of add-ons. It was operated at 80 kV with either a Tungsten or LaB_6 filament, and optimised for obtaining contrast rather than high resolution. It was very stable and simple to operate as it was intended for a single purpose, namely imaging of biological samples. Additionally, the 80 kV electron beam meant that it provided a good contrast due to the higher scattering probability of low acceleration voltages compared to the Tecnai.

The high contrast and its ease of use meant that this was the preferred TEM for imaging CNT interactions with lung tissue (Paper II and Paper III).

2.4.5 FEI Tecnai T20 G2

TEM located at DTU CEN, the microscope was geared towards material science with a wide array of add-ons. The possibilities include STEM-HAADF, energy filtered TEM, EDS and cryo-TEM. The Tecnai was operated at 200 kV with a LaB_6 filament, which provided less contrast than the CM 100 on biological samples, but was well suited for high resolution work.

The microscope was preferred in cases where high resolution was needed (e.g. for resolving lattice fringes or CNT sidewall spacing), or when the add-ons were tested on the samples. EF-TEM was not tested, but could as previously noted be used for imaging the thicker TEM slides.

Chapter 3

Cellular interactions with nanostructured substrates

Researchers are working on understanding how cells interact with nanostructures and are aiming at designing devices that can be used for cell manipulation and intracellular sensors (Chapter 1). Nanostructures affect many cellular functions, such as cell mobility, and cell proliferation, but their behaviour is complex and unpredictable. So far there is an insufficient understanding of cell-nanostructure interfaces. This calls for thorough investigation of the vast parameter space in a controlled fashion, but also to investigate the complex interactions on a nanoscale using electron microscopy, the latter being the focus of this chapter.

The current knowledge of how cells react on nanostructured substrates will be reviewed in section 3.1. Next, my main contribution to this field will be presented, in the form of a slightly edited version of Paper I (Section 3.2). Herein, the developed FIB-SEM method used to investigate cells grown on nanostructured substrates without the need for substrate removal is described, and the wide phenotypic variety of the interactions observed are categorised and documented. Subsequently, section 3.3 presents a summary of work done together with partners from Lund University, where FIB-SEM images were used to show how certain nanowires can physically indent nuclear membranes. This information helped in the interpretation of the observed lowered motility, the increased cell division failure and the DNA damage.

3.1 State-of-art

The state-of-art will describe the current understanding of cellular interactions with nanostructured substrates in terms of cell behaviour such as adhesion, migration, and division (Section 3.1.1). Second, the current literature discussing nanostructure access to the cytosol will be presented and related to the work done during this PhD project (Section 3.1.2).

3.1.1 Nanostructure influence on cell behaviour

By varying the nanostructures on the substrate it is possible to influence and control several aspects of cell such as cellular movement (motility), adhesion, morphology and cell population growth (proliferation) (Table 1). However, it is not possible to predict cell behaviour on untested nanostructured substrates, as cell behaviour on nanostructured substrates vary widely depending on both cell type and substrate.

	Study	Material	Cell	Effect
MOTILITY	Chen et al., 2012	Glass	Stem cells (hESCs) and fibroblast (3T3)	Cell-type specific response. Fibroblast moved to nanorough surface, while hESC moved to plain surface.
	Paper IV	Si	3T3 fibroblast	Great variation in motility across substrates, no clear relation observed.
	Paper VI	GaP	L929 fibroblast	Lowered motility on taller nanostructures.
	Xie et al., 2010	Pt	Embryonic cortical neurons	Nanostructures used to reduce cell movement in certain areas.
ADHESION	Bonde et al., 2013	InAs	HEK293	Improved adhesion on nanostructures compared to glass and planar InAs.
	Hällström et al., 2007	GaP	DRG-neuron	Improved adhesion on nanostructures compared to glass and planar GaP.
	Hällström et al., 2010	GaP	DRG-neuron	Measured cellular forces using bending nanostructures.
	Kim & Yang, 2013	Si	HeLa	Fewer focal adhesion sites on nanostructured substrates.
	Kim et al., 2005	PEG	Fibroblast and P19 EC	Better adhesion on structured PEG, but not compared to glass (for both cells).
	Qi et al., 2009	Si	HepG2	Greater adhesion on nanostructured silicon than glass.
MORPHOLOGY	Bonde et al., 2013	InAs	HEK293	Cell area decreases as nanostructure density increases. Cells lie as on a "bed-of-nails" for high nanostructure densities.
	Bucaro et al., 2012	SiNW	Stem cells	Cell area decreases as nanostructure density increases until a critical point is reached. Directed cellular outgrowth.
	Dalby et al., 2004	PMMA	Fibroblast (hTERT-BJ1)	Larger filopedia production on nanostructures and more rounded cells.
	Kim et al., 2012	Si	A549 (human lung carinoma cell line)	Smaller area on nanostructured substrates and higher number of filopedia per cell.
	Paper IV	Si	3T3 fibroblast	Various morphologies and surface areas.
	Paper VI	GaP	L929 fibroblast	Multinuclear cells and nuclear indentation more prevalent on taller nanostructures.
	Piret et al., 2013	GaP	Retinal cells from mice	Neurite outgrowth enhanced on tall nanostructures.
	Paper I	Si	3T3 fibroblast	Large phenotypic variation and tendency to "bed-of-nails" effect on dense nanowires.
GROWTH	Chen et al., 2012	Glass	Stem cells and fibroblast (3T3)	Stem cells proliferated slower on nanostructured surfaces.
	Paper IV	Si	3T3 fibroblast	Changes in cell proliferation.
	Paper VI	GaP	L929 fibroblast	More failed cell division on longer nanostructures.

Table 1 Selection of studies investigating cellular behaviour on nanostructured substrates.

An early example of how two closely related cell types have opposite preferences on nanostructured substrates were documented in 1997 [81]. Turner et al., described the effects of sub-100 nm (40-60 nm wide and 230-320 nm high) silicon nanostructures on two astrocyte cell types (non-neuronal brain cell). The cells were strongly influenced by these structures, but the two types of astrocytes showed opposite substrate preferences [81]. They speculate this was due to the difference in cell preparation, where one cell type through culturing may have inadvertently been selected to be grown on flat substrates. Chen et al., made use of cell types different surface preferences for segregating cells [82]. A mixture of stem cells and fibroblast were cultured on a substrate which had RIE generated nanostructured areas (RIE: refer to Chapter 1). After 48 hours of co-culture the two populations had divided spatially with about 90% efficiency, such that the fibroblast was found mainly on the nanostructured areas, and the stem cells on the smooth regions of the same sample. These two examples showcase some of the difference between cell types. It is important to note that there is a great difference between a neuronal cell and a fibroblast, but even between cells found the body and the so-called immortalised cell lines typically used [43].

Our studies on how fibroblasts were influenced by nanostructured substrates showed that in particular cell motility was a sensitive indicator for differences in nanostructured substrates (Paper IV). However, the silicon nanowire substrates did not express a clear relation between the substrate topography and the motility (Paper IV). The reason why we did not observe a clear structure-motility correlation, might have been due to the great variance in the nanostructured substrates (70-1700 nm in diameter, 60-4200 nm tall and 0.2-5 μm pitch). In contrast when varying only the length of the nanowires (GaP), a simple correlation between decreased cell motility and cell proliferation for increasing nanowire lengths was found (Paper VI). Using knowledge of nanostructures influence on motility, researchers are experimenting with limiting cellular movement for electrophysiological measurements [83], or for guiding cellular movement and growth [84]–[86].

The decreased motility observed on some nanostructures might be due to increased adhesion compared to control samples. For example, 4.4 μm tall and 92 nm wide nanowires at various densities all lead to significantly stronger adhesion compared to the flat controls as tested by rinsing [87]. This was linked to slightly larger and elongated focal adhesion sites[8], at similar focal adhesion densities, possibly explaining the improved adhesion. In literature adhesion is often improved on nanostructured substrates [87]–[89], but this is not always the case. For example, Kim & Yang observed a significant decrease in focal adhesions per HeLa cell on silicon nanowires, and along with a diffusive behaviour of the focal adhesion sites, the adhesion to the substrate appeared lower than controls [90]. Likewise, Kim et al. noted an increased cellular adhesion of P19 EC cells and fibroblasts on PEG nanostructured substrates compared to control PEG substrates, but the adhesion was worse when compared to flat glass substrates [91]. Nanostructures therefore do not unequivocally result in stronger adhesion, but rather adhesion varies with material, nanostructures and cell types.

Nanostructures have also been used to estimate the adhesion forces of cells. Recently, SEM of dried cells on bending nanowires where used to describe cellular forces [92]. FIB-SEM was used to reveal nanowires bending underneath a CPD dried cell (CPD: refer to

8 Focal adhesions are large and dynamic protein complexes which are formed by the cells to anchor themselves to the substrate and for driving cellular movement.

Chapter 2). However, interpretation of the forces based on dried cells may be misleading as the cells most likely endures volume changes during dehydration and drying [93], [94]. Li et al., investigated cell forces based on nanowire bending observed with SEM after CPD of cell, and found forces in the range of 2-4 μN for three different cell types [95]. In contrast, experiments performed on live cells on nanostructures report forces in nanonewton [96]–[99]. Differences may naturally be due to cell variations or other variations, but we think that the effects of sample processing should be considered.

The morphology of cells is greatly influenced by nanostructures. This involves larger filopedia production presumably used for cells navigating the nanotopographical landscape [92], [100], and directed cellular outgrowth [84], [101]. In several instances, the cells appear more rounded (presenting a smaller projected cell area) on nanostructured substrates (Table 1). Interestingly, for a particular set of cells and nanostructures, a study has found that decreasing cell area for increasing nanostructure densities occurs up to a certain critical point, at which the cells starts resting on top of the nanowires ('bed-of-nails') [101]. Although we did not have the necessary statistical foundation for arguing that more densely packed nanowires causes cells to rest on top of nanowires in Paper I, it has been documented in other cases [87], [101]. Control of surface morphology has potential for use in tissue-engineering applications and for growing neuronal networks [102].

In both Paper I and Paper VI we describe how nanowires cause nuclear indentations. Paper VI further describes that longer nanowire structures cause failed cell division and multinuclear cells, and that this might be due to the extreme nuclear indentation observed. We also noted changes in cell proliferation in Paper IV, and Chen et al., similarly found slower proliferations of cells on nanostructured surfaces [82]. In general it appears that cell population growth is lower on nanowire arrays than flat substrates [102].

3.1.2 Nanostructure access to the cytosol

There is a large interest in obtaining intracellular access with nanostructures for molecular delivery [8], [10], [103], [104] and intracellular measurements [5], [7], [105]. However there is some discussion in literature as to how easily this is obtained [10].

On several occasions scientific studies have claimed to have penetrated cellular membranes with nanowires, but generally these statements relied on the expression of biomolecules, AFM[9] force measurements readings or CLSM imaging [8], [88], [106], [107]. Penetration might in many cases have occurred, but seeing as in-cell recordings can be achieved by extracellular electrodes [108] and spontaneous cellular access is rare [50], [109], one could argue that some of the data indicating cellular penetration might simply be proximity effects. In addition, TEM have shown that cell membranes can wrap closely around nanowires, thereby excluding them from the cytosol [110]. This tight wrapping of nanostructures weakens claims of cellular penetration based solely on CLSM images showing nanowires apparently within cells, as it would not have the needed resolution to resolve a 5 nm thick cellular membrane (Chapter 2.1).

Recently, methods relying on light microscopy making it possible to detect cellular entry have been developed. Berthing et al., used a membrane staining protocol and were able to show thin membranes enveloping nanowires apparently going all the way through cells, they found that about 95% of the investigated nanowires were enclosed by a membrane

9 Atomic force microscopy (AFM) scans the surface with a tip mounted on a cantilever, thereby resulting in a topological map of the surface.

[50]. Live view imaging of the delivery and effect of fluorescently quenching ions via hollow nanowires have further been used to develop a rapid method for detecting cellular access [109]. Using the method they found that spontaneous cellular access was a rare event occurring for less than 10% of the nanostructures [109]. We have further substantiated the notion of extreme membrane folding, and provided a method for electron microscopic verification of the developed LM methods for assessing cellular entry using FIB-SEM (Paper I and Paper VI).

In spite of the seemingly low efficiency of cellular entry observed in literature, nanostructure mediated delivery of biomolecules to the cytosol still have a potential. For even though less than 10% of the nanowire entered the cells, due to the dense nanowire pattern, this meant that about 10 nanowires actually penetrated the cell, and this could be improved by coating the nanostructures [109]. Likewise, the efficiency of cellular delivery has been increased by using diamond nanostructures and centrifugation to let material from the medium enter cells [9]. In any case, nanowire arrays for intracellular access and delivery should be tuned for each specific cell type, and when this is done it may be a valuable tool in providing insights into disease variability [104].

Simply relying on random and low cellular entry efficiency may not suffice in brain-machine interfaces or for electrophysiological measurements. To further increase cytosol access, electrical pulses have been used to temporarily permeabilise cells [10], [67], [111]. Electroporation, as this technique is called, has successfully been used to increase the delivery efficiency of nanostructures and improve intracellular measurements with nanostructures. For instance, measurements after permeabilisation resulted in a larger signal in the case of intracellular recordings, and the signal gradually decreased in the time scale of a few minutes, indicating partial recovery of the outer membrane [67].

The apparent robustness of cellular membranes and the ability to recover from some membrane piercings [67], helps explains how cells can have reasonable viability on nanostructuers [13], [87], [88], even when nanostructures indents nuclear membranes (Paper VI) or goes all the way through a cell [50].

3.2 Paper I

Mapping the Complex Morphology of Cell Interactions with Nanowire Substrates Using FIB-SEM

I would like to thank Rafał Wierzbicki for the extensive work he carried out on this project before my involvement. He fabricated the substrates, performed the embedding and did part of the FIB-SEM imaging. Additionally, I would like to thank Mikkel Jensen, Joanna Łopacińska, Michael Schmidt, Maciej Skolimowski and Fabien Abeille for contributing to the experimental setup. Minor non-essential corrections to the manuscript have been performed since publication, and the format changed to fit that of the present thesis.

3.2.1 Abstract

Using high resolution focused ion beam scanning electron microscopy (FIB-SEM) we study the details of cell-nanostructure interactions with serial block face imaging.

3T3 Fibroblast cellular monolayers are cultured on flat glass as a control surface and on

two types of nanostructured scaffold substrates made from silicon black (Nanograss) with low- and high nanowire density. After culturing for 72 hours the cells were fixed, heavy metal stained, embedded in resin, and processed with FIB-SEM block face imaging without removing the substrate. The sample preparation procedure, image acquisition and image post-processing were specifically optimised for cellular monolayers cultured on nanostructured substrates.

Cells display a wide range of interactions with the nanostructures depending on the surface morphology, but also greatly vary from one cell to another on the same substrate, illustrating a wide phenotypic variability. Depending on the substrate and cell, we observe that cells could for instance: break the nanowires and engulf them, flatten the nanowires or simply reside on top of them. Given the complexity of interactions, we have categorised our observations and created an overview map. The results demonstrate that detailed nanoscale resolution images are required to understand the wide variety of individual cells' interactions with a structured substrate. The map will provide a framework for light microscopy studies of such interactions indicating what modes of interactions must be considered.

3.2.2 Introduction

Nano- and micro-fabricated structured substrates achieve an increasing amount of interest in cell biology, where their uses are as diverse as biochemical manipulation [8], [112], supporting and controlling cell movement [13], [113], [114], electrophysiological measurements [105], [115], [116] and intracellular measurements [117], [118]. Despite this multitude of uses and large interest in nanowires in cell biology, the basic modes of interaction between nanostructured substrates and cells are poorly understood, both in terms of the topography on an ultrastructural level, and in terms of the biological processes when compared to for instance endocytosis of dispersed particles where several pathways have been studied intensely [119], [120].

Examples in literature often show critically point dried (CPD) cells imaged by a scanning electron microscope (SEM). This method provides excellent images showing how cells lie on the particular substrate, and one can get an idea of the level of interaction with the substrate by cell protrusions such as lamellipodia [8], [13], [88], [117], [121]. However it cannot be seen how the nanowires behave below or inside the cells. Combining CPD cells on substrates and focused ion beam SEM (FIB-SEM) does provide some answers about the cell-substrate interaction, but CPD leaves little intracellular ultrastructure intact [71], [122], [123]. Drobne *et al*. managed to obtain some detail by critically point drying a chemically fixed and stained digestive gland epithelium and demonstrates that FIB-SEM can be used for imaging internal structures in biological samples [124]. The method proved suitable for obtaining gross tissue morphology and comparison with embedded TEM images, but the method lacks intracellular detail due to poor contrast which is also illustrated in [113].

Studies have also been done with light microscopy methods such as confocal microscopy, were cells have been imaged in contact with nanostructures in the form of substrates or probes [8], [107], [117]. These images can be made in physiological relevant solutions, but they require fluorescent labelling and are generally limited to a resolution of about 200 nm [125].

Transmission electron microscopes (TEM) together with heavy metal stained and

embedded samples provide high resolution and detailed ultrastructural information in biological specimens [105], [110], [113], [126]. The required thin samples are typically cut using an ultramicrotome. However, for samples also containing glass or silicon substrates as used in this work, there is a risk of delamination and distortions during ultramicrotomy [127], [128]. Therefore the substrate is often removed prior to thin sectioning by either etching [105], [110], temperature induced cleavage [113], [122] or other methods [64], [126], [129]. Exceptions are Dalby *et al*., who manages to avoid substrate removal as they use PMMA structured substrates which can be sectioned by an ultramicrotome [100], and Gnauck *et al*., who uses a FIB to gain access to fibroblast cells on silicon microstructures [130]. Substrate removal could pose an obstacle if nanostructured substrates are to be removed mechanically as the process risks deformation of the nanostructures, but if suitable chemical agents exist, part of or all the substrate can be chemically etched away leaving the structures intact [105]. By using FIB-SEM, substrate removal is not required and this is beneficial in circumstances when the substrate for some reason cannot be removed and is not suitable for microtomy. Alternatively, one can make use of lamella cut-outs made using a focused ion beam (FIB) and image them in the TEM, but this is a very time consuming process [131] although providing higher ultimate resolution than SEM. Here we use block face imaging with the FIB-SEM to image cell volumes at the expense of the higher resolution in TEM.

The large interest in nanostructures and their possible applications in cell biology have sparked many studies investigating the cell-substrate interactions. In 2004, Dalby *et al*., published a study showing how fibroblast would use filopodia to probe a substrate covered with PMMA nanopillars. They provided SEM images of CPD cells and TEM images of embedded cells [100]. Several other studies have also been published on the subjects of cell morphology [100], [132], differentiation [15], [133], [134], and motility [13], [135] on nanostructured substrates. There is in particular a large interest in excitable cells on nanostructures for electrical signalling and recording. For instance, increasing cell signalling by growing cells on CNT covered substrates [115], [136], or close-proximity or penetrating nanostructured arrays for measurement and activation [8], [67], [105], [137]. Several electron microscopy studies have been made of the interfaces [71], [105], [122]. In the Thomson Reuters Web of Science database, the search term “nanowire* and cell* and bio*” indicates about 200 publications per year in the field. It highlights the importance of furthering our knowledge of cell-nanostructure interactions, and the need for categorising the effects we see to gain an insight into the biology involved as has been partly done with endocytosis of nanoparticles [119], [120].

In-situ FIB-SEM imaging gives the opportunity to do serial block face imaging which can be reconstructed into a 3D representation of the sample and provide a large 3D image volume [65]. Several reports present how FIB-SEM can be used to image frozen biological samples [128], [131], [138], but ultrastructure visibility is limited due to the poor contrast. Combining the techniques known from polymer embedded TEM samples, and the fast FIB-SEM method it is possible to achieve a fair quality of the ultrastructure and volume imaging [63]–[65], [113], [126], [138]. Except for Bittermann *et al*., the literature on embedded FIB-SEM on biological samples tends to focus on various forms of substrate removal as was the case for TEM – depending on the sample this may introduce artefacts or simply be impractical. The focus on removal comes from the embedding method which leaves a large volume of resin above the cells, and removing the substrate makes the cells easily available from below.

In this paper we present a study of block face FIB-SEM imaging of polymer embedded 3T3 Fibroblast cell monolayers on nanostructured substrates without prior removal of the substrate. To our knowledge we are one of the few (together with [130]) to show FIB-SEM images of resin embedded cells on nanostructured samples without any removal of the underlying substrate, and present FIB-SEM images of cells cultured on a set of different substrates: Flat glass is used as a reference and two morphologies of silicon nanowires are used. We tested both a tilted- and a non-tilted milling approach depending on the sample.

We present an overview map of the observed interactions between the nanostructured substrate and the cells. Some of these intricate interactions have, to our knowledge, not been reported previously and demonstrate how complex these can be. For example we observed how nanowires were broken off from the substrate and subsequently engulfed by the cells and ordered in tightly packed clusters. We also observed how microvilli of cells could probe into the nanostructures they rested on. Lastly, we show an instance of nanowires indenting the nucleus without penetrating it. This leads to numerous issues to consider when performing light microscopy on such samples as many of the nanostructures used for optical studies are often not directly observed by e.g. fluorescence from the nanostructure itself. The map also provides a starting point for organizing observations from the many different reported experiments and is a beginning to categorise the many different interactions and eventually studying the detailed underlying pathways.

3.2.3 Materials and methods

Nanostructure substrate fabrication

Two different black silicon substrates also known as "nanograss" (Jansen et al., 1995) were used: one provides high density silicon nanograss (Nanograss A), while the other has sparser nanowires (Nanograss B). A table of the substrates' different characteristics can be seen in Table 1, refer to Appendix B for SEM images of the substrates.

Sample	Height [nm]	Width [nm]	Density [μm^{-2}]
Nanograss A	990 ± 190	80 ± 60	9.6 ± 0.8
Nanograss B	1170 ± 280	70 ± 40	4.5 ± 0.3

Table 2: Overview of the different nanostructured substrates. The uncertainties are 2 times the standard deviation giving a two sigma / 95% confidence.

The black silicon nanograss was made from 4" low doped silicon wafers using maskless deep reactive ion etching (DRIE). Differing nanostructures were obtained by controlling the reactive ion etch parameters [139]. For instance the density is controlled by varying the process chamber pressure and coil electrode power, whereas the height scales linearly with processing time. DRIE was performed in an advanced silicon etcher (Surface Technology Systems), the SF_6/O_2 ratio was 1.11, while the platen power was 120 W, and the chamber pressure was between 8 and 56 mTorr. This formed nanostructured "silicon grass" at a rate of about 2 nm/s [139].

Cell monolayer culturing

Mouse embryonic fibroblasts (NIH3T3) were cultured on plain glass substrates, and 10 x 10 mm diced silicon chips with Nanograss A and Nanograss B (Table 1). Before culturing, the chips were sterilised with 70% ethanol for 20 minutes, and flushed 3-4 times

with pure water or PBS. The cells were cultured in Dulbecco's modified Eagle's medium with Glutamax (DMEM; GIBCO Life Technologies), 10% fetal bovine serum (FBS; Sigma) and 1% penicillin-streptomycin (P/S; GIBCO Life Technologies). Standard conditions of 37°C and an atmosphere of 5% CO_2 were applied. As capillary forces during drying are known to result in nanowire bending and clustering [140], care was taken to always have liquid covering the samples during preparation.

Cell monolayer post-culture processing

After culturing for 72 hours the cells were fixed, stained and embedded. First, the samples were fixed with 2% glutaraldehyde in 0.05 M sodium cacodylate buffer, pH 7.2 (isotonic, 300 mOsm) for 1 hr, rinsed in 0.15M sodium cacodylate buffer pH 7.2 (2 x 30 min), and postfixed in 1% osmium tetroxide in 0.12 M cacodylate buffer pH 7.2 (isotonic, 300 mOsm) for 1 hour. Next, the specimens were rinsed in Milli-Q water (2 x 10 min) to remove osmium residues, and stained with 1% tannic acid in Milli-Q for 1 hr. Following a rinse in Milli-Q (2 x 10 min), the sample was stained with 1% uranyl acetate for 2 hrs. The specimens were dehydrated and embedded in Epon according to standard procedures (Appendix B).

The polymerised Epon formed a meniscus over the substrate, leading to a thick resin layer in the centre and a thinner layer near the chip edges. This meant that a circular band of cells were directly accessible with the FIB-SEM, with an excessive thick layer in the centre which thinned out towards the periphery leaving only collapsed cells outermost.

FIB-SEM

Two FIB-SEM beam systems from FEI were used: the Quanta FEG 3D, and the Helios NanoLab 600. The first system makes use of a dedicated backscatter detector and the second an in-lens detector.

The cells of interest were localised from atop in standard SEM, using the highest acceleration voltage (30 kV) to detect cells underneath the embedding material. In this paper, results are presented which were typically buried 5 µm deep in the embedding medium (cell top to surface). When a cell of interest was located, the acceleration voltage was lowered to 1.5-5 kV depending on the equipment and crossover alignment of both electron and ion beams was performed. To gain access to the cell, rough milling at high ion beam current (7-20 nA) was used, forming a trench in front of the cell. The time for trench milling was approximately 10-20 minutes, followed by finer milling (0.26-1 nA) prior to image recording.

Both microscopes have installed *G2 Slice and View* software provided by FEI Company. It offers recording of slice stacks with a practical slice thickness as low as 10 nm in our experience, and image sizes and resolution allowing detailed imaging of whole cells. The thickness is limited by the ion beam alignment and stability and not the software. Automatic refocusing of the image is possible when the specimen holder is tilted and milling is done normal to the sample surface, but not for larger samples where non-tilted milling had to be performed (also called slanted milling [63]).

To avoid damaging the dedicated vC backscatter detector in the Quanta FEG 3D large samples could not be tilted. Thus to compare non-tilted and tilted sample images a post-processing algorithm was developed to get representative image volumes and comparable images (please refer to Appendix B). Besides allowing milling of large samples, another advantage of non-tilted milling is the decreased brightness gradient resulting from deep

trench imaging [63]. However, this process is more computational heavy, and suffers more if the slice thickness is not sufficient for resolving 1D nanostructures compared to tilted-milling.

If the slice thickness is not sufficiently small for resolving the 1D nanostructures, slanted milling (horizontal sample) would to a larger degree lead to these appearing as pearls on a string (see Figure 5 of cells on Nanograss B).

Image processing

After the slice and view stack has been recorded several steps are required to convert it into a useful 3D dataset. To do this three steps are required: image scaling to correct for imaging on a slanted surface; alignment of the individual slices; and a coordinate transformation to match the original volume – all of which was done with the freely available ImageJ software.

The image is first scaled to obtain the image aspect ratio of the true slice surface instead of the compressed projection image from the tilted view. When image stacks are obtained, small random shifts between the slices occur, which is corrected with the stackreg plugin for imageJ. Lastly, affine volume transformations and rotation is performed to level the substrate to reshape the image volume to the original sample geometry. This procedure was done both for ordinary tilted milling, but also for non-tilted milling showing how a representative 3D stack can be obtained also when using non-tilted milling. To illustrate some of these transformations, the image stack obtained with non-tilted milling of a cell on glass can be observed from the side in Illustration 3.1. For further detail refer to Appendix B.

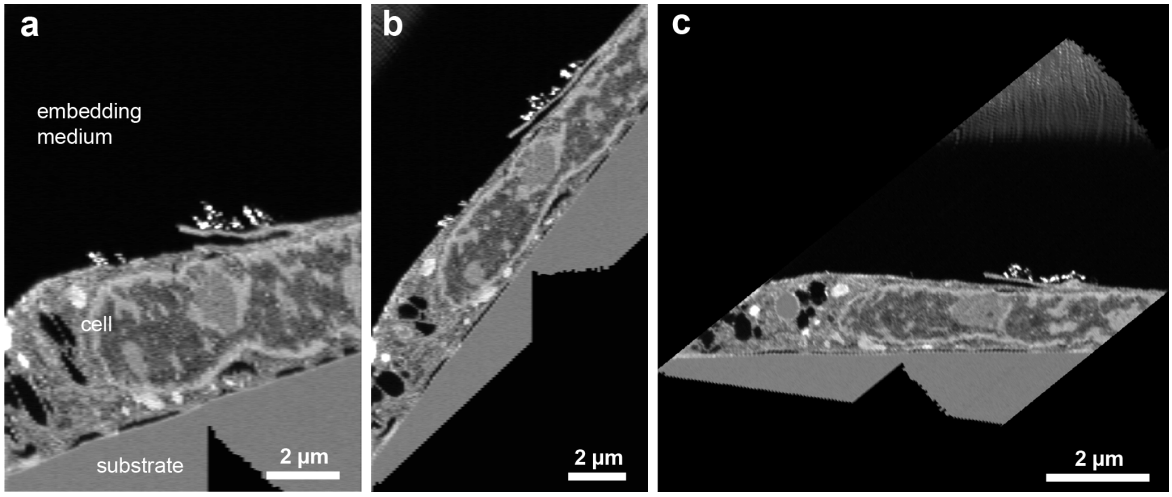

Illustration 3.1: Side views of the non-tilted milling image stack obtained of a cell on glass showing the sequential processing operations' effects. A) The individual slices have been aligned forming a fairly smooth image using stack-reg algorithm. B) Then the substrate is corrected such as to annul the effects of automatic E-beam shifts in the Slice and View program, resulting in a 52 degree substrate. C) Finally the image stack is rotated 52 degrees to represent the sample on the flat substrate having been cut at an angle.

3.2.4 Results

We first describe the blank sample with cells on glass and evaluate the FIB-EM quality. Next, an overview map of the observed interactions on nanostructures is presented, followed by discussions on interactions observed on different substrates.

Cells on a flat substrate

For the NIH3T3 cells cultured on the unstructured blank sample of flat Pyrex glass and investigated with FIB-SEM the final stack's resolution given by the pixels of the original image was 10 nm in X direction, 10 nm in Y direction and 100 nm in Z direction. Please note that the coordinates differ from that of typical cell microscopy as the FIB mills perpendicular to the sample making the X- and Y direction the width and the height of the cell respectively, instead of letting the Z direction denote the height of the cells as in confocal microscopy (cf. Appendix B).

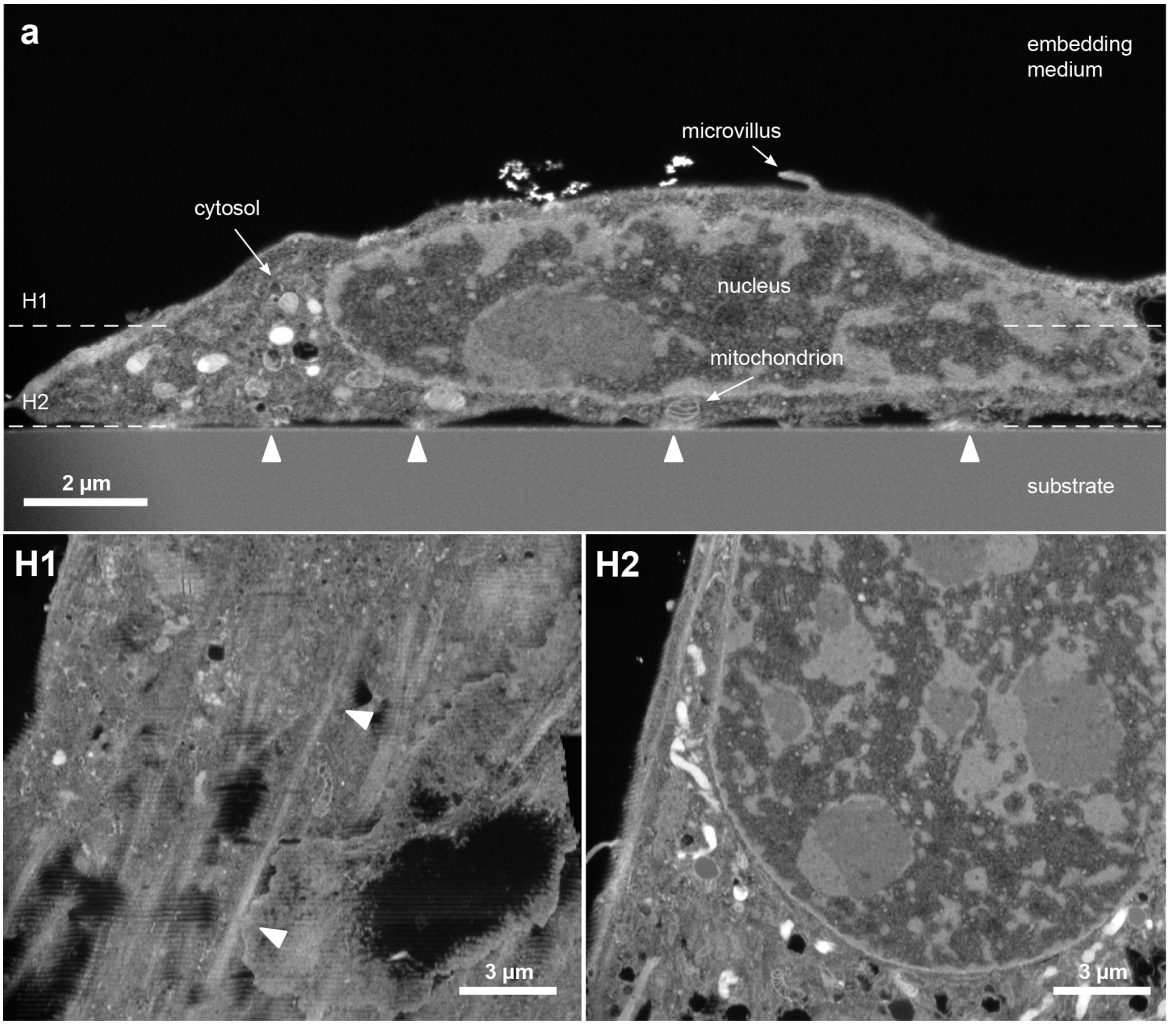

Illustration 3.2: FIB-SEM image of cell on glass showing front view and top views. A) Front view shows a non-processed as-imaged slice of a cell on a glass substrate. One can see the nucleus, microvillius, and organelles such as mitochondria in the cell cytosol. The arrowhead highlight the discrete points where the substrate and cell are in contact. Dashed white lines indicate the two height levels of the horizontal top view sections shown below. H1) Horizontal top view section of the cell close to the substrate level for the fully corrected stack, here it is seen that the cell contacts with the substrate in lines. The two white arrowheads show one such site where the cell touches the substrate. H2) A top view of the stack is shown higher up in the cell.

The correction procedure compromises the resolution in the Y direction as each pixel here have been multiplied with 1.27 as the SEM image is a projection of a 52 degree slanted surface, see Appendix B for a comparison of as-imaged and corrected front view images.

The image of the cell on glass (Illustration 3.2) shows a cell with well-defined organelles, membranes, and nucleus. Some vacuoles are seen in the cytoplasm of the cell on plain

glass which is to be expected for fibroblasts, however no vacuoles were seen in the nucleus and vacuolisation indicating apoptosis was not observed [141]. The reconstruction was done for 100 slices of non-tilted milling and only limited distortions are seen in Illustration 3.2 H1 where horizontal ripples appear, whereas there are no distortions to mention in the section shown in Illustration 3.2 H2. The ripples visible near the substrate are possibly due to imperfect alignment of the images using the stack-reg algorithm, which is less evident higher in the cell where there is no sharp transition between a flat substrate and the cell.

Even though no specific staining has been used to mark specific organelles or adhesion sites, the FIB-SEM method gives a high resolution three dimensional stack which here provide unique images. For instance when the stack has been corrected (and even before) it is possible to directly observe where the cell is in contact with the substrate. This can be observed both in the front view and top view, cf. Illustration 3.2. From these images one can see that the cell interfaces with the substrate in lines, and not as points. This could be correlated with fluorescent labelled actin or focal adhesion stains to determine what these lines exactly represent [96], [126], [142]. Illustration 3.2 A is a non-processed SEM image front view, since the processing steps diminish the resolution and image quality slightly (cf. Appendix B); however, the same adhesion sites are observed in the fully processed stack as observed from Illustration 3.2 H2.

Cells on silicon nanowires, an overview

During experimentation we have found several different ways that the cells interact with nanostructured substrates. In some instances the cell appeared to break off the nanostructures and engulf them, in other cases the nanowires appear to have penetrated the cell and in some the cells were observed lying on top of the nanostructures, these and more interactions can be found in Illustration 3.3.

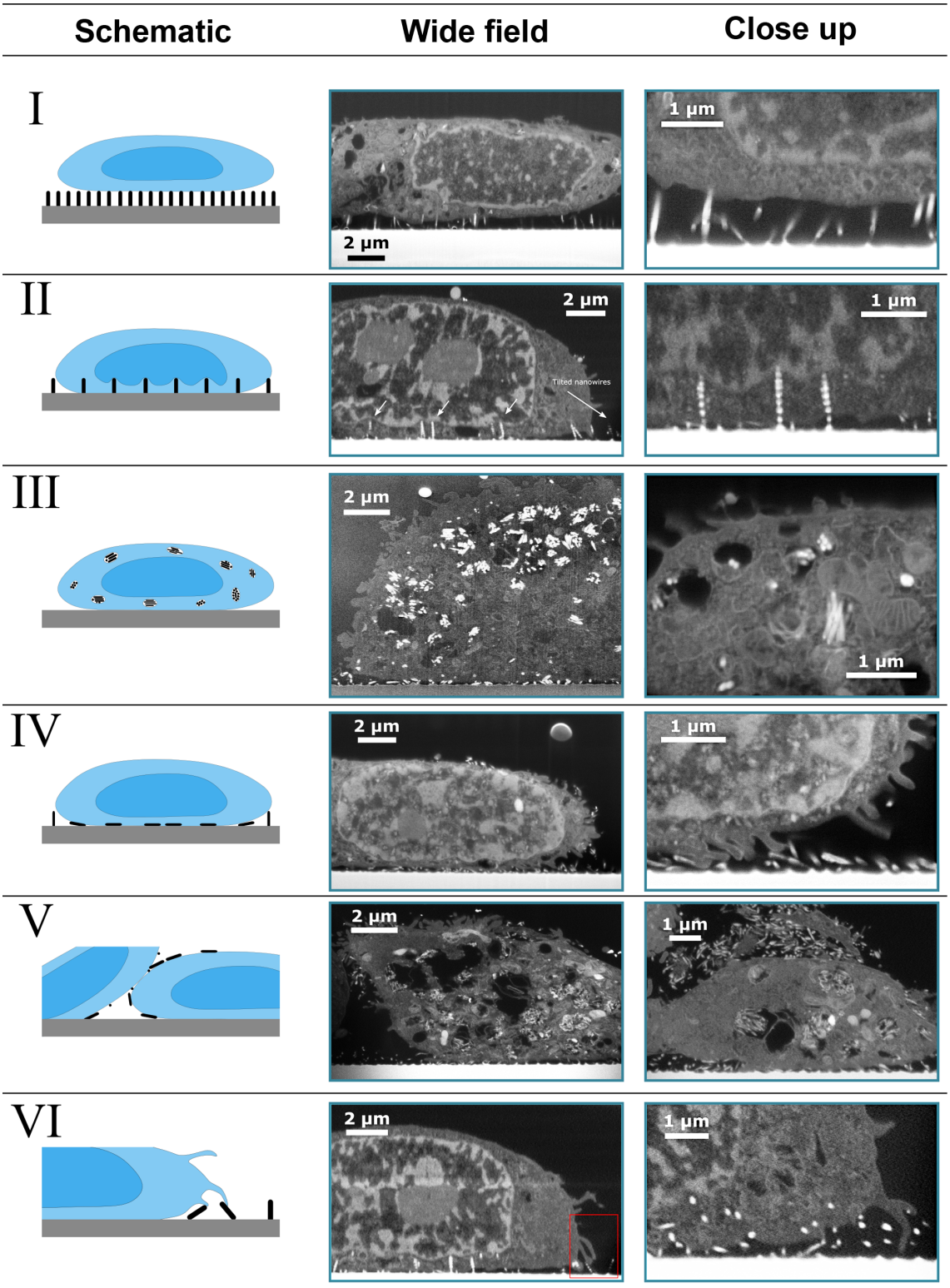

Illustration 3.3: Map of the various cell-nanowire interactions observed. 6 cases are outlined with a schematic view and two supporting FIB-SEM images illustrating the case. Case VII, vacuolisation is to a large degree observed in images displaying Case III and Case VI. The close-up images are either regions from the lower magnification image or higher resolution images from a different image.

Based on the observations, we have defined 7 overall different interactions between the silicon nanowires and the cells, creating a starting point for a map of cell interaction with nanostructured substrates (Illustration 3.3). It is a map showing cell morphology and not behaviour such as differentiation, toxicology or motility. The figure shows a schematic presentation of the interaction, a wide field image and a larger magnification of the same interaction (although not necessarily on the same cell or sample).

Many of the nanowire-cell interactions would not have been easily observable using light microscopy, ordinary SEM with CPD cells, or TEM of single microtomed slices. The images hence illustrate the unique capability of the FIB-SEM for imaging cells on nanostructured substrates. All these cases show that studying cells on nanostructures can lead to complicated interactions most likely affecting the cells in numerous ways compared to the blank glass sample.

The different morphological cases observed in the investigated cells:

Case I ***On top***: A nanowire forest working as a scaffold for the cell, where the cell has little to no contact with the underlying flat substrate beneath the wires, but rather the cell rests on top of the nanowires, which may create inwards bulging of the cell membrane. Observed for both types of nanograss, however more common on Nanograss B.

Case II ***Indented membrane***: The outer membrane may be indented to fold closely around the nanowire. The nanowire could penetrate the outer membrane although the present images do not clearly show if that is the case. In extreme cases, the nanowires were seen to indent the nuclear envelope. Some nanowires have been flattened, meaning that the pitch between the remaining nanowires have increased, possibly allowing the cell to sink down on the remaining nanowires thereby allowing the nanowires to reach further into the cell than **Case I** and to affect the nucleus shape. This was only observed for Nanograss B.

Case III ***Uptaken:*** Nanowires, torn off from the substrate, and taken up by the cell. Nanowires can be found inside the cell in clusters within vesicles, an interaction seen in all cells, but more extreme in Nanograss A.

Case IV ***Flattening:*** Cell flattening weak nanowire forest. This effect is in particular seen in Nanograss A, but also seen to a lesser extent in Nanograss B.

Case V ***Interface:*** In some instances nanowires were torn off the substrate and would remain in the interface between cells. Only observed in Nanograss A.

Case VI ***Probing:*** All cells showed varying degree of microvilli or bleb like structures probing the nanowires, but were in particular prevalent in Nanograss A.

Case VII ***Vacuolisation*****:** Increased vacuolisation in the cell, in some cases these contained nanowires. Illustrated by images from **Case II** and **Case IV**

These different cases are based on the FIB-SEM images from 10 different cells, 5 cells on Nanograss A and 5 on Nanograss B. Table 2 gives an overview of the interactions observed in the different cells. With the limited number of cells examined we cannot

conclude much about the general frequency of these cases, nor give any indication as to the dynamic processes involved. For half of the studied cells, the cell was found to be on top of the nanowires (**Case I**), while **Case IV** was observed for the remaining 5 cells. All of the cells expressed multiple cases as can be seen in Table 2.

Only a single cell showed **Case II** behaviour, whereas uptaken nanowires (**Case III**) were observed in all the cases, however the most extreme cases were observed in the cells which also displayed a high degree of nanowire flattening (**Case IV**). In a single instance nanowires in between two cells were seen (**Case V**). As mentioned all 10 cells showed varying degree of nanostructure probing (**Case VI**), and 3 cells showed increased vacuolisation (**Case VIII**) while having rather extreme nanowire uptake (**Case III**).

#	Substrate	Case I	Case II	Case III	Case IV	Case V	Case VI	Case VII
1	A			X	X		X	
2	A	X		X			X	
3	A			X	X	X	X	X
4	A			X	X		X	X
5	A			X	X		X	X
6	B	X		X			X	
7	B	X		X			X	
8	B	X		X			X	
9	B	X		X			X	
10	B		X	X	X		X	

Table 3: Overview of the different cases observed in the 10 cells. Here it is evident that cells express more than one case and that some of these might be related, and in some instances be prerequisites for certain cases.

High density silicon nanowires (Nanograss A)

In the case of cells cultured on Nanograss A, the images indicate that the nanowires did not have sufficient mechanical strength to withstand forces exerted by the cell. The cells would typically flatten the nanowires (**Case IV**) and engulf them (**Case III**), as seen in Illustration 3.4 A. Nanowires were also observed stuck in between two adjacent cells' membranes (**Case V**). Five cells were imaged (not whole cell 3D slice and view), all of them showed varying degrees of nanowire uptake into organelles appearing like vesicles (Illustration 3.4). Two cells showed significantly lower concentration of engulfed NWs than Illustration 3.4 A. Four cells almost completely flattened the nanowires, whereas the remaining was situated on top of the nanowires. Generally the substrate also induced a high level of microvilli activity probing the nanowires as illustrated by **Case VI**, and in some instances increased vacuolisation as **Case VII**.

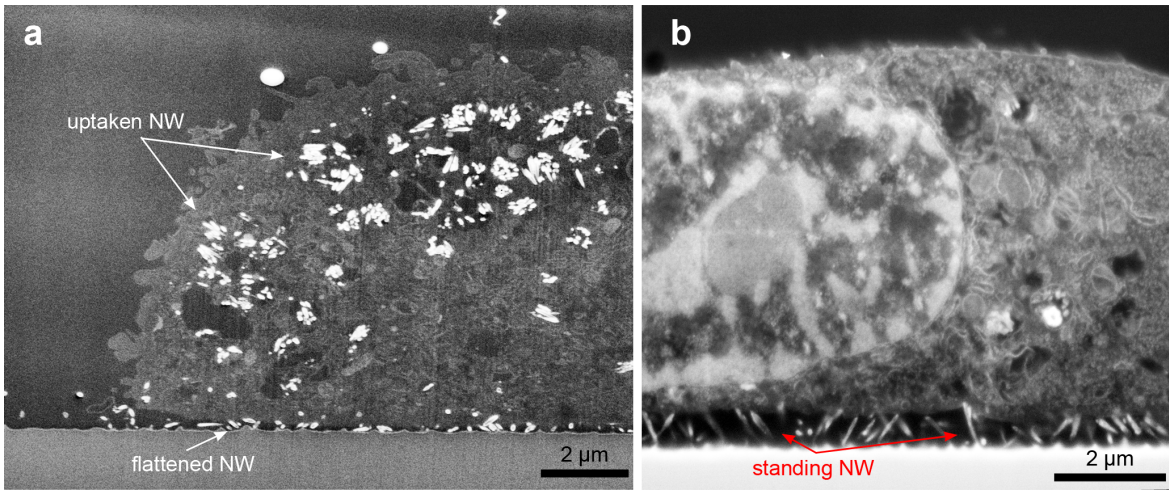

Illustration 3.4: FIB-SEM images of cells on Nanograss A, illustrating different cell behaviours on the same substrate. A) FIB-SEM image showing a cell having engulfed broken-off nanowires, and clearly bent silicon nanowires underneath the cell. The nanowires are closely packed in tightly formed clusters inside what appears to be vesicles. B) Another cell on the same substrate, this time the nanowires have been bent by the cell but not completely flattened.

Once inside the cell, nanowires tended to agglomerate in vesicles or areas with a distinct lack of heavy metal staining. It is not clear whether the agglomeration of the nanowires was caused during endocytosis, where the cell uptakes the nanowires in vesicles to avoid direct contact with the cytoplasm, or the nanowires had agglomerated prior to intake due to nanowire clustering or a wetting effect.

In some instances the nanowires appear as hollow cylindrical objects with ellipsoidal cross section when cut at oblique angles; while direct end-on imaging provides round cross sections (cf. Illustration 3.4). However, the nanowires are not expected to be hollow, as they are created by a top-down processing approach by etching of a monocrystalline silicon substrate. This observation can be explained with the formation of a native silicon dioxide at the nanowires' surfaces or even some plausible oxide growth during processing. Silicon dioxide has a higher secondary electron yield than bare silicon, in fact, K. Okamoto in 1980 showed how measuring the ratio in secondary electron signals from bare silicon and silicon oxide could be used to determine the thickness of the oxide [143]. This effect means that surface oxide would yield a larger generation of secondary electrons than bare silicon, resulting in higher brightness. The images showing 'hollow' nanowires have been obtained with an in-lens system from FEI, which also captures secondary electrons. This explains why the nanowires have a bright oxide ring around an inner silicon core, producing the hollow looking nanowires. This is not observed in the other images presented in this paper as a designated backscatter electron detector has been used (for instance see Illustration 3.3, **Case III** close up), limiting the visual effect of the increased secondary electron generation from the oxide.

Nanowires could to some degree have been flattened during handling or perhaps be a result of cell deformation or shear forces during the embedding process. However as the nanowires in Illustration 3.4 B show, the nanowires appear to be tilted in either direction indicating that it is due to a specific cell interaction with microvilli instead of overall cell volume changes or any dislocation during the embedding procedure. Furthermore, the nanowires outside the range of the cells are freely standing up, and images of standing embedded nanowires having endured the same treatment can be seen in Appendix B.

Low density silicon nanowires (Nanograss B)

For the cells cultured on Nanograss B many of the same phenomena were observed as with Nanograss A. For the 5 investigated cells, 4 of them were found to be lying on top of the silicon nanowires as illustrated by **Case I** (see Illustration 3.3). To some extent nanowires were also bent underneath the cell as **Case IV**. Like Nanograss A, nanowires were found inside the cells as described by **Case III**, and microvilli interaction with the nanograss was observed (**Case VI**), albeit both cases appear to be less prominent compared to Nanograss A. Unique to a single investigated cell, nanowires were seen indenting the nuclear membrane (**Case II**).

For one cell cultured on low density silicon nanowires, the nanowires appear to enter the cytosol and penetrate the cellular membrane (cf. Illustration 3.5). However, the resolution of the images is not sufficient to unambiguously determine whether the nanowires are enveloped by a membrane or not. The nuclear envelope appears not to have been penetrated but rather indented and remains on top of the nanowires (cf. Illustration 3.3) much like the case for the outer membrane when cells lie on top of nanowires (**Case I**). Also observed on the figure is the difference between an 'as imaged' and corrected image. On the 'as imaged' slice, the nanowires appear as isolated white dots due to the nanowires being cut by the FIB at a non-normal angle. In the fully corrected stack, the nanowires appear as a string of white dots, which illustrates a case of insufficient Z-resolution (excessive slice thickness) in slanted milling. The slices were made at an interval of 100 nm for this particular sample, exceeding the diameter of the nanowires (approximately 70 nm). This means that the nanowires cannot be fully represented in the recreated volume and accordingly takes shape as a string of spheres. Illustration 3.5 therefore illustrates the suboptimal sampling frequency which gives rise to artefacts in the reconstruction, even though important cellular features are still discernible.

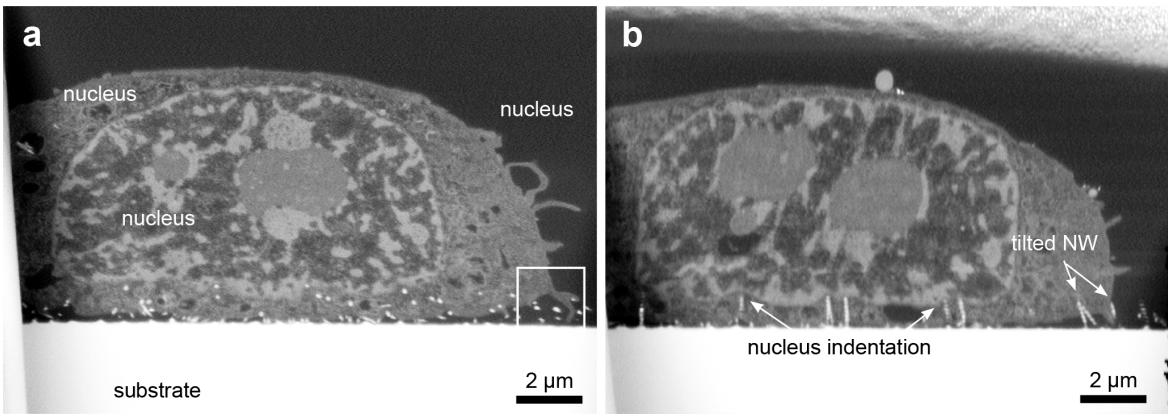

Illustration 3.5: FIB-SEM images of a cell on Nanograss B. A) As imaged (y-corrected) slice showing the nanowires which appear as white dots due to insufficient sampling frequency. Also worth noting is the example of Case III behaviour with microvilli probing the nanograss as outline by the white frame. B) The fully corrected stack can be seen, here the stack has been fully corrected such that independent white dots representing a single nanowire align, illustrating the suboptimal sampling frequency. In some cases the nanowires are not shown from top to bottom as they are slightly tilted compared to the section, quite possibly due to interaction with the cell. Also seen is how the nucleus is avoiding the nanowires (white arrows), and the rippling artefacts which occurs in the corrected front view as previously mentioned.

The reason why the nanowires in the corrected image in some cases do not show the entire length of the nanowire (top-to-bottom) is that the nanowires were tilted compared to the imaging plane (cf. Illustration 3.5). In general, the cell appears to have exerted significant force to the nanowires, in some instances slightly tilting them, and in others bending them

such that they lie under the cell (cf. Illustration 3.6).

This stack (Figure 5) is a good example of multiple behaviours observed in a single cell with **Case II**, **Case IV** and **Case VI** behaviour. The cell's nuclear membrane is indented by the nanowires (**Case II**), but it also flattens some of the nanowires (**Case IV**) while probing the nanowires (**Case VI**). Flattening of nanowires is best seen in Illustration 3.6 where horizontal top view sections are displayed, again illustrating the unique volume viewing quality of the FIB-SEM.

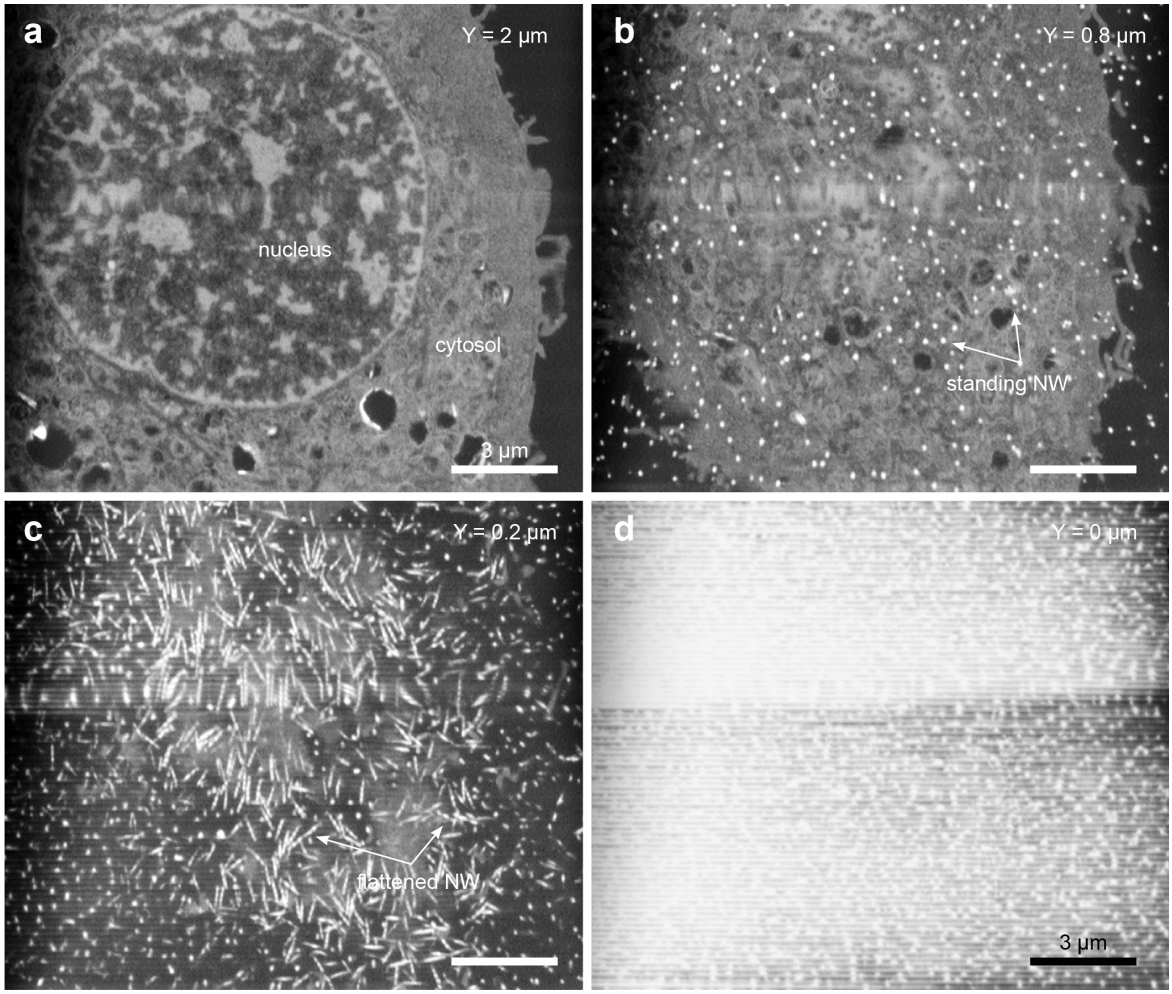

Illustration 3.6: Image series showing the top view FIB-SEM images of the same cells as in FIG5 on Nanograss B. The sections have been made from 2 µm above the substrate and down. The illustrates the major forces in play, clearly showing how several nanowires were bent underneath the cell leaving only a few left to indent the nucleus membrane.

Compared to Nanograss B, the dense silicon nanowires in Nanograss A seem more fragile even though their characteristics are fairly similar except for their density; Nanograss A was to a larger extent not able to withstand adhesion forces exerted by the cell. In addition, Cells on Nanograss A also seemed to have higher silicon uptake and it is accordingly fair to assume that it would have a significant influence on the cells, and possibly also induce apoptosis as the vacuolisation in some cells suggest [141]. It is unclear whether the nanowires are uptaken only directly from the substrate's surface or whether they are taken up from the surrounding solution, which could be possible for **Case V** where loose nanowires are situated in the interface between cells.

3.2.5 Discussion

The cells breaking up and bending the nanowires implies a certain amount of force applied to the substrate. Regarding the forces in play responsible for the nanowire perturbations seen in the different cases, it is a well-known issue that capillary forces can result in nanowire clustering, which is why samples were kept wet after the first wetting [140]. It is evident from the images showing standing nanowires underneath cells and from the blank nanowire samples (Appendix B) that capillary forces and processing did not induce extensive clustering or breaking of wires, although some collapsed nanowires are always to be expected during fabrication and processing.

Several studies have been made on forces involved in nanowire bending and breaking. Using AFM measurements on silicon nanowires Hoffmann *et al*., measured standing silicon nanowires bending strengths. For a variety of nanowire sizes (diameters from 90-190 nm) with height width ratios between 4 and 12 they obtained a maximum force before fracture between 1 μN and 7 μN [144]. The relationship between the maximum force and the aspect ratio of the nanowire appears to be linear. Assuming similar conditions for our silicon nanowires, the fracture force for the used nanowires can be calculated to be around 300 nN.

If we only look at gravitational forces, a cell used in this experiment is estimated to be no heavier than 5 ng (mass of a HeLa cells is about 2-3 ng). This will give rise to a force of about 50 pN when ignoring the buoyancy. Assuming that the density of the cell is 10% higher than the medium, this only results in a gravitational force of 5 pN, which according to the rough estimate of the nanowire strength should not be sufficient to flatten or break the nanowires as we have observed and would in the observed cases also be distributed over many wires. The cells can, however, apply considerable in-plane forces: single focal adhesion site (FAS) forces of 10-30 nN have been reported by Balaban *et al*., and in addition a single cell has been shown to be able to resist a transverse pulling force of 450 nN without detaching from the substrate [96]. Forces measured on single pillars have been reported in the 50 nN range for fibroblasts [98], [99]. Measuring the lateral deflection of silicon nanowires for CPD dried cell on the substrate, Li *et al*. reported cell traction forces in the μN range for three different cells lines [95]. Munevar *et al*. reported average traction forces for migrating fibroblast in the order of 1-5 μN per cell, by measuring the displacement of substrate integrated beads in the wet state [145].

We speculate that these numbers from the literature describing cell forces could indicate that focal adhesion sites and cell movement do have the necessary strength to cause some of the effects which we have observed. In most cases (6 out of 10 observed), the cell was seen lying on top of the nanostructures where cell forces were not sufficient to bend a large amount of nanowires. Migrating cells, however, might incur higher traction forces and possibly be able to flatten larger areas of nanowires as seen in some instances in literature [145].

Regarding the presented map it should be seen as a first attempt at organising the cell-nanostructure interactions as has been done e.g. with endocytosis of nanoparticles [119], [120]. Many of the observed cases have also been seen or hinted in literature on a wide variety of cell types and substrates. For instance cells have been found to reside on top of nanostructures (**Case I**) in several papers [88], [110], [130]. Hanson *et al*. used ultramicrotomed thin sections to image the interface between cortical neurons on nanopillars. By varying the dimensions and density of the pillars they found cells that lied

on top of the structures (**Case I**) and also how a cell could sink down onto the pillars resembling **Case II** [110] though they did not observe nuclear indentation. TEM images of nuclear indentation (**Case II**) were obtained by Hai *et al*., where spine shaped gold protrusions indents the nucleus membrane [105].

Regarding the uptake of 1D nanostructures (**Case III**), a lot of the focus has been on carbon nanotubes and their possible toxicological effects [39], [146], but other materials has also been investigated [147]–[149]. Common for these studies is that the nanostructures were in some form of suspension, while uptake of initially substrate fixed nanowires does not appear to have been reported elsewhere.

As discussed above, certain cell types are able to exert significant forces on nanostructures [96], [98], [99]. But the structures they used were quite robust as they were used for force measurements so the same flattening effect (**Case IV**) was not seen to such an extreme degree. Cell probing of the nanostructures (**Case VI**) have been seen in multiple instances [91], [100], whereas increased vacuolisation (**Case VII**) due to nanowire uptake to our knowledge has not been reported, but increased vacuolisation due to other perturbations have been documented [150], [151]. By organising the interactions one might find correlations between the complex interactions and better our biological understanding of the underlying pathways as has been done with endocytosis of nanoparticles [119], [120].

3.2.6 Conclusions

FIB-SEM imaging of cells on nanowires provides a unique 3D imaging modality, and has the ability to resolve a variety of different internal and external interactions between cells and a nanostructured substrate, based on embedded and heavy metal stained samples. The method presented show interactions with a resolution not obtainable with confocal/fluorescence microscopy, and allows 3D reconstruction of the sample not easily obtained with TEM.

Regarding the trueness of our images, many of the interactions were seen in multiple cells. In addition, the ultrastructure of the cells seems well preserved with visible cell membranes, nuclei and organelles. The fact that the nanowires did not collapse during sample handling also indicates that the images provide a fair representation of what could actually have taken place *in vitro*.

It was also shown that non-tilted FIB-SEM milling could be performed and the stack be reconstructed with the developed method using the freely available software (ImageJ). For non-tilted milling, one should be mindful of having sufficient sampling frequency, while tilted milling was less susceptible to the issue when imaging vertical nanostructures.

Even though the two nanowire substrates were quite similar, differences in cell behaviour could be observed. Nanograss A appeared to have more fragile nanowires which more easily broke of the substrate, were engulfed by cells or simply flattened underneath the cell. Nanograss B in contrast proved to be a more sturdy substrate, but still nanowires were flattened, tilted, and uptaken. The difference between these two substrates seems to be linked to the density of nanowires, where Nanograss A had a higher density of wires leading to groups of nanowires sticking together and more nanowires being bent. In either case both substrates has a strong perturbing effect on the cell morphology.

As we have shown, the vast phenotypic variability gives a large difference in cell appearance on nanostructures, and illustrates that single cell investigation is not sufficient.

Quantification of cell-nanostructure interactions thus requires careful statistics by methods with higher throughput, for instance light microscopy methods, and then supported with representative imaging with FIB-SEM, which is outside the scope of this paper. This study provides an overview map that serves as a starting point for development of high throughput light microscopy methods capable of investigating cell-nanostructure interactions taking due care of the many possible types of interactions. Additionally, to make the map more complete we suggest using TEM for higher resolution imaging cell-nanostructure interfaces imaging as it can be used to resolve how the cell membrane bends and if it has been penetrated, thus expanding on previous work performed [105], [110].

Investigations using electron microscopy have led to an increased understanding of the vast complexity of cellular membrane anatomy; this is particular true for the different nanoparticle uptake pathways in cells which have been observed [120]. The field of endocytic pathways has evolved from a singular focus on clathrin-mediated endocytosis to 10 different mechanisms [120], illustrating the complexity of cellular membrane transport. Likewise the case of uptaken nanowires will likely utilise numerous pathways, and the way the cells interact with anchored nanostructures may cause novel pathways to come into action. Furthermore, the 7 cases presented in the map should by no means be interpreted as an exhaustive list, the vast complexity of endocytic pathways illustrates that more research is warranted into this field.

Our work focused on ultrastructural FIB-SEM investigations of cell-nanostructure interactions. To attain a greater understanding of the interactions we would suggest extensive correlated studies with fluorescent markers, and the usage of molecular techniques to block certain molecular mechanisms to be able to pin-point the biological processes involved, using the presented map as a starting point.

3.2.7 Acknowledgements

We thank for electron microscopy assistance from the Core Facility for Integrated Microscopy (CFIM) at the Faculty of Health and Medical Sciences, University of Copenhagen, and the Centre for Electron Nanoscopy (CEN) at the Technical University of Denmark.

3.3 Paper VI summary

Fibroblasts Cultured on Nanowires Exhibit Low Motility, Impaired Cell Division, and DNA Damage

In a continued effort to uncover how cells interact with nanostructured surfaces we investigated how they influence cell division (Paper VI). The purpose of this study was to increase our understanding of cell-nanostructure interactions, and allow for better design and interpretation of experiments for cellular measurements or for biomolecular delivery. The nanostructures were made by random deposition of 80 nm particles onto a galium phosphide (GaP) substrate and VLS growth (Chapter 1). Instead of varying the density of the nanowires, we varied the height, as it has been suggested that altering the height of the nanowires can be used to target certain parts of the cell for intracellular measurements or biomolecular delivery [152]. Such that short nanowires only reach the cytosol of the cell while longer structures can penetrate deeper and interface directly with the nucleus.

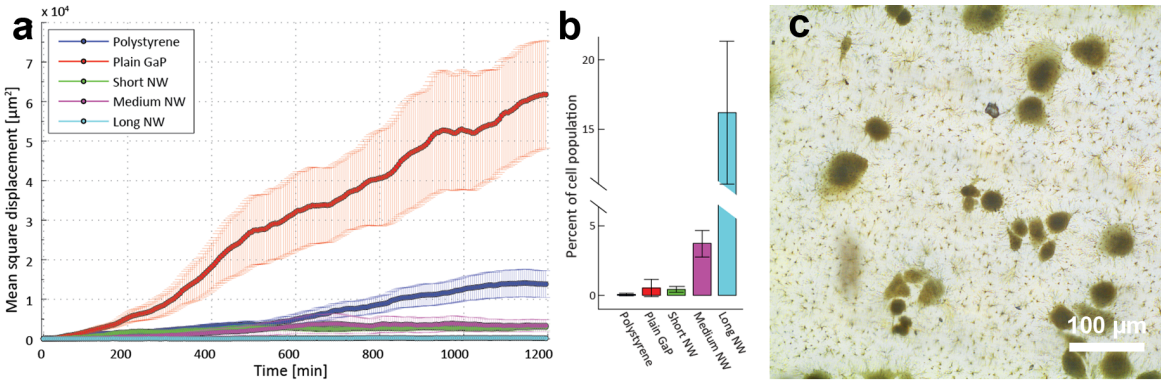

Illustration 3.7: A) Mean square displacement of cells on the nanowire and control substrates. The cells on the long nanowires are the ones moving the least. B) Percent of cells having more than one nucleus. This increases for longer nanowires. C) Light micrograph of cells embedded in Epon. The cells were located visually and selected prior to FIB-SEM. Data analysis and figures A and B were made by Henrik Persson (Paper VI).

Decreased cell motility and cell growth was seen to be directly proportional to the length of the nanostructures (Illustration 3.7 a). The reason behind the decreased cell proliferation on the nanowire samples was investigated using time-lapse microscopy by Ph.D. student Henrik Persson (main author of the article). By studying the phase holographic time-lapse data, Henrik uncovered that cell division was more frequently aborted on substrates with the tallest nanowires, and more so on nanowire substrates than on the control substrates. On all substrates cell division was initiated by the cell rolling up, and at successful division two daughter cells were produced. However, on the long nanowires cells more often rolled up and then spread out without dividing and simply resulted in a larger cell. Using fluorescence microscopy, cells on long nanowires were seen to result in significant increase of multinuclear cells due to failed cell division (Illustration 3.7 b). A study showed that multinuclear fibroblast in cell cultures were caused either by fusing with macrophages or by cells no longer undergoing cytokinesis whilst continuing DNA replication [153]. Seeing as the fibroblast in our case was in a single culture and the process followed with time-lapse, failed cytokinesis and continued DNA replication appear to be the most likely explanation of the multinuclear cells.

3.3.1 FIB-SEM results

The samples with the long and short nanowires were prepared for FIB-SEM as described in Paper I. Light microscopy images of the Epon embedded cells, like the time-lapse data, suggested that larger than normal cells were produced on the nanowire substrates (Illustration 3.7 c). Using the optical images as a guide, the larger cells could be found and investigated with FIB-SEM. Nanowires were found physically impeding deep into the cell for the tall nanowires (Illustration 3.9), and we speculate that the tall nanowires may physically hinder cytokinesis while still maintaining DNA replication (Paper VI). Whereas cells on the short nanowires more easily divide as they can lift and free their nucleus from the nanowires during division.

High resolution images of tall nanowires apparently deep in the cell revealed that some of these were excluded by the cytosol (Illustration 3.8). So in certain cases, nanowires 80 nm thick could be protruding deep into the cell (+4 µm) and still be encapsulated by a very flexible outer membrane. As already mentioned in Section 3.1.2, this observation further supported the notion that cellular penetration is harder to obtain than first imagined.

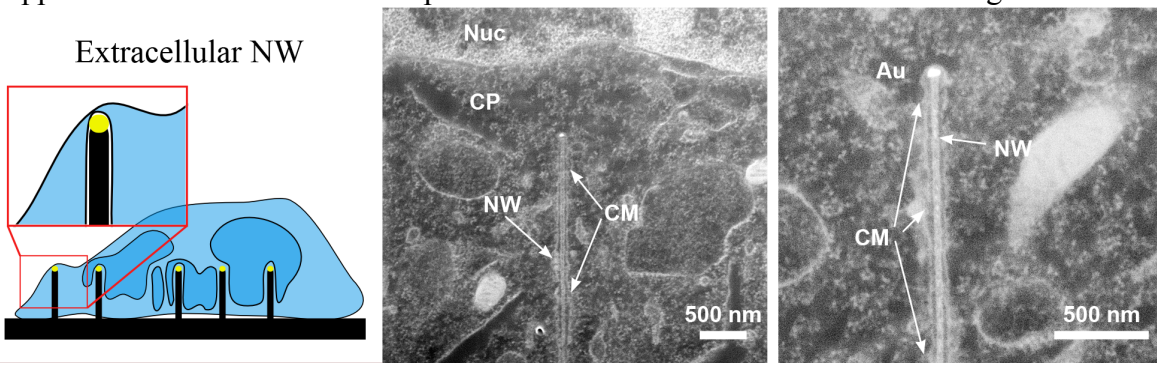

Illustration 3.8: FIB-SEM images showing the nanowires being excluded by the cytosol by a thin lipid membrane. Legend: Nucleus (Nuc), cytoplasm (CP), cellular membrane (CM), nanowire (NW), gold catalyst particle (Au).

FIB-SEM images also revealed that even the longest nanowires did not appear to penetrate the nucleus, but instead lead to expressed nucleus avoidance which we had previously observed to a lesser degree (Paper I). However, Xu et al., states that about 5% of their samples had nanostructures penetrating the nuclei [109]. So we cannot completely rule out that nuclear penetration in fact occurs in our samples due to the limited FIB-SEM sample size. When coupled with immonofluorescence microscopy showing DNA damage and increased concentrations of reactive oxygen species (ROS) in the cells cultured on nanowires, it was speculated that DNA damage was caused by increased ROS formation and not by direct DNA-nanowire interaction. Extreme nuclear avoidance was later described and confirmed using CLSM [87].

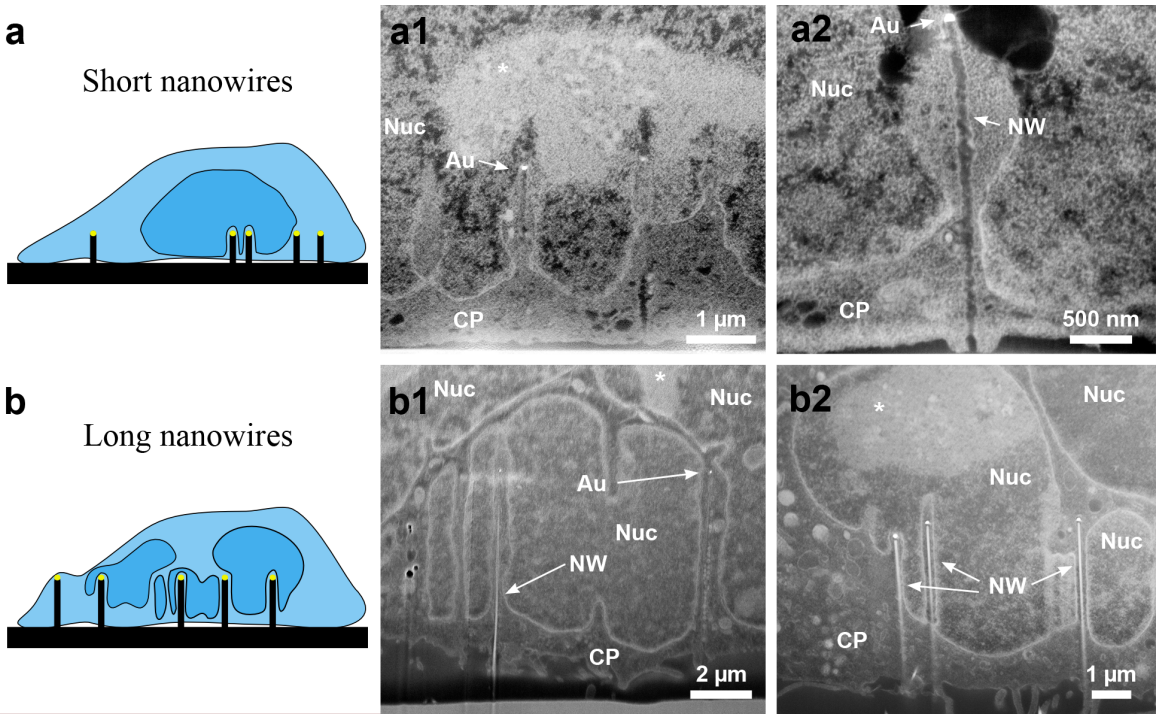

Illustration 3.9: FIB-SEM images of nanowires in cells, with a sketch illustrating overall cell appearances. A) Short nanowires induce significant nucleus indentation, and does not appear to penetrate the nucleus. B) The long nanowires show larger nucleus indentation and cells showcase multiple nuclei or alternatively a very lobed nucleus. Legend: Nucleus (Nuc), cytoplasm (CP), nanowire (NW), gold catalyst particle (Au) and DNA dense areas in nucleus (*).

3.4 Summary

Based on literature and our studies, the behaviour of cells is influenced greatly when grown on nanostructures (Paper IV and VI). It was determined that nanostructures could affect cellular motility, viability and division, but that the results usually could not be generalised to other cell types or substrates. Even on very similar substrates there was a great cell-to-cell variance when imaged using SEM (Paper IV) and FIB-SEM (Paper I). This is also expressed in the wide variability observed using FIB-SEM (Paper I).

Following initial development and testing of the FIB-SEM method for imaging cells on hard nanostructured substrates, we have provided the first EM map of how cells interacts with nanostructures on a substrate. However, the investigations revealed very complex nanoscale interactions, which suggest that further studies involving light microscopy methods should be correlated with EM. Additionally, we have helped highlight how difficult it can be to design nanostructures to penetrate cellular membrane (Paper VI). In several instances we saw both extreme outer membrane and nuclear envelope indentation caused by nanostructures, excluding the nanowires from the cytosol and nucleus, respectively.

Chapter 4

Electron microscopy of CNTs in lung tissue

To complement the *in vitro* investigations focusing on nanostructures potential uses, we have studied the interactions of nanostructures *in vivo* in relation to their potential health hazards. For that purpose lung tissue was chosen since it is currently considered to be the most important route of human exposure to the nanoparticles in production today. The toxicity of CNTs has in several cases been compared to that of asbestos, and CNTs are known to cause pulmonary toxicity even at low concentrations. Developing methods for studying CNT interaction *in vivo* for the purpose of understanding their effects is therefore highly relevant in terms of being able to design non-toxic CNTs.

In order to visualise how CNTs interact with lung tissue, TEM has been the preferred method as it provides the necessary high resolution images to resolve the interactions. However, we believe that FIB-SEM represents a potential asset in this field which is currently unexploited. Therefore, this chapter will describe, my contribution to developing, testing, and discussing the usability of FIB-SEM as a complimentary technique to TEM.

This chapter will start out by describing the tissue fixation quality which we obtained, as it is important for further analysis (Section 4.1). The state-of-art for EM imaging of biological samples is described in Chapter 2 and Paper II. A reprint of Paper II will be provided, describing my main results in this field (Section 4.2). It focuses on exploring the potential of FIB-SEM for imaging CNTs in tissue and compares it to the more standard TEM method. This will be followed by section 4.3, describing the possible origin of the CNT contrast. The work done in this chapter was carried out in collaboration with the National Research Centre for the Working Environment (NRCWE).

4.1 Tissue fixation

As mentioned in Chapter 2, the animal studies performed in this work, relied on immersion fixation. To limit image artefacts, the lungs were filled with fixative prior to extraction and immersion fixation. This allowed fixative to flow to the air spaces in the lung and ensured fair fixation, even though areas having been poorly fixed were observed (Illustration 4.1). To ensure optimal fixation, perfusion fixation should have been performed, but this is a more troublesome and thus requires animal handling staff experienced with this procedure. Additionally, some of the samples were stored longer in fixative prior to embedding, and this appeared to cause some lipid extraction, visible in poorly fixed mitochondria in samples stored for longer.

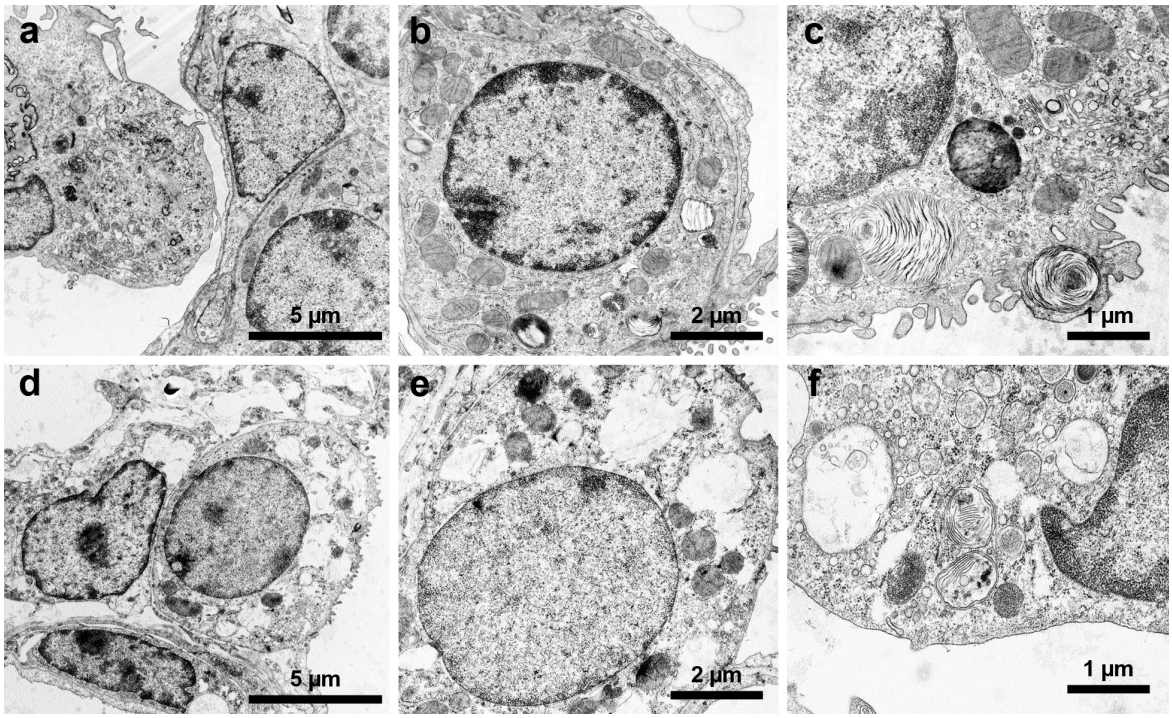

Illustration 4.1: A-C) TEM images of a fair fixation. D-F) TEM images of poor fixation with burst organelles.

4.2 Paper II

FIB-SEM imaging of carbon nanotubes in mouse lung tissue

Before presenting Paper II, I would like to thank and acknowledge my co-authors, in particular the collaborators at NRCWE where the animal exposure was planned and carried out. Minor edits have been made to incorporate the manuscript in this thesis, but the nature of the text is the same.

4.2.1 Abstract

Ultrastructural characterisation is important for understanding carbon nanotube (CNT) toxicity and how the CNTs interact with cells and tissues. The standard method for this involves using transmission electron microscopy (TEM). However, in particular the sample preparation, using a microtome to cut thin sample sections for TEM, can be challenging for investigation of regions with agglomerations of large and stiff CNTs because the CNTs cut with difficulty. In consequence, the sectioning diamond knife may be damaged and the uncut CNTs are left protruding from the embedded block surface excluding them from TEM analysis.

To provide an alternative to ultramicrotomy and subsequent TEM imaging, we studied the use of focused ion beam scanning electron microscopy (FIB-SEM) of CNTs in the lungs of mice, and we evaluate the applicability of the method compared to TEM.

FIB-SEM can provide serial section volume imaging not easily obtained with TEM, but it is time consuming to locate CNTs in the tissue. We demonstrate that protruding CNTs after ultramicrotomy can be used to locate the region of interest, and we present FIB-SEM

images of CNTs in lung tissue.

FIB-SEM imaging was applied to lung tissue from mice which have been intratracheally instilled with two different multiwalled CNTs; one being short and thin, and the other longer and thicker. FIB-SEM was found to be most suitable for detection of the large CNTs (Ø ca. 70 nm), and to be well suited for studying CNT agglomerates in biological samples which is challenging using standard TEM techniques.

4.2.2 Introduction

Carbon nanotubes (CNTs) are a very promising nanomaterial in a wide variety of applications due to their excellent mechanical and electrical properties [154], [155]. However, concerns have been raised about safety due to their chemical stability and structural similarity to asbestos fibres. Pulmonary exposure is the exposure route of primary concern both in the working environment and in the general environment. Accordingly, it is important to understand the potential interaction between CNTs and the lung, which is why lung tissue has been chosen for this study. The concerns have been strengthened as pulmonary exposure to CNTs in a number of animal studies has shown a very consistent asbestos-like toxicological response characterised by inflammation, granulomas and fibrosis with low no-effect levels [35]–[37].

In order to predict the toxicity of CNTs and to make them safe-by-design, it is important to be able to link the toxicity of engineered CNTs to their physical and chemical properties such as length, diameter, coating, charge, and impurities, and to understand how they affect, enter, and eventually locate within the different cell types in the lung. High resolution electron microscopy has aided in the understanding of the uptake mechanisms of CNTs [156], [157], which unlike asbestos are able to penetrate and enter cells directly without endocytosis [158]. Additionally, advanced TEM techniques have demonstrated how CNTs can escape endosomal membranes [159] and thereby challenge phagocytic cells in a manner not recognised from asbestos fibre research, as the toxicity of asbestos to a higher degree is caused by “frustrated phagocytosis” [38].

In the bright field transmission electron microscopy (BF-TEM) imaging mode, agglomerates (non-specifically bound bundles) or even single multi-walled CNTs (MWCNT) have been observed using various *in vitro* models [159]–[161]. Pantarotto *et al*. studied HeLa cells exposed to CNTs, the TEM images revealed that CNTs were dispersed in the cytosol and appeared absorbed via a non-endocytotic pathway, which was confirmed using endocytosis inhibitors. Both Lee *et al*. [160] and Al-Jamal *et al*. [159] studied CNT uptake by macrophages, which mainly revealed CNTs being located in agglomerates within vesicles inside the cells. Interestingly, Al-Jamal *et al*. noted that 14 days after exposure, TEM images showed that the CNTs were more individually dispersed in the cytoplasm, indicating that the CNTs had escaped the vesicle enclosure [159]. Additionally, Al-Jamal *et al*. imaged individual CNTs apparently in the process of directly crossing the plasma membrane and showed how the plasma membrane could enwrap single CNTs [159]. TEM imaging has also been performed on *in vivo* samples [162], [163]. Using light microscopy (LM), Ronzani *et al*. observed bundles of MWCNTs in alveolar macrophages, and this was confirmed with TEM [162]. However, BF-TEM imaging further revealed CNTs in neutrophils and in the mucus layer lining the ciliated epithelial cells, which was not resolved with LM due to the low CNT concentration present in these cell types [162].

BF-TEM has its disadvantages particularly in resolving smaller CNTs, such as single-walled CNTs (SWCNT), from the carbon rich environment. Especially, Alexandra Porter and her group have employed materials science TEM techniques such as High Angular Annular dark field TEM (HAADF-TEM), energy filtered TEM (EF-TEM), and TEM tomography, to provide more selective detection of CNTs against a carbon rich background such as the embedding resin. For example, EF-TEM has been used to create contrast between CNTs and non-stained cells [57]. For a review of these methods please refer to [157].

A major drawback with TEM when trying to resolve how CNTs enter cells is the loss of the third dimension, as it can be difficult to distinguish between whether CNTs are inserted through the membrane, are membrane bound, or have been dislodged during microtomy and thereby lie on the surface of the TEM section [159]. The issue can in part be circumvented by performing 3D TEM tomography, where a tilt series of TEM images are reconstructed into a 3D representation of the sample [159], [164]. Tomography adds time consuming complexity to the imaging while still only obtaining data from a very limited volume only about 300 nm thick [164].

Both ordinary TEM and TEM tomography of CNTs in biological samples are prone to preparation artefacts when using ultramicrotomy to cut the ultrathin sections [158], [164]. The hard particles (e.g. CNTs) often cause damage to the diamond knife used in ultramicrotomy as they are not readily cut, instead the particles are often torn from the sections and cause scratches and holes in the section [158], [164], [165].

To circumvent the ultramicrotomy artefacts from TEM preparation, a focused ion beam (FIB) in combination with a scanning electron microscope (FIB-SEM) is an alternative method. The samples for FIB-SEM are processed and stained much in the same manner as embedded TEM samples [14], [65], [66], but instead of using a diamond knife an ion beam is used to expose the sample. The ion beam mills through the embedded sample material and uncovers a new surface of the sample which can be imaged with the SEM. FIB-SEM can be operated in an automated mode with sequential milling and image recording. After 3D reconstruction the image stack can provide a larger volume compared to TEM tomography, but with a slightly lower resolution (typically 5-20 nm) compared to TEM (typically 2-5 nm in biological samples)[55], [65]. With FIB-SEM, the orientation of the CNTs in relation to the cell membrane is not critical, as the 3D image data can be reconstructed to a 3D volume with potential isometric resolution. Compared to TEM, the FIB-SEM has the potential to avoid microtomy artefacts and render fast 3D images to uncover the CNT-cell interaction. Even though FIB-SEM has been noted to have great potential for mapping nanoparticles inside tissue and has been used to image MWCNTs in monocyte cells [157], this method has yet to be applied to investigating CNTs in tissue, and tested whether it in fact provides easy and artefact-free volume imaging of CNT exposures.

In this paper, we present TEM images of two types of CNTs in mouse lung tissue and some of the consequences of ultramicrotomy artefacts. In addition, we present SEM images of the microtomed block face, which can be used to localise regions of interest due to protruding un-cut CNTs. Subsequently, we study how FIB-SEM can be used to provide images of CNTs in lung tissue, and the artefacts linked to this method. Additionally we discuss how to limit milling artefacts and introduce a new milling geometry (called double-non-tilted milling) to avoid such artefacts. Using two types of CNTs with varying size and stiffness, we illustrate the applicability and critically assess the limitations of this

method. We also document how the FIB-SEM can work as a complementary tool to TEM for imaging CNTs in biological samples especially in 'hot-spot' regions with high concentration of agglomerated CNTs.

4.2.3 Materials and methods

CNTs

A large and a small type of MWCNTs have been used (TEM images in Illustration 4.2). The small CNT sample was NRCWE-026 (CNT_{Small}) from Nanocyl with an average length and width of 850 nm and 10 nm. The second type (CNT_{Large}), was NM-401 which is a test material in the Nanogenotox project (Nanogenotox, 2013), and compared to CNT_{Small} these are about 5 times larger, measuring an average length of 4 μm and having a thickness of about 70 nm. Further information regarding the two types of CNTs is presented in Appendix C.

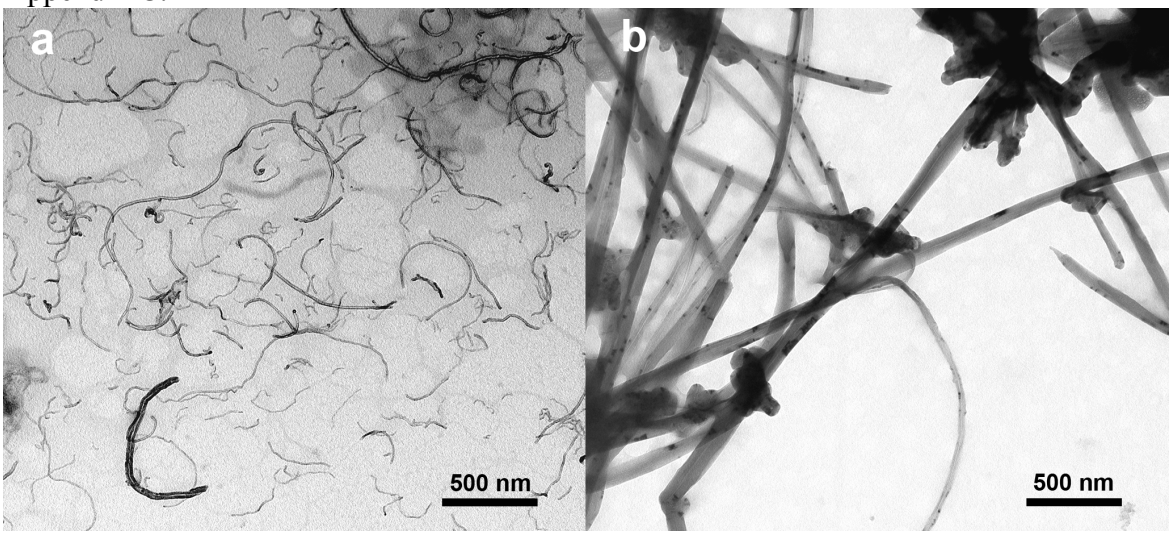

Illustration 4.2: TEM micrographs of the two CNT types used. A) CNT_{Small}. B) CNT_{Large}.

Mice

Female C57BL/6 mice 5-7 weeks old were obtained from Taconic (Ry, Denmark). The mice were allowed to acclimatise for 2 weeks before the experiment. All mice were fed (Altromin no. 1324, Christian Petersen, Denmark) and allowed water *ad libitum* during the whole experiment. The mice were group housed in polypropylene cages with sawdust bedding and enrichment at controlled temperature 21 ± 1°C and humidity 50 ±10% with a 12-h light: 12-h dark cycle. Female mice were studied at 8 weeks of age. The experiments were approved by the Danish "Animal Experiments Inspectorate" (permit 2010/561-1779) and carried out following their guidelines for ethical conduct and care when using animals in research.

Preparation of exposure stock and intratracheal instillation of CNTs

CNTs were suspended by sonication in NanoPure water containing 2% serum collected from C57BL/6 mice. The particle suspensions (3.24 mg/ml) were sonicated using a Branson Sonifier S-450D (Branson Ultrasonics Corp., Danbury,CT, USA) equipped with a disruptor horn (Model number: 101-147-037). Total sonication time was 16 min at 400 W and 10% amplitude. During the sonication procedure the samples were continuously cooled on ice. The mice were treated with a single intratracheal instillation of 162 μg of CNTs in a 50 μl volume, as previously described [166]. The mice were anesthetized with

4% isoflurane in the chamber until fully relaxed and 2.5% during the instillation. Vehicle controls were intratracheally instilled with NanoPure water with 2% serum sonicated as described for the CNT suspensions. The samples were part of a toxicological study in which three doses were used (18, 54 and 162 μg/mouse). Only the highest dose was chosen for the electron microscopy method development presented in this study. The dose studied (162 μg) corresponds to pulmonary deposition during 32 8-hour working days at the current Danish occupational exposure level for carbon black (3.5 mg/m^3) assuming a 10% deposition rate [35] and a ventilation rate of 1.8 L/h for mice [167]. Clearance of CNTs from lung has a reported half-life of ca. 1 year [37] and therefore we assume that none of the deposited CNTs would be removed within this time frame.

Lung tissue

24 hours after the intratracheal instillation, mice were anaesthetised by subcutaneous injection of Hypnorm–Dormicum and the mice were bled by cutting the groin. The lungs were fixed *in situ*, by cannulating the trachea and delivering 2% glutaraldehyde in 0.05 M cacodylate buffer (pH 7.2) at a constant fluid pressure of 30 cm before the thorax was opened. The fixative was mixed from glutaraldehyde (SPI Supplies #02608) and sodium cacodylate (Sigma-Aldrich #C4945). Thereafter the lungs were excised and immersed in 2% glutaraldehyde 0.05 M cacodylatebuffer (pH 7.2) and stored refrigerated until further processing.

Sample treatment

Following fixation, homogeneous looking 1 mm^3 samples of the alveolar regions of the lung were cut out by a scalpel. The samples were rinsed in 0.15 M phosphate buffer (pH 7.2) and subsequently in 0.15 M sodium cacodylate buffer (pH 7.2) and postfixed in 2% osmium tetroxide (Polysciences #0972A) and 0.05 M potassium ferricyanide (Sigma-Aldrich #702587) in 0.12 M sodium cacodylate buffer (pH 7.2) for 2 hours. Following 3 rinses with Milli-Q the samples were en bloc stained with 1% Uranyl acetate (Leica Microsystems, Ultrastain-1) in Milli-Q water overnight at 4° C. The samples were dehydrated in ethanol and embedded in Epon according to standard procedures (TAAB Laboratories Equipment, TAAB 812 resin kit).

To prepare the embedded samples for FIB-SEM, and to allow for a comparison between the information gained from TEM and FIB-SEM, ultrathin sections (80 nm) were cut with an ultramicrotome (Leica Ultracut UCT). The diamond knife angle was 6 degrees, while the cutting speed was set to 1.5 mm/s. The sections for TEM were post-stained with uranyl acetate and lead citrate (Leica Microsystems, Ultrastain-2). Following ultramicrotomy the exposed surfaces were ready for FIB-SEM imaging. TEM imaging was performed on a CM 100 BioTWIN from Philips operated at 80 kV.

FIB-SEM

Following microtomy the Epon block samples were mounted with conductive silver paste (EMSdiasum, 12686-15) on SEM stubs and sputter coated with gold. Imaging was performed in high vacuum, and both an in-lens and a designated backscatter detector were used on two different FIB-SEM systems: FEI Helios and FEI Quanta FEG 3D. The Helios in-lens system, with immersion mode operated in either SE or BSE mode, had a higher ultimate resolution than the Quanta FEG 3D FIB-SEM with the designated backscatter detector (vCD – low **v**oltage high **c**ontrast **d**etector). In return, the Quanta FEG 3D detector is more sensitive to backscattered electrons and as the contrast in the sample stems from inelastic scattering on electrons on the heavy metal staining (Z-contrast) [65],

[157] the Quanta FEG 3D in our case provided images with better contrast. In SEM, regions of interest with lung tissue and neighbouring protruding CNTs were located with high acceleration voltages (30 kV) for the maximum penetration depth to visualise tissue within the resin block. The angle between the electron- and ion beam was 52° and FIB milling was performed using a 30 kV Ga-ion beam with beam currents ranging from 0.44 nA to 7 nA during fine- and rough milling, respectively (Illustration 4.3 a). SEM images of the embedded CNTs were obtained using low acceleration voltages (2-5 kV) and low beam currents (1.4-4 nA) to limit beam damage. Image stacks were processed either according to the tilted-milling or non-tilted milling approach as previously described [66], and subsequently post-processed in Amira.

To limit milling artefacts for obtaining a 3D FIB-SEM image stack, a new milling strategy was introduced, named double non-tilted milling (Illustration 4.3 b). This involves locating an area of interest, where non-tilted milling is performed in front of the protruding CNTs. Next, the sample is rotated 180 degrees around a vertical axis, and again non-tilted milling is performed in front of the CNTs resulting in a blunt wedge (Illustration 4.3). Now the sample is rotated 180 degrees again to clean up the 'milling surface' and deposit a 0.5 µm to 1 µm thick platinum layer on the 'top surface', afterwards ordinary slice and view imaging performed.

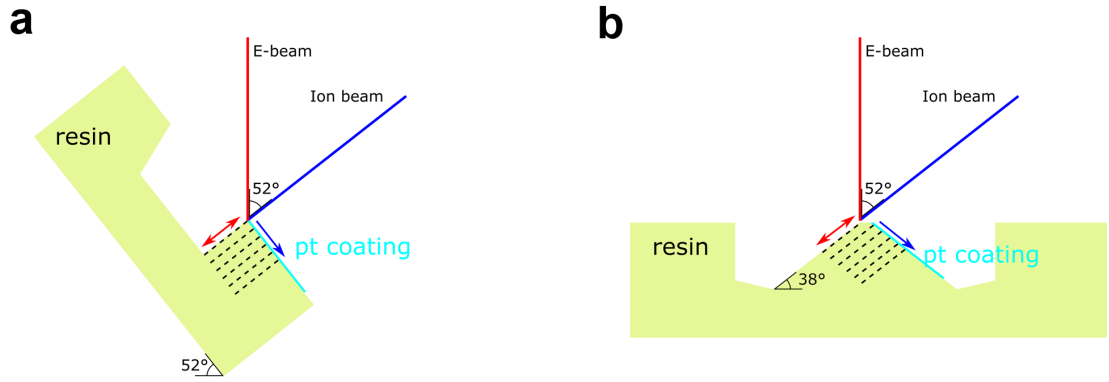

Illustration 4.3: Schematic of the milling geometries used. A) Standard milling approach where the sample is tilted 52 degrees. B) The double non-tilted milling method, where milling is performed without tilting the sample whereby a wedge is created which has two FIB polished surfaces.

4.2.4 Results

TEM of CNTs in lung tissue

TEM analysis verified that the fixation and embedding had maintained adequate preservation of ultrastructure. The control samples displayed well fixed and stained tissue with preservation of organelles such as lamellar bodies and mitochondria.

As expected, the samples from CNT-treated mice contained more microtomy artefacts than the control sample. Agglomerates of CNT_{Small} tended to give rise to marks (Illustration 4.4 a) caused by the diamond knife failing to cut the CNTs, but the context and ultrastructure of the cells surrounding the agglomerates were still resolvable. Artefacts were especially apparent in the sample with CNT_{Large}, see Illustration 4.4 c-d. The CNT_{Large} caused scratches and holes in the sections, in some cases obfuscating the context of the CNTs. TEM images with microtomy artefacts have been observed previously [159], [168]–[170], generally the artefacts presented in the literature are not as pronounced as in the present study (Illustration 4.4). The reason may be that relatively clear areas are normally chosen for publications and/or that smaller CNTs are studied. However, studying

only small CNTs or regions with no sectioning artefacts introduces a bias in the sampling and excludes agglomerates and high concentration 'hot-spots' from being studied in the same detail.

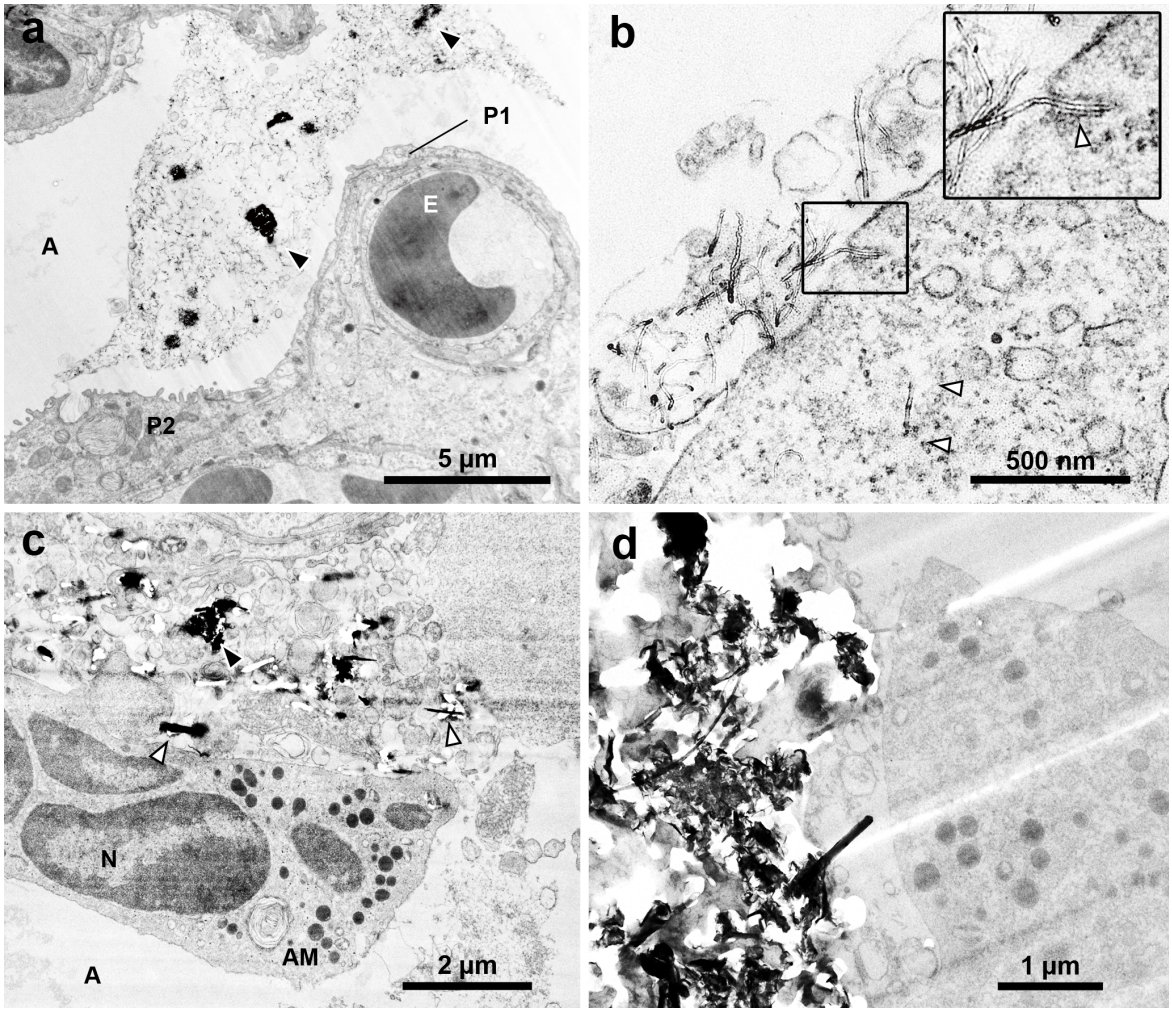

Illustration 4.4 TEM micrographs of lung tissue with CNT_{Small} (a-b) and CNT_{Large} (c-d). A) Overview image of a large agglomeration of CNT_{Small} in the region where black arrowheads highlight very dense CNT agglomerates in the alveolar lumen. The CNTs are causing minor microtomy artefacts (stripes extending from the middle of the image towards the lower right corner). B) A CNT_{Small} is seen interacting with a cell (insert), and a CNT observed freely inside the cytosol (white arrowhead). C) Overview image showing CNT_{Large} between cells causing major microtomy artefacts. D) TEM image of a dense agglomeration of CNT_{Large} resulting in holes and stripes in the ultrasection. A – alveole, AM – Alveolar macrophage, E – erythrocyte, N – nucleus, P1 – pneumocyte (type I), and P2 – pneumocyte (type II). Black arrowheads indicate CNT agglomerates, whereas white arrowheads indicate single CNTs

Generally, the artefacts comprised of folds, knife marks and holes, but in some instances CNTs were dragged across the sample surface and deposited elsewhere, as was also documented for hard particles [165]. In the case of CNT_{Large}, artefacts were linked with obvious scratches and drag marks, but besides the marks it was not possible with standard bright field TEM to document whether the CNT were part of the sample or deposited on top of the section. Clear drag marks were not observed on the CNT_{Small} sample and we found examples of CNTs both inside and outside the cells. In some cases it was clear that the CNT was imaged in place as they would seem to be in the process of penetrating the cell by indentation of the membrane, while others would appear inside a cell without any indication of CNT-cell interaction (Illustration 4.4 b). Accordingly such images may be

interpreted as further proof of CNTs avoiding or escaping the endosomal pathway [159], [161], or alternatively they may represent CNTs which have been dragged and deposited onto the cell leaving an irresolvable dragging path.

SEM of ultramicrotomed blocks

To emphasise the effect that the hard CNTs can have during ultramicrotomy, the blocks were imaged with SEM after ultramicrotomy (Illustration 4.5). This revealed that both CNT_{Small} and CNT_{Large} remain protruding from the block following sectioning, leaving much of the desired CNTs unsectioned. Similar protrusions have been observed following fracturing CNT composite materials [171], [172]. In the paper by Choi *et al*., the CNT could in some instances leave indentations of where it had been in the material prior to fracturing. Likewise, we have observed that CNTs can leave an imprint in the Epon layer, which is caused by the diamond knife forcing them to bend and flatten along the surface of the block. Once clear of the diamond knife edge the stiffness of the CNTs apparently makes them straighten up again.

It should be noted that the microtomy artefacts presented here for the CNT_{Large} samples are quite extreme, but the SEM images can still serve as an example of how much insufficient cutting by the diamond knife can influence what is imaged in the TEM. This could also explain why CNTs are rarely imaged from "atop" having been cut orthogonal to their long axes, as even the small CNTs in this example had protruding CNTs still remaining in the block.

To confirm that the structures protruding from the ultramicrotomed block faces of the embedded lung tissue were indeed CNTs, pure CNTs were embedded and ultramicrotomed. The same protruding structures were seen as in the lung tissue samples (data not shown). Additionally, we did not observe such structures in the control samples.

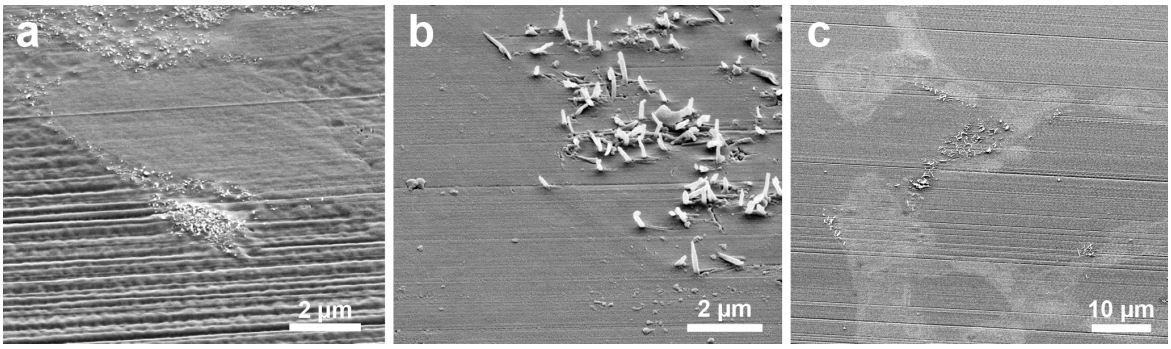

Illustration 4.5 SEM micrographs of the exposed block surface following ultramicrotomy. A) Image of the CNT_{Small} sample protruding slightly from the microtomed surface. B) A CNT_{Large} sample after microtomy, where large protruding CNTs are seen which in some cases have left an impression in the Epon block during flattening. C) Low magnification overview of how lung tissue in close proximity to CNTs can be visualised and later targeted with FIB-SEM.

FIB-SEM of CNTs in lung tissue

To avoid the massive ultramicrotomy artefacts especially around 'hot-spot' regions which obscure actual cell-CNT interactions, the ion beam of the FIB-SEM can be used to mill through the CNT rich sample.

Illustration 4.6 shows recorded FIB-SEM images of CNTs in a toxicologically relevant tissue sample. Previously FIB-SEM images of CNTs in cultured cells have been presented [157]. FIB-SEM images of unexposed mouse lung (control) can be found in the online supplementary material. The images clearly show the outline of cells, their nuclei and

distinctive organelles. The CNT_{Small} sample (Illustration 4.6 a-b) showcases areas with material outside the cell which looks similar to the agglomerates of CNTs observed in Illustration 4.4 a, but unlike the TEM, SEM does not have the required resolution to distinguish CNTs from other cellular material (also refer to the discussion below and Illustration 4.8). Due to the resolution of the SEM it can therefore be difficult to determine whether and how the CNTs and cells interact, but some of the agglomerates appear to be in contact with the cell membrane. The limitations of the FIB-SEM are clearly seen in the highlighted invagination, which could be CNTs in the process of being taken up by the cell (Illustration 4.6b), but unfortunately the FIB-SEM cannot distinguish these structures from cellular material making confirmation of the observation challenging.

The CNT_{Large} sample (Illustration 4.6 c-f) contains larger structures making them easier to distinguish from the cellular material. CNTs were mostly observed in the intercellular space, an observation confirmed by TEM imaging. However, the FIB-SEM demonstrates that it can produce images of agglomerates of CNT_{Large} with no sectioning artefacts, compared to the shredded ultrasection shown in Illustration 4.4 c-d, which makes it possible to image CNTs apparently penetrating the cell membrane (Illustration 4.6 c-d). The images are not completely artefact free (Fig. 5 c-e), as is evident from vertical white lines (curtaining) and protruding CNTs from the milled surface (Illustration 4.6 f).

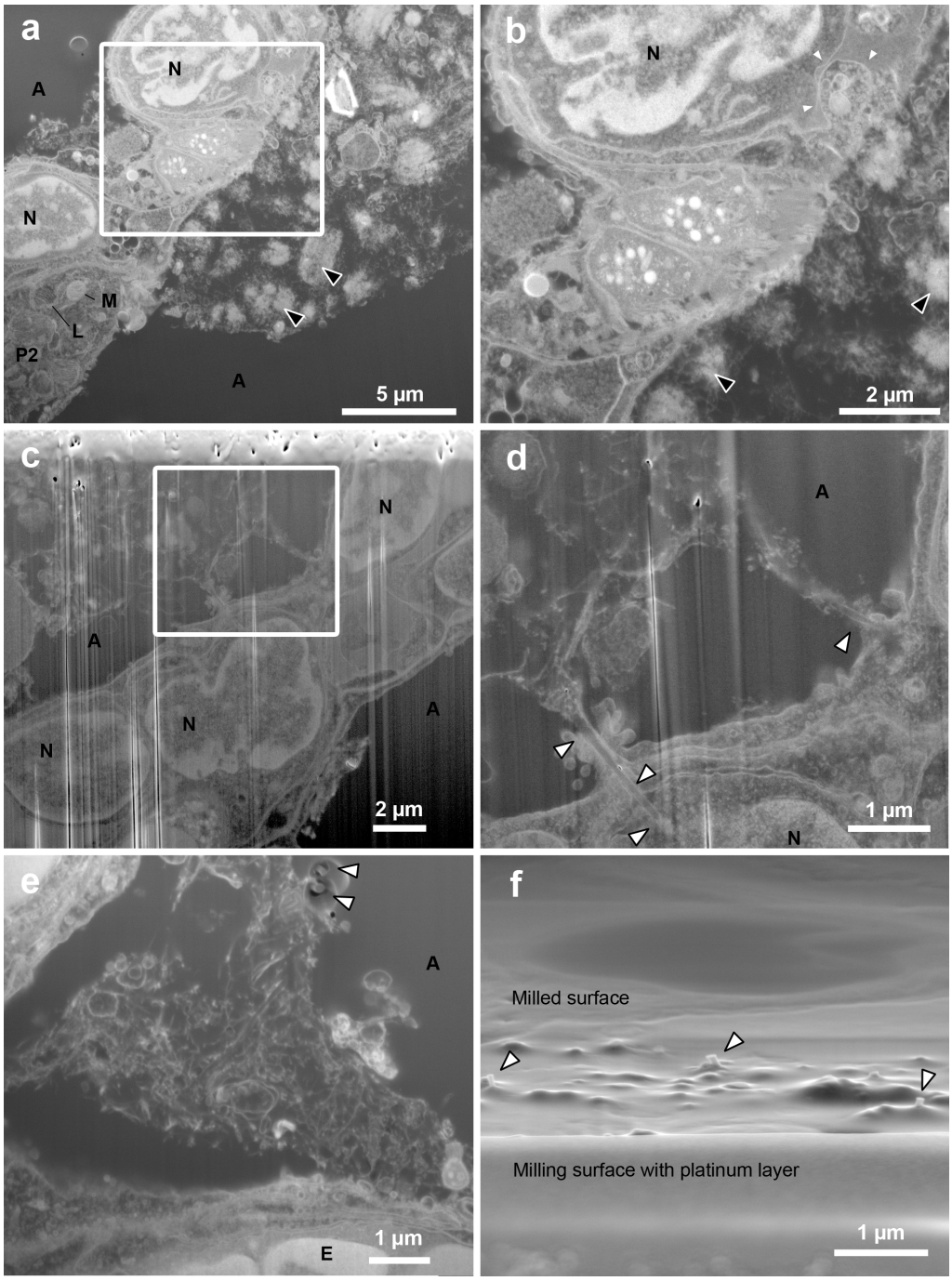

Illustration 4.6 FIB-SEM micrographs of both types of CNTs in the lung samples. A-B) The CNT_{Small} sample imaged with standard milling including a platinum layer, where it can be difficult to discern CNTs from cellular material. Black arrowheads mark the likely agglomerations of CNTs not observed in control samples and correlated with CNTs protruding from the surface of the Epon block. One cell appears to have a large invagination, possibly containing CNTs (small white arrowheads). C-D) CNT_{Large} samples obtained via standard milling, but without protective platinum layer. Here the milling artefacts (vertical white lines) caused by surface roughness is clearly seen (especially in c). However, the cells and CNTs are still visible, and single CNTs can be found to interact closely with the tissue, but are only in very few cases observed to appear entering the alveolar wall (white arrowheads in d). E-F) FIB-SEM of CNT_{Large} using the double non-tilted milling approach limiting surface roughness caused artefacts, with arrowheads highlighting the protruding CNTs caused by differing milling yields. F) SEM image obtained from the viewpoint of the ion beam, showcasing that CNTs protrude from the milled surface. A – alveole, E – erythrocyte, L – lamella body, M – mitochondrion, N – nucleus, and P2 – pneumocyte (type II).

Milling artefacts such as curtaining were most pronounced on CNT_{Large} samples and were a result of either the rough milling surface with the protruding CNTs, or the difference in milling yields between the Epon and the CNTs. In areas with extensive protruding CNTs, a smooth milling surface was sought obtained by slow deposition of a thick platinum layer (about 1.5 µm) with the gaseous injection system and the ion beam. The platinum limited the artefacts, but the CNTs underneath created small irregular pockets without platinum thus giving rise to milling artefacts. To provide a smooth milling surface, we introduced a non-tilted milling strategy where the ion beam was used to polish the back and front side of a wedge by rotating the stage (Illustration 4.3). This resulted in an excellent milling surface, albeit it increased the initial milling time significantly.

Both the thick platinum layer and the alternate milling strategy where the milling surface was polished prior to slice and view imaging decreased the milling artefacts, but artefacts originating from the block caused by differing milling yields remained (highlighted by arrowheads in Illustration 4.6 e). The SEM images of the artefacts caused by insufficient ion milling of the CNTs looks similar to the SEM images by Ke *et al*. showing CNTs protruding from a surface [173]. To investigate whether it was in fact protruding CNTs, the sample was rotated to image the milled surface (almost) from the point of view of the ion beam (Illustration 4.6 f). This revealed that the newly ion milled surface had small bumps and CNTs protruding from it.

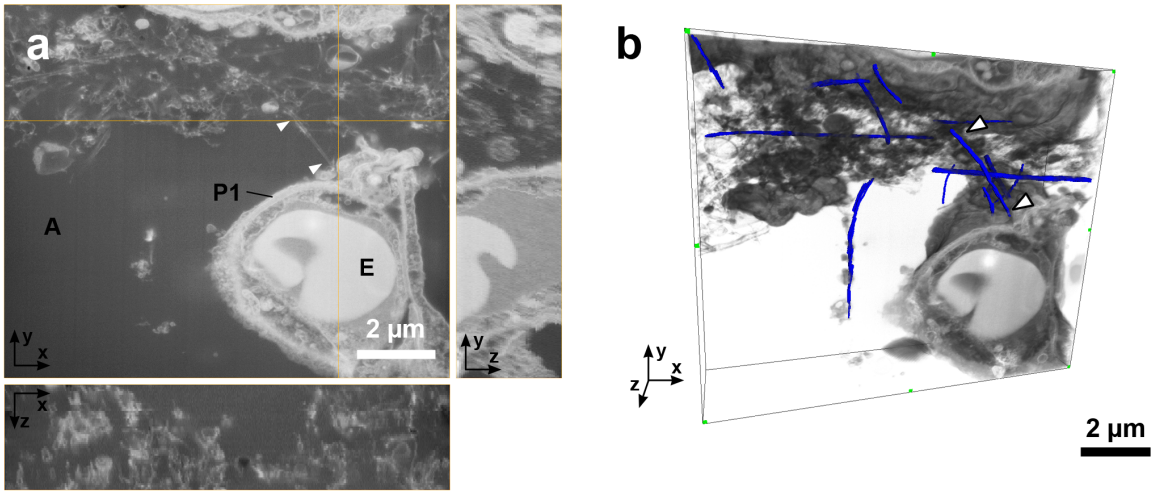

Illustration 4.7 3D FIB-SEM image reconstruction of CNT_{Large} sample obtained with the double non-tilted milling method. A) Orthogonal xy, xz and yz-views of the stack. B) 3D view with semi-transparent rendering of the stack. To illustrate the possibility of manually tracing CNTs in 3D, a few of the CNTs have been manually coloured blue in Amira. The white arrows point to the same CNT in both views. A – alveole, E – erythrocyte, and P1 – Type I pneumocyte.

FIB-SEM allows volume imaging as illustrated in Illustration 4.7 and the movie found in the online supplementary material. The 3D stack has been obtained using the double non-tilted milling method (Cf. Illustration 4.3 b). The stack of images is aligned and reconstructed as described [66]. The stack consists of 55 slices which were each 50 nm thick, while the x-y pixel size was 8.3 nm. This image stack demonstrates one of the strengths of the FIB-SEM, as the 3D information is gathered relatively fast (here in 1 hour) and the volume is 2.5 µm thick instead of the 100-300 nm typical for single slice TEM tomography [157]. The TEM slices thereby often only show fragments of the 4 µm long tube as the section is too thin to contain a long CNT in its entirety. In contrast we have traced a few of the visible CNTs in the volume to illustrate the capabilities of the

FIB-SEM to follow CNTs in 3D (Illustration 4.7). CNTs were discerned from other tubes and cellular material by following the distinctive parallel lines through the volume. Single pieces of the same CNTs can thereby be traced across multiple slices and thus follow the entire length of the CNTs (CNT_{Large} mean length 4μm), instead of only being able to image CNT fragments. Data were obtained from CNT_{Large} samples in areas with a high concentration of agglomerated CNTs, which would have been difficult using standard TEM methods due to microtoming artefacts.

4.2.5 Discussion

CNTs in tissue can lead to several artefacts when investigated with standard TEM techniques as demonstrated (Illustration 4.5 and 4.6). To limit the artefacts one could optimise the hardness of the embedding medium and the cutting parameters, or even experiment with using a vibrating knife or cryo-ultramicrotome to improve the section quality. Alternatively, some choose to use thicker sections (e.g. 500 nm) at the expense of lower resolution in order to leave a larger volume in which the CNT can remain undisturbed [158]. However, microtomy artefacts are a general issue with particularly large CNTs and many articles contain TEM images of CNTs in cells/tissue with varying degrees of microtomy artefacts which is likely caused by the stiff CNTs [158]–[161], [168]–[170], [174]. Although none of the observed artefacts appear as extreme as we have shown, it is desirable to circumvent these artefacts and also to avoid any sampling bias due to only being able to prepare reasonable images from regions with sparse CNTs for TEM.

We have shown that FIB-SEM can be used to study relatively large CNTs, without physically displacing the CNTs, damaging a diamond knife or causing severe microtomy artefacts. Naturally, FIB-SEM is not artefact free which can be seen in some of the presented images (e.g. Illustration 4.6 c-f), where curtaining and protruding CNTs can be observed on the milled surface. Ion beam milling artefacts were caused by either surface roughness caused by the protruding CNTs after ultramicrotomy, or by the difference in milling yields between the Epon and the CNTs. To limit the effects of differing milling yields, one could explore the possibility of milling at lower temperatures, adding gasses (etchants / water) or changing milling parameters (dwell times, approach, and geometry).

The images obtained with the FIB-SEM are quite similar to TEM imaging (with inverse contrast), but the FIB-SEM has lower contrast and resolution. This means that in the FIB-SEM images of CNTs in lung tissue, it can be difficult to discern the CNTs from biological material such as stained extracellular matrix proteins, lipid layers, mucus, etc. (cf. Illustration 4.6 and Illustration 4.8). To illustrate the difference between TEM and FIB-SEM, Illustration 4.8 shows images of both CNT_{Large} and CNT_{Small} with both methods. In TEM both types of CNTs can be distinguished from what is considered to be cellular material which has been either excreted from the cells (e.g. from lamella bodies), or is caused by fixation artefacts as described in [165]. The resolution of the TEM even allows for visualisation of CNT_{Small}, which is wider and have a different structure than the cellular material (Cf. Illustration 4.8 a), this is not possible in the corresponding FIB-SEM images (Illustration 4.8 c). Using the lamella cut-out method, as demonstrated by Heymann *et al*., it would be possible to combine the FIB-SEM and TEM, to obtain high resolution images without the use of a microtome [138]. However, the lamella cut-out method is rather time consuming and hinders 3D volume imaging.

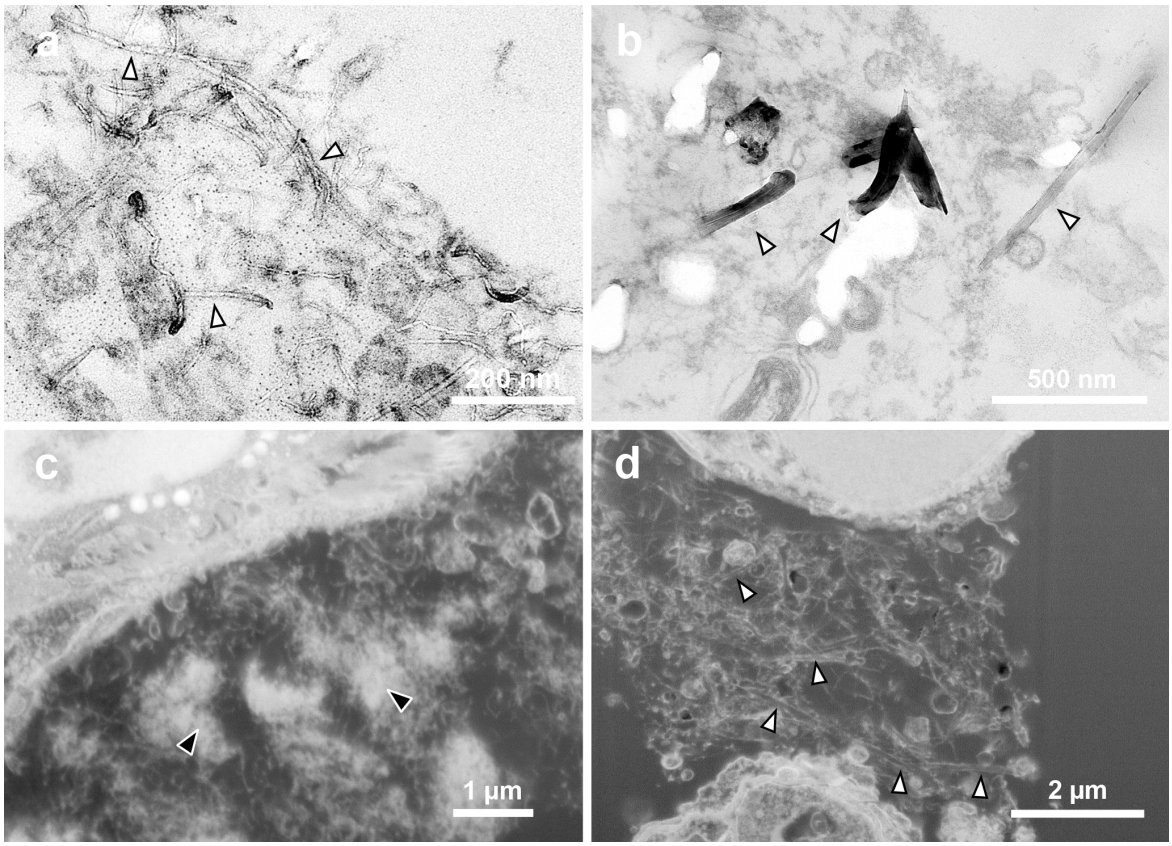

Illustration 4.8 Comparison of the resolution obtainable with TEM and FIB-SEM images of CNTs in lung tissue. A-B) TEM micrographs of the CNT_{Small} and CNT_{Large} sample, respectively. The CNTs can be distinguished from cellular material. C-D) FIB-SEM equivalents of the CNT_{Small} and CNT_{Large} sample, respectively. The micrographs were obtained with the standard milling method including the platinum layer. CNT_{Large} can be visualised as two parallel lines which depending on the imaging method have a weak signal from the centre. But as we approach the resolution limitations of the FIB-SEM the small CNTs are simple lines undistinguishable from cellular material. White arrowheads denote single CNTs, and black arrowheads agglomerates of CNTs.

A drawback of the FIB-SEM is that it is an abrasive method, so there is no way of retrieving an interesting field to obtain a higher resolution image. Likewise, there is little opportunity to characterise interesting sites using methods such as electron dispersive x-ray spectroscopy (EDS), although some groups have managed to perform FIB-SEM and EDS simultaneously [175]. Furthermore, even though large areas can be milled automatically [65] it is very time consuming and will generally result in an available field of view some 10-100 times smaller than TEM sections. In this paper the largest milling surface was 30 µm wide whereas the ultrathin sections were approximately 1 mm wide.

In the current study, the interactions are few in number so even though we can find relevant sites, a significant amount of milling time still has to be invested to catch CNTs in the action. For the CNT_{Large} sample alone, 10 different sites were investigated and only in two cases, evidence of direct cell-CNT interaction was found and this was for a total slice-and-view time of 20 hours (excluding the preparatory work). However, the method itself of locating regions of interest with tissue in close relation to CNTs proved to have an 85% hit rate when aimed at the regions with protruding CNTs from the sample surface. A higher number of CNT-cell interactions might be observable for longer CNT exposures than those studied in the present study with only 1 day after exposure, as the immune system then would have more time to react. This paper illustrates that FIB-SEM can also

be used to image 'hot-spot' CNT agglomerates where interaction also occurs.

In order to understand the toxicity of CNTs more information is required on the underlying mechanism by which CNTs cross cellular membranes, but this can be difficult with the limited sample volume of TEM imaging. Thicker sections coupled with 3D tomography can aid in the visualisation [159], [164], [176]. But it has its drawbacks such as a non-isotropic resolution, electron beam caused section shrinkage, and it would still be cumbersome to get nice artefact-free sections containing larger CNTs. To determine whether large CNTs cross cellular membranes or study larger agglomerations of particles, the FIB-SEM has potential because it can be operated in a fairly automated manner. Naturally, the technique is not limited to only investigating the toxicity of CNTs, but could also be applied to many other relevant hard structures that are challenging to microtome [14], [66].

	CNT_{Small}	**CNT_{Large}**	**Control**
TEM of microtomed sections	Minor microtomy artefacts. CNTs resolvable.	Major microtomy artefacts: obscuring CNT-cell interaction CNTs resolvable.	Minor microtomy artefacts. Excellent ultrastructure detail. No CNTs.
SEM of microtomed block	Small protruding CNTs. Excellent for locating area of interest (85% success).	Large protruding CNTs. Excellent for locating area of interest (85% success).	No CNT protrusions.
FIB-SEM	CNT agglomerates visible. CNT-cell interaction not resolvable. Possibility of 3D slice and view.	CNT agglomerates visible. CNT-cell interaction observable. Possibility of 3D slice and view.	Acceptable ultrastructure detail. No CNTs. Possibility of 3D slice and view.
Conclusion	FIB-SEM not suitable for CNT_{Small}. TEM is the best option.	FIB-SEM suitable for CNT_{Large}: including agglomerated CNTs. Suitable for 3D imaging	Better resolution in TEM. Faster 3D imaging in FIB-SEM.

Table 4 Overview of the results from the different methods on the different lung tissue samples from mice exposed to CNT_{Small}, CNT_{Large} and control mice instilled with vehicle.

4.2.6 Conclusion

The aim of this study was to provide an alternative to ultramicrotomy and TEM imaging of CNTs in biological samples. Samples with CNT_{Large} (70 nm wide) caused significant artefacts, especially in 'hot-spots' with high CNT concentration, thus potentially leading to sampling bias. Consequently, the feasibility of using FIB-SEM to study CNTs in lung tissue was investigated, and the results compared to standard BF-TEM imaging, as summarised in Table 1.

Using FIB-SEM it is very important to be able to localise regions of interest. Following initial sectioning protruding CNTs from the block surface were used to locate regions with CNTs in close proximity to the tissue. CNT_{Large} (70 nm wide) were visualised and could be distinguished from the otherwise carbon rich environment (embedding material). The FIB-SEMs limited imaging resolution and contrast meant that samples with CNT_{Small} (10 nm wide) could not be distinguished from cellular material.

A 3D FIB-SEM image stack was obtained of the CNT_{Large} sample, by first minimising surface roughness from protruding CNTs. The slice and view stack managed to give a 3D image of an agglomerate of CNT_{Large} in the intercellular space with CNTs in some cases slightly touching the cells, which would be troublesome using standard TEM protocols.

In conclusion, we have shown that FIB-SEM can serve as a complementary tool to TEM. It is currently limited to larger CNTs (70 nm wide in our case), but it offers the

opportunity to obtain 3D images, without the risk of physically moving CNTs during the sample preparation, and allows the visualisation of the entire CNTs instead of just the fraction present in a 300 nm thick section.

4.2.7 Acknowledgements

We are grateful for electron microscopy assistance from CFIM and the DTU CEN. The authors would also like to thank Zhila Nikrozi for sample preparation assistance and ultramicrotomy, and Michael Guldbrandsen and Lisbeth Meyer Petersen for animal handling. This work was supported by Danish Centre for Nanosafety (20110092173/3) and the FP7/2007-2013 under grant agreement n° 247989 (Nanosustain).

4.3 CNT contrast

In Paper II, the parallel lines in the FIB-SEM image are interpreted as being CNTs, and at first glance it indicates a tubular structure with a wide inner diameter and a comparably large empty core (Illustration 4.9 a). The rather strong contrast from the CNTs was somewhat surprising due to the in-principle limited Z-contrast difference between CNTs and Epon. Additionally, high resolution TEM revealed, that CNT_{Large} appears to have a narrow empty inner core (Illustration 4.9 b).

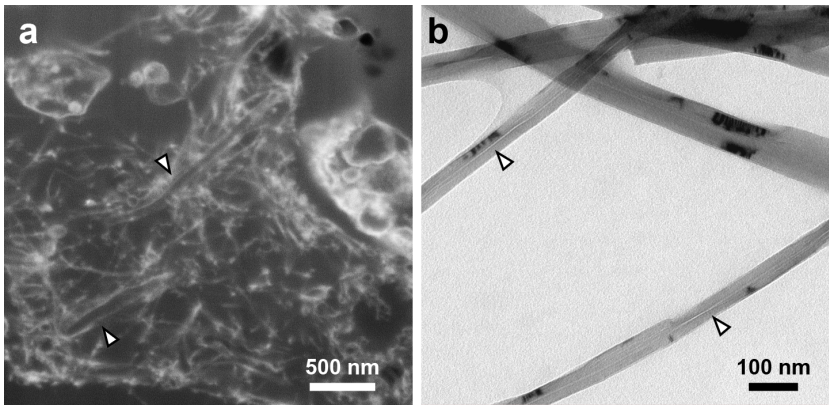

Illustration 4.9: A) FIB-SEM image of a CNT_{Large} cluster where individual CNTs (arrowheads) indicate a wide inner diameter of CNTs. B) TEM image showing the narrow inner core of the CNT_{Large} (arrowheads).

Seeing as the contrast did not match our expectations, and the CNTs appear different in the TEM, we believe that the observed lines represent heavy metal stained pulmonary surfactants (consisting of about 90 % lipids and 10 % proteins) adhered to the walls of the CNTs. Lung surfactants have previously been observed to adhere to CNTs [177]. The surface coating is believed to be an important factor in the toxicity and uptake of the CNTs. Lowered toxicity has been reported as a consequence of serum proteins adherence to CNTs, and enhanced *in vitro* uptake of CNTs in macrophages due to surfactant coatings [177].

4.4 Summary

The FIB-SEM technique was developed, tested, and evaluated for studying CNT exposures of lung tissue. FIB-SEM was found to serve as an excellent complimentary technique to TEM, especially well-suited for 3D imaging of larger objects resolvable with the SEM. Areas of interest were located by the protruding CNTs left after ultramicrotomy, which also serves to highlight the issues standard EM techniques have for studying CNTs.

Chapter 5

CNT distribution and interaction with exposed mouse lung

Carbon nanotubes may serve as potential health hazard after pulmonary exposure and are model nanomaterials for nanotoxicology. In consequence, several *in vitro* and *in vivo* studies have been performed to respectively uncover the nanoscale interactions using electron microscopy and the time and dose dependent impact on the immune response. We find it essential to combine these two types of studies, and to investigate the ultrastructural CNT-cell interaction in a time resolved manner in the presence of an active immune system.

Seeing as CNT interaction with the lung will be emphasised in this chapter, a brief introduction to the cell types in the lung will be provided. Section 5.2 contains my main results in the form of Paper III. It covers the ultrastructural interaction and distribution of CNTs within the lung 1, 3, and 28 days after exposure, and describes the differences observed for two types of CNTs. Additionally, a crystal formation in alveolar macrophages due to CNT exposure is characterised and further discussed in Section 5.3. Work performed in this chapter was done in collaboration with NRCWE and Health Canada, and is a continuation of the work of Chapter 4.

5.1 Cells of the respiratory system

The respiratory system contains a wide variety of cell types, of most interest to this work are the cells in the respiratory bronchioles, the alveolar epithelium, and the white blood cells (Illustration 5.1).

The respiratory bronchioles (final stages of the bronchi) are lined with Clara- and ciliated cells, and occasionally brush cells. Clara cells secrete protein which serves to avoid the walls of bronchioles from sticking together during exhalation. They are recognised by their cuboid shape, granules, and placement. The ciliated cells are involved in the clearance of inhaled particle, it is part of the mucociliary escalator and moves the mucous coating the airway passages upward towards the pharynx where it can be swallowed. They are easily recognised by the hair-like cilia structures extending from the cell and into the airway [40].

Type I and Type II pneumocytes make up the alveolar epithelium, with a few occasional brush cells. Type I cells make up most of the alveolar surface, they are elongated and thin, except for where they make place for the nucleus. Type II cells contain recognisable lamella bodies which produces lung surfactants that are excreted and help avoid alveoli collapse. They are placed in between Type I cells and are more numerous (60% of the cell

population), but are more compact and only cover about 5% of the alveolar surface. Type II cells have small microvilli at the surface and often bulge into the air space. Brush cells are recognised by the blunt microvilli at the apical surface, are very few in number, and even though the complete function of this cell type remains to be found, it appears to be involved in sensing bacterial products [178]. Additionally, as the alveoli are where the gas exchange occurs, capillaries carrying red blood cells can also be found (Illustration 5.1).

Another type of cells which we expect to see in the lung micrographs are the leukocytes also known as the white blood cells. The leukocytes are part of the immune system which will react to nanoparticle exposure and seek to clear the particles. The main leukocytes types encountered in the lung: neutrophils, lymphocytes, monocytes, eosinophils, and basophils.

Neutrophils are the most common leukocyte in the blood (~60%). They are fairly short lived (hours), but they are very mobile and are generally the first responders of the immune system. They accumulate in the affected tissue, activate other immune cells, excrete chemicals for destroying microorganisms, and can even phagocytote smaller objects. The neutrophils have several types of granules, a highly lobed nucleus (typically 2 or 4 lobes), and a wide band of tightly packed DNA (heterochromatin) in the periphery of the nucleus.

Lymphocytes are the second most common white blood cell (~30%), and can be smaller or larger than neutrophils depending on the type. They are long lived (months) and are involved in the recognition and destruction of infected cells. The small lymphocytes (B- and T cells) cannot be visually distinguished, as both contain a large nucleus filling most of the cytosol. The large granular lymphocytes (natural killer cells) are of the same origin, and have a cytosol relatively devoid of organelles much like the smaller lymphocytes, but also contain large electron-dense granules.

Monocytes travel via the bloodstream to affected areas and differentiate into phagocytes usually resident in the tissue. Alveolar macrophages are derived from monocytes, and are found both in the tissue near the air-blood barrier (septum), and in the air spaces clearing inhaled particulates, bacteria and cell debris via phagocytosis. Alveolar macrophages are typically rather large compared to neutrophils, have an irregular cell periphery and lobed nucleus.

Eosinophils which are involved in allergic reactions, chronic inflammation and in neutralising larger parasites have an overall appearance similar to neutrophils with a bi-lobed nucleus. However, they also contain distinctive crystalline bodies in granules, observable with TEM (Illustration 5.1).

Basophils, the least common of the white blood cell (<0.5%), have a lobed nucleus and numerous large granules in the cytosol. Like eosinophils, basophils are involved in allergic reactions and in neutralising parasitic infections, but also in easing blood flow to affected tissue and delaying blood clotting.

The above mentioned cell types cover most of what was seen in this project. However, there are further derivatives of cells (e.g. plasma and mast cells) and more tissue types associated with the lung (e.g. muscle tissue used during inhalation). Additionally, there are structures and cells which we had difficulty in characterising, some of which are shown in Appendix D.

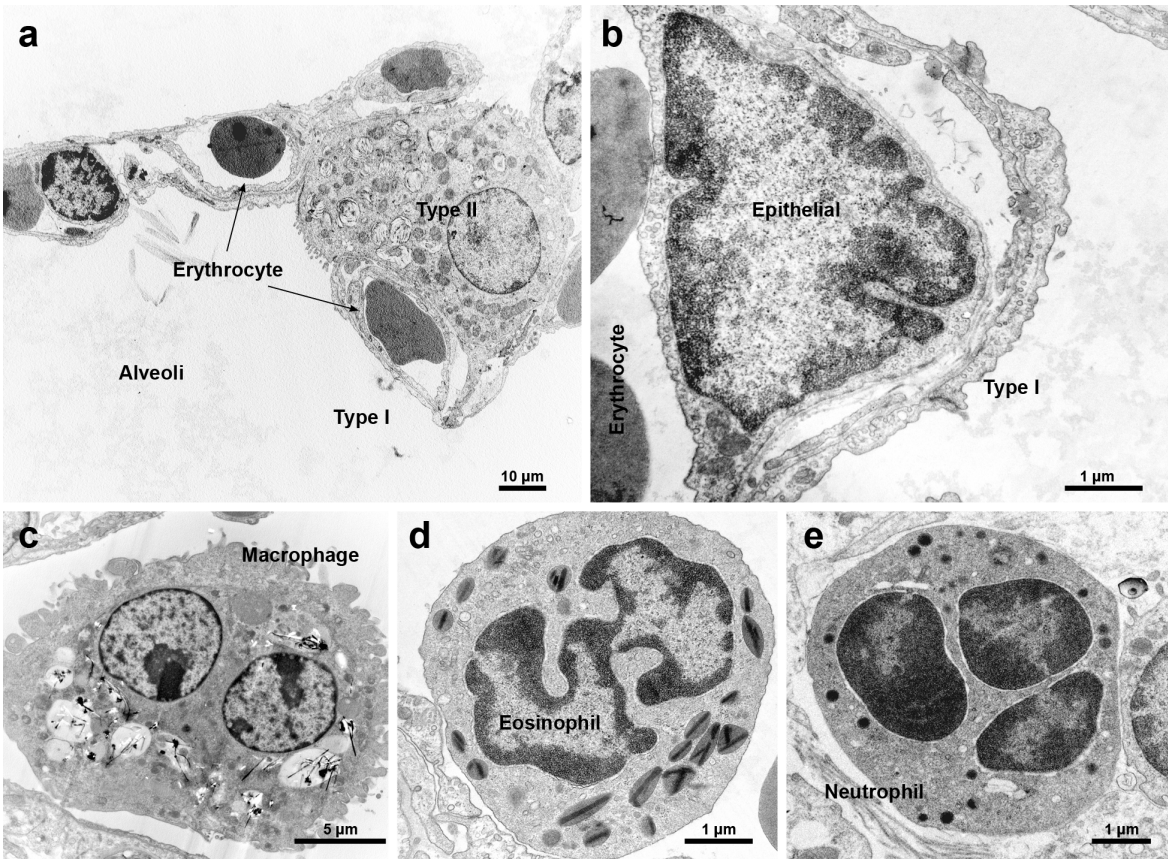

Illustration 5.1: A) Overview image showing both type I and II pneumocytes in addition to some blood capillaries. B) Epithelial cell and Type I cell lining the wall of a capillary. C) Macrophage found in the alveoli spacing showing a lobed nucleus and ruffled surface containing CNTs. D) Eosinophil with crystalline bodies found in a capillary. E) Neutrophil with lobed nucleus and electron dense granules. Also notice the significant size difference between the alveolar macrophage and the eosinophil and neutrophil.

5.2 Paper III

Time-dependent subcellular distribution and effects of carbon nanotubes in lung tissue

The paper was made in collaboration with the NRCWE and Health Canada. NRCWE was responsible for animal exposures, and the statistical analysis of BAL cell composition data, whereas the gene expression was performed by Sarah Søs Poulsen in Health Canada under supervision from Carole Yauk and Sabina Halappanavar. I would in particular like to acknowledge Sarah Søs Poulsen, PhD student at NRWCE and Roskilde University, who performed and analysed the gene expression data and authored the corresponding section in the paper. The manuscript has passed internal review at Health Canada.

5.2.1 Abstract

There is limited information about how carbon nanotubes (CNTs) interact with lung tissue and cause pulmonary toxicity over time. To address this, three different multiwalled CNTs were intratracheally instilled into female C57BL/6 mice: one short (850 nm) and tangled, and two longer (4 µm and 5.7 µm) and thicker. We investigated pulmonary deposition of these CNTs by transmission electron microscopy (TEM), bronchoalveolar lavage cell

(BAL) composition[10] and global transcriptional profiles 1, 3 and 28 days after instillation.

TEM analysis revealed a high degree of similarity in tissue distribution over time for the different CNT types. CNTs were taken up either by what appeared to be endocytosis into vesicles or by piercing through the membrane. At later time points, the longer CNTs in particular appeared to escape vesicular enclosures. BAL cell counts showed that instillation of CNTs induced both neutrophil and eosinophil influx, while eosinophil influx was greater in response to the longer CNTs. Eosinophil influx was linked to the expression of chemokines.

The two longer CNTs induced eosinophilic crystalline pneumonia (ECP), which was characterized by crystalline bodies within alveolar macrophages and increased tissue expression of Chitinase 3-like protein 3 precursor gene (*Chi3L3*). ECP is an idiopathic disease found in certain strains of laboratory mice, including C57BL/6, and is exacerbated by pulmonary events such as allergic reactions and inflammation. The observed eosinophil influx, *Chi3L3L* gene expression and ECP is therefore linked to the mouse strain used, thereby calling for cautious interpretation and additional study of these effects using other animal models.

5.2.2 Introduction

Carbon nanotubes (CNTs) have excellent mechanical and electrical properties and thus have been of great interest to researchers since their discovery some 50 year ago [20]. Consequently, as more possible applications for CNTs are identified, there is an increasing need to investigate their toxicity. Of particular concern are suggestions that the toxicity of CNTs is comparable to that of asbestos [179]. In the present study we investigate the toxicological properties of multi-walled CNTs (MWCNTs), selected due to their increasing usage as additives in composite materials [21] combined with their known ability to cause pulmonary inflammation, fibrosis and granulomas in rodents [37], [146], [180]. Human workplace exposure to CNTs can occur through dermal and pulmonary exposure routes, but the primary route of toxicological concern and most studied in relation to the working environment is inhalation [44], [180].

Assessment of CNT-toxicity is complicated by the wide variety of physical and chemical properties with which they can be manufactured. For instance, the physical dimensions of CNTs have been reported to play an important role in their toxicity [39], [181], [182], and the length/width ratios of some CNTs are consistent with the fibre pathogenicity paradigm [179]. The number of defects in the lattice structure of CNTs also plays a role in their toxicity [183], together with agglomeration level [184] and functionalization [185]–[187]. In addition to the direct interaction between CNTs and cells, their toxicity is further complicated by the ability of CNTs to adsorb biomolecules and essentially transform into different biological identities [177].

Several ultrastructural studies on uptake and clearance mechanisms of CNTs have been published. Transmission electron microscopy (TEM) has, for example, revealed low CNT concentrations in neutrophils and type II pneumocytes, whereas high CNT-concentrations were readily visible in alveolar macrophages using light microscopy [162]. The current literature, mostly covering *in vitro* investigations, indicates that CNTs can be taken up either as agglomerates entering the endosomal pathway by endocytosis, or as single CNTs

10 Standard procedure performed in toxicology where the lungs of the animals are flushed and the fluid is analysed.

piercing the cell membrane in what appears to be a non-endocytotic diffusion driven process [159], [161], [182], [186], [188]. In addition, it has been argued that after direct non-endocytotic uptake CNTs can subsequently be engulfed in vesicles [186], [188], and that CNTs already contained in vesicles can escape to the cytosol [159], [188]. Lastly, CNTs are able to escape the cell via microvesicles [189] or membrane disruption [186]. These *in vitro* studies illustrate the complexity of the interactions, the need for high resolution microscopy to understand CNT toxicity and the need for *in vivo* studies to test if these conclusions hold in the presence of an active immune response.

The lung responds to CNTs by a rapid influx of neutrophils and macrophages [35], [146], [190], and in certain cases also by eosinophil influx [190]–[193]. Within a few days to weeks, exposure to even small doses of CNTs induces inflammation, granulomas and fibrosis [35], [37], [179], to such a severe degree that the current recommendation is to lower occupational exposure limits to the detection level [36].

We have observed a strong development of eosinophilic crystalline pneumonia (ECP), also known as acidophilic macrophage pneumonia, in mice following exposure to CNTs, and this has briefly been mentioned in a recent report [194]. ECP in mice is characterised by eosinophilic crystals in alveolar macrophages [195]. Eosinophilic crystals are composed of chitinase 3-like 3 (Chi3L3) proteins [196], [197] and increased levels of these proteins have also been found in CNT exposed mice compared to controls [198]. Both eosinophil influx and ECP development [195], [199] could indicate an allergy-like response, but the relation to CNT exposure remains undetermined.

Here we study the time course of ultrastructural CNT distribution *in vivo* following pulmonary exposure. In addition, we document the differences and similarities in pulmonary toxicological response of mice exposed to different CNTs, and characterise the observed eosinophil influx and ECP development indicative of an allergic-like response to CNT exposure.

Three MWCNTs of different dimensions were delivered intratracheally to C57BL/6 mice, and pulmonary response was investigated 1, 3 or 28 days after exposure. We compared the effects of two physically different CNTs (CNT_{Small} and CNT_{Large}), and used a third type of CNT (Mitsui-7), to evaluate the reproducibility of the two physically similar CNTs (CNT_{Large} and Mitsui-7). We also examined CNT-induced ECP and the 3D structure of the crystals using focused ion beam scanning electron microscopy (FIB-SEM). Lung samples were imaged with transmission electron microscopy (TEM) and the results compared with bronchoalveolar lavage (BAL) cell composition and relevant gene expression data [190].

5.2.3 Materials and methods

CNTs

Three types of multiwalled CNTs (MWCNT) were used (more details in Appendix C):

- NRCWE-026 (CNT_{Small}) has an average length of 850 nm and width of 10 nm. It was used in a previous study [200].
- NM-401 (CNT_{Large}) is on average 4 μm long and 70 nm wide. It was also used in a previous study [200] and was a test material in the Nanogenotox project [201].
- The last MWCNT (denoted Mitsui-7) has an average length of 5.7 μm and width of 75 nm [190], [191], [194]. It was also used in the Nanogenotox project, under the name NRCWE-006 [201].

Mice

Female C57BL/6 mice, 5-7 weeks old, obtained from Taconic, were allowed water and food (Altromin # 1324) *ad libitum* during the experiment. The animals were acclimatised for two weeks and housed in experimental groups in polypropylene cages with sawdust. The environment was controlled with a temperature of 21 ± 1 °C, a humidity of 50 ± 10 % and a 12-h light/dark cycle. Experiments were approved and carried out following guidelines by the Danish "Animal Experiments Inspectorate" (permit 2010/561-1779).

Exposure

Particle suspensions and intratracheal instillation were done as described previously [190], [200]. Briefly, the Mitsui-7 CNTs were suspended in 0.9%wt NaCl and 10% v/v acellular bronchoalveolar lavage (BAL) fluid. CNT_{Small} and CNT_{Large} were suspended in 2% serum in Nanopure water. Serum and BAL fluid were obtained from unexposed C57BL/6 mice. The Mitsui-7 (4.05 mg/ml) and the CNT_{Small} and CNT_{Large} (3.24 mg/ml) suspensions were sonicated on ice using a Branson Sonifier S-450D equipped with a disruptor horn (Model number: 101-147-037). Mitsui-7 was sonicated for a total of 4 minutes at 10% amplitude, with alternating 10 s pulses and pauses, while CNT_{Small} and CNT_{Large} were sonicated for a total of 16 min at 400 W and 10% amplitude. These suspensions were used for the high dose (162 μg) and diluted 1:3 in vehicle for the medium (54 μg) dose and diluted further 1:3 for the low dose (18 μg). Between the dilutions the suspensions were mixed by pipetting. Vehicle control solutions were prepared with 0.9% NaCl and 10% acellular BAL fluid, and 2% serum in Nanopure water, respectively, and were sonicated as described above. Mice were intratracheally instilled with 40 μl (Mitsui-7) and 50 μL (CNT_{Small} and CNT_{Large}) particle suspension, respectively. Animals were exposed to 18, 54 or 162 μg/mouse, and respectively correspond to the pulmonary deposition of CNTs during 4, 11 or 32 eight-hour working days at the current Danish occupational exposure level for carbon black (3.5 mg/m^3) assuming 10% pulmonary deposition [35].

Lung tissue

One, 3, and 28 days after the intratracheal instillation, mice dedicated for electron microscopy were anaesthetised by subcutaneous injection of Hypnorm–Dormicum and the mice were bled by cutting the groin. The lungs were fixed *in situ* by cannulating the trachea and infusing 2 % glutaraldehyde in 0.05 M cacodylate buffer (pH 7.2) at a constant fluid pressure of 30 cm before the thorax was opened. The lungs were excised and immersed in 2 % glutaraldehyde 0.05 M cacodylate buffer (pH 7.2) and stored refrigerated until further processing.

BAL cells composition

One, 3, and 28 days after intratracheal instillation, mice dedicated for the other endpoints (BAL cell counts and microarray gene expression on lung tissue) were anaesthetised by subcutaneous injection of Hypnorm–Dormicum. BAL fluid was collected directly after cardiac puncture and centrifuged. The cellular pellet was collected on glass slides and stained with standard May-Grünwald-Giemsa. The number of neutrophils, macrophages, eosinophils, lymphocytes and epithelial cells were counted (n = 6). Lung tissue was snap frozen in liquid nitrogen and stored at -80°C until RNA purification. Statistical analysis was performed in SAS v. 9.2. A non-parametric one-way ANOVA test with a Tukey-type mean comparison was used to determine statistical significance.

Gene expression

Total RNA (n = 6 per dose group) was extracted and isolated from the lung tissue of

Mitsui-7 exposed mice (doses: 18, 54 and 162 µg on post-exposure day 1, and 54 µg on post-exposure day 28), from the CNT_{Small} and CNT_{Large} exposed mice (doses: 18, 54 and 162 µg on post-exposure day 1, 3 and 28), and from concurrent controls as previously described [190]. All samples passed quality control and were used in the microarray hybridization measurement. The microarray hybridization was performed on Agilent 8 x 60K oligonucleotide microarrays (Agilent Technologies Inc., Mississauga, ON, Canada) using 200 ng total RNA from each sample. Both the hybridization procedures and statistical analyses have previously been described [190]. Global gene expression results will be published elsewhere (Paper X) and only the expression of relevant genes will be presented here.

Electron microscopy sample preparation

We investigated one CNT sample (164 µg) from each time point by electron microscopy. Approximately 1 mm^3 samples of lung tissue were cut with a scalpel and embedded in Epon [200]. Briefly, the samples were rinsed in buffer and postfixed in 2% osmium tetroxide and 0.05 M potassium ferricyanide in 0.12 M sodium cacodylate buffer (7.2 pH) for 2 hours. Samples were then rinsed in ultrapure water, *en bloc* stained with 1% uranyl acetate in water overnight, dehydrated in ethanol and embedded in Epon following standard protocols for the TAAB 812 resin kit, TAAB Laboratories Equipment.

Ultramicrotomy of the samples was performed on a Leica Ultracut with a diamond-knife-angle of 6° and a cutting speed of 1.5 mm/s. Due to extensive microtomy artefacts caused by the hard CNTs [200], we used thicker TEM sections (approximately 200-300 nm) on selected CNT_{Large} and Mitsui-7 samples. TEM sections were poststained with uranyl acetate and lead citrate (Ultrastain-2, Leica Microsystems), and imaged on a CM 100 BioTWIN (Philips) operated at 80 kV. For 3D imaging of ECP crystals, focused ion beam scanning electron microscopy (FIB-SEM) imaging was performed using a FEI QuantaFEG 3D with a dedicated vC backscattered electron detector operated at 3 kV and spot 1. Milling was performed on the ultramicrotomy prepared blocks and the images processed as previously described [200].

5.2.4 Results

Interaction	CNT_{Small}	CNT_{Large}	Comment
Between cells 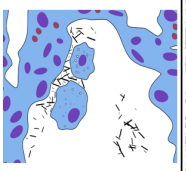	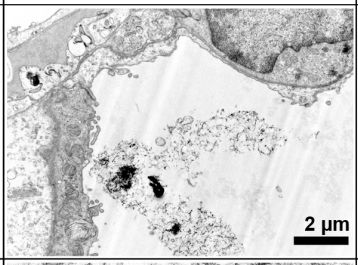	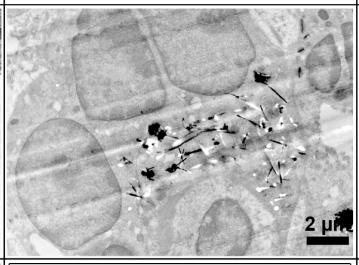	CNTs were observed between cells at all time points, going from being freely placed in the alveolar ducts to being surrounded by cells on day 3 and 28.
Piercing 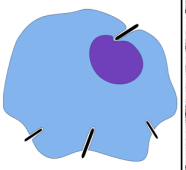	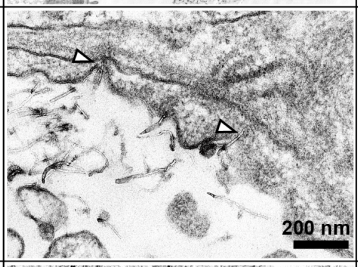	**Not observed**	CNTs in the apparent process of penetrating the cell membrane. **CNT_{Small}:** Very rare interaction. Observed on day 1 and day 3. **CNT_{Large}:** Not observed. Possibly due to sectioning artefacts and a low incidence.
Inclusions 	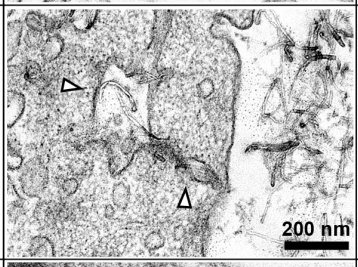	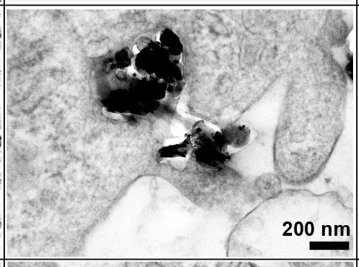	Cellular inclusions with agglomerated CNTs. Mainly observed on day 3. **CNT_{Small}:** Included small and large agglomerations. **CNT_{Large}:** Rarely seen, possibly due to sectioning artefacts.
In cytosol 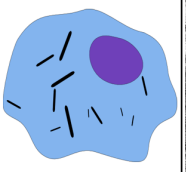	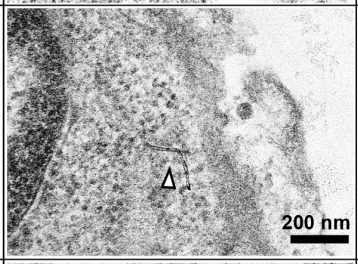	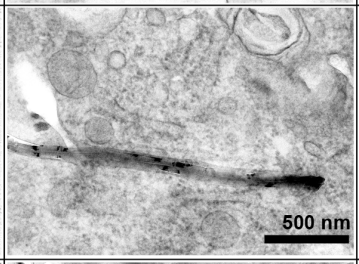	CNTs were observed freely in the cytosol on day 1, 3 and 28. **CNT_{Small}:** Interaction occurred rarely, but sightings increased on day 28. **CNT_{Large}:** CNTs were mainly found in vesicles at day 3, and mostly in the cytosol on day 28.
In vesicles 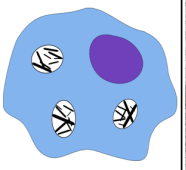	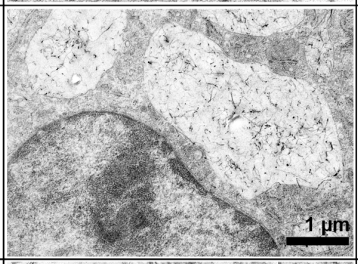		CNTs observed inside vesicles at day 3 and 28. **CNT_{Small}:** Increased number of vesicles filled with CNTs at day 28 compared to on day 3. **CNT_{Large}:** Distribution went from being mostly in vesicles on day 3 to cells having fewer vesicles.
Vesicular escape 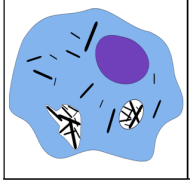	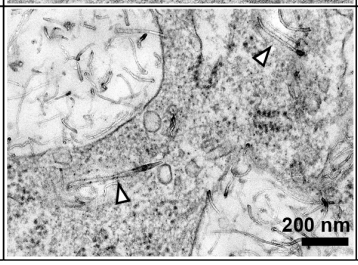	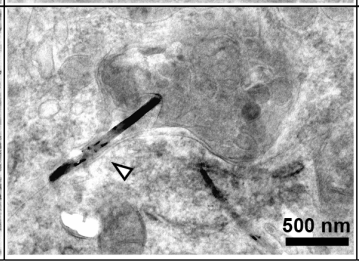	Vesicles and single CNTs seen in the same cell, with CNTs deforming the vesicles. **CNT_{Small}:** Few CNTs located freely in cytosol on day 28. **CNT_{Large}:** CNTs appearing outside of vesicles on day 3 and 28, and larger degree of vesicular deformation seen.

Illustration 5.2 Overview of the observed CNT-cell interactions. Each interaction has a descriptive sketch, an example image of how the interaction was expressed in CNT_{Small} and CNT_{Large} exposed samples, and a description of the differences and progression of the interaction. White arrowheads point to CNTs in TEM images.

Electron microscopy

The interactions of three types of CNTs with lung tissue were studied by TEM. We compared CNT-tissue interactions of CNT_{Small} (850 nm long and 10 nm wide) and CNT_{Large} (4 µm long and 70 nm wide) for structurally induced differences. Furthermore, the reproducibility of the interactions was evaluated by comparing CNT_{Large} and Mitsui-7 (5.7 µm long and 75 nm wide). TEM imaging showed that the two similar tubes showed similar CNT-cell behaviour, and thus in this work we only show images of CNT_{Small} and CNT_{Large}. An overview image of all of the different observed types of interactions is shown in Illustration 5.2.

Day 1

There was minimal CNT-cell interaction on post exposure day 1 (Illustration 5.3 a-b). The CNTs were primarily aggregated outside cells in the alveolar lumen (Illustration 5.2 'between cells'). Individual CNTs were in close proximity to cells, and in certain cases were possibly in the process of entering the cell via physical indentation and subsequent piercing of the cellular membrane (Illustration 5.2 'piercing'). However, these observations were rare, and for CNT_{Large} and Mitsui-7 it was difficult to ascertain if cells were pierced due to ultramicrotomy artefacts caused by the large CNTs. We did not observe any clear signs of vesicular uptake at this time point, and only few immune cells were seen. The limited immune response on day 1 is also reflected in the BAL cell counts showing low numbers of total BAL cells (Appendix E).

Day 3

Three days after the exposure we observed increasing cell-CNT interaction and more of what appeared to be inflammatory cells (Illustration 5.3 c-d), which correlated with the larger BAL cell counts at this time point. Large and small open cytoplasmic inclusions were observed containing agglomerated CNTs, apparently in the process of being taken up by the cells (Illustration 5.2 'inclusions'). Again, CNT_{Small} were observed directly entering the cytosol, whereas this could not be verified for CNT_{Large} (Illustration 5.2 'piercing'). Three days post exposure CNT_{Small} were primarily enclosed in vesicles (Illustration 5.2 'in vesicles'), and few CNTs were observed free in the cytosol. CNT_{Large} uptake resulted in CNTs being enclosed in vesicles (Illustration 5.2 'in vesicles'), in addition to single CNTs found freely in the cytosol (Figure 1 'in cytosol'). In certain cases CNT_{Large} caused clear deformation of the vesicles, which was not observed to the same extent for CNT_{Small}, and appeared to be involved in the process of vesicular escape (Illustration 5.2 'vesicular escape').

Day 28

There were fewer CNTs present 28 days post exposure relative to on day 3, and they were almost exclusively found inside cells and not in the alveolar lumen. CNTs were located within single alveolar macrophages and in larger inflammatory sites with multinucleate giant cells [202]. CNT_{Small} were found in both small and large vesicles with large amounts of CNTs inside some individual cells (Illustration 5.3 e). In certain cases, CNTs were found between these vesicles and were perturbing vesicle membranes (Illustration 5.2 'vesicular escape'). CNT_{Large} progressed from being primarily small CNT agglomerates within cellular vesicles on day 3, to being present in more deformed vesicles or sporadically distributed in the cytosol on day 28 (Illustration 5.3 f). Generally for CNT_{Large} there were fewer obvious CNT-containing vesicular structures compared to day 3.

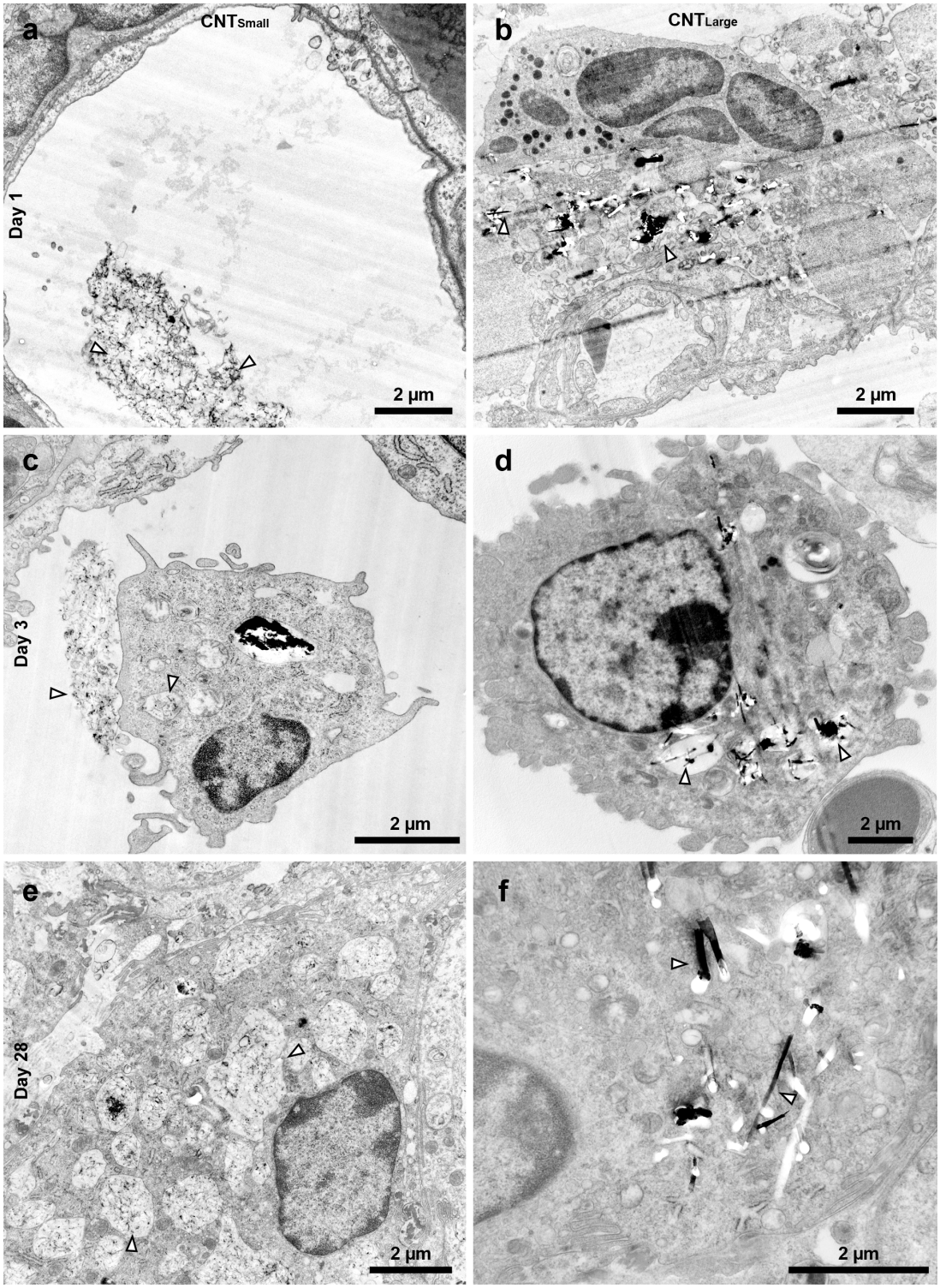

Illustration 5.3: Representative images of the samples 1 day (A-B), 3 days (A-D), and 28 days (E-F) post exposure for CNT_{Small} (A,C,E) and CNT_{Large} (B,D,F). A-B) Show respectively CNT_{Small} and CNT_{Large} on day 1, where CNTs are mainly found in the alveolar lumen or in the interface between cells. C-D) On day 3 CNTs are increasingly found in vesicles inside what appears to be alveolar macrophages, but some CNTs still remain outside cells. E) On day 28 CNT_{Small} are found inside vesicles and in the cytosol of cells in large cell agglomerations, but were also found inside vesicles in singular cells. F) On day 28 there were fewer vesicles containing CNT_{Large} and the CNTs were more individually spaced in the cytosol. In addition, immune cells were found in large agglomerations indicating inflammation at this stage. Arrowheads indicate single or agglomerations of CNTs.

All days

CNTs were found in alveolar macrophages, identified by their ultrastructure and location in the alveoli. We did not observe any CNTs in what appeared to be type II pneumocytes, but we did see a few CNT_{Small} that appeared to be inside what looked like type I pneumocytes. Likewise, no CNTs were found inside well-defined neutrophils or eosinophils. Cells were recognised and classified according to their morphological traits [40]. However, in some instances, especially in lung tissue on day 28, it was difficult to determine the cell types containing the CNTs as they were strongly perturbed by the CNTs (Illustration 5.3 e), and cells were found in agglomerates. CNTs were never observed inside the nucleus (except for what appeared to be caused by ultramicrotomy artefacts) although CNTs on occasion caused nucleus indentation, as previously described for cells grown on nanowires [49], [66].

Eosinophilic crystalline pneumonia

TEM images revealed crystalline bodies in alveolar macrophages (Illustration 5.4 a-c) and multinucleated-cells in the CNT_{Large} and Mitsui-7 exposed mice. These were similar to those found in mice with eosinophilic crystalline pneumonia (ECP) [195], [203]–[205]. Crystal bodies were observed in lung tissues from Mitsui-7 exposed mice for the highest dose on day 3, and both the medium and high doses on day 28. For CNT_{Large} treated mice, crystalline bodies were observed on day 28 for the medium and high doses.

In some cases, the crystals appeared as needle-like structures similar in size to CNT_{Large} and Mitsui-7, but occasionally massive crystalline bodies up to 40 µm long and 5 µm wide were observed (Illustration 5.4 a). The crystalline structures were found in two variants: sharply defined inside vesicles, and more diffusely defined inside vesicles. ECP crystals were also observed outside cells, as previously documented [199], [203], [204]. Some of the observed crystalline structures had periodic lattice structures in the longitudinal direction (about 5 nm), a feature previously described [205], the structures were clearly not CNTs as they did not cause microtomy artefacts similar as CNTs do.

In order to elucidate the three dimensional structure of the crystals, we examined a sample containing crystals with slice-and-view 3D FIB-SEM (Illustration 5.4 d-f). In single slices the crystals were very similar to those observed in TEM with an inverted contrast (Illustration 5.4 e), but assembled crystals appeared as orthorhombic plates that often were stacked and piled up (Illustration 5.4 f).

ECP is considered to be a background lesion in certain mice strains, and the crystal formation is linked to accumulation of Chi3L3 protein [196], [197].

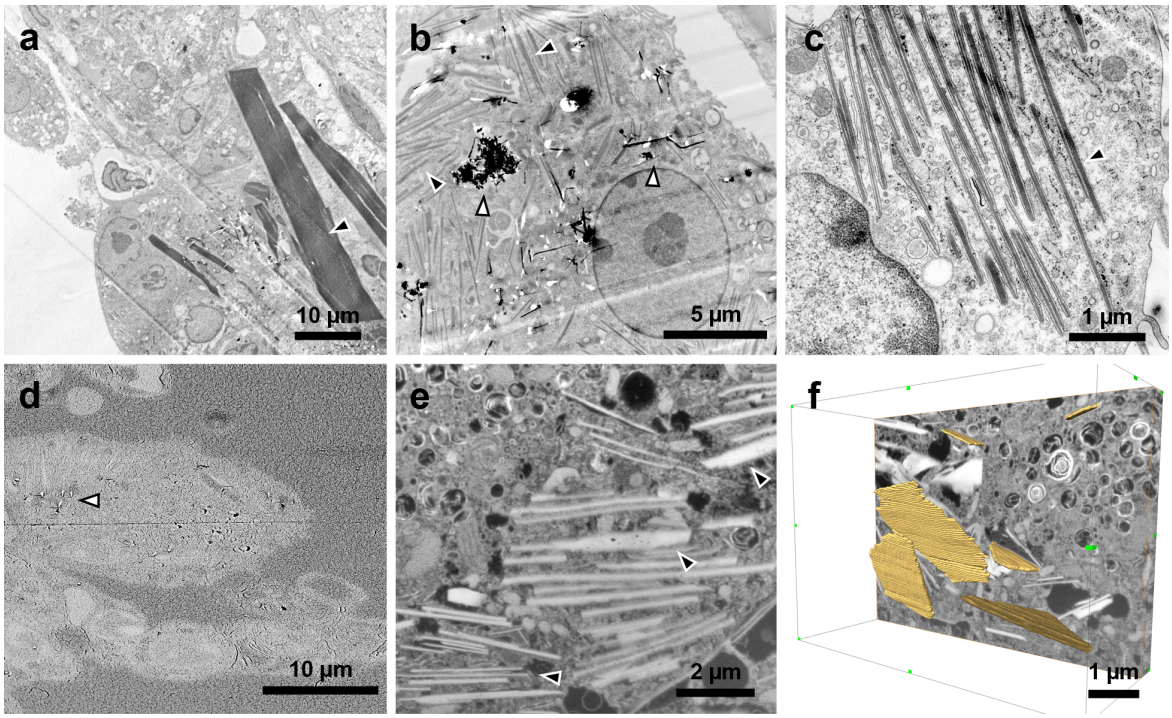

Illustration 5.4: TEM (A-C) and SEM (D-F) images of crystalline bodies observed on day 28 in CNT_{Large} samples. A) Low magnification TEM image showing large crystals, some up to 40 µm long. B) Image showing scattered crystalline bodies and CNTs in clusters. C) Ordered crystalline bodies in the cytosol. D) SEM image of the ultramicrotomed block revealing the underlying cells prior to milling. The image also shows a few protruding CNTs (white arrowhead). E) FIB-SEM image of crystals in a cell. F) 3D representation of the FIB-SEM stack where a few of the crystals have been traced (yellow), revealing their plate-like structure. Black arrowheads indicate ECP crystals while white arrowheads indicate the CNTs.

Gene expression

Detailed description of the global gene expression analysis of lung tissues following pulmonary exposure to Mitsui-7 was done previously [190], while CNT_{Small} and CNT_{Large} will be described elsewhere (Paper X). In brief, pulmonary exposure to Mitsui-7 resulted in strong, dose-dependent differential expression of genes involved in inflammatory and acute-phase responses on post-exposure day 1 in whole lung [190]. A similar response was observed following exposure to CNT_{Small} and CNT_{Large}, peaking on post-exposure day 3 and sustained until post-exposure day 28 for both nanotube types (Paper X). Gene expression analysis revealed differential expression of chitinase 3-like 3 (*Chi3L3)* in some of the samples (Table 1). Because eosinophilic crystals consist of Chi3L3, *Chi3L3* expression is an important indicator of ECP [196], [197], [199]. Chi3L3 protein, also known as Ym1 and ECF-L, is accumulated in alveolar macrophages and is associated with inflammatory diseases and parasite infestations [196], [197].

No differential expression of *Chi3L3* was observed following CNT_{Small} exposure, whereas both Mitsui-7 and CNT_{Large} appeared to induce significant increases in *Chi3L3* expression (Table 1). Increased *Chi3L3* expression on post-exposure day 1 and 3 following CNT_{Large} exposure occurred for the two lower doses, while a significant increase was only present for the highest dose on day 28 (Table 1). Increased expression of *Chi3L3* coincided with ECP crystals on day 28. Similar observations were made following Mitsui-7 exposure (Table 1).

In addition to the increased expression of Chi3L3, the expression profile of several chemokines and cytokines specific to eosinophil activity were found altered following

exposure to all types of CNTs. Eosinophil migration and influx into the lung lumen is highly dependent on CCR3, a chemokine receptor that is abundant on eosinophils [206]. The chemokines CCL11 (eotaxin 1) and CCL24 (eotaxin 2) are produced by epithelial cells, smooth muscle cells and macrophages, and they have a high affinity for CCR3 [206]–[209]. The expression of these chemokines varied greatly following exposure to Mitsui-7, CNT_{Small} and CNT_{Large} (Appendix E). *CCL11* and *CCL24* were differentially expressed only at the high dose on day 3 following exposure to CNT_{Small}, whereas both chemokines were expressed continuously at all doses on day 1 and 3 following exposure to CNT_{Large} and Mitsui-7. This could, in part, explain why a higher eosinophil influx was observed following CNT_{Large} and Mitsui-7 exposure, compared to CNT_{Small}.

		Day 1		Day 3		Day 28		
	Dose	Chi3L3	Eos	Chi3L3	Eos	Chi3L3	Eos	ECP
CNT_{Small}	0	-	1	-	2.4	-	0.6	0/6
	18	2.0	**17**	1.4	**69**	1.0	0.5	2/6
	54	1.0	1.4	0.5	**72**	0.9	0.2	1/6
	162	1.0	3.4	0.7	7.1	1.7	0.0	3/6
CNT_{Large}	0	-	1	-	5.3	-	20	1/6
	18	**2.8**	**51**	**5.8**	**317**	1.8	34	6/6
	54	**3.1**	**86**	**4.3**	**138**	2.5	32	5/6
	162	1.1	1.7	1.1	1.8	9.2	46	4/6
Mitsui-7	0	-	0.3	-	0.4	-	0.3	1/6
	18	**2.9**	**39**	-	**341**	-	5.5	6/6
	54	1.8	**23**	-	**268**	**3.9**	**22**	6/6
	162	2.0	**2.2**	-	101	-	**46**	6/6

Table 5 Overview of Chi3L3 mRNA levels, BAL eosinophil counts (x10) and presence of eosinophilic crystals in BAL cell fluid.

Chi3L3 expression is given as the relative fold-increase in Chi3L3 mRNA levels relative to concurrent controls, where values below 1 indicate a decreased mRNA level. Eos denotes the number of eosinophils. Red numbers are statistically significantly different from controls ($p<0.05$). ECP indicates how many of the samples (n=6) contained eosinophilic crystals. Dashes (–) indicate missing data point.

BAL cell composition

BAL fluid was collected from CNT_{Small}, CNT_{Large} and Mitsui-7 exposed mice at all times and exposures (Appendix E). In general the data showed a similar BAL cell response for the three different CNT types with a few exceptions as described previously [190] and (Paper X). The BAL cell influx was similar for all of the CNTs, and was dominated by a high neutrophil influx that peaked on day 3 compared to vehicle-exposed controls.

Eosinophil counts were high for all the CNT types on day 1 and 3 with relatively larger effect observed for CNT_{Large} and Mitsui-7 compared to CNT_{Small} (Table 1). On day 28, the eosinophilic response was elevated for both CNT_{Large} and Mitsui-7, but only the results of the two highest doses of Mitsui-7 were statistically significant.

Light microscopy investigation of extracellular crystals related to ECP in BAL cells [199], [204], revealed an increased crystal incidence in the CNT_{Large} and Mitsui-7 exposed samples on day 28, which was not observed to the same degree in CNT_{Small} exposed samples or the control samples (Table 1). In addition, the crystals found in CNT_{Small} and control samples were fewer in number and smaller compared to the crystals found in

CNT_{Large} and Mitsui-7 exposed samples. Generally, the crystals varied vastly in size and were mostly stained blue or had a blue periphery (Illustration 5.5).

BAL cells recovered from mice 28 days after intratracheal instillation with similar doses of carbon black [167], and two single walled carbon nanotubes (SWCNT) [210], were also investigated for the presence of crystals. 10% (2/17) of carbon black (Printex 90) samples contained crystals, whereas the two SWCNTs had a 50% crystal incidence in the 18 samples investigated per SWCNT (Appendix E).

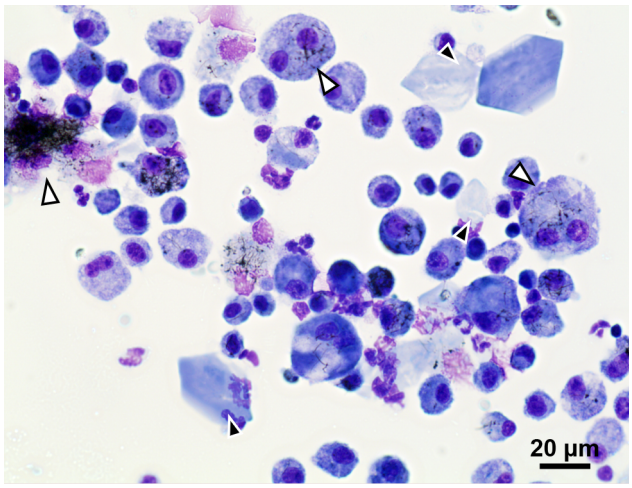

Illustration 5.5: Example image of stained eosinophilic crystals in a BAL cell sample for the highest dose (162 µg) of CNT_{Large} on day 28. Large amounts of crystals were also observed for the two lower doses (18 µg and 54 µg), and similarly for Mitsui-7 samples on day 28. Black arrowheads point to crystals, whereas white arrowheads indicate CNTs or cells containing CNTs.

5.2.5 Discussion

Electron microscopy of CNT interactions

Cellular interactions of the three different CNTs were quite similar, with uptake following a general CNT distribution progression as illustrated in Illustration 5.6. Only small differences in cellular distribution were observed between the CNTs. The initial cell response on day 1 was dominated by CNTs situated in the alveoli, with only a few in the apparent process of piercing cellular membranes. Three days post exposure CNTs were free in the cytosol and in intracellular vesicles, with a majority of CNTs agglomerated in vesicles. On day 28, more individually dispersed intracellular CNTs were observed, together with stressed vesicles with CNTs deforming and penetrating the enclosing membrane, which was particularly evident for CNT_{Large} and Mitsui-7. This time-dependent development agrees with the working model based on *in vitro* experiments [188], although we only observed CNTs in the nucleus when ultramicrotomy artefacts were suspected.

The TEM studies revealed two different pathways by which CNTs may enter cells. First, agglomerates of CNTs present in cellular inclusions indicates an endocytic and actively driven uptake mechanism, although we could not discern which endocytic pathway [119]. Second, single CNTs traversing the cellular membrane were indicative of physical piercing of the cell membrane, as observed *in vitro* [159], [161], [182]. The ratio between CNTs taken up via physical piercing and via endocytosis was not quantified, but physical piercing was observed at day 1 whereas endocytic uptake was not. On day 3 CNTs were predominately found inside vesicles, suggesting earlier endocytic uptake. It is unclear whether the CNTs are taken up by piercing and subsequently enter vesicles as some

propose [186], [188], or whether direct non-endocytic uptake occurs more quickly and thus dominates on day 1 [186]. Nevertheless, the overall observed non-phagocytic uptake is small compared to the extensive phagocytic uptake seen on post exposure day 3 for all CNTs.

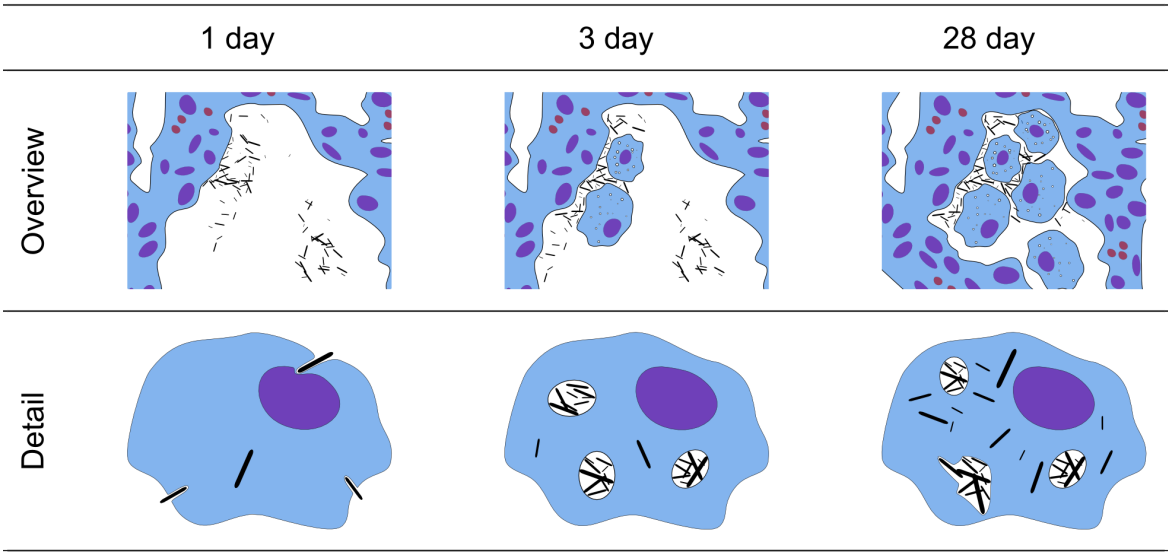

Illustration 5.6: Observed timeline for CNT uptake and development in vivo. It is currently not clear whether the individual CNTs on day 1 agglomerate into vesicles post-entry on day 3 or if agglomerations of CNTs are taken up via endocytosis. On day 3 and 28 vesicular escape or a continued uptake of individual CNT uptake is observed.

The observed decrease in vesicles containing CNTs, the stressed vesicles on day 28, and also the higher level of cytosolic CNTs, particularly for CNT_{Large} and Mitsui-7 exposed samples, indicates that CNTs can escape vesicles *in vivo* as described previously for *in vitro* samples [159], [188]. This mechanism could be size related, as CNT escape was less significant for CNT_{Small} exposed samples. In the literature on rodent exposures to CNTs, CNTs similarly sized to CNT_{Large} have been observed freely in the cytosol of cells weeks to months after exposure [163], [168], whereas smaller and tangled CNTs have been found predominantly within vesicles weeks [211] to months [168], [212] after exposure. Based on our observations and the reviewed literature, we speculate that comparably long and thick CNTs (30-70 nm wide, and 0.5-5µm long) more easily escape the endosomal system, which may have implications for their toxicity. Thus, although the CNTs in the size range studied here did not incur frustrated phagocytosis, they might disrupt the endosomes and phagosomes and thereby cause single cell damage and be more difficult to clear. This may also explain why we see a more pronounced long-term toxicological effect for CNT_{Large} compared to CNT_{Small} both in terms of gene expression and BAL cell counts (Paper X).

Eosinophilic crystalline pneumonia

Several mice in this study developed eosinophilic crystalline pneumonia (ECP), as evident from light and electron microscopy investigations. However, at first glance, the crystals appeared to be needle-like in the TEM sections (Illustration 5.4 a-c), whereas they in the light microscopy of BAL cell samples, were more cuboid or hexagonal (Illustration 5.5). 3D FIB-SEM imaging revealed that the needle-like structures in the TEM sections were caused by the sectioning, and that the crystals were in fact more plate-like and appeared to be more similar to those observed in the BAL cell samples.

Since ECP is especially prevalent in the C57BL/6 mouse strain [195], the natural

occurrence of ECP must be considered. The incidence of ECP in aged female C57BL mice (10-30 months old) is approximately 16% [213], and generally younger mice are said to showcase ECP granulation less often than aged mice [197]. Therefore, the observed 10% incidence (2 out of 18) of ECP in the vehicle exposed mice on day 28 suggests a reasonable ECP background level in our studies (Table 1). Based on the background level, an 80% crystal incidence in both the CNT_{Large} and Mitsui-7 samples indicates a substantial increase (Appendix E). Furthermore, even though the crystals observed in CNT_{Small} and the two SWCNTs were less pronounced in positive sample, the 30-50% ECP incidence still suggests heightened ECP development. In contrast, carbon black nanoparticle exposure showed crystal incidence on par with background. This suggests that the enhanced development of ECP crystals may be related to the specific dimensions of carbon-based particles.

To further support the notion that the crystals observed are related to ECP, gene expression of *Chi3L3* was investigated as the eosinophilic crystals consists of Chi3L3 proteins [199]. Samples showing a statistically significant increase in Chi3L3 on days 1, 3 or 28 had an increased incidence of crystals (Table 1). An increase in Chi3L3 protein levels has previously been observed for SWCNT and asbestos exposed mice [198], but the presence of ECP was not mentioned.

The reason why high *Chi3L3* gene levels at the early time points were not accompanied by ECP (Table 1) might be because the crystals need to mature and grow over time before they are visible with light microscopy, similar delayed reactions have been observed in other cases [214].

Eosinophilic response

The larger observed eosinophilic response to CNT_{Large} and Mitsui-7 suggests that these CNTs cause a stronger allergy-like effect than CNT_{Small} [191], [215]. Eosinophilic inflammation is not a typical response following a single pulmonary exposure to particles [167], [216], [217], and since ECP [199] and the *Chi3L3* gene [197], [198] is linked to inflammatory diseases and allergic asthma, it is unclear whether the eosinophil influx was an actual direct response to the CNTs or was a response to ECP development. Additionally, we observed no notable BAL cell count or histological differences in the vehicle control samples, where we used 2% serum for CNT_{Small} and CNT_{Large} and 10% acellular BAL for Mitsui-7 samples. Hence, in the present study, vehicle does not appear to be a confounding variable, suggesting that the eosinophil reaction occurs as a result of direct cellular CNT interactions, a combination of CNT and protein interactions, or the ECP sensitised mouse strain affected by CNTs.

The very large eosinophilic response on day 3 for the two long CNTs (Table 1) correlates with the observed crystals in the BAL cell fluids on day 28. However, the observed increase in eosinophil influx does not appear to correlate directly with *Chi3L3* levels or crystal occurrence as this was not detectable in the case of CNT_{Small} exposed samples.

The eosinophilic response in the present study had an almost reversed dose response relationship. There are several possible reasons for this. Gene expression analysis showed that although the chemokines CCL11 and CCL24 were differentially expressed following CNT_{Large} and Mitsui-7 exposure, no statistically significant increase was observed for CCL24 at the high dose on post-exposure day 1 for either CNT (Appendix E). On day 3 the expression of CCL24 at the 162 μg dose was much lower than for 18 and 54 μg. In contrast to CLL11, CCL24 has been linked specifically to eosinophil influx into BAL

[209]. The low eosinophil influx at the high doses could therefore be due to low or lack of expression of CCL24. We also speculate that the generally high levels of neutrophils and a high expression of non-eosinophil chemotactic cytokines at the 162 μg dose might quench a possible eosinophil influx. Lastly, the reverse dose-response observed could be an experimental artefact if the time dependency of the eosinophilic response is different for the high and low doses.

Eosinophilic response in ECP sensitive mice

It has been reported that eosinophils are able to biodegrade CNTs [218], although they are generally known to be involved in extracellular degradation responsible for parasite elimination, which can be larger than the cell [218]. We speculate that the increased eosinophilic response, prevalent primarily in Mitsui-7 and CNT_{Large}, might be due to long and thick CNTs being more difficult to internalise and degrade by alveolar macrophages. This correlates with the high extracellular CNT content on days 1 and 3 where the eosinophil influx was observed and the subsequent drop in eosinophil number on day 28 when most tubes have been internalised.

However, although an MWCNT induced eosinophilic response has been observed in literature, this has often been in studies using C57BL/6 or other ECP sensitive strains [184], [190]–[192], [219]. In contrast, studies noting an eosinophil influx using non-ECP sensitised strains as a response to CNT exposure are relatively few; e.g., experiments conducted on rats [193] or experiments involving other allergens [215], [220].

The literature available to demonstrate how CNTs cause an eosinophil influx in non-ECP sensitised rodents is limited [193]. Therefore, based on this, we speculate that MWCNT in general do not induce an eosinophilic response, but rather that our observed results might be linked to the use of an ECP sensitive mouse strain.

5.2.6 Conclusion

Our ultrastructural investigations revealed that all of the CNTs examined in this study appear to follow the same overall progression: CNTs are taken up either by a diffusion mechanism or via endocytosis, CNTs are agglomerated in vesicles, and lastly the CNTs appear to escape the vesicle bounds. Our *in vivo* studies thereby support *in vitro* studies [188] showing a similar overall sequence of events for CNT-cell for uptake of MWCNTs.

TEM imaging further suggests that CNT_{Large} and Mitsui-7 are better able to perturb and escape vesicular enclosures in immune cells than CNT_{Small}. We speculate that comparably large and stiff CNTs (30-70 nm wide and 0.5-5 μm long) can more easily escape the endosomal system than smaller more tangled CNTs.

The main observed difference between the CNTs is an allergy-like response related to ECP development, *Chi3L3* gene expression and BAL eosinophil influx, which is less pronounced for CNT_{Small} than CNT_{Large} and Mitsui-7. We conclude that CNT_{Large} and Mitsui-7 cause a substantial increase in ECP occurrence, whereas CNT_{Small} and the additional SWCNT that were investigated exhibit a much less pronounced effect on ECP development, and the carbon black particles cause no increased incidence of ECP above background levels as observed with light microscopy.

However, we caution that development of ECP is linked to the mouse strain used, in this case C57BL/6, which might render these mice more prone to react allergically to CNT exposure. This was supported by the observed CNT-induced eosinophil influx, which has

not been thoroughly documented in other non-ECP sensitive mice strains. We therefore suggest that alternate mice strains that are not prone to develop ECP are used to study allergic reactions to CNT exposure.

5.2.7 Acknowledgements

We are grateful to Zhila Nikrozi, Michael Guldbrandsen and Lisbeth Meyer Petersen for technical assistance. The authors would also like to thank the Core Facility for Integrated Microscopy at the Faculty of Health and Medical Sciences, University of Copenhagen for providing electron microscopy facilities. Mitsui-7 was a kind gift from Mitsui & Co, Ltd. Work was supported by Danish Centre for Nanosafety (20110092173/3) from the Danish Working Environment Research Foundation, the European Community's Seventh Framework Programme (FP7/2007-2013) under grant agreement n° 247989 (Nanosustain) and Chemicals Management Plan of Health Canada.

5.3 Additional notes on ECP crystals and Chi3L3

The exact origin of the ECP crystals is unclear, it was originally suggested that the crystals were formed as a consequence of macrophages phagocytosing eosinophils [205]. However, the low number of eosinophils compared to other immune cells during inflammation (neutrophils, macrophages etc.) leading up to the development of ECP has raised doubt to this hypothesis. Instead, Chi3L3 is a chemoattractant of eosinophils [196], indicating that the main Chi3L3 protein concentration may not be due to eosinophils. Harbord et al., have found evidence that Chi3L3 is synthesised in neutrophils [221], and is also produced in some macrophages [196]. However, neutrophils are generally short lived to avoid unwanted tissue damage and perform apoptosis[11] (life time of 6-12 h). Neutrophil debris is phagocytosed and rapidly digested by macrophages where Chi3L3 protein accumulate, as macrophages can live for months. Purified Chi3L3 is known to crystalise *in vitro* [222], and the same is believed to occur in macrophages that have digested neutrophils over a longer period and thereby accumulating Chi3L3 intracellularly [221]. This could explain why our results mainly found crystalline bodies in macrophages at later time points (Paper III day 28).

The crystals were readily visible in the BAL cell slides, but were not noticed when cells were counted and probably disregarded as being staining artefacts or dirt. Now, the laboratory staff has been alerted to the presence of eosinophilic crystals, such that future BAL cell counts can be marked as ECP positive or not.

11 Programmed cell death

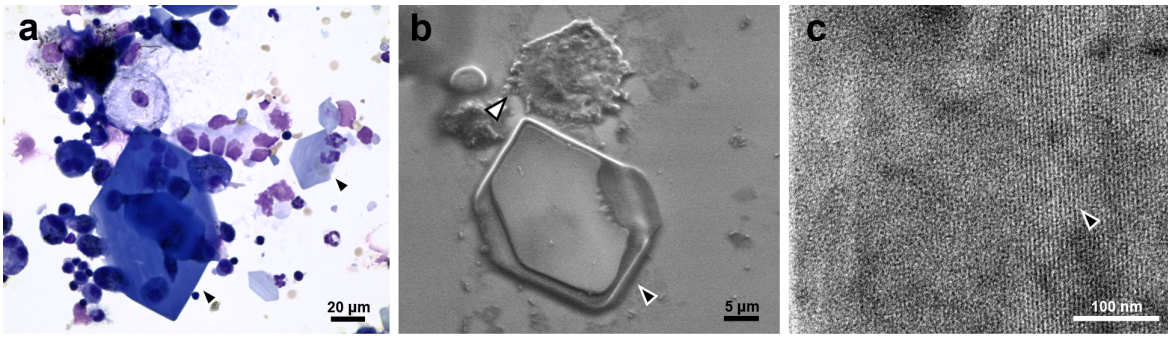

Illustration 5.7: A) LM of crystals on BAL slide. Crystals were found in many variations and sizes. B) SEM image of crystal on BAL slide showing the flat nature of the crystal. The white arrowhead points to a dehydrated cell which has collapsed as it was not stabilised prior to dehydration. C) TEM image of the periodic ~5 nm structure observed in some of the ECP crystals.

5.4 Summary

Ultrastructural interactions of two types of CNTs with lung tissue were studied at three time points. The interaction of the CNTs compared well to interactions observed for *in vitro* experiments performed in literature. The biological responses were very similar for the two CNTs types. However, the longer CNT type appeared be better able to disrupt macrophage vesicles, and resulted in a slightly larger pulmonary reaction which included the development of eosinophilic crystalline pneumonia (ECP). The development of ECP due to CNT exposure was not previously linked in literature. The development of ECP was coupled to *Chi3L3* gene expression and overall results indicated an allergic-like toxicity response. However, literature suggest that ECP in itself is connected to an allergic response and is linked to specific laboratory mice strains, thereby raising doubt about a general allergic reaction stemming from the CNT exposure.

Chapter 6

Conclusion & outlook

Overall the project was focused on developing and exploring EM techniques for imaging nanostructures in cells, and then to test and evaluate the methods on both *in vitro* and *in vivo* samples, as outlined by the goals stated in Chapter 1:

Goal I: Develop and explore EM techniques

Electron microscopy techniques have been explored and developed for studying engineered nanoparticles in biological cells and tissue (Paper I and II).

FIB-SEM was found suitable for providing high resolution 3D images of hard-to-microtome samples such as nanostructured substrates or CNT exposed mice lungs. In order to allow for FIB-SEM imaging of the samples, we have developed methods for obtaining smooth milling surfaces by ultramicrotomy and FIB polishing for subsequent FIB-SEM imaging (Paper II). We have also developed a work flow for reconstructing non-tilted milled volumes (Paper I). Areas of interest were found either via light microscopy on polished embedded samples (Paper VI), or via protruding CNTs from ultramicrotomed samples (Paper II).

The FIB-SEM was able to resolve very detailed and complex internal interactions with nanostructures (Paper I). The limitations of FIB-SEM in terms of resolution and contrast have also been highlighted, as current equipment limits to only large CNTs (~ 70 nm wide) due to their low inherent contrast and high resolution requirements (Paper II). In return it was the largest CNT structures that were most difficult to process for TEM, making FIB-SEM a usable tool. The usefulness of FIB-SEM was demonstrated in Paper III where it was used to resolve the 3D structure of the ECP crystals in lung tissue.

Goal II: Map and document cellular interactions with nanostructures

Cellular interactions with nanostructures were found to be very complex and showcase a large phenotypic variability. In the case of cells adhered to nanostructured substrates, seven different kinds of interactions were observed and documented, some of which had been previously described, whereas others, such as cells being able to break and internalise substrate bound nanostructures, had not been documented previously (Paper I). FIB-SEM showcased how nanowires pertubed the nuclear envelope, and helped establish that nanowires can be enveloped by a thin outer membrane deep within the cell (Paper VI).

Regarding the interactions observed *in vivo* for CNTs in lung tissue, we similarly sought to categorise the interactions and speculated that comparably large and stiff CNTs (about 70 nm wide and 5 μm long) could more easily escape the endosomal system than smaller more tangled CNTs.

The many types of interactions both *in vivo* and *in vitro* were not observed in all instances,

and illustrate the need to correlate results with biological tests bringing better statistics, such that the very time consuming EM investigations can be limited.

Goal III: Time dependent distribution of CNTs *in vivo*

The time resolved studies of CNT uptake *in vivo*, supports *in vitro* observations from literature, and showed an overall progression for all CNT types: CNTs are taken up either by a diffusion mechanism or via endocytosis, CNTs are agglomerated in vesicles, and lastly the CNTs appear to escape the vesicle bounds. The effects of an active immune system were evident with the development of crystalline structures in alveolar macrophages. By correlating the TEM findings with FIB-SEM, light microscopy, and gene expression data, it was established that the crystalline structures were connected to eosinophilic crystalline pneumonia (ECP). ECP was triggered by CNT exposure, and possibly linked to a greater allergic-like reaction to larger CNTs. However, development of ECP is limited to certain mice strains, and therefore the need to use alternate mice strains was proposed, especially if the allergic reaction of CNTs is to be investigated.

6.1 Outlook

The developed methods, proof-of-concepts and scientific results have provided tools and expanded our knowledge regarding nanostructure-cell interactions. But it has also highlighted how little we actually know and the large number of cellular phenotypic variations.

Currently, we can therefore not predict nanostructure-cell interactions in relation to designing devices or evaluating their toxicity. This is due to the huge variability in both cell types and nanostructure materials, together with the fundamental lack of knowledge regarding the underlying biological processes. Our current understanding of endocytosis was obtained by combining electron microscopy with tools for marking and blocking specific pathways [119]. Similarly, we need to study the biological processes behind cell-nanostructure interactions. This could elucidate how nanowires are taken up by fibroblast (Paper I), how cells react to nuclear indentations (Paper VI), or whether CNTs are able to escape lysosomes (Paper III).

In order to improve intracellular signals and delivery efficiencies of nanostructures, blocking specific biological pathways, gene expression and labelling can be used to understand the underlying processes. Verification of intracellular access should include both light and electron microscopy. Low through-put FIB-SEM imaging could be correlated with the fluorescent quenching method for quantifying cellular access [109], thereby providing a faster workflow for optimising cellular entry than by relying on EM data alone.

To investigate the systemic behaviour of nanostructures in terms of translocation, accumulation and nanoscale cellular interactions, correlating EM and quantitative methods such as radioimaging and ICP-MS may prove valuable in the future. Radioactively labelled CNTs were used to study their spreading and accumulation in exposed mice [41]. Using this method, CNT exposure was characterised, and it would then be possible to investigate organs of similarly exposed mice using the methods of this project for finding and imaging CNTs in tissue. Furthermore, as an extension of Raffa et al., lysosome tracking can be performed at longer time scales and correlated with EM to detect whether CNTs can disrupt lysosomes [223].

Since nanostructure-cell interactions in this thesis and in the future will continue to rely on electron microscopic imaging techniques, one should consider the artefacts coupled with the methods. For instance, the appearance of the lamella bodies identified in this thesis is a result of fixation [77], while various ultramicrotomy artefacts were noted in Paper II. We also know that electron microscopy processing will cause volume changes [94], and this is acceptable for investigating tissues where the volume changes are (almost) uniform. However, when investigating cellular interactions with rigid nanostructures, small volume changes might drastically influence the resulting sample. We had one instance of cells showing a lack of ultrastructure detail which bent rigid nanowires (not shown), this was likely caused by a poorly buffered step during sample processing. However, what if sample processing causes other artefacts, such as for instance introducing nanoparticles into cells during the Epon infiltration? Therefore, further studies should be correlated and we also suggest looking into cryogenic techniques for verification (which have their own set of artefacts).

Appendices

Appendix A

Dissemination activities

Podium presentations

- CEN seminar, Center for Electron Nanoscopy at DTU, 04.2012
- iNAP seminar, the national research centre for the working environment, 08.2013
- SCANDEM 2013, yearly conference for the Nordic Microscopy Society, 06.2013
- CFIM symposium, yearly symposium for CFIM, 11.2013
- Steering meeting for the Danish Centre for Nanosafety, 11.2013
- CEN seminar, Center for Electron Nanoscopy at DTU, 01.2014
- Yearly meeting for the Danish Centre for Nanosafety, 04.2014
- Ultramicrotomy workshop, arranged by Axlab, 05.2014

Poster contributions

- Wierzbicki R, Købler C, Lopacinska J, Qvortrup K, Bøggild P, Mølhave K (**2011**). *Three dimensional imaging of carbon nanotube and biological cell interfaces*. Carbonhagen, Copenhagen, Denmark.
- Købler C, Saber AT, Vogel UB, Qvortrup K, Mølhave K (**2013**). *Investigating CNTs in Lung Tissue with FIB-SEM*. Microscopy and Microanalysis 2013, Indianapolis, USA.
- Købler C, Wierzbicki R, Qvortrup K and Mølhave K (**2013**). *Obtaining high resolution electron microscope images of cells on hard nanostructured substrates*. Scandem 2013, Copenhagen, Denmark.
- Löschner K, Navratilova J, Købler C, Mølhave K, Wagner S, Kammer FVD, Larsen EH (**2013**). *Detection and characterization of silver nanoparticles in chicken meat*. International symposium of recent advances in food analysis, Prague, Czech Republic.
- Skjolding LM, Sørensen SN, Thit A, Købler C, Mølhave K and Baun A (**2014**). *Assessment of gold nanoparticle uptake in Daphnia magna gut in the presence and absence of food using three types of microscopy*. SETAC Europe 2014. Basel, Switzerland.

Student supervision

- Sigurd F. Truelsen, 20 ECTS Bachelor project (**2012**). *Fabrication and Test of Microelectrode Array Devices*.
- Lean G. Pedersen, 7.5 ECTS special course (**2012**). *Confocal Study of Fibroblast Cells' Volume for FIB-SEM*.
- Lars M. Skjolding, Sara N. Sørensen and Amalie Thit, 5 ECTS special course

(**2013**). *Assessment of gold nanoparticle uptake in Daphnia magna gut in the presence and absence of food using Electron Microscopy.*

- Josephine Licht, 10 ECTS special course (**2014**). *Interactions between human colonic HT 29 cells and potential synbiotics visualised by scanning electron microscopy.*
- Vaclav Torcik, 5 ECTS special course (**2014**). *Developing a Series of Nanotechnology Experiments*.

Additional activities

Performed science shows for high school and elementary students in the DTU Nanoshows and DTU Mindshow, and were involved in the development of the DTU Nanoshow. Member of the Ph.D. committee 'Electronics and Communication' for two years, and involved in hosting an electron microscopy workshop for members of the FP7 Nanolyse project.

Conference contributions

- Skjolding LM, Sørensen SN, Thit A, Købler C, Mølhave K and Baun A. *Assesment of gold nanoparticle uptake in Daphnia magna gut in the presence and absence of food using three types of microscopy* (**2014**). SETAC Europe 2014. Basel, Switzerland.
- Löschner K, Navratilova J, Købler C, Mølhave K, Wagner S, Kammer FVD, Larsen EH. *Detection and characterization of silver nanoparticles in chicken meat* (**2013**). International symposium of recent advances in food analysis, Prague, Czech Republic.
- Købler C, Wierzbicki R, Qvortrup K and Mølhave K. *Obtaining high resolution electron microscope images of cells on hard nanostructured substrates* (**2013**). Scandem 2013, Copenhagen, Denmark.
- Købler C, Saber AT, Vogel UB, Qvortrup K and Mølhave K. *Investigating CNTs in Lung Tissue with FIB-SEM (**2013**). Microscopy and Microanalysis* 2013, Indianapolis, USA.
- Wierzbicki R, Købler C, Lopacinska J, Qvortrup K, Bøggild P and Mølhave K. *Three dimensional imaging of carbon nanotube and biological cell interfaces* (**2011**). Carbonhagen, Copenhagen, Denmark.

List of publications

Key papers

The thesis is based on the following key papers:

I Wierzbicki R[§], Købler C[§], Jensen MRB, Łopacińska J, Schmidt MS, et al. (**2013**). *Mapping the Complex Morphology of Cell Interactions with Nanowire Substrates Using FIB-SEM*. PLoS ONE.

II Købler C, Saber AT, Jacobsen NR, Wallin H, Vogel U, et al. (**2014**). *FIB-SEM imaging of carbon nanotubes in mouse lung tissue*. Analytical and Bioanalytical Chemistry.

III Købler C, Poulsen SS, Saber AT, Jacobsen NR, Wallin H, et al. (**Ready for submission**). *Subcellular distribution and effects of carbon nanotubes in mouse lung over time*.

Additional papers

Additionally, I have contributed to the following peer-reviewed papers:

IV Łopacińska JM, Grădinaru C, Wierzbicki R, Købler C, Schmidt MS, et al. (**2012**). *Cell motility, morphology, viability and proliferation in response to nanotopography on silicon black*. Nanoscale.

V Jensen E, Købler C, Jensen PS, Mølhave K (**2013**). *In-situ SEM microchip setup for electrochemical experiments with water based solutions*. Ultramicroscopy.

VI Persson H, Købler C, Mølhave K, Samuelson L, Tegenfeldt JO, et al. (**2013**). *Fibroblasts Cultured on Nanowires Exhibit Low Motility, Impaired Cell Division, and DNA Damage*. Small.

VII Loeschner K, Navratilova J, Købler C, Mølhave K, Wagner S, et al. (**2013**). *Detection and characterization of silver nanoparticles in chicken meat by asymmetric flow field flow fractionation with detection by conventional or single particle ICP-MS*. Analytical and Bioanalytical Chemistry.

VIII Poulsen SS, Jacobsen NR, Labib S, Wu D, Købler C, et al. (**2013**). *Transcriptomic Analysis Reveals Novel Mechanistic Insight into Murine Biological Responses to Multi-Walled Carbon Nanotubes in Lungs and Cultured Lung Epithelial Cells*. PLoS ONE.

IX Poulsen SS, Saber AT, Williams A, Andersen O, Købler C, et al. (**Submitted to ACS Nano**). *Different lengths of multi-walled carbon nanotubes cause similar effects in inflammatory response pathways, but differences in the expression of genes involved in fibrosis in mouse lung*.

X Loeschner K, Navratilova J, Grombe R, Linsinger TPJ, Købler C, et al. (**Submitted to Food Chemistry**). *In-house validation of a method for determination of silver nanoparticles in chicken meat based on asymmetric flow-field flow fractionation and ICP-MS detection*.

§ Co-first author

Paper contributions

My contributions to the papers:

I Performed some of the FIB-SEM experiments, analysed the data and wrote the manuscript.

II Involved in planning and designing experiments for electron microscopy. Performed the electron microscopy imaging, analysed the data and wrote the manuscript.

III Involved in planning and designing experiments for light and electron microscopy. Performed the imaging, analysed the data and wrote the manuscript.

IV Performed SEM imaging and corrected the manuscript.

V Contributed to the setup design, membrane deflection measurements, burst tests and provided feedback on the manuscript.

VI Carried out sample processing, FIB-SEM imaging and contributed and corrected the manuscript.

VII Responsible for TEM imaging and analysis. Contributed with discussions and corrected the manuscript.

VIII Responsible for TEM imaging and analysis, and provided feedback for the manuscript.

IX Responsible for LM and TEM imaging and analysis, and provided feedback on the manuscript.

X Responsible for TEM imaging and analysis, and provided feedback for the manuscript.

Appendix B

Selected supplementary information for Paper I

Embedding protocol

Fixation	2% GDA (0.2 M) + 0.05 M cacodylate buffer (total 300 mOsm)	Min. 1 hour
Flush	0.15 M cacodylate buffer	2 X 30 min
Post-fix/stain	1 % OsO4 + 0.12 M cacodylate buffer	1 hour
Rinse	Milli-Q	2 X 10 min
Mordant	1%wt tannic acid in Milli-Q	1 hour
Rinse	Milli-Q	2 X 10 min
Stain	1%wt Uranyl acetate in Milli-Q (can be left overnight)	2 hours
Dehydration	70% ethanol (can be stored in 70%)	2 X 10 min
Dehydration	96% ethanol	2 X 10 min
Dehydration	100% ethanol	2 X 10 min
Dehydration	Propylene oxide	2 X 10 min
Embedding	1:3 Epon / Propylene oxide	30 min
Embedding	1:1 Epon / Propylene oxide	overnight
Embedding	3:1 Epon / Propylene oxide	1 hour
Embedding	100% Epon	2 hours
Curing	Cure at 60 deg.	48 hours

Image processing

After the slice and view stack has been recorded several steps are required to convert it into a useful 3D model. To do this three steps are required: scaling of the Y-direction, alignment of the individual slices, and a coordinate transformation to match the original volume – all of which has been done with ImageJ[12].

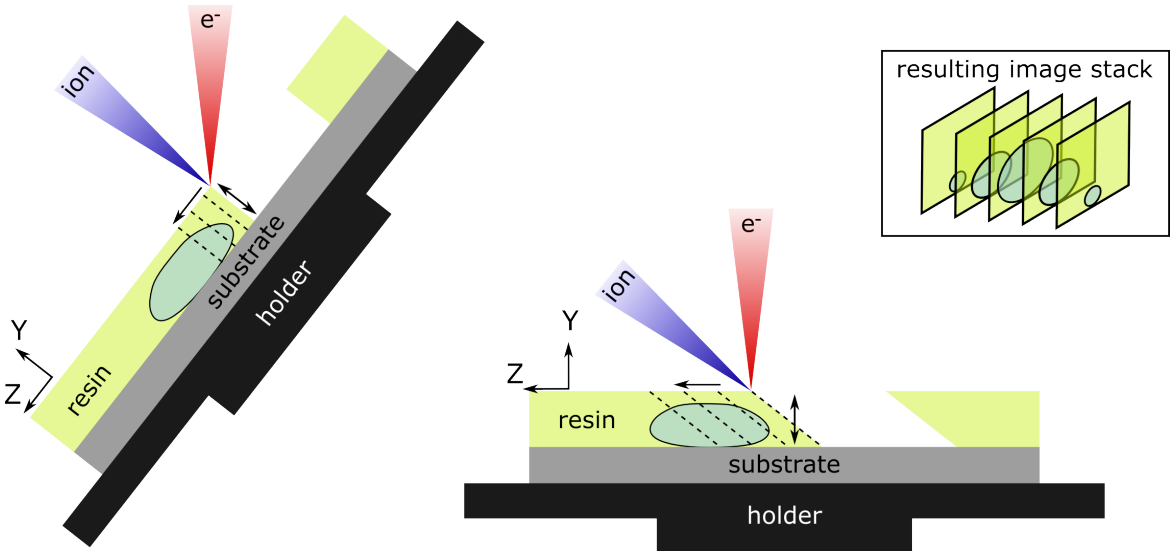

Supplementary Illustration 7.1 Left, the usual method in FIB-SEM is illustrated, here the sample is tilted towards the ion beam, resulting in normal incidence milling. Right, instead of tilting the sample, the ion beam is milling at an angle. The insert shows how an image stack is build up, representing the sample. Notice the Z-direction is parallel to the substrate.

First, as the FIB is at an angle to the SEM, each slice is tilted versus the e-beam; therefore the obtained image for each slice is a compressed projection which needs to be stretched to match the actual aspect ratio of the original slice. With an angle of 52 degrees between the FIB and SEM, this correction in the Y-scale amounts to approximately 1.27 – simply performed in ImageJ.

Second, the SEM imaging will have small random shifts between the slices, most likely due to surface charging. This creates a significant distortion of the 3D geometry when the slices are stacked together. A pyramid registration alignment algorithm [224], the stackreg plugin[13], was used for matching of the consecutive slices.

Third, depending on the amount of automatic beam shift between slices the stack will exhibit an angled substrate in the ZY plane. For the tilted sample the data is skewed using the affine function to level the substrate. If the automatic beam shift had matched the displacement of the substrate in the Y-direction exactly as it was milled this had not been necessary. For the non-tilted sample however skewing of the stack to level the substrate would lead to a distorted stack. Instead the stack is skewed to obtain a substrate angle of 52 degrees after which is rotated to represent the original volume. Refer to (Supplementary Illustration 7.2 and 7.4) to see the different transformations – these transformations are performed using the affine function[14] in ImageJ [225].

12 Java based image processing and analysis program. Available from: http://rsbweb.nih.gov/ij/.
13 Stackreg plugin for imageJ. Available from: http://bigwww.epfl.ch/thevenaz/stackreg/
14 TransformJ. Available from: http://www.imagescience.org/meijering/software/transformj/

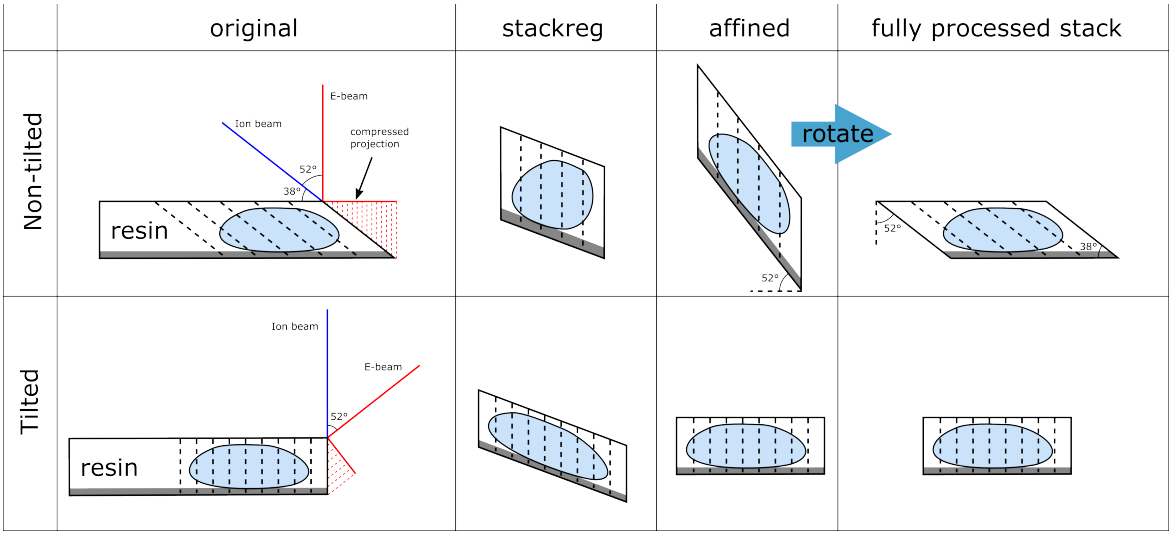

Supplementary Illustration 7.2: The different transformations made to obtained image stack to make it represent the original volume.

To illustrate how the transformations look for a non-tilted sample, the individual steps for the non-tilted cell on a glass substrate is shown in Supplementary Illustration 7.4 and 7.5.

An image stack was obtained with a non-tilted sample, a single slice and the stack seen from the side can be seen in Supplementary Illustration 7.3. This stack has to be post processed as outlined above, that is, it has to be: stretched in the y-direction, individual slice aligned using the stackreg algorithm, the substrate corrected using the affine function, and then the stack has to be adjusted for not being obtained with normal angle milling (cf. Supplementary Illustration 7.2 for the side view showing the different effects of the post processing).

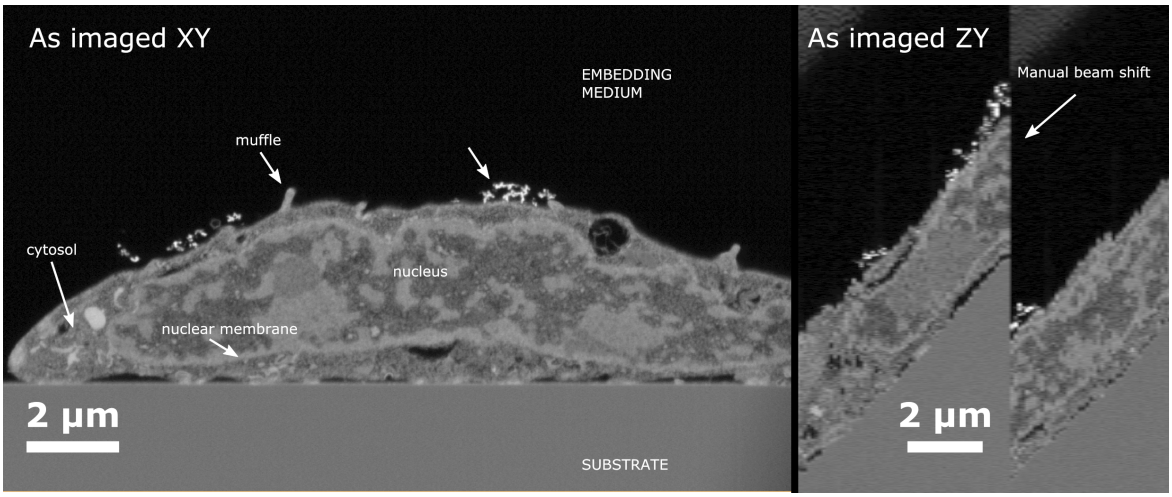

Supplementary Illustration 7.3: Left, a single slice of the raw data can be seen (as imaged), showing how the cell is situated on the substrate and some internal structures in the cell can be seen. Right, here the raw image stack is seen from the side, no post processing done. A large manual beam shift was performed during imaging resulting in the large jump, together with smaller slice to slice variations.

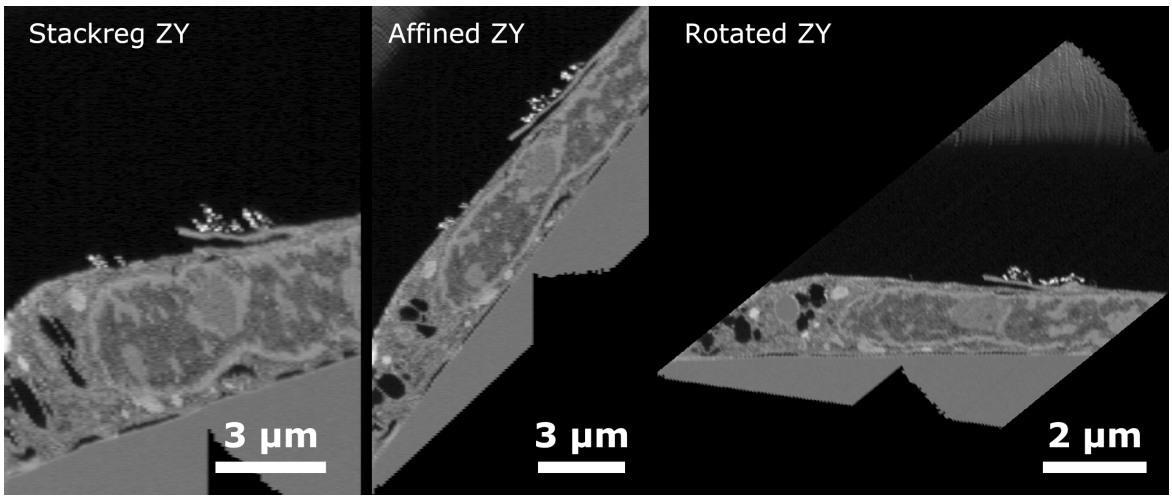

Supplementary Illustration 7.4: Sideviews of the obtained image stack showing the sequential processing operations' effects. Left, the individual slices are aligned forming a fairly smooth image using stack-reg algorithm. Middle, then the substrate is corrected such as to annul the effects of automatic E-beam shifts in the Slice and view program, resulting in a 52 degree substrate. Right, finally the image stack is rotated 52 degrees to represent the sample on the flat substrate having been cut at an angle.

Particularly the non-tilted substrate required a large amount of computer memory, which meant that these samples had to be downscaled to 50%, thus decreasing the resolution of the images. In addition, some image ghosting and alignment errors take place sometimes giving rise to ripples.

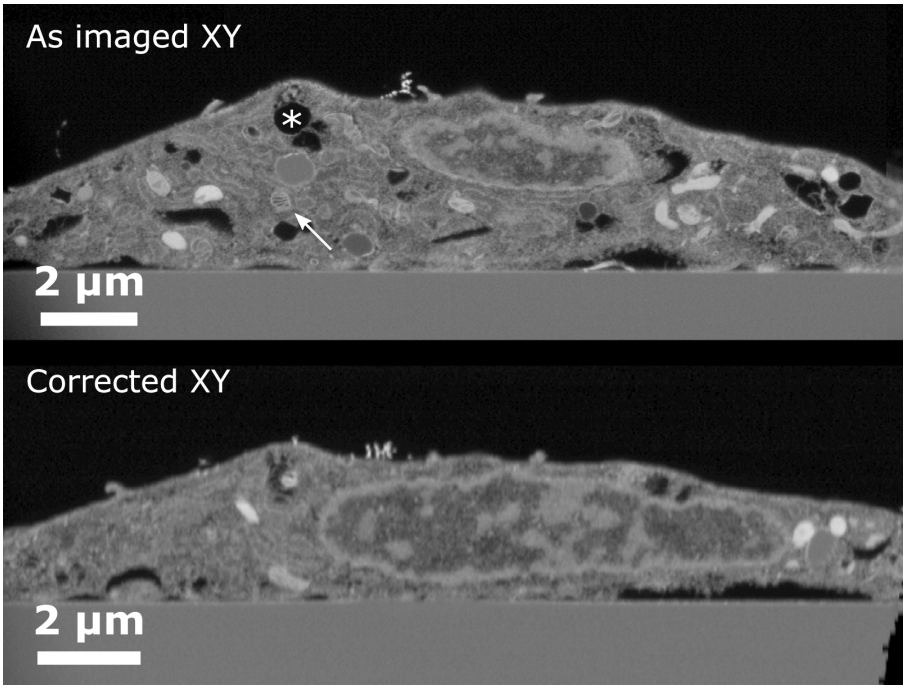

*Supplementary Illustration 7.5: Top, high detail image of the as imaged cell y-scale corrected cell. The arrow indicates what looks similar to mitochondria. Also observed at * (and other) is what appears to be empty vesicles without staining inside the cytosol. Lower, a slice of the fully processed stack is shown. The corrected stack has less detail due to a decreased resolution limited by computer memory, and the non-slanted milling approach where the quality here relies on the stackreg algorithm to limit misalignment between the multiple slices represented in this single image.*

Standing nanowires

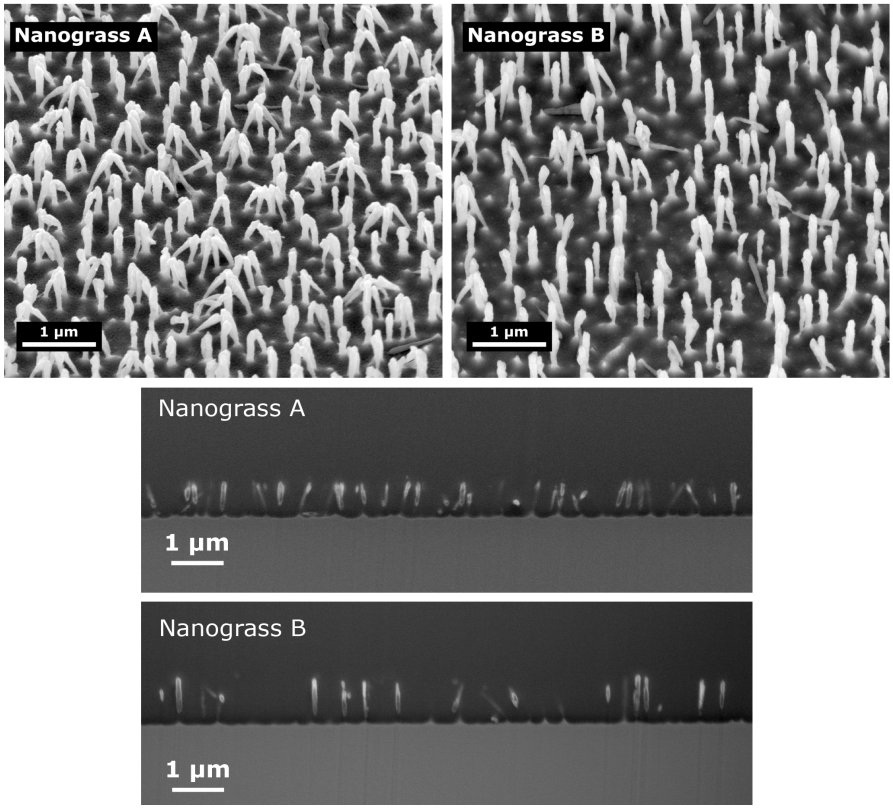

Supplementary Illustration 7.6: SEM images of the two types of nanograss substrates used. The two upper images show ordinary SEM images of the substrates, whereas the two below show the nanograss substrates having endured the embedding process. The embedded substrate images show standing nanowires and some which have tilted like the non-embedded ones.

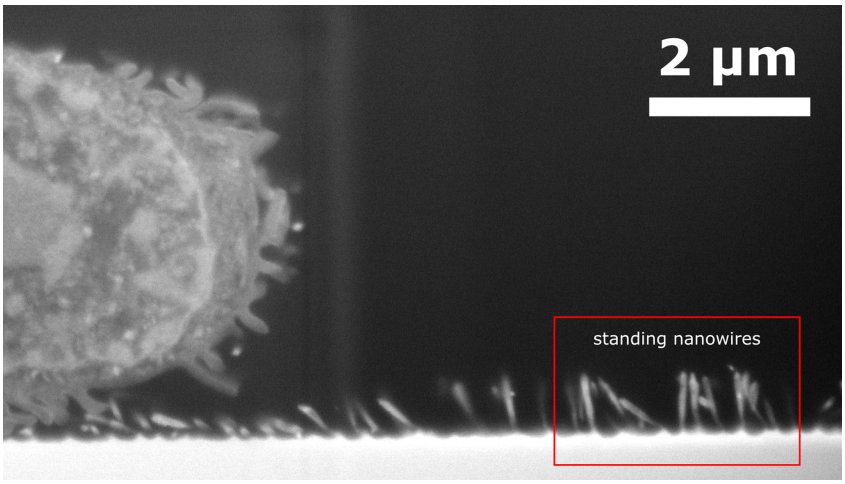

Supplementary Illustration 7.7: Nanograss A showing standing nanowires next to the cell.

Appendix C

Carbon nanotube characteristics

	CNT_{Small}	CNT_{Large}	Mitsui-7
Mean length ± SEM	846 ± 102	4048 ± 366	5730 ± 490
Mean width ± SEM	11 ± 0.7	67 ± 4	74 ± 4
Minimal width	5.7	23.6	28.8
Maximum width	17	138	173
BET SSA [m^2]	254	18	22
Minor elements	Al (10‰) Fe (2‰) Na (1.3‰) Ni (< 1‰)	Na (< 1‰) Fe (< 1‰) Al (< 1‰) Ni (< 1‰) Mg (< 1‰)	Na (< 1‰) Fe (< 1‰) Mn (-) Al (< 1‰) Ni (< 1‰) Mg (< 1‰)

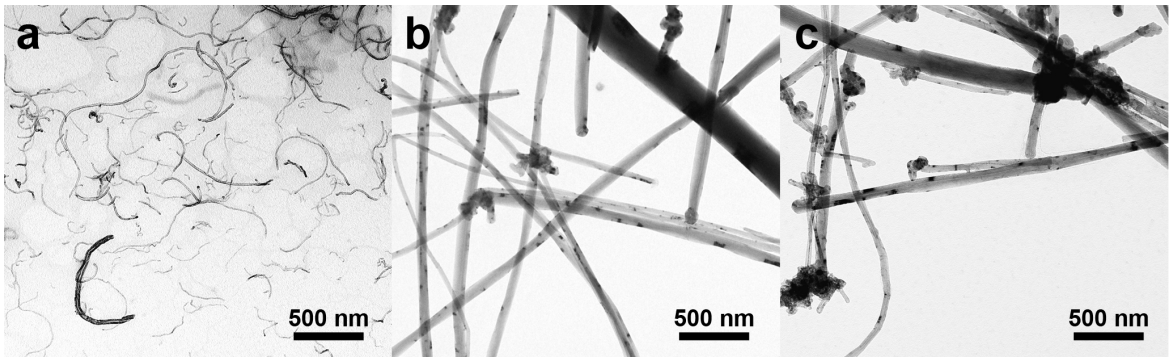

TEM micrographs of pure CNTs A) CNT_{Small}. B) CNT_{Large}. C) Mitsui-7.

Appendix D

Additional structures and cells found in lung tissue

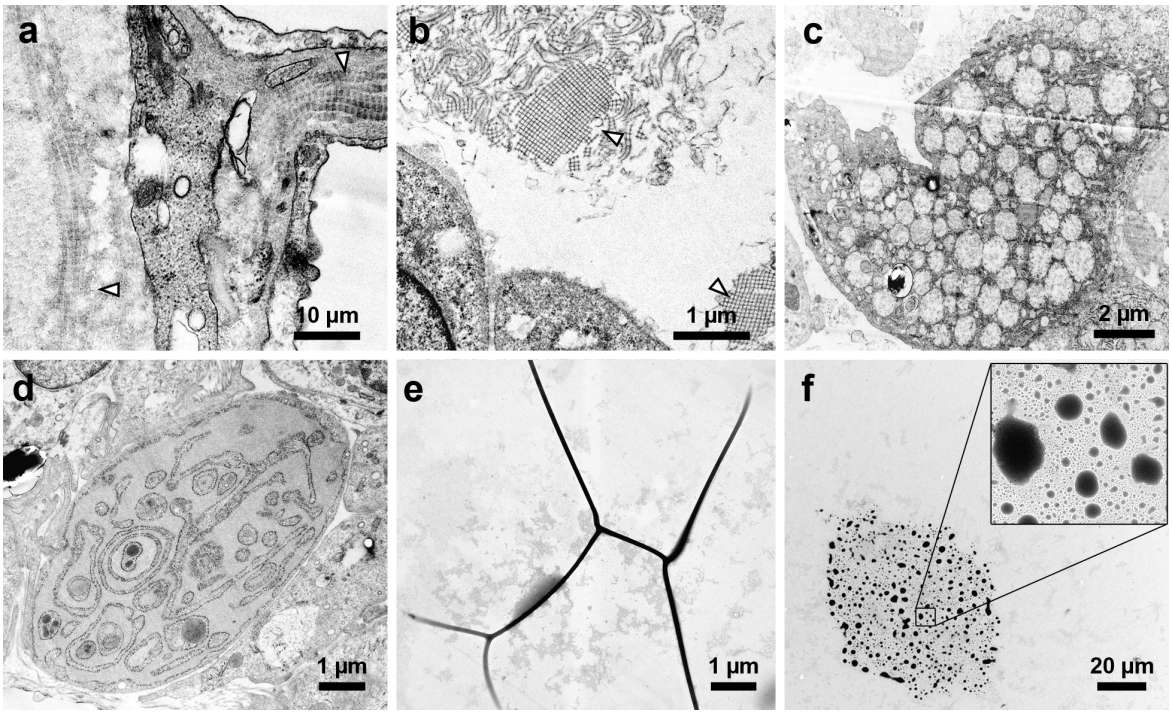

A) Fibres found in the tissue which could be elastin or collagen, but with a measured pattern periodicity between 50-70 nm, it is most likely collagen as it has a 68 nm periodicity whereas elastin does not [40].

B) Cellular debris was found outside cells (often type II pneumocytes) which might stem from the lamella bodies of Type II cells [226]. The mesh like structure sometimes observed, appear to identify the debris as being tubular myelin which is part of the surfactants excreted from type II pneumocytes.

C-D) As mentioned in Chapter 5 we on occasion ran into cells which we had difficulty categorising. C) The large vesicles or granules could suggest that this was a basophil, which have been poorly fixed such that the contents of the granules have leaked into the cytosol. D) The appearance of this cell is rather strange and might be subject to fixation artefacts.

E-F) Preparation artefacts were observed throughout the samples and were rarely included in the main text. E) Fold in the section after ultramicrotomy. F) Probably a staining precipitate artefact.

Appendix E

Selected supplementary information for Paper III

BAL cell counts

			CNT_{Small}				CNT_{Large}				Mitsui7		
		0 µg	18 µg	54 µg	162 µg	0 µg	18 µg	54 µg	162 µg	0 µg	18 µg	54 µg	162 µg
1 day	Neutrophils	9.4 (2.5)	**54.7 (10.1)**	**116.5 (55.7)**	**89.5 (39.9)**	9.4 (2.5)	**49.9 (6.3)**	**94.1 (2.9)**	**118.0 (15.5)**	7.7 (1.7)	**55.1 (10.6)**	**60.6 (4.5)**	**140.2 (31.9)**
	Macrophages	62.8 (5.9)	49.9 (9.2)	33.3 (5.3)	**22.5 (4.4)**	62.8 (5.9)	45.7 (9.4)	46.5 (4.9)	**15.4 (2.9)**	53.2 (2.5)	38.2 (5.1)	37.4 (7.4)	**30.3 (8.5)**
	Eosinophils	1.0 (0.5)	**17.2 (6.2)**	1.4 (0.4)	3.4 (1.5)	1.0 (0.5)	**50.6 (11.7)**	**86.2 (15.0)**	1.7 (0.7)	0.3 (0.1)	**38.8 (11.7)**	**23.1 (11.1)**	**2.2 (0.5)**
	Lymphocytes	0.8 (0.2)	1.1 (0.5)	0.9 (0.4)	0.5 (0.3)	0.8 (0.2)	2.1 (0.3)	2.5 (0.7)	1.7 (0.7)	1.6 (0.5)	2.8 (0.5)	1.7 (0.5)	**0.6 (0.3)**
	Epithelial	8.8 (1.6)	4.1 (0.6)	8.0 (0.5)	7.6 (2.2)	8.8 (1.6)	8.2 (1.4)	11.2 (2.9)	17.2 (3.7)	11.1 (1.6)	7.9 (1.2)	11.9 (1.9)	22.1 (3.7)
	Total	82.8 (8.3)	127.0 (11.1)	160.0 (53.2)	123.5 (45.8)	82.8 (8.3)	**156.5 (11.6)**	**240.5 (14.9)**	**154.0 (20.1)**	73.8 (3.6)	**142.8 (22.3)**	**134.7 (19.5)**	**195.3 (40.8)**
3 days	Neutrophils	0.5 (0.2)	**109.8 (13.5)**	**163.0 (16.3)**	**458.6 (83.5)**	2.6 (1.2)	**36.1 (8.8)**	**101.3 (33.0)**	**159.7 (33.9)**	3.0 (0.2)	**84.3 (13.6)**	**154.9 (34.3)**	**163.2 (49.9)**
	Macrophages	67.4 (5.9)	120.0 (26.7)	**190.6 (22.6)**	37.5 (10.9)	57.8 (5.8)	72.7 (11.1)	79.7 (11.7)	56.5 (8.5)	56.4 (4.2)	**103.1 (9.7)**	**119.7 (15.9)**	80.6 (18.5)
	Eosinophils	2.4 (0.8)	**69.2 (11.1)**	**72.2 (12.8)**	7.1 (2.7)	5.3 (4.4)	**317.3 (37.4)**	**138.3 (33.3)**	1.8 (0.5)	0.4 (0.6)	**341.3 (122.7)**	**268.0 (94.0)**	**100.9 (57.6)**
	Lymphocytes	1.1 (0.4)	9.9 (3.7)	**19.5 (5.9)**	2.8 (1.0)	1.7 (0.6)	**19.7 (6.2)**	**16.9 (3.6)**	2.4 (0.8)	0.9 (0.2)	**27.0 (9.7)**	**42.4 (10.2)**	**16.5 (5.9)**
	Epithelial	10.6 (1.6)	19.5 (4.6)	28.5 (4.6)	14.5 (4.4)	7.1 (1.5)	**19.2 (5.1)**	10.7 (1.8)	11.0 (1.4)	8.5 (0.8)	**25.3 (9.1)**	**25.4 (1.4)**	**17.2 (3.9)**
	Total	82.0 (7.2)	**328.5 (30.2)**	473.0 (16.2)	**520.5 (87.4)**	74.5 (8.8)	**465.0 (43.6)**	**347.0 (43.6)**	**231.5 (41.8)**	69.2 (6.4)	**581.0 (121.0)**	**610.3 (148.1)**	**378.3 (75.5)**
28 days	Neutrophils	0.7 (0.2)	**29.0 (8.9)**	**28.9 (12.0)**	**38.0 (7.5)**	6.8 (4.2)	**26.1 (11.0)**	**17.6 (5.1)**	**81.2 (15.6)**	1.1 (0.3)	**10.2 (2.4)**	**30.2 (7.5)**	**90.4 (14.2)**
	Macrophages	54.3 (4.6)	76.0 (16.8)	73.1 (23.4)	**141.7 (18.1)**	60.3 (5.7)	76.2 (9.3)	78.3 (15.8)	86.5 (18.6)	82.4 (5.7)	87.5 (8.2)	99.8 (14.3)	97.5 (7.8)
	Eosinophils	0.6 (0.5)	0.5 (0.2)	0.2 (0.2)	0.0 (0.0)	20.4 (10.1)	33.5 (13.2)	32.3 (14.2)	46.3 (17.5)	0.3 (0.0)	**5.5 (1.8)**	**21.7 (8.5)**	**45.5 (13.6)**
	Lymphocytes	1.0 (0.3)	**16.6 (6.0)**	7.1 (3.3)	**9.2 (2.0)**	4.9 (1.6)	**14.9 (3.6)**	**19.9 (8.2)**	**9.5 (2.3)**	2.1 (0.4)	**16.8 (6.2)**	**23.1 (5.8)**	**45.8 (9.3)**
	Epithelial	9.9 (1.9)	15.0 (3.0)	12.7 (3.1)	17.1 (3.1)	9.8 (1.9)	16.3 (4.9)	11.5 (2.6)	17.0 (2.7)	10.0 (2.2)	13.3 (2.8)	14.3 (3.3)	14.3 (3.1)
	Total	66.5 (5.3)	**137.0 (23.6)**	122.0 (38.4)	**206.0 (28.5)**	102.3 (16.3)	167.0 (34.7)	159.5 (35.5)	**240.5 (41.2)**	95.9 (5.8)	133.2 (16.3)	**189.1 (31.6)**	**293.3 (34.4)**

Differential BAL cell counts ($x10^3$) together with the SEM in the parentheses are given for all the CNTs. Red numbers indicate statistically significant data ($p<0.05$).

ECP overview

Type	Dose [µg]	Day 1				Day 3				Day 28			
		Chi3L3	Eos	ECP		Chi3L3	Eos	ECP		Chi3L3	Eos	ECP	
				LM	TEM			LM	TEM			LM	TEM
CNTSmall	0	-	1	-	No	-	2.4	-	No	-	0.6	0/6	No
	18	2.0	**17.2**	0/1	-	1.4	**69.2**	0/2	-	1.0	0.5	2/6	No
	54	1.0	1.4	0/1	-	0.5	**72.2**	0/2	-	0.9	0.2	1/6	No
	162	1.0	3.4	0/1	No	0.7	7.1	0/2	No	1.7	0.0	3/6	No
CNTLarge	0	-	1	-	-	-	5.3	-	-	-	20.4	1/6	-
	18	**2.8**	**50.6**	**-**	-	**5.8**	**317.3**	0/2	-	1.8	33.5	6/6	No
	54	**3.1**	**86.2**	**-**	-	**4.3**	**138.3**	1/2	-	2.5	32.3	5/6	Yes
	162	1.1	1.7	-	No	1.1	1.8	0/2	No	**9.2**	46.3	4/6	Yes
Mitsui7	0	-	0.3	-	-	-	0.4	-	-	-	0.3	1/6	No
	18	**-**	**38.8**	**-**	-	-	**341.3**	0/2	-	-	5.5	6/6	-
	54	**-**	**23.1**	**-**	-	-	**268.0**	0/2	-	**-**	**21.7**	6/6	Yes
	162	**-**	**2.2**	**-**	No	-	100.9	0/2	Yes	-	**45.5**	6/6	Yes
Carbon Black (Printex 90)	18	-	-	-	-	-	-	-	-	-	-	1/6	
	54	-	-	-	-	-	-	-	-	-	-	1/6	
	162	-	-	-	-	-	-	-	-	-	-	0/5	
SWCNT1 (Thomas Swan)	18	-	-	-	-	-	-	-	-	-	-	2/6	
	54	-	-	-	-	-	-	-	-	-	-	3/3	
	162	-	-	-	-	-	-	-	-	-	-	4/6	
SWCNT2 (Sigma Long)	18	-	-	-	-	-	-	-	-	-	-	5/6	
	54	-	-	-	-	-	-	-	-	-	-	3/6	
	162	-	-	-	-	-	-	-	-	-	-	3/6	

Overview of the *Chi3L3* level, eosinophil count (Eos) and the samples where ECP crystal has been observed visually in BAL cells with light microscopy (LM) and in lung sections with TEM. Dash (-) denotes samples where there is no relevant data or which have not been investigated, while bold text highlights statistically significant data ($p<0.05$).

Thomas Swan and Sigma Long BAL cell slides were acquired from a previous study: Saber AT, Lamson JS, Jacobsen NR, et al. (2013) Particle-Induced Pulmonary Acute Phase Response Correlates with Neutrophil Influx Linking Inhaled Particles and Cardiovascular Risk. PLoS ONE 8:e69020. doi: 10.1371/journal.pone.0069020

CCL11 and CCL24

CCL11 and CCL24 expression is given as the relative fold-increase in mRNA levels relative to concurrent controls, where values below 1 indicate a decreased mRNA level. Statistically significant changes ($p<0.05$) are marked with an asterix (*).

Mitsui-7			
CCL11			
	18 μg	**54 μg**	**162 μg**
Day 1	3.0*	5.2*	3.4*
Day 3	-	-	-
Day 28	-	1.5	-
CCL24			
	18 μg	**54 μg**	**162 μg**
Day 1	10.7*	9.8*	2.7
Day 3	-	-	-
Day 28	-	1.6	-

CNT_{Small}			
CCL11			
	18 μg	**54 μg**	**162 μg**
Day 1	3.3	2.2	2.2
Day 3	1.2	2.9	7.1*
Day 28	1.6	1.0	2.6
CCL24			
	18 μg	**54 μg**	**162 μg**
Day 1	3.6	1.2	0.8
Day 3	1.2	2.3	8.5*
Day 28	0.7	1.1	0.8

CNT_{Large}			
CCL11			
	18 μg	**54 μg**	**162 μg**
Day 1	5.6*	9.3*	4.3*
Day 3	5.4*	7.4*	3.9*
Day 28	1.5	1.5	3.6
CCL24			
	18 μg	**54 μg**	**162 μg**
Day 1	6.1	20.6	2.3
Day 3	11.7*	21.5*	4.6*
Day 28	0.9	0.8	2.4

Appendix F

Other projects

FIB-SEM of cells on CNT substrates

In preparation for the planned study of CNTs in tissue, FIB-SEM experiments were carried out on cells grown on vertically grown CNT substrates [19]. Work was carried out in collaboration with Arto Heiskanen Senior researcher at DTU Nanotech, then bachelor student Sigurd Friis Truelsen and Ph.D. student Rafał Wierzbicki. The intended purpose of the substrates was to use the CNTs as electrodes for intracellular cell measurements. Therefore, Sigurd worked on fabricating devices with well-defined CNTs grown at specific locations such that signal from each CNT could be individually measured. In the process, he also fabricated chips with areas of randomly placed CNTs in order to optimise fabrication conditions.

NIH3T3 fibroblast were grown on a selection of the samples, and processed for FIB-SEM as described in Paper I and Paper VI. Unfortunately, cells were grown beyond confluence and did not adhere well to the substrate, as a result the FIB-SEM images show cells which are not in direct contact with the CNTs (Illustration 7.8). The FIB-SEM is however able to resolve the CNTs with its catalytic particle and the carbon nanostructure itself.

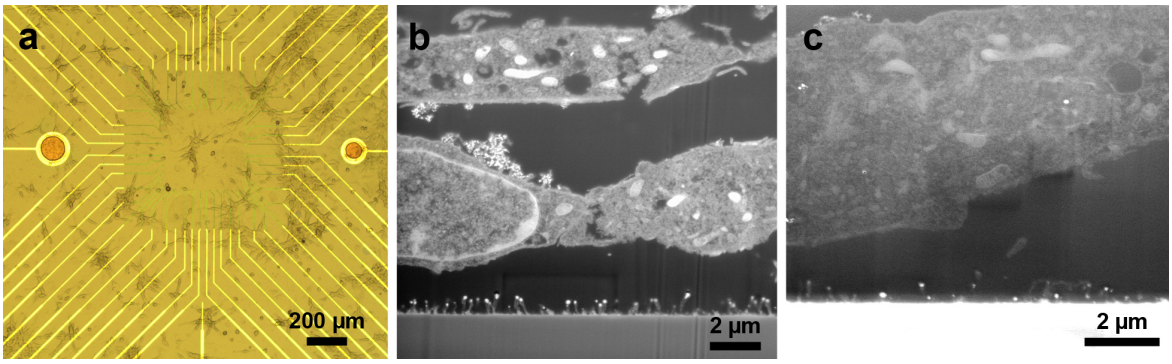

Illustration 7.8: A) Light micrograph of cells grown on the chip, showing the electrode design in the centre. B) Backscatter FIB-SEM image of cells near the CNT substrate, where the catalyst used for CNT growth is easily observable. C) SE FIB-SEM image of a cell hovering over CNTs where there is limited contrast.

In response to the issues, Arto worked on developing a protocol for ensuring proper adherence for a more relevant cell-line, and Sigurd developed the fabrication scheme. Unfortunately, this took longer than expected so we did not manage to perform more FIB-SEM experiments.

Gold nanoparticle uptake in Daphnia magna

In collaboration with Ph.D. students Lars M. Skjolding, Sara N. Sørensen and Professor Anders Baun from DTU Environment and Ph.D. student Amalie Thit from Roskilde University, we used EM to investigate gold nanoparticle uptake in Daphnia magna (Illustration 7.9).

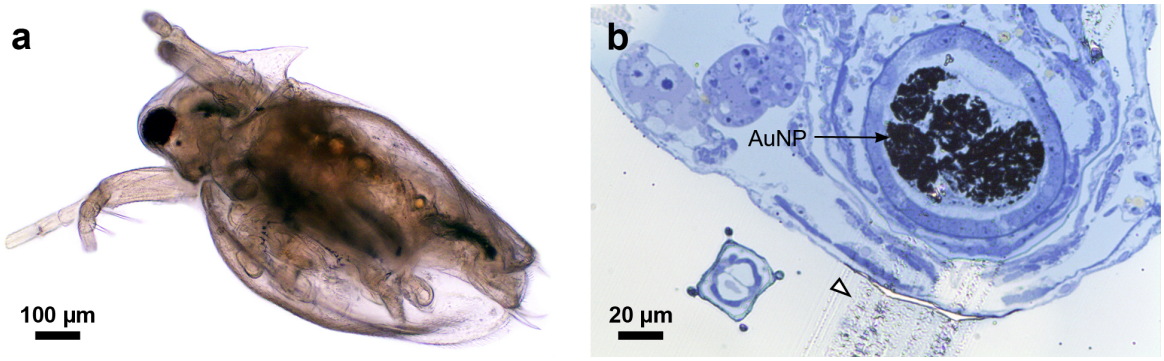

Illustration 7.9: A) LM of a whole Daphnia magna. B) LM micrograph of a thin section where the gold nanoparticles can be seen in the gut of the daphnia. The nanoparticles have given rise to extensive ultramicrotomy artefacts (arrowhead).

The purpose was to study the uptake and internalisation of gold nanoparticles in the Daphnia using electron microscopy, and study how feeding would influence the nanoparticle uptake. The gold particles were found in both the TEM and FIB-SEM images in the gut of the Daphnia (Illustration 7.10).

The particles appeared able to cross the peritrophic membrane[15] and interact with the microvili of the cells lining the gut (Illustration 7.10 a). TEM also revealed that some nanoparticles even appeared to have been internalised by gut cells (Illustration 7.10 b). Unfortunately, as discussed in Chapter 4 the nanoparticles apparently inside cells may be a sectioning artefact, and rather be caused by a dislocation and relocation of particles during ultramicrotomy. FIB-SEM was used to verify that nanoparticles were in fact inside the cells, but the limited volume investigated showed no nanoparticles inside gut cells, although they readily were distinguished interacting with microvili (Illustration 7.10 **c**). FIB-SEM was not able to resolve the nanoparticles, but the backscatter detector installed on the FEI Helios system may be able to provide sufficient resolution images.

The project is still in progress and they are currently working on verifying the presence of nanoparticles using EDS, and also verifying that the intracellular particles observed were not due to an embedding artefact using a variety of different embedding protocols. Additionally, further 3D FIB-SEM using the backscatter detector installed on the FEI Helios system may be able to provide higher resolution images, and be able to reveal whether the nanoparticles were in fact inside cells. Alternatively, one could experiment with thicker sections and sample tilting to determine if the nanoparticles are inside the ultrasection.

15 It is a barrier between the lumen and the cells lining the gut.

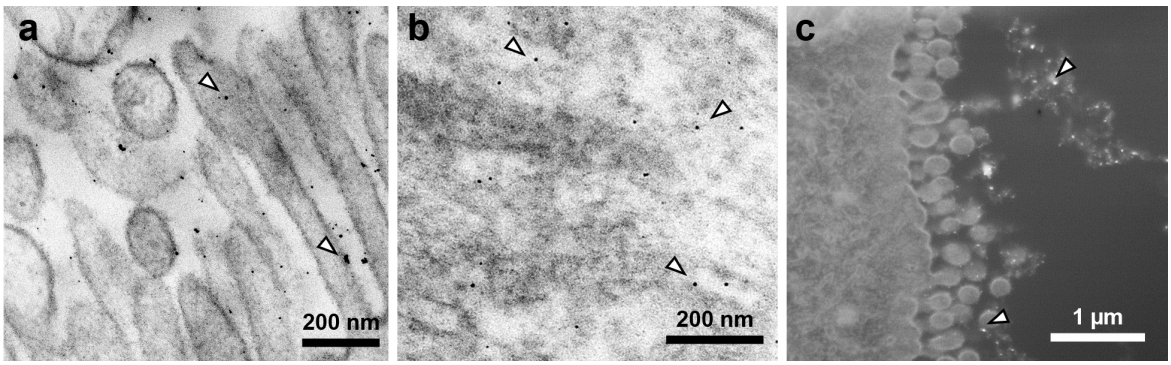

Illustration 7.10: A) TEM image of the nanoparticles interacting with the microvilli. B) TEM image of nanoparticles apparently taken up by the cell. C) FIB-SEM image of gold nanoparticles interacting with the microvilli of the cells lining the gut.

Miscellaneous SEM

Throughout my project I have also been involved in various small projects seeking to test the usability of the SEM.

The adherence of probiotics to mammalian cells where investigated together with the two projects students Mads Olsen, Josephine Licht and Ph.D. student Hasan U. Çelebioglu from DTU Biosys (Illustration 7.11 a). SEM of intestinal cells (Caco-2) growth on porous membrane structures (Illustration 7.11 b), together with Ph.D. student Hsih-Yin Tan from DTU Nanotech. Together with Daniel Höglund and Leifeng Chen from DTU Biosustain, graphene coatings on carbon fibre material used for cellular growth were investigated (Illustration 7.11 c).

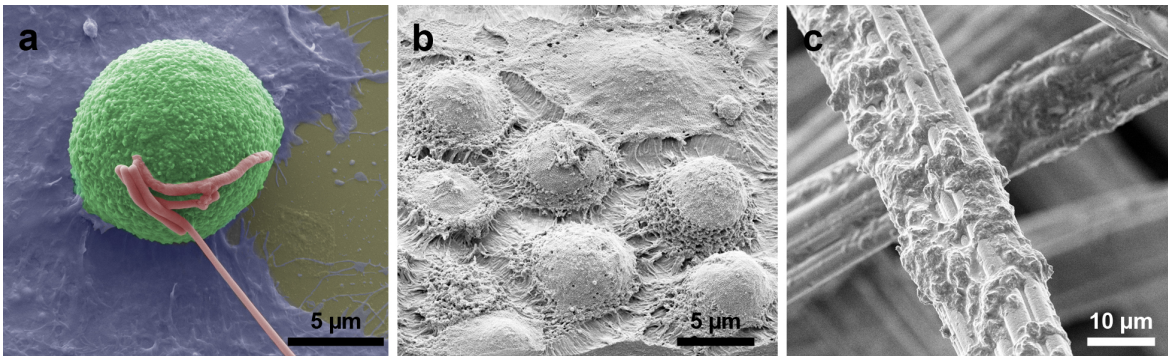

Illustration 7.11: A) Probiotic bacteria (red) adhering to HT-29 cell (green). B) SEM of Caco-2 cells cultured on perforated membrane (not visible). C) Graphene coating on carbon fibre.

Nanoparticle characterisation and detection in meat

Methods for characterising and detection of silver nanoparticles (AgNP) in meat were tested in collaboration with DTU Food and the department of Environmental Geosciences, University of Vienna. The nanoparticles in meat where mainly characterised using asymmetric flow-field flow fractionation (AF^4) by Katrin Loeschner and Jana Navratilova. We supplied TEM imaging of the particle distributions, where the number-based size distribution of the AgNP (Illustration 7.12). Along with inductively coupled plasma mass spectrometry (ICP-MS), the TEM size distribution were able to verify that the particle sizes did not change when observed in the enzymatically digested meat. Rather the AF^4 measurements were influenced by the presence of digested meat. More information can be found in **Paper VII and X**.

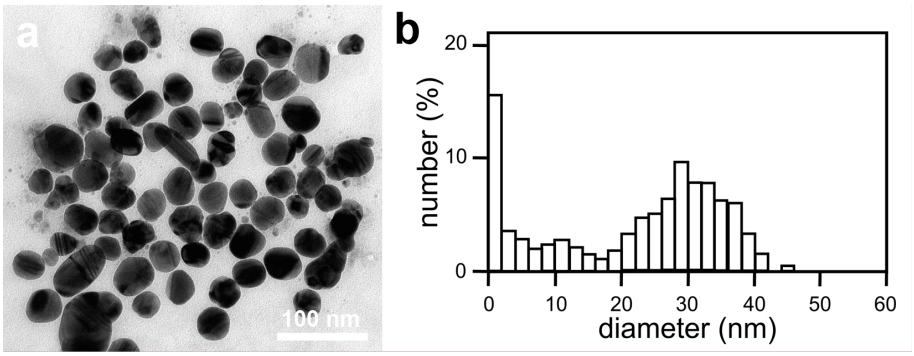

Illustration 7.12: A) TEM micrograph of silver nanoparticles. B) Size distribution of nanoparticles determined by TEM imaging.

Bibliography

[1] M. Kwiat, S. Cohen, A. Pevzner, and F. Patolsky, "Large-scale ordered 1D-nanomaterials arrays: Assembly or not?," *Nano Today*, vol. 8, no. 6, pp. 677–694, Dec. 2013.

[2] A. I. Hochbaum and P. Yang, "Semiconductor Nanowires for Energy Conversion," *Chemical Reviews*, vol. 110, no. 1, pp. 527–546, Jan. 2010.

[3] S. R. Gowda, A. Leela Mohana Reddy, X. Zhan, and P. M. Ajayan, "Building Energy Storage Device on a Single Nanowire," *Nano Letters*, vol. 11, no. 8, pp. 3329–3333, Aug. 2011.

[4] R. M. Penner, "Chemical Sensing with Nanowires," *Annual Review of Analytical Chemistry*, vol. 5, no. 1, pp. 461–485, Jul. 2012.

[5] J. T. Robinson, M. Jorgolli, and H. Park, "Nanowire electrodes for high-density stimulation and measurement of neural circuits," *Frontiers in Neural Circuits*, vol. 7, 2013.

[6] C. M. Lieber, "Semiconductor nanowires: A platform for nanoscience and nanotechnology," *MRS Bulletin*, vol. 36, no. 12, pp. 1052–1063, Dec. 2011.

[7] D. B. Suyatin, L. Wallman, J. Thelin, C. N. Prinz, H. Jörntell, L. Samuelson, L. Montelius, and J. Schouenborg, "Nanowire-Based Electrode for Acute In Vivo Neural Recordings in the Brain," *PLoS ONE*, vol. 8, no. 2, p. e56673, Feb. 2013.

[8] A. K. Shalek, J. T. Robinson, E. S. Karp, J. S. Lee, D.-R. Ahn, M.-H. Yoon, A. Sutton, M. Jorgolli, R. S. Gertner, T. S. Gujral, G. MacBeath, E. G. Yang, and H. Park, "Vertical silicon nanowires as a universal platform for delivering biomolecules into living cells," *Proceedings of the National Academy of Sciences*, vol. 107, no. 5, pp. 1870–1875, Jan. 2010.

[9] Y. Wang, Y. Yang, L. Yan, S. Y. Kwok, W. Li, Z. Wang, X. Zhu, G. Zhu, W. Zhang, X. Chen, and P. Shi, "Poking cells for efficient vector-free intracellular delivery," *Nature Communications*, vol. 5, Jul. 2014.

[10] X. Xie, A. M. Xu, S. Leal-Ortiz, Y. Cao, C. C. Garner, and N. A. Melosh, "Nanostraw–Electroporation System for Highly Efficient Intracellular Delivery and Transfection," *ACS Nano*, vol. 7, no. 5, pp. 4351–4358, May 2013.

[11] I. Ilie, R. Ilie, T. Mocan, D. Bartos, and L. Mocan, "Influence of nanomaterials on stem cell differentiation: designing an appropriate nanobiointerface," *International Journal of Nanomedicine*, p. 2211, Apr. 2012.

[12] H. N. Kim, A. Jiao, N. S. Hwang, M. S. Kim, D. H. Kang, D.-H. Kim, and K.-Y. Suh, "Nanotopography-guided tissue engineering and regenerative medicine," *Advanced Drug Delivery Reviews*, vol. 65, no. 4, pp. 536–558, Apr. 2013.

[13] J. M. Łopacińska, C. Grădinaru, R. Wierzbicki, C. Købler, M. S. Schmidt, M. T. Madsen, M. Skolimowski, M. Dufva, H. Flyvbjerg, and K. Mølhave, "Cell motility, morphology, viability and proliferation in response to nanotopography on silicon black," *Nanoscale*, vol. 4, no. 12, p. 3739, 2012.

[14] H. Persson, C. Købler, K. Mølhave, L. Samuelson, J. O. Tegenfeldt, S. Oredsson, and C. N. Prinz, "Fibroblasts Cultured on Nanowires Exhibit Low Motility, Impaired Cell Division, and DNA Damage," *Small*, vol. 9, no. 23, pp. 4006–4016, Jun. 2013.

[15] E. K. F. Yim, S. W. Pang, and K. W. Leong, "Synthetic nanostructures inducing differentiation of human mesenchymal stem cells into neuronal lineage," *Experimental Cell Research*, vol. 313, no. 9, pp. 1820–1829, May 2007.

[16] R. S. Wagner and W. C. Ellis, "Vapor-liquid-solid mechanism of single crystal growth," *Applied Physics Letters*, vol. 4, no. 5, p. 89, 1964.

[17] H. Jansen, M. de Boer, R. Legtenberg, and M. Elwenspoek, "The black silicon method: a universal method for determining the parameter setting of a fluorine-based reactive ion etcher in deep silicon trench etching with profile control," *Journal of Micromechanics and Microengineering*, vol. 5, no. 2, pp. 115–120, Jun. 1995.

[18] R. Legtenberg, "Anisotropic Reactive Ion Etching of Silicon Using SF6/O2/CHF3 Gas Mixtures," *Journal of The Electrochemical Society*, vol. 142, no. 6, p. 2020, 1995.

[19] R. D. Wierzbicki, "PhD thesis: Nanostructured micro-electrode arrays for electrophysiological measurements," Department of Micro- and Nanotechnology, Technical University of Denmark, PhD thesis, 2013.

[20] M. Monthioux and V. L. Kuznetsov, "Who should be given the credit for the discovery of carbon

nanotubes?," *Carbon*, vol. 44, no. 9, pp. 1621–1623, Aug. 2006.
[21] M. F. L. De Volder, S. H. Tawfick, R. H. Baughman, and A. J. Hart, "Carbon Nanotubes: Present and Future Commercial Applications," *Science*, vol. 339, no. 6119, pp. 535–539, Jan. 2013.
[22] A. P. Graham, G. S. Duesberg, W. Hoenlein, F. Kreupl, M. Liebau, R. Martin, B. Rajasekharan, W. Pamler, R. Seidel, W. Steinhoegl, and E. Unger, "How do carbon nanotubes fit into the semiconductor roadmap?," *Applied Physics A*, vol. 80, no. 6, pp. 1141–1151, Mar. 2005.
[23] M. D. Lima, N. Li, M. Jung de Andrade, S. Fang, J. Oh, G. M. Spinks, M. E. Kozlov, C. S. Haines, D. Suh, J. Foroughi, S. J. Kim, Y. Chen, T. Ware, M. K. Shin, L. D. Machado, A. F. Fonseca, J. D. W. Madden, W. E. Voit, D. S. Galvao, and R. H. Baughman, "Electrically, Chemically, and Photonically Powered Torsional and Tensile Actuation of Hybrid Carbon Nanotube Yarn Muscles," *Science*, vol. 338, no. 6109, pp. 928–932, Nov. 2012.
[24] N. Saito, H. Haniu, Y. Usui, K. Aoki, K. Hara, S. Takanashi, M. Shimizu, N. Narita, M. Okamoto, S. Kobayashi, H. Nomura, H. Kato, N. Nishimura, S. Taruta, and M. Endo, "Safe Clinical Use of Carbon Nanotubes as Innovative Biomaterials," *Chemical Reviews*, vol. 114, no. 11, pp. 6040–6079, Jun. 2014.
[25] F. H. Gojny, M. H. G. Wichmann, U. Köpke, B. Fiedler, and K. Schulte, "Carbon nanotube-reinforced epoxy-composites: enhanced stiffness and fracture toughness at low nanotube content," *Composites Science and Technology*, vol. 64, no. 15, pp. 2363–2371, Nov. 2004.
[26] M. Kumar and Y. Ando, "Chemical Vapor Deposition of Carbon Nanotubes: A Review on Growth Mechanism and Mass Production," *Journal of Nanoscience and Nanotechnology*, vol. 10, no. 6, pp. 3739–3758, Jun. 2010.
[27] T. Gebel, R. Marchan, and J. G. Hengstler, "The nanotoxicology revolution," *Archives of Toxicology*, vol. 87, no. 12, pp. 2057–2062, Nov. 2013.
[28] J. Ferin, G. Oberdörster, D. . Penney, S. . Soderholm, R. Gelein, and H. . Piper, "Increased pulmonary toxicity of ultrafine particles? I. Particle clearance, translocation, morphology," *Journal of Aerosol Science*, vol. 21, no. 3, pp. 381–384, Jan. 1990.
[29] G. Oberdörster, J. Ferin, G. Finkelstein, P. Wade, and N. Corson, "Increased pulmonary toxicity of ultrafine particles? II. Lung lavage studies," *Journal of Aerosol Science*, vol. 21, no. 3, pp. 384–387, Jan. 1990.
[30] D. Brown, "Size-Dependent Proinflammatory Effects of Ultrafine Polystyrene Particles: A Role for Surface Area and Oxidative Stress in the Enhanced Activity of Ultrafines," *Toxicology and Applied Pharmacology*, vol. 175, pp. 191–199, Sep. 2001.
[31] C. Johnston, "Pulmonary Effects Induced by Ultrafine PTFE Particles," *Toxicology and Applied Pharmacology*, vol. 168, no. 3, pp. 208–215, Nov. 2000.
[32] G. Oberdörster, "Pulmonary effects of inhaled ultrafine particles," *International Archives of Occupational and Environmental Health*, vol. 74, pp. 1–8, Nov. 2000.
[33] G. Oberdörster, V. Stone, and K. Donaldson, "Toxicology of nanoparticles: A historical perspective," *Nanotoxicology*, vol. 1, no. 1, pp. 2–25, Jan. 2007.
[34] K. Donaldson and C. A. Poland, "Nanotoxicity: challenging the myth of nano-specific toxicity," *Current Opinion in Biotechnology*, vol. 24, no. 4, pp. 724–734, Aug. 2013.
[35] L. Ma-Hock, S. Treumann, V. Strauss, S. Brill, F. Luizi, M. Mertler, K. Wiench, A. O. Gamer, B. van Ravenzwaay, and R. Landsiedel, "Inhalation Toxicity of Multiwall Carbon Nanotubes in Rats Exposed for 3 Months," *Toxicological Sciences*, vol. 112, no. 2, pp. 468–481, Jul. 2009.
[36] NIOSH, "Current Intelligence Bulletin 65: Occupational Exposure to Carbon Nanotubes and Nanofibers," Apr-2013. [Online]. Available: Available at www.cdc.gov/niosh/. [Accessed: 27-Aug-2013].
[37] J. Pauluhn, "Subchronic 13-Week Inhalation Exposure of Rats to Multiwalled Carbon Nanotubes: Toxic Effects Are Determined by Density of Agglomerate Structures, Not Fibrillar Structures," *Toxicological Sciences*, vol. 113, no. 1, pp. 226–242, Oct. 2009.
[38] K. Donaldson, F. A. Murphy, R. Duffin, and C. A. Poland, "Asbestos, carbon nanotubes and the pleural mesothelium: a review and the hypothesis regarding the role of long fibre retention in the parietal pleura, inflammation and mesothelioma," *Part Fibre Toxicol*, vol. 7, no. 1, p. 5, 2010.
[39] C. A. Poland, R. Duffin, I. Kinloch, A. Maynard, W. A. H. Wallace, A. Seaton, V. Stone, S. Brown, W. MacNee, and K. Donaldson, "Carbon nanotubes introduced into the abdominal cavity of mice show asbestos-like pathogenicity in a pilot study," *Nature Nanotech*, vol. 3, no. 7, pp. 423–428, May 2008.
[40] M. H. Ross, *Histology: a text and atlas: with correlated cell and molecular biology*, 6th ed. Philadelphia: Wolters Kluwer/Lippincott Williams & Wilkins Health, 2011.

[41] B. Czarny, D. Georgin, F. Berthon, G. Plastow, M. Pinault, G. Patriarche, A. Thuleau, M. M. L'Hermite, F. Taran, and V. Dive, "Carbon Nanotube Translocation to Distant Organs after Pulmonary Exposure: Insights from *in Situ* ^{14} C-Radiolabeling and Tissue Radioimaging," *ACS Nano*, vol. 8, no. 6, pp. 5715–5724, Jun. 2014.

[42] D. Shier, *Hole's essentials of human anatomy & physiology*, 10th ed. Boston: McGraw-Hill Higher Education, 2009.

[43] T. Hartung and E. Sabbioni, "Alternative in vitro assays in nanomaterial toxicology," *Wiley Interdisciplinary Reviews: Nanomedicine and Nanobiotechnology*, vol. 3, no. 6, pp. 545–573, Nov. 2011.

[44] V. Castranova, P. A. Schulte, and R. D. Zumwalde, "Occupational Nanosafety Considerations for Carbon Nanotubes and Carbon Nanofibers," *Accounts of Chemical Research*, vol. 46, no. 3, pp. 642–649, Mar. 2013.

[45] J. S. Brown, K. L. Zeman, and W. D. Bennett, "Ultrafine Particle Deposition and Clearance in the Healthy and Obstructed Lung," *American Journal of Respiratory and Critical Care Medicine*, vol. 166, no. 9, pp. 1240–1247, Nov. 2002.

[46] D. Warheit, "Inhalation of High Concentrations of Low Toxicity Dusts in Rats Results in Impaired Pulmonary Clearance Mechanisms and Persistent Inflammation," *Toxicology and Applied Pharmacology*, vol. 145, no. 1, pp. 10–22, Jul. 1997.

[47] S. Clarke and D. Pavia, "Lung mucus production and mucociliary clearance: methods of assessment.," *British Journal of Clinical Pharmacology*, vol. 9, no. 6, pp. 537–546, Jun. 1980.

[48] L. Schermelleh, R. Heintzmann, and H. Leonhardt, "A guide to super-resolution fluorescence microscopy," *The Journal of Cell Biology*, vol. 190, no. 2, pp. 165–175, Jul. 2010.

[49] K. Adolfsson, H. Persson, J. Wallentin, S. Oredsson, L. Samuelson, J. O. Tegenfeldt, M. T. Borgström, and C. N. Prinz, "Fluorescent Nanowire Heterostructures as a Versatile Tool for Biology Applications," *Nano Letters*, vol. 13, no. 10, pp. 4728–4732, Oct. 2013.

[50] T. Berthing, S. Bonde, K. R. Rostgaard, M. H. Madsen, C. B. Sørensen, J. Nygård, and K. L. Martinez, "Cell membrane conformation at vertical nanowire array interface revealed by fluorescence imaging," *Nanotechnology*, vol. 23, no. 41, p. 415102, Oct. 2012.

[51] R. Fiolka, L. Shao, E. H. Rego, M. W. Davidson, and M. G. L. Gustafsson, "Time-lapse two-color 3D imaging of live cells with doubled resolution using structured illumination," *Proceedings of the National Academy of Sciences*, vol. 109, no. 14, pp. 5311–5315, Apr. 2012.

[52] G. Schneider, P. Guttmann, S. Heim, S. Rehbein, F. Mueller, K. Nagashima, J. B. Heymann, W. G. Müller, and J. G. McNally, "Three-dimensional cellular ultrastructure resolved by X-ray microscopy," *Nat Meth*, vol. 7, no. 12, pp. 985–987, Nov. 2010.

[53] Y. Zhu, X. Cai, J. Li, Z. Zhong, Q. Huang, and C. Fan, "Synchrotron-based X-ray microscopic studies for bioeffects of nanomaterials," *Nanomedicine: Nanotechnology, Biology and Medicine*, vol. 10, no. 3, pp. 515–524, Apr. 2014.

[54] D. Williams and C. B. Carter, *Transmission electron microscopy: a textbook for materials science*, 2nd ed. New York: Springer, 2009.

[55] W. Denk, K. L. Briggman, and M. Helmstaedter, "Structural neurobiology: missing link to a mechanistic understanding of neural computation," *Nature Reviews Neuroscience*, Feb. 2012.

[56] A. E. Yakushevska, M. N. Lebbink, W. J. C. Geerts, L. Spek, E. G. van Donselaar, K. A. Jansen, B. M. Humbel, J. A. Post, A. J. Verkleij, and A. J. Koster, "STEM tomography in cell biology," *Journal of Structural Biology*, vol. 159, no. 3, pp. 381–391, Sep. 2007.

[57] A. E. Porter, M. Gass, K. Muller, J. N. Skepper, P. A. Midgley, and M. Welland, "Direct imaging of single-walled carbon nanotubes in cells," *Nature Nanotechnology*, vol. 2, no. 11, pp. 713–717, Oct. 2007.

[58] G. D. Danilatos, "Environmental scanning electron microscopy and microanalysis," *Mikrochim Acta*, vol. 114–115, no. 1, pp. 143–155, Dec. 1994.

[59] A. A. Tseng, "Recent developments in micromilling using focused ion beam technology," *J. Micromech. Microeng.*, vol. 14, no. 4, pp. R15–R34, Apr. 2004.

[60] K. P. Arkill, K. Qvortrup, T. Starborg, J. M. Mantell, C. Knupp, C. Michel, S. J. Harper, A. H. Salmon, J. M. Squire, D. O. Bates, and C. R. Neal, "Resolution of the three dimensional structure of components of the glomerular filtration barrier," *BMC Nephrology*, vol. 15, no. 1, p. 24, 2014.

[61] A. J. Bushby, K. M. Y. P'ng, R. D. Young, C. Pinali, C. Knupp, and A. J. Quantock, "Imaging three-dimensional tissue architectures by focused ion beam scanning electron microscopy," *Nat Protoc*, vol. 6, no. 6, pp. 845–858, May 2011.

[62] R. L. Felts, K. Narayan, J. D. Estes, D. Shi, C. M. Trubey, J. Fu, L. M. Hartnell, G. T. Ruthel, D. K.

Schneider, K. Nagashima, J. W. Bess, S. Bavari, B. C. Lowekamp, D. Bliss, J. D. Lifson, and S. Subramaniam, “From the Cover: 3D visualization of HIV transfer at the virological synapse between dendritic cells and T cells,” *Proceedings of the National Academy of Sciences*, vol. 107, pp. 13336–13341, Jul. 2010.

[63] D. A. M. D. Winter, C. T. W. M. Schneijdenberg, M. N. Lebbink, B. Lich, A. J. Verkleij, M. R. Drury, and B. M. Humbel, “Tomography of insulating biological and geological materials using focused ion beam (FIB) sectioning and low-kV BSE imaging,” *Journal of Microscopy*, vol. 233, no. 3, pp. 372–383, Mar. 2009.

[64] N. Jiménez, E. G. Van Donselaar, D. A. M. De Winter, K. Vocking, A. J. Verkleij, and J. A. Post, “Gridded Aclar: preparation methods and use for correlative light and electron microscopy of cell monolayers, by TEM and FIB-SEM,” *Journal of Microscopy*, vol. 237, no. 2, pp. 208–220, Feb. 2010.

[65] G. Knott, H. Marchman, D. Wall, and B. Lich, “Serial Section Scanning Electron Microscopy of Adult Brain Tissue Using Focused Ion Beam Milling,” *Journal of Neuroscience*, vol. 28, no. 12, pp. 2959–2964, Mar. 2008.

[66] R. Wierzbicki, C. Købler, M. R. B. Jensen, J. Łopacińska, M. S. Schmidt, M. Skolimowski, F. Abeille, K. Qvortrup, and K. Mølhave, “Mapping the Complex Morphology of Cell Interactions with Nanowire Substrates Using FIB-SEM,” *PLoS ONE*, vol. 8, no. 1, p. e53307, Jan. 2013.

[67] J. T. Robinson, M. Jorgolli, A. K. Shalek, M.-H. Yoon, R. S. Gertner, and H. Park, “Vertical nanowire electrode arrays as a scalable platform for intracellular interfacing to neuronal circuits,” *Nature Nanotechnology*, vol. 7, no. 3, pp. 180–184, Jan. 2012.

[68] D. Drobne, M. Milani, A. Zrimec, V. Leser, and M. Berden Zrimec, “Electron and ion imaging of gland cells using the FIB/SEM system,” *Journal of Microscopy*, vol. 219, no. 1, pp. 29–35, Jul. 2005.

[69] P. Papareddy, V. Rydengård, M. Pasupuleti, B. Walse, M. Mörgelin, A. Chalupka, M. Malmsten, and A. Schmidtchen, “Proteolysis of Human Thrombin Generates Novel Host Defense Peptides,” *PLoS Pathogens*, vol. 6, no. 4, p. e1000857, Apr. 2010.

[70] D. Brüggemann, B. Wolfrum, V. Maybeck, Y. Mourzina, M. Jansen, and A. Offenhäusser, “Nanostructured gold microelectrodes for extracellular recording from electrogenic cells,” *Nanotechnology*, vol. 22, no. 26, p. 265104, Jul. 2011.

[71] A. Friedmann, A. Hoess, A. Cismak, and A. Heilmann, “Investigation of cell–substrate interactions by focused ion beam preparation and scanning electron microscopy,” *Acta Biomaterialia*, vol. 7, no. 6, pp. 2499–2507, Jun. 2011.

[72] M. A. Hayat, *Principles and techniques of electron microscopy: biological applications*, 4th ed. Cambridge, UK ; New York: Cambridge University Press, 2000.

[73] J. A. Kiernan, “Formaldehyde, formalin, paraformaldehyde and glutaraldehyde: What they are and what they do,” *Microscopy Today*, vol. 00–1, pp. 8–12, 2000.

[74] V. Lešer, D. Drobne, ž. Pipan, M. Milani, and F. Tatti, “Comparison of different preparation methods of biological samples for FIB milling and SEM investigation,” *Journal of Microscopy*, vol. 233, no. 2, pp. 309–319, Feb. 2009.

[75] J. Kuo, *Electron microscopy: methods and protocols.*, 2nd ed. /. Totowa N.J.: Humana Press, 2007.

[76] P. C. Hawes, C. L. Netherton, T. E. Wileman, and P. Monaghan, “The Envelope of Intracellular African Swine Fever Virus Is Composed of a Single Lipid Bilayer,” *Journal of Virology*, vol. 82, no. 16, pp. 7905–7912, Aug. 2008.

[77] D. Vanhecke, G. Herrmann, W. Graber, T. Hillmann-Marti, C. Mühlfeld, D. Studer, and M. Ochs, “Lamellar body ultrastructure revisited: high-pressure freezing and cryo-electron microscopy of vitreous sections,” *Histochemistry and Cell Biology*, vol. 134, no. 4, pp. 319–326, Oct. 2010.

[78] A. Schertel, N. Snaidero, H.-M. Han, T. Ruhwedel, M. Laue, M. Grabenbauer, and W. Möbius, “Cryo FIB-SEM: Volume imaging of cellular ultrastructure in native frozen specimens,” *Journal of Structural Biology*, vol. 184, no. 2, pp. 355–360, Nov. 2013.

[79] C. Hsieh, T. Schmelzer, G. Kishchenko, T. Wagenknecht, and M. Marko, “Practical workflow for cryo focused-ion-beam milling of tissues and cells for cryo-TEM tomography,” *Journal of Structural Biology*, vol. 185, no. 1, pp. 32–41, Jan. 2014.

[80] E. Villa, M. Schaffer, J. M. Plitzko, and W. Baumeister, “Opening windows into the cell: focused-ion-beam milling for cryo-electron tomography,” *Current Opinion in Structural Biology*, vol. 23, no. 5, pp. 771–777, Oct. 2013.

[81] S. Turner, “Cell attachment on silicon nanostructures,” *Journal of Vacuum Science & Technology B: Microelectronics and Nanometer Structures*, vol. 15, no. 6, p. 2848, Nov. 1997.

[82] W. Chen, L. G. Villa-Diaz, Y. Sun, S. Weng, J. K. Kim, R. H. W. Lam, L. Han, R. Fan, P. H.

Krebsbach, and J. Fu, "Nanotopography Influences Adhesion, Spreading, and Self-Renewal of Human Embryonic Stem Cells," *ACS Nano*, vol. 6, no. 5, pp. 4094–4103, May 2012.

[83] C. Xie, L. Hanson, W. Xie, Z. Lin, B. Cui, and Y. Cui, "Noninvasive Neuron Pinning with Nanopillar Arrays," *Nano Letters*, vol. 10, no. 10, pp. 4020–4024, Oct. 2010.

[84] G. Piret, M.-T. Perez, and C. N. Prinz, "Neurite outgrowth and synaptophysin expression of postnatal CNS neurons on GaP nanowire arrays in long-term retinal cell culture," *Biomaterials*, vol. 34, no. 4, pp. 875–887, Jan. 2013.

[85] C. Prinz, W. Hällström, T. Mårtensson, L. Samuelson, L. Montelius, and M. Kanje, "Axonal guidance on patterned free-standing nanowire surfaces," *Nanotechnology*, vol. 19, no. 34, p. 345101, Aug. 2008.

[86] X. Wang, C. A. Ohlin, Q. Lu, and J. Hu, "Cell directional migration and oriented division on three-dimensional laser-induced periodic surface structures on polystyrene," *Biomaterials*, vol. 29, no. 13, pp. 2049–2059, May 2008.

[87] S. Bonde, T. Berthing, M. H. Madsen, T. K. Andersen, N. Buch-Månson, L. Guo, X. Li, F. Badique, K. Anselme, J. Nygård, and K. L. Martinez, "Tuning InAs Nanowire Density for HEK293 Cell Viability, Adhesion, and Morphology: Perspectives for Nanowire-Based Biosensors," *ACS Applied Materials & Interfaces*, vol. 5, no. 21, pp. 10510–10519, Nov. 2013.

[88] W. Hällström, T. Mårtensson, C. Prinz, P. Gustavsson, L. Montelius, L. Samuelson, and M. Kanje, "Gallium Phosphide Nanowires as a Substrate for Cultured Neurons," *Nano Letters*, vol. 7, no. 10, pp. 2960–2965, Oct. 2007.

[89] S. Qi, C. Yi, S. Ji, C.-C. Fong, and M. Yang, "Cell Adhesion and Spreading Behavior on Vertically Aligned Silicon Nanowire Arrays," *ACS Applied Materials & Interfaces*, vol. 1, no. 1, pp. 30–34, Jan. 2009.

[90] S. Y. Kim and E. G. Yang, "Collective behaviors of mammalian cells on amine-coated silicon nanowires," *Nanotechnology*, vol. 24, no. 45, p. 455704, Nov. 2013.

[91] P. Kim, D. H. Kim, B. Kim, S. K. Choi, S. H. Lee, A. Khademhosseini, R. Langer, and K. Y. Suh, "Fabrication of nanostructures of polyethylene glycol for applications to protein adsorption and cell adhesion," *Nanotechnology*, vol. 16, no. 10, pp. 2420–2426, Oct. 2005.

[92] D.-J. Kim, J.-K. Seol, G. Lee, G.-S. Kim, and S.-K. Lee, "Cell adhesion and migration on nanopatterned substrates and their effects on cell-capture yield," *Nanotechnology*, vol. 23, no. 39, p. 395102, Oct. 2012.

[93] G. F. Bahr, G. Bloom, and U. Friberg, "Volume changes of tissues in physiological fluids during fixation in osmium tetroxide or formaldehyde and during subsequent treatment," *Experimental Cell Research*, vol. 12, no. 2, pp. 342–355, Aug. 1957.

[94] A. Boyde and E. MacOnnachie, "Volume changes during preparation of mouse embryonic tissue for scanning electron microscopy," *Scanning*, vol. 2, no. 3, pp. 149–163, 1979.

[95] Z. Li, J. Song, G. Mantini, M.-Y. Lu, H. Fang, C. Falconi, L.-J. Chen, and Z. L. Wang, "Quantifying the Traction Force of a Single Cell by Aligned Silicon Nanowire Array," *Nano Letters*, vol. 9, no. 10, pp. 3575–3580, Oct. 2009.

[96] N. Q. Balaban, U. S. Schwarz, D. Riveline, P. Goichberg, G. Tzur, I. Sabanay, D. Mahalu, S. Safran, A. Bershadsky, L. Addadi, and B. Geiger, "Force and focal adhesion assembly: a close relationship studied using elastic micropatterned substrates," *Nat. Cell Biol.*, vol. 3, no. 5, pp. 466–472, 2001.

[97] W. Hällström, M. Lexholm, D. B. Suyatin, G. Hammarin, D. Hessman, L. Samuelson, L. Montelius, M. Kanje, and C. N. Prinz, "Fifteen-Piconewton Force Detection from Neural Growth Cones Using Nanowire Arrays," *Nano Letters*, vol. 10, no. 3, pp. 782–787, Mar. 2010.

[98] J. L. Tan, J. Tien, D. M. Pirone, D. S. Gray, K. Bhadriraju, and C. S. Chen, "Cells lying on a bed of microneedles: An approach to isolate mechanical force," *Proceedings of the National Academy of Sciences*, vol. 100, no. 4, pp. 1484–1489, Jan. 2003.

[99] M. Ghibaudo, A. Saez, L. Trichet, A. Xayaphoummine, J. Browaeys, P. Silberzan, A. Buguin, and B. Ladoux, "Traction forces and rigidity sensing regulate cell functions," *Soft Matter*, vol. 4, no. 9, p. 1836, 2008.

[100] M. J. Dalby, M. O. Riehle, D. S. Sutherland, H. Agheli, and A. S. G. Curtis, "Changes in fibroblast morphology in response to nano-columns produced by colloidal lithography," *Biomaterials*, vol. 25, no. 23, pp. 5415–5422, Oct. 2004.

[101] M. A. Bucaro, Y. Vasquez, B. D. Hatton, and J. Aizenberg, "Fine-Tuning the Degree of Stem Cell Polarization and Alignment on Ordered Arrays of High-Aspect-Ratio Nanopillars," *ACS Nano*, vol. 6, no. 7, pp. 6222–6230, Jul. 2012.

[102] R. Elnathan, M. Kwiat, F. Patolsky, and N. H. Voelcker, "Engineering vertically aligned

semiconductor nanowire arrays for applications in the life sciences," *Nano Today*, vol. 9, no. 2, pp. 172–196, Apr. 2014.

[103] E. Peer, A. Artzy-Schnirman, L. Gepstein, and U. Sivan, "Hollow Nanoneedle Array and Its Utilization for Repeated Administration of Biomolecules to the Same Cells," *ACS Nano*, vol. 6, no. 6, pp. 4940–4946, Jun. 2012.

[104] A. K. Shalek, J. T. Gaublomme, L. Wang, N. Yosef, N. Chevrier, M. S. Andersen, J. T. Robinson, N. Pochet, D. Neuberg, R. S. Gertner, I. Amit, J. R. Brown, N. Hacohen, A. Regev, C. J. Wu, and H. Park, "Nanowire-Mediated Delivery Enables Functional Interrogation of Primary Immune Cells: Application to the Analysis of Chronic Lymphocytic Leukemia," *Nano Letters*, vol. 12, no. 12, pp. 6498–6504, Dec. 2012.

[105] A. Hai, A. Dormann, J. Shappir, S. Yitzchaik, C. Bartic, G. Borghs, J. P. M. Langedijk, and M. E. Spira, "Spine-shaped gold protrusions improve the adherence and electrical coupling of neurons with the surface of micro-electronic devices," *Journal of The Royal Society Interface*, vol. 6, no. 41, pp. 1153–1165, May 2009.

[106] W. Kim, J. K. Ng, M. E. Kunitake, B. R. Conklin, and P. Yang, "Interfacing Silicon Nanowires with Mammalian Cells," *Journal of the American Chemical Society*, vol. 129, pp. 7228–7229, Jun. 2007.

[107] I. Obataya, C. Nakamura, Han, N. Nakamura, and J. Miyake, "Nanoscale Operation of a Living Cell Using an Atomic Force Microscope with a Nanoneedle," *Nano Letters*, vol. 5, no. 1, pp. 27–30, Jan. 2005.

[108] A. Hai, J. Shappir, and M. E. Spira, "In-cell recordings by extracellular microelectrodes," *Nature Methods*, vol. 7, no. 3, pp. 200–202, Jan. 2010.

[109] A. M. Xu, A. Aalipour, S. Leal-Ortiz, A. H. Mekhdjian, X. Xie, A. R. Dunn, C. C. Garner, and N. A. Melosh, "Quantification of nanowire penetration into living cells," *Nature Communications*, vol. 5, Apr. 2014.

[110] L. Hanson, Z. C. Lin, C. Xie, Y. Cui, and B. Cui, "Characterization of the Cell–Nanopillar Interface by Transmission Electron Microscopy," *Nano Letters*, p. 121022094057009, Oct. 2012.

[111] X. Duan, R. Gao, P. Xie, T. Cohen-Karni, Q. Qing, H. S. Choe, B. Tian, X. Jiang, and C. M. Lieber, "Intracellular recordings of action potentials by an extracellular nanoscale field-effect transistor," *Nature Nanotechnology*, vol. 7, no. 3, pp. 174–179, Dec. 2011.

[112] T. E. McKnight, A. V. Melechko, G. D. Griffin, M. A. Guillorn, V. I. Merkulov, F. Serna, D. K. Hensley, M. J. Doktycz, D. H. Lowndes, and M. L. Simpson, "Intracellular integration of synthetic nanostructures with viable cells for controlled biochemical manipulation," *Nanotechnology*, vol. 14, no. 5, pp. 551–556, May 2003.

[113] A. G. Bittermann, C. Burkhardt, and H. Hall, "Imaging of Cell-to-Material Interfaces by SEM after in situ Focused Ion Beam Milling on Flat Surfaces and Complex 3D-Fibrous Structures," *Adv. Eng. Mater.*, vol. 11, no. 11, pp. B182–B188, Nov. 2009.

[114] C. Grădinaru, J. M. Łopacińska, J. Huth, H. A. Kestler, H. Flyvbjerg, and K. Molhave, "Assessment of Automated Analyses of Cell Migration on Flat and Nanostructured Surfaces," *Computational and Structural Biotechnology Journal*, vol. 1, no. 2, Jul. 2012.

[115] G. Cellot, E. Cilia, S. Cipollone, V. Rancic, A. Sucapane, S. Giordani, L. Gambazzi, H. Markram, M. Grandolfo, D. Scaini, F. Gelain, L. Casalis, M. Prato, M. Giugliano, and L. Ballerini, "Carbon nanotubes might improve neuronal performance by favouring electrical shortcuts," *Nature Nanotechnology*, vol. 4, no. 2, pp. 126–133, Dec. 2008.

[116] Z. Yu, T. E. McKnight, M. N. Ericson, A. V. Melechko, M. L. Simpson, and B. Morrison, "Vertically Aligned Carbon Nanofiber Arrays Record Electrophysiological Signals from Hippocampal Slices," *Nano Letters*, vol. 7, no. 8, pp. 2188–2195, Aug. 2007.

[117] T. Berthing, S. Bonde, C. B. Sørensen, P. Utko, J. Nygård, and K. L. Martinez, "Intact Mammalian Cell Function on Semiconductor Nanowire Arrays: New Perspectives for Cell-Based Biosensing," *Small*, vol. 7, no. 5, pp. 640–647, Mar. 2011.

[118] E. A. Vitol, Z. Orynbayeva, M. J. Bouchard, J. Azizkhan-Clifford, G. Friedman, and Y. Gogotsi, "In Situ Intracellular Spectroscopy with Surface Enhanced Raman Spectroscopy (SERS)-Enabled Nanopipettes," *ACS Nano*, vol. 3, no. 11, pp. 3529–3536, Nov. 2009.

[119] I. Canton and G. Battaglia, "Endocytosis at the nanoscale," *Chemical Society Reviews*, vol. 41, no. 7, p. 2718, 2012.

[120] G. J. Doherty and H. T. McMahon, "Mechanisms of Endocytosis," *Annual Review of Biochemistry*, vol. 78, no. 1, pp. 857–902, Jun. 2009.

[121] P. Yang, R. Yan, and M. Fardy, "Semiconductor Nanowire: What's Next?," *Nano Letters*, vol. 10, pp. 1529–1536, May 2010.

[122] F. Greve, S. Frerker, A. G. Bittermann, C. Burkhardt, A. Hierlemann, and H. Hall, “Molecular design and characterization of the neuron–microelectrode array interface,” *Biomaterials*, vol. 28, no. 35, pp. 5246–5258, Dec. 2007.
[123] E. Martinez, E. Engel, C. Lopeziglesias, C. Mills, J. Planell, and J. Samitier, “Focused ion beam/scanning electron microscopy characterization of cell behavior on polymer micro-/nanopatterned substrates: A study of cell–substrate interactions,” *Micron*, vol. 39, no. 2, pp. 111–116, Feb. 2008.
[124] D. Drobne, M. Milani, V. Lešer, F. Tatti, A. Zrimec, N. Žnidaršič, R. Kostanjšek, and J. Štrus, “Imaging of intracellular spherical lamellar structures and tissue gross morphology by a focused ion beam/scanning electron microscope (FIB/SEM),” *Ultramicroscopy*, vol. 108, no. 7, pp. 663–670, Jun. 2008.
[125] G. Cox and C. J. R. Sheppard, “Practical limits of resolution in confocal and non-linear microscopy,” *Microscopy Research and Technique*, vol. 63, no. 1, pp. 18–22, Jan. 2004.
[126] G. E. Murphy, K. Narayan, B. C. Lowekamp, L. M. Hartnell, J. A. W. Heymann, J. Fu, and S. Subramaniam, “Correlative 3D imaging of whole mammalian cells with light and electron microscopy,” *Journal of Structural Biology*, vol. 176, no. 3, pp. 268–278, Dec. 2011.
[127] R. L. Edwards, G. Coles, and W. N. Sharpe, “Comparison of tensile and bulge tests for thin-film silicon nitride,” *Experimental Mechanics*, vol. 44, no. 1, pp. 49–54, Feb. 2004.
[128] E. Lamers, X. F. Walboomers, M. Domanski, G. McKerr, B. M. O’Hagan, C. A. Barnes, L. Peto, R. Luttge, L. A. J. A. Winnubst, H. J. G. E. Gardeniers, and J. A. Jansen, “Cryo DualBeam Focused Ion Beam–Scanning Electron Microscopy to Evaluate the Interface Between Cells and Nanopatterned Scaffolds,” *Tissue Engineering Part C: Methods*, vol. 17, no. 1, pp. 1–7, Jan. 2011.
[129] G. Wrobel, M. Holler, S. Ingebrandt, S. Dieluweit, F. Sommerhage, H. P. Bochem, and A. Offenhausser, “Transmission electron microscopy study of the cell-sensor interface,” *Journal of The Royal Society Interface*, vol. 5, no. 19, pp. 213–222, Feb. 2008.
[130] P. Gnauck, C. Burkhardt, H. Wolburg, and W. Nisch, “Investigation of the Interface Between Biological Cell Tissue and Hard Substrate Materials using CrossBeam Technology,” *Microscopy and Microanalysis*, vol. 11, no. S02, Aug. 2005.
[131] H. K. Edwards, M. W. Fay, S. I. Anderson, C. A. Scotchford, D. M. Grant, and P. D. Brown, “An appraisal of ultramicrotomy, FIBSEM and cryogenic FIBSEM techniques for the sectioning of biological cells on titanium substrates for TEM investigation,” *Journal of Microscopy*, vol. 234, no. 1, pp. 16–25, Apr. 2009.
[132] P. M. Stevenson and A. M. Donald, “Identification of Three Regimes of Behavior for Cell Attachment on Topographically Patterned Substrates,” *Langmuir*, vol. 25, no. 1, pp. 367–376, Jan. 2009.
[133] L. E. McNamara, R. J. McMurray, M. J. P. Biggs, F. Kantawong, R. O. C. Oreffo, and M. J. Dalby, “Nanotopographical Control of Stem Cell Differentiation,” *Journal of Tissue Engineering*, vol. 2010, pp. 1–13, 2010.
[134] J. Park, S. Bauer, K. A. Schlegel, F. W. Neukam, K. von der Mark, and P. Schmuki, “TiO2 Nanotube Surfaces: 15 nm-An Optimal Length Scale of Surface Topography for Cell Adhesion and Differentiation,” *Small*, vol. 5, no. 6, pp. 666–671, Mar. 2009.
[135] E. Yim, R. Reano, S. Pang, A. Yee, C. Chen, and K. Leong, “Nanopattern-induced changes in morphology and motility of smooth muscle cells,” *Biomaterials*, vol. 26, no. 26, pp. 5405–5413, Sep. 2005.
[136] V. Martinelli, G. Cellot, F. M. Toma, C. S. Long, J. H. Caldwell, L. Zentilin, M. Giacca, A. Turco, M. Prato, L. Ballerini, and L. Mestroni, “Carbon Nanotubes Promote Growth and Spontaneous Electrical Activity in Cultured Cardiac Myocytes,” *Nano Letters*, vol. 12, no. 4, pp. 1831–1838, Apr. 2012.
[137] H. Persson, J. P. Beech, L. Samuelson, S. Oredsson, C. N. Prinz, and J. O. Tegenfeldt, “Vertical oxide nanotubes connected by subsurface microchannels,” *Nano Research*, vol. 5, no. 3, pp. 190–198, Feb. 2012.
[138] J. A. W. Heymann, M. Hayles, I. Gestmann, L. A. Giannuzzi, B. Lich, and S. Subramaniam, “Site-specific 3D imaging of cells and tissues with a dual beam microscope,” *Journal of Structural Biology*, vol. 155, no. 1, pp. 63–73, Jul. 2006.
[139] M. S. Schmidt, J. Hübner, and A. Boisen, “Large Area Fabrication of Leaning Silicon Nanopillars for Surface Enhanced Raman Spectroscopy,” *Advanced Materials*, vol. 24, no. 10, pp. OP11–OP18, Mar. 2012.
[140] J. J. Hill, K. Haller, B. Gelfand, and K. J. Ziegler, “Eliminating Capillary Coalescence of Nanowire

Arrays with Applied Electric Fields," *ACS Applied Materials & Interfaces*, vol. 2, no. 7, pp. 1992–1998, Jul. 2010.
[141] M. M. Marques, A. N. Pereira, N. A. Fujihara, F. N. Nogueira, and C. P. Eduardo, "Effect of low-power laser irradiation on protein synthesis and ultrastructure of human gingival fibroblasts," *Lasers in Surgery and Medicine*, vol. 34, no. 3, pp. 260–265, Mar. 2004.
[142] S.-R. Ryoo, Y.-K. Kim, M.-H. Kim, and D.-H. Min, "Behaviors of NIH-3T3 Fibroblasts on Graphene/Carbon Nanotubes: Proliferation, Focal Adhesion, and Gene Transfection Studies," *ACS Nano*, vol. 4, no. 11, pp. 6587–6598, Nov. 2010.
[143] K. Okamoto, "Thickness measurement of a thin oxide layer by secondary electron emission," *Review of Scientific Instruments*, vol. 51, no. 3, p. 302, 1980.
[144] S. Hoffmann, I. Utke, B. Moser, J. Michler, S. H. Christiansen, V. Schmidt, S. Senz, P. Werner, U. Gösele, and C. Ballif, "Measurement of the Bending Strength of Vapor−Liquid−Solid Grown Silicon Nanowires," *Nano Letters*, vol. 6, no. 4, pp. 622–625, Apr. 2006.
[145] S. Munevar, Y. Wang, and M. Dembo, "Traction Force Microscopy of Migrating Normal and H-ras Transformed 3T3 Fibroblasts," *Biophysical Journal*, vol. 80, no. 4, pp. 1744–1757, Apr. 2001.
[146] D. W. Porter, A. F. Hubbs, R. R. Mercer, N. Wu, M. G. Wolfarth, K. Sriram, S. Leonard, L. Battelli, D. Schwegler-Berry, and S. Friend, "Mouse pulmonary dose- and time course-responses induced by exposure to multi-walled carbon nanotubes," *Toxicology*, vol. 269, no. 2–3, pp. 136–147, Mar. 2010.
[147] D. Choi, A. Fung, H. Moon, D. Ho, Y. Chen, E. Kan, Y. Rheem, B. Yoo, and N. Myung, "Transport of living cells with magnetically assembled nanowires," *Biomedical Microdevices*, vol. 9, no. 2, pp. 143–148, Nov. 2006.
[148] N. H. Kwon, M. F. Beaux, C. Ebert, L. Wang, B. E. Lassiter, Y. H. Park, D. N. McIlroy, C. J. Hovde, and G. A. Bohach, "Nanowire-Based Delivery of Escherichia coli O157 Shiga Toxin 1 A Subunit into Human and Bovine Cells," *Nano Letters*, vol. 7, no. 9, pp. 2718–2723, Sep. 2007.
[149] M. Safi, M. Yan, M.-A. Guedeau-Boudeville, H. Conjeaud, V. Garnier-Thibaud, N. Boggetto, A. Baeza-Squiban, F. Niedergang, D. Averbeck, and J.-F. Berret, "Interactions between Magnetic Nanowires and Living Cells: Uptake, Toxicity, and Degradation," *ACS Nano*, vol. 5, no. 7, pp. 5354–5364, Jul. 2011.
[150] G. V. Kulkarni and C. A. McCulloch, "Serum deprivation induces apoptotic cell death in a subset of Balb/c 3T3 fibroblasts," *J. Cell. Sci.*, vol. 107 (Pt 5), pp. 1169–1179, May 1994.
[151] Z. Somosy, "Radiation response of cell organelles," *Micron*, vol. 31, no. 2, pp. 165–181, Apr. 2000.
[152] T. Berthing, C. B. Sørensen, J. Nygård, and K. L. Martinez, "Applications of Nanowire Arrays in Nanomedicine," *Journal of Nanoneuroscience*, vol. 1, no. 1, pp. 3–9, Jun. 2009.
[153] D. J. Holt and D. W. Grainger, "Multinucleated giant cells from fibroblast cultures," *Biomaterials*, vol. 32, no. 16, pp. 3977–3987, Jun. 2011.
[154] J. N. Coleman, U. Khan, W. J. Blau, and Y. K. Gun'ko, "Small but strong: A review of the mechanical properties of carbon nanotube–polymer composites," *Carbon*, vol. 44, no. 9, pp. 1624–1652, Aug. 2006.
[155] C. B. Jacobs, M. J. Peairs, and B. J. Venton, "Review: Carbon nanotube based electrochemical sensors for biomolecules," *Analytica Chimica Acta*, vol. 662, no. 2, pp. 105–127, Mar. 2010.
[156] Z. Liu, S. Tabakman, K. Welsher, and H. Dai, "Carbon nanotubes in biology and medicine: In vitro and in vivo detection, imaging and drug delivery," *Nano Research*, vol. 2, no. 2, pp. 85–120, Mar. 2009.
[157] H. C. Nerl, C. Cheng, A. E. Goode, S. D. Bergin, B. Lich, M. Gass, and A. E. Porter, "Imaging methods for determining uptake and toxicity of carbon nanotubes in vitro and in vivo," *Nanomedicine*, vol. 6, pp. 849–865, Jul. 2011.
[158] H. Nagai and S. Toyokuni, "Differences and similarities between carbon nanotubes and asbestos fibers during mesothelial carcinogenesis: Shedding light on fiber entry mechanism," *Cancer Science*, vol. 103, no. 8, pp. 1378–1390, Aug. 2012.
[159] K. T. Al-Jamal, H. Nerl, K. H. Müller, H. Ali-Boucetta, S. Li, P. D. Haynes, J. R. Jinschek, M. Prato, A. Bianco, K. Kostarelos, and A. E. Porter, "Cellular uptake mechanisms of functionalised multi-walled carbon nanotubes by 3D electron tomography imaging," *Nanoscale*, vol. 3, no. 6, p. 2627, 2011.
[160] J. Lee, B. C. Sayers, K.-S. Chun, H.-C. Lao, J. K. Shipley-Phillips, J. C. Bonner, and R. Langenbach, "Multi-walled carbon nanotubes induce COX-2 and iNOS expression via MAP Kinase-dependent and -independent mechanisms in mouse RAW264.7 macrophages," *Particle and Fibre Toxicology*, vol. 9, no. 1, p. 14, 2012.
[161] D. Pantarotto, R. Singh, D. McCarthy, M. Erhardt, J.-P. Briand, M. Prato, K. Kostarelos, and A.

Bianco, “Functionalized Carbon Nanotubes for Plasmid DNA Gene Delivery,” *Angewandte Chemie International Edition*, vol. 43, no. 39, pp. 5242–5246, Oct. 2004.

[162] C. Ronzani, C. Spiegelhalter, J.-L. Vonesch, L. Lebeau, and F. Pons, “Lung deposition and toxicological responses evoked by multi-walled carbon nanotubes dispersed in a synthetic lung surfactant in the mouse,” *Archives of Toxicology*, vol. 86, no. 1, pp. 137–149, Jul. 2012.

[163] J. P. Ryman-Rasmussen, M. F. Cesta, A. R. Brody, J. K. Shipley-Phillips, J. I. Everitt, E. W. Tewksbury, O. R. Moss, B. A. Wong, D. E. Dodd, M. E. Andersen, and J. C. Bonner, “Inhaled carbon nanotubes reach the subpleural tissue in mice,” *Nature Nanotechnology*, vol. 4, no. 11, pp. 747–751, Oct. 2009.

[164] C. Cheng, K. H. Müller, K. K. K. Koziol, J. N. Skepper, P. A. Midgley, M. E. Welland, and A. E. Porter, “Toxicity and imaging of multi-walled carbon nanotubes in human macrophage cells,” *Biomaterials*, vol. 30, no. 25, pp. 4152–4160, Sep. 2009.

[165] A. B. Maunsbach and B. Afzelius, *Biomedical electron microscopy illustrated methods and interpretations*. San Diego, Calif.: Academic Press, 1999.

[166] P. Jackson, S. P. Lund, G. Kristiansen, O. Andersen, U. Vogel, H. Wallin, and K. S. Hougaard, “An Experimental Protocol for Maternal Pulmonary Exposure in Developmental Toxicology,” *Basic & Clinical Pharmacology & Toxicology*, vol. 108, no. 3, pp. 202–207, Mar. 2011.

[167] J. A. Bourdon, A. T. Saber, N. R. Jacobsen, K. A. Jensen, A. M. Madsen, J. S. Lamson, H. Wallin, P. Møller, S. Loft, C. L. Yauk, and U. B. Vogel, “Carbon black nanoparticle instillation induces sustained inflammation and genotoxicity in mouse lung and liver,” *Particle and Fibre Toxicology*, vol. 9, no. 1, p. 5, 2012.

[168] N. Kobayashi, M. Naya, M. Ema, S. Endoh, J. Maru, K. Mizuno, and J. Nakanishi, “Biological response and morphological assessment of individually dispersed multi-wall carbon nanotubes in the lung after intratracheal instillation in rats,” *Toxicology*, vol. 276, no. 3, pp. 143–153, Oct. 2010.

[169] B. B. Manshian, G. J. Jenkins, P. M. Williams, C. Wright, A. R. Barron, A. P. Brown, N. Hondow, P. R. Dunstan, R. Rickman, K. Brady, and S. H. Doak, “Single-walled carbon nanotubes: differential genotoxic potential associated with physico-chemical properties,” *Nanotoxicology*, vol. 7, no. 2, pp. 144–156, Mar. 2013.

[170] Y. Morimoto, M. Hirohashi, A. Ogami, T. Oyabu, T. Myojo, M. Todoroki, M. Yamamoto, M. Hashiba, Y. Mizuguchi, B. W. Lee, E. Kuroda, M. Shimada, W.-N. Wang, K. Yamamoto, K. Fujita, S. Endoh, K. Uchida, N. Kobayashi, K. Mizuno, M. Inada, H. Tao, T. Nakazato, J. Nakanishi, and I. Tanaka, “Pulmonary toxicity of well-dispersed multi-wall carbon nanotubes following inhalation and intratracheal instillation,” *Nanotoxicology*, vol. 6, no. 6, pp. 587–599, Sep. 2012.

[171] S. R. Choi, N. P. Bansal, and A. Garg, “Mechanical and microstructural characterization of boron nitride nanotubes-reinforced SOFC seal glass composite,” *Materials Science and Engineering: A*, vol. 460–461, pp. 509–515, Jul. 2007.

[172] P. C. Ma, B. Z. Tang, and J.-K. Kim, “Effect of CNT decoration with silver nanoparticles on electrical conductivity of CNT-polymer composites,” *Carbon*, vol. 46, no. 11, pp. 1497–1505, Sep. 2008.

[173] X. Ke, S. Bals, A. Romo Negreira, T. Hantschel, H. Bender, and G. Van Tendeloo, “TEM sample preparation by FIB for carbon nanotube interconnects,” *Ultramicroscopy*, vol. 109, no. 11, pp. 1353–1359, Oct. 2009.

[174] N. A. Monteiro-Riviere, R. J. Nemanich, A. O. Inman, Y. Y. Wang, and J. E. Riviere, “Multi-walled carbon nanotube interactions with human epidermal keratinocytes,” *Toxicology Letters*, vol. 155, no. 3, pp. 377–384, Mar. 2005.

[175] K. Scott, “3D elemental and structural analysis of biological specimens using electrons and ions,” *Journal of Microscopy*, vol. 242, no. 1, pp. 86–93, Apr. 2011.

[176] T. Thurnherr, C. Brandenberger, K. Fischer, L. Diener, P. Manser, X. Maeder-Althaus, J.-P. Kaiser, H. F. Krug, B. Rothen-Rutishauser, and P. Wick, “A comparison of acute and long-term effects of industrial multiwalled carbon nanotubes on human lung and immune cells in vitro,” *Toxicology Letters*, vol. 200, no. 3, pp. 176–186, Feb. 2011.

[177] A. A. Kapralov, W. H. Feng, A. A. Amoscato, N. Yanamala, K. Balasubramanian, D. E. Winnica, E. R. Kisin, G. P. Kotchey, P. Gou, L. J. Sparvero, P. Ray, R. K. Mallampalli, J. Klein-Seetharaman, B. Fadeel, A. Star, A. A. Shvedova, and V. E. Kagan, “Adsorption of Surfactant Lipids by Single-Walled Carbon Nanotubes in Mouse Lung upon Pharyngeal Aspiration,” *ACS Nano*, vol. 6, no. 5, pp. 4147–4156, May 2012.

[178] G. Krasteva, B. J. Canning, T. Papadakis, and W. Kummer, “Cholinergic brush cells in the trachea mediate respiratory responses to quorum sensing molecules,” *Life Sciences*, vol. 91, no. 21–22, pp.

992–996, Nov. 2012.
[179] K. Donaldson, C. A. Poland, F. A. Murphy, M. MacFarlane, T. Chernova, and A. Schinwald, "Pulmonary toxicity of carbon nanotubes and asbestos — Similarities and differences," *Advanced Drug Delivery Reviews*, vol. 65, no. 15, pp. 2078–2086, Dec. 2013.
[180] K. Aschberger, H. J. Johnston, V. Stone, R. J. Aitken, S. M. Hankin, S. A. K. Peters, C. L. Tran, and F. M. Christensen, "Review of carbon nanotubes toxicity and exposure—Appraisal of human health risk assessment based on open literature," *Critical Reviews in Toxicology*, vol. 40, no. 9, pp. 759–790, Oct. 2010.
[181] R. F. Hamilton, Z. Wu, S. Mitra, P. K. Shaw, and A. Holian, "Effect of MWCNT size, carboxylation, and purification on in vitro and in vivo toxicity, inflammation and lung pathology," *Particle and Fibre Toxicology*, vol. 10, no. 1, p. 57, 2013.
[182] H. Nagai, Y. Okazaki, S. H. Chew, N. Misawa, Y. Yamashita, S. Akatsuka, T. Ishihara, K. Yamashita, Y. Yoshikawa, H. Yasui, L. Jiang, H. Ohara, T. Takahashi, G. Ichihara, K. Kostarelos, Y. Miyata, H. Shinohara, and S. Toyokuni, "Diameter and rigidity of multiwalled carbon nanotubes are critical factors in mesothelial injury and carcinogenesis," *Proceedings of the National Academy of Sciences*, vol. 108, no. 49, pp. E1330–E1338, Nov. 2011.
[183] J. Muller, F. Huaux, A. Fonseca, J. B. Nagy, N. Moreau, M. Delos, E. Raymundo-Piñero, F. Béguin, M. Kirsch-Volders, I. Fenoglio, B. Fubini, and D. Lison, "Structural Defects Play a Major Role in the Acute Lung Toxicity of Multiwall Carbon Nanotubes: Toxicological Aspects," *Chemical Research in Toxicology*, vol. 21, no. 9, pp. 1698–1705, Sep. 2008.
[184] X. Wang, T. Xia, S. Addo Ntim, Z. Ji, S. Lin, H. Meng, C.-H. Chung, S. George, H. Zhang, M. Wang, N. Li, Y. Yang, V. Castranova, S. Mitra, J. C. Bonner, and A. E. Nel, "Dispersal State of Multiwalled Carbon Nanotubes Elicits Profibrogenic Cellular Responses That Correlate with Fibrogenesis Biomarkers and Fibrosis in the Murine Lung," *ACS Nano*, vol. 5, no. 12, pp. 9772–9787, Dec. 2011.
[185] H. Ali-Boucetta, A. Nunes, R. Sainz, M. A. Herrero, B. Tian, M. Prato, A. Bianco, and K. Kostarelos, "Asbestos-like Pathogenicity of Long Carbon Nanotubes Alleviated by Chemical Functionalization," *Angewandte Chemie*, vol. 125, no. 8, pp. 2330–2334, Feb. 2013.
[186] L. Lacerda, J. Russier, G. Pastorin, M. A. Herrero, E. Venturelli, H. Dumortier, K. T. Al-Jamal, M. Prato, K. Kostarelos, and A. Bianco, "Translocation mechanisms of chemically functionalised carbon nanotubes across plasma membranes," *Biomaterials*, vol. 33, no. 11, pp. 3334–3343, Apr. 2012.
[187] T. M. Sager, M. W. Wolfarth, M. Andrew, A. Hubbs, S. Friend, T. Chen, D. W. Porter, N. Wu, F. Yang, R. F. Hamilton, and A. Holian, "Effect of multi-walled carbon nanotube surface modification on bioactivity in the C57BL/6 mouse model," *Nanotoxicology*, vol. 8, no. 3, pp. 317–327, May 2014.
[188] Q. Mu, D. L. Broughton, and B. Yan, "Endosomal Leakage and Nuclear Translocation of Multiwalled Carbon Nanotubes: Developing a Model for Cell Uptake," *Nano Letters*, vol. 9, no. 12, pp. 4370–4375, Dec. 2009.
[189] I. Marangon, N. Boggetto, C. Ménard-Moyon, E. Venturelli, M.-L. Béoutis, C. Péchoux, N. Luciani, C. Wilhelm, A. Bianco, and F. Gazeau, "Intercellular Carbon Nanotube Translocation Assessed by Flow Cytometry Imaging," *Nano Letters*, vol. 12, no. 9, pp. 4830–4837, Sep. 2012.
[190] S. S. Poulsen, N. R. Jacobsen, S. Labib, D. Wu, M. Husain, A. Williams, J. P. Bøgelund, O. Andersen, C. Købler, K. Mølhave, Z. O. Kyjovska, A. T. Saber, H. Wallin, C. L. Yauk, U. Vogel, and S. Halappanavar, "Transcriptomic Analysis Reveals Novel Mechanistic Insight into Murine Biological Responses to Multi-Walled Carbon Nanotubes in Lungs and Cultured Lung Epithelial Cells," *PLoS ONE*, vol. 8, no. 11, p. e80452, Nov. 2013.
[191] A. Erdely, A. Liston, R. Salmen-Muniz, T. Hulderman, S.-H. Young, P. C. Zeidler-Erdely, V. Castranova, and P. P. Simeonova, "Identification of Systemic Markers from A Pulmonary Carbon Nanotube Exposure:," *Journal of Occupational and Environmental Medicine*, vol. 53, pp. S80–S86, Jun. 2011.
[192] T. A. Girtsman, C. A. Beamer, N. Wu, M. Buford, and A. Holian, "IL-1R signalling is critical for regulation of multi-walled carbon nanotubes-induced acute lung inflammation in C57Bl/6 mice," *Nanotoxicology*, vol. 8, no. 1, pp. 17–27, Feb. 2014.
[193] J. Muller, F. Huaux, N. Moreau, P. Misson, J.-F. Heilier, M. Delos, M. Arras, A. Fonseca, J. B. Nagy, and D. Lison, "Respiratory toxicity of multi-wall carbon nanotubes," *Toxicology and Applied Pharmacology*, vol. 207, no. 3, pp. 221–231, Sep. 2005.
[194] D. W. Porter, A. F. Hubbs, B. T. Chen, W. McKinney, R. R. Mercer, M. G. Wolfarth, L. Battelli, N. Wu, K. Sriram, S. Leonard, M. Andrew, P. Willard, S. Tsuruoka, M. Endo, T. Tsukada, F. Munekane, D. G. Frazer, and V. Castranova, "Acute pulmonary dose–responses to inhaled multi-walled carbon

nanotubes," *Nanotoxicology*, vol. 7, no. 7, pp. 1179–1194, Nov. 2013.
[195] S. A. Elmore, B. R. Berridge, M. C. Boyle, M. C. Cora, M. J. Hoenerhoff, L. Kooistra, V. A. Laast, J. P. Morrison, D. Rao, M. Rinke, and K. Yoshizawa, "Proceedings of the 2012 National Toxicology Program Satellite Symposium," *Toxicologic Pathology*, vol. 41, no. 2, pp. 151–180, Dec. 2012.
[196] J. Nio, W. Fujimoto, A. Konno, Y. Kon, M. Owhashi, and T. Iwanaga, "Cellular expression of murine Ym1 and Ym2, chitinase family proteins, as revealed by in situ hybridization and immunohistochemistry," *Histochemistry and Cell Biology*, vol. 121, no. 6, May 2004.
[197] I. Waern, J. Jia, G. Pejler, E. Zcharia, I. Vlodavsky, J.-P. Li, and S. Wernersson, "Accumulation of Ym1 and formation of intracellular crystalline bodies in alveolar macrophages lacking heparanase," *Molecular Immunology*, vol. 47, no. 7–8, pp. 1467–1475, Apr. 2010.
[198] J. G. Teeguarden, B.-J. Webb-Robertson, K. M. Waters, A. R. Murray, E. R. Kisin, S. M. Varnum, J. M. Jacobs, J. G. Pounds, R. C. Zanger, and A. A. Shvedova, "Comparative Proteomics and Pulmonary Toxicity of Instilled Single-Walled Carbon Nanotubes, Crocidolite Asbestos, and Ultrafine Carbon Black in Mice," *Toxicological Sciences*, vol. 120, no. 1, pp. 123–135, Dec. 2010.
[199] M. J. Hoenerhoff, M. F. Starost, and J. M. Ward, "Eosinophilic Crystalline Pneumonia as a Major Cause of Death in 129S4/SvJae Mice," *Veterinary Pathology*, vol. 43, no. 5, pp. 682–688, Sep. 2006.
[200] C. Købler, A. T. Saber, N. R. Jacobsen, H. Wallin, U. Vogel, K. Qvortrup, and K. Mølhave, "FIB-SEM imaging of carbon nanotubes in mouse lung tissue," *Analytical and Bioanalytical Chemistry*, Jan. 2014.
[201] Nanogenotox, "Towards a method for detecting the potential genotoxicity of nanomaterials," Mar-2013. [Online]. Available: Available at www.nanogenotox.eu. [Accessed: 28-Apr-2014].
[202] K. Bhattacharya, F. T. Andón, R. El-Sayed, and B. Fadeel, "Mechanisms of carbon nanotube-induced toxicity: Focus on pulmonary inflammation," *Advanced Drug Delivery Reviews*, vol. 65, no. 15, pp. 2087–2097, Dec. 2013.
[203] M. Feldmesser, Y. Kress, and A. Casadevall, "Intracellular Crystal Formation as a Mechanism of Cytotoxicity in Murine Pulmonary Cryptococcus neoformans Infection," *Infection and Immunity*, vol. 69, no. 4, pp. 2723–2727, Apr. 2001.
[204] L. Guo, "Biochemical Characterization of Endogenously Formed Eosinophilic Crystals in the Lungs of Mice," *Journal of Biological Chemistry*, vol. 275, no. 11, pp. 8032–8037, Mar. 2000.
[205] A. B. Murray and A. Luz, "Acidophilic macrophage pneumonia in laboratory mice," *Vet. Pathol.*, vol. 27, no. 4, pp. 274–281, Jul. 1990.
[206] A. A. Humbles, B. Lu, D. S. Friend, S. Okinaga, J. Lora, Al-garawi A., T. R. Martin, N. P. Gerard, and C. Gerard, "The murine CCR3 receptor regulates both the role of eosinophils and mast cells in allergen-induced airway inflammation and hyperresponsiveness," *Proceedings of the National Academy of Sciences*, vol. 99, no. 3, pp. 1479–1484, Feb. 2002.
[207] R.-F. Guo, A. B. Lentsch, R. L. Warner, M. Huber-Lang, J. V. Sarma, T. Hlaing, M. M. Shi, N. W. Lukacs, and P. A. Ward, "Regulatory Effects of Eotaxin on Acute Lung Inflammatory Injury," *The Journal of Immunology*, vol. 166, no. 8, pp. 5208–5218, Apr. 2001.
[208] H. Heath, S. Qin, P. Rao, L. Wu, G. LaRosa, N. Kassam, P. D. Ponath, and C. R. Mackay, "Chemokine receptor usage by human eosinophils. The importance of CCR3 demonstrated using an antagonistic monoclonal antibody.," *Journal of Clinical Investigation*, vol. 99, no. 2, pp. 178–184, Jan. 1997.
[209] C. Ben-Yehuda, R. Bader, I. Puxeddu, F. Levi-Schaffer, R. Breuer, and N. Berkman, "Airway eosinophil accumulation and eotaxin-2/CCL24 expression following allergen challenge in BALB/c mice," *Experimental Lung Research*, vol. 34, no. 8, pp. 467–479, Jan. 2008.
[210] A. T. Saber, J. S. Lamson, N. R. Jacobsen, G. Ravn-Haren, K. S. Hougaard, A. N. Nyendi, P. Wahlberg, A. M. Madsen, P. Jackson, H. Wallin, and U. Vogel, "Particle-Induced Pulmonary Acute Phase Response Correlates with Neutrophil Influx Linking Inhaled Particles and Cardiovascular Risk," *PLoS ONE*, vol. 8, no. 7, p. e69020, Jul. 2013.
[211] X. Wang, J. J. Zang, H. Wang, H. Nie, T. C. Wang, X. Y. Deng, Y. Q. Gu, Z. H. Liu, and G. Jia, "Pulmonary Toxicity in Mice Exposed to Low and Medium Doses of Water-Soluble Multi-Walled Carbon Nanotubes," *Journal of Nanoscience and Nanotechnology*, vol. 10, no. 12, pp. 8516–8526, Dec. 2010.
[212] S. Treumann, L. Ma-Hock, S. Groters, R. Landsiedel, and B. van Ravenzwaay, "Additional Histopathologic Examination of the Lungs from a 3-Month Inhalation Toxicity Study with Multiwall Carbon Nanotubes in Rats," *Toxicological Sciences*, vol. 134, no. 1, pp. 103–110, Apr. 2013.
[213] M. . van Zweiten, C. Zurcher, H. A. Solleveld, and C. F. Hollander, *Immunological techniques applied to aging research*. Boca Raton, Fla: CRC Press, 1981.

[214] M. Husain, A. T. Saber, C. Guo, N. R. Jacobsen, K. A. Jensen, C. L. Yauk, A. Williams, U. Vogel, H. Wallin, and S. Halappanavar, "Pulmonary instillation of low doses of titanium dioxide nanoparticles in mice leads to particle retention and gene expression changes in the absence of inflammation," *Toxicology and Applied Pharmacology*, vol. 269, no. 3, pp. 250–262, Jun. 2013.

[215] U. C. Nygaard, J. S. Hansen, M. Samuelsen, T. Alberg, C. D. Marioara, and M. Lovik, "Single-Walled and Multi-Walled Carbon Nanotubes Promote Allergic Immune Responses in Mice," *Toxicological Sciences*, vol. 109, no. 1, pp. 113–123, Mar. 2009.

[216] A. Saber, N. Jacobsen, A. Mortensen, J. Szarek, P. Jackson, A. Madsen, K. Jensen, I. K. Koponen, G. Brunborg, K. Gützkow, U. Vogel, and H. Wallin, "Nanotitanium dioxide toxicity in mouse lung is reduced in sanding dust from paint," *Particle and Fibre Toxicology*, vol. 9, no. 1, p. 4, 2012.

[217] A. T. Saber, I. K. Koponen, K. A. Jensen, N. R. Jacobsen, L. Mikkelsen, P. Møller, S. Loft, U. Vogel, and H. Wallin, "Inflammatory and genotoxic effects of sanding dust generated from nanoparticle-containing paints and lacquers," *Nanotoxicology*, vol. 6, no. 7, pp. 776–788, Nov. 2012.

[218] F. T. Andón, A. A. Kapralov, N. Yanamala, W. Feng, A. Baygan, B. J. Chambers, K. Hultenby, F. Ye, M. S. Toprak, B. D. Brandner, A. Fornara, J. Klein-Seetharaman, G. P. Kotchey, A. Star, A. A. Shvedova, B. Fadeel, and V. E. Kagan, "Biodegradation of Single-Walled Carbon Nanotubes by Eosinophil Peroxidase," *Small*, vol. 9, no. 16, pp. 2721–2729, Aug. 2013.

[219] C. A. Beamer, T. A. Girtsman, B. P. Seaver, K. J. Finsaas, C. T. Migliaccio, V. K. Perry, J. B. Rottman, D. E. Smith, and A. Holian, "IL-33 mediates multi-walled carbon nanotube (MWCNT)-induced airway hyper-reactivity via the mobilization of innate helper cells in the lung," *Nanotoxicology*, vol. 7, no. 6, pp. 1070–1081, Sep. 2013.

[220] K. Inoue, E. Koike, R. Yanagisawa, S. Hirano, M. Nishikawa, and H. Takano, "Effects of multi-walled carbon nanotubes on a murine allergic airway inflammation model," *Toxicology and Applied Pharmacology*, vol. 237, no. 3, pp. 306–316, Jun. 2009.

[221] M. Harbord, "Ym1 Is a Neutrophil Granule Protein That Crystallizes in p47phox-deficient Mice," *Journal of Biological Chemistry*, vol. 277, no. 7, pp. 5468–5475, Feb. 2002.

[222] N.-C. A. Chang, "A Macrophage Protein, Ym1, Transiently Expressed during Inflammation Is a Novel Mammalian Lectin," *Journal of Biological Chemistry*, vol. 276, no. 20, pp. 17497–17506, May 2001.

[223] V. Raffa, G. Ciofani, S. Nitodas, T. Karachalios, D. D'Alessandro, M. Masini, and A. Cuschieri, "Can the properties of carbon nanotubes influence their internalization by living cells?," *Carbon*, vol. 46, no. 12, pp. 1600–1610, Oct. 2008.

[224] P. Thevenaz, U. E. Ruttimann, and M. Unser, "A pyramid approach to subpixel registration based on intensity," *IEEE Transactions on Image Processing*, vol. 7, no. 1, pp. 27–41, Jan. 1998.

[225] E. H. W. Meijering, W. J. Niessen, and M. A. Viergever, "Quantitative evaluation of convolution-based methods for medical image interpolation," *Medical Image Analysis*, vol. 5, no. 2, pp. 111–126, Jun. 2001.

[226] D. W. Fawcett, *A textbook of histology*, 12th ed. New York: Chapman & Hall, 1986.

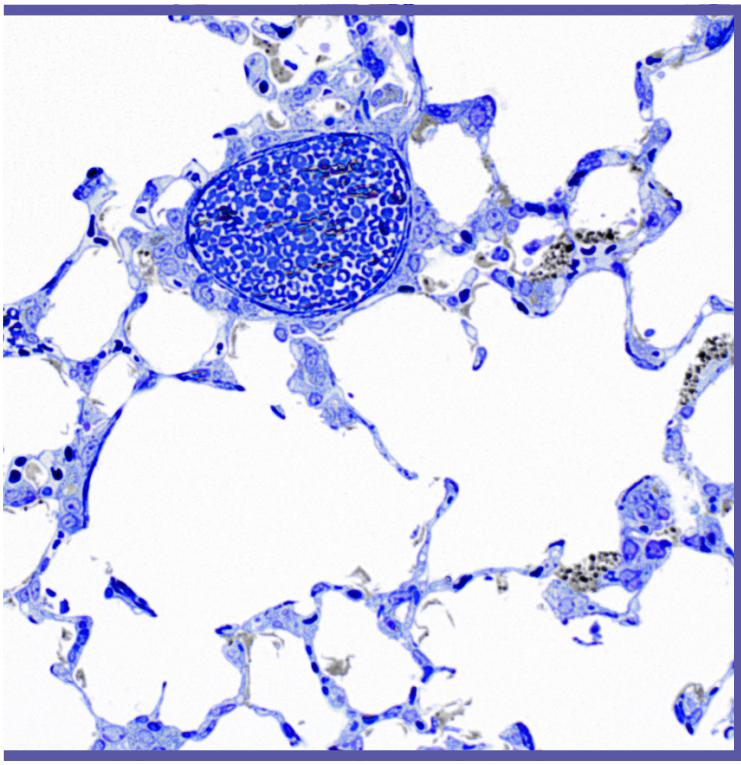

Published by:
DTU Nanotech
Department of Micro- and Nanotechnology
Technical University of Denmark
Ørsteds Plads, building 345B
DK-2800 Kgs. Lyngby